A microcavity-enhanced spin–photon interface for color centers in diamond

Kerim Köster

Karlsruhe 2026

A microcavity-enhanced spin–photon interface for color centers in diamond

Zur Erlangung des akademischen Grades eines

Doktors der Naturwissenschaften (Dr. rer. nat.)

von der KIT-Fakultät für Physik des
Karlsruher Instituts für Technologie
angenommene

Dissertation

von

Kerim Köster, M.Sc.

aus Karlsruhe

Tag der mündlichen Prüfung: 13.02.2026
Erster Gutachter: Prof. Dr. David Hunger
Zweiter Gutachter: Prof. Dr. Wolfgang Wernsdorfer

Abstract

Realizing long-distance quantum networks requires efficient interfaces between photons and stationary quantum memories. Color centers in diamond constitute a promising solid-state platform for spin–photon interfaces, owing to their spin-selective optical transitions, long memory times, and efficient spin control. These properties enabled the first demonstration of a three-node quantum network based on nitrogen-vacancy centers in diamond; however, further scaling was hindered by the limited collection efficiency of coherent photons. This limitation motivates continued development of improved spin–photon interfaces, necessitating efficient coupling between spin defects and optical cavities, as well as the exploration of alternative color centers that intrinsically emit a larger fraction of coherent photons. Here, we present a combined approach that integrates a fiber-based microcavity platform for efficient light–matter coupling with tin-vacancy centers in diamond featuring intrinsically favorable optical properties.

This dissertation demonstrates the successful integration of a fully tunable fiber-based Fabry–Pérot microcavity platform into a dilution refrigerator. The resulting system enables exceptionally low mechanical-noise operation, achieving passive stability below 10 pm in an open configuration and below 1 pm when the fiber and planar mirror are in mechanical contact, at a cavity temperature of 1 K. As a result, this platform allows operation at high cavity finesses and correspondingly large light–matter coupling, while accessing a temperature regime in which phonon-induced spin decoherence is strongly suppressed.

Furthermore, we present the complete process from commercially available diamond plates to tin-vacancy–hosting, cavity-integrated diamond membranes. Through careful sample preparation and cavity integration, we demonstrate operation of the hybrid cavity in a regime where the high-refractive-index of diamond can be exploited to concentrate the cavity field within the diamond region, thereby achieving enhanced light–matter coupling. This regime is usually challenging to access due to diamond surface imperfections and the resulting scattering losses.

The experimental platform is subsequently used to demonstrate Purcell-enhanced emission from individual tin-vacancy centers in diamond. We observe a Purcell-induced reduction of the excited-state lifetime corresponding to a cooperativity of up to $C_0 = 4.1$ for a diamond-confined cavity mode, nearly twice the value obtained for an air-confined mode ($C_0 = 2.2$), attributable to careful sample preparation and cavity integration. Operating in this high-cooperativity regime, we observe pronounced emitter-induced extinction in the cavity transmission probed with a weak coherent field, evidencing coherent coupling between a tin-vacancy center and the microcavity. The measured extinction contrast of

$C = 0.81$ corresponds to a coherent cooperativity of $C = 1.4$. Finally, the application of an external magnetic field lifts the degeneracy of the spin sublevels, allowing the resulting Zeeman splitting of the optical transition to be resolved in the cavity transmission. This represents a substantial step toward a microcavity-enhanced spin–photon interface for tin-vacancy centers in diamond, relevant to the realization of memory-assisted long-distance quantum networks.

In contrast to the single-emitter cavity quantum electrodynamics regime explored throughout much of this thesis, we also investigate a distinctly different regime in which an ensemble of emitters is collectively coupled to a microcavity, enabling the study of collective light–matter effects mediated by a shared radiation field. Coupling a small ensemble of approximately 15 nitrogen-vacancy centers to the cavity reveals experimental signatures of collective emission and superfluorescence. While not directly motivated by quantum-network applications, these results highlight the broader scope of cavity quantum optics experiments with color centers in diamond.

Zusammenfassung

Die Realisierung von Quantennetzwerken über große Distanzen erfordert effiziente Schnittstellen zwischen Photonen und stationären Quantenspeichern. Farbzentren in Diamant stellen hierfür eine vielversprechende festkörperbasierte Plattform für Spin–Photon-Schnittstellen dar, da sie spinselektive optische Übergänge, lange Speicherzeiten und eine effiziente Spinkontrolle aufweisen. Diese Eigenschaften ermöglichten die erste Demonstration eines Quantennetzwerks mit drei Knoten auf Basis von Stickstoff-Fehlstellen-Zentren in Diamant. Eine Skalierung auf Netzwerke mit mehr als drei Knoten wurde jedoch bislang durch die begrenzte Aufsammeleffizienz kohärenter Photonen verhindert. Diese Einschränkung motiviert die kontinuierliche Weiterentwicklung effizienterer Spin–Photon-Schnittstellen, wobei sowohl die Kopplung von Spindefekten an optische Resonatoren als auch die Erforschung alternativer Farbzentren, die intrinsisch einen größeren Anteil kohärenter Photonen emittieren, von zentraler Bedeutung sind. Hier wird ein kombinierter Ansatz präsentiert, der die Integration von Zinn-Fehlstellen-Zentren mit intrinsisch vorteilhaften optischen Eigenschaften in eine faserbasierte Mikroresonator-Plattform zur effizienten Licht–Materie-Wechselwirkung realisiert.

Diese Arbeit demonstriert die Integration einer vollständig durchstimmbaren faserbasierten Fabry–Pérot-Mikroresonatorplattform in einen Entmischungskryostaten. Das System kann bei extrem niedrigem mechanischem Rauschen betrieben werden und erreicht passive Stabilitäten des Spiegelabstands von unter 10 pm in offener Konfiguration sowie unter 1 pm bei mechanischem Kontakt zwischen Faser- und planarem Spiegel, jeweils bei einer Resonatortemperatur von 1 K. Dadurch lässt sich die Plattform bei hoher Finesse und entsprechend starker Licht–Materie-Wechselwirkung in einem Temperaturregime betreiben, in dem phononinduzierte Spin-Dekohärenz stark unterdrückt ist.

Darüber hinaus präsentieren wir den vollständigen Prozess von kommerziell verfügbaren Diamantsubstraten bis hin zu resonatorintegrierten Diamantmembranen mit eingebetteten Zinn-Fehlstellen-Zentren. Durch sorgfältige Probenpräparation und -integration können wir den hybriden Luft–Diamant-Resonator in einem Regime betreiben, in dem die hohe Brechzahl der Diamantmembran genutzt wird, um das Feld in der Diamantregion zu konzentrieren. Dieses Regime, in dem die Licht–Materie-Wechselwirkung besonders stark ist, ist typischerweise schwer zugänglich, da Oberflächenrauigkeit an der Diamant-Luft-Grenzfläche mit hohen Streuverlusten einhergeht.

Die präsentierte experimentelle Plattform wird anschließend genutzt, um Purcell-verstärkte Emission von einzelnen Zinn-Fehlstellen-Zentren in Diamant zu demonstrieren. Wir beobachten eine Purcell-induzierte Verkürzung der Lebensdauer des optisch angeregten

Zustands für eine diamantkonzentrierte Resonatormode, die einer Kooperativität von bis zu $C_0 = 4.1$ entspricht. Dieser Wert ist etwa doppelt so hoch wie der für eine luftkonzentrierte Mode beobachtete Wert ($C_0 = 2.2$) und lässt sich auf die sorgfältige Probenpräparation sowie die damit verbundenen geringen Streuverluste zurückführen. In diesem Regime hoher Kooperativität weisen wir zudem kohärente Kopplung zwischen einem Zinn-Fehlstellen-Zentrum und dem Mikroresonator nach, die sich experimentell in einer emitterinduzierten Extinktion in der Resonatortransmission äußert und mittels eines schwachen kohärenten Feldes ausgelesen wird. Aus dieser Messung wird eine kohärente Kooperativität von $C = 1.4$ extrahiert, entsprechend einem Extinktionskontrast von $\mathcal{C} = 0.81$. Schließlich wird durch Anlegen eines externen Magnetfeldes die Entartung der Spin-Unterzustände aufgehoben, sodass die resultierende Zeeman-Aufspaltung spin-selektiver optischer Übergänge in der Transmission aufgelöst werden kann. Diese Ergebnisse stellen einen entscheidenden Schritt hin zu einer mikroresonatorverstärkten Spin–Photon-Schnittstelle für Zinn-Fehlstellen-Zentren in Diamant dar, die eine zentrale Voraussetzung für quantenspeicherassistierte Quantennetzwerke über große Distanzen bildet.

Im Kontrast zum Einzelemitter-Regime, das im Großteil der vorliegenden Arbeit untersucht wird, betrachten wir zusätzlich ein grundlegend anderes Regime, in dem ein Ensemble von Emittern kollektiv an einen Mikroresonator gekoppelt ist. Dieses ermöglicht die Untersuchung kollektiver Effekte der Licht–Materie-Wechselwirkung, die durch ein gemeinsames Strahlungsfeld vermittelt werden. Durch die Kopplung eines kleinen Ensembles von etwa 15 Stickstoff-Fehlstellen-Zentren an die optische Mode weisen wir experimentelle Signaturen kollektiver Emission und Superfluoreszenz nach. Auch wenn diese Experimente nicht direkt durch Anwendungen in Quantennetzwerken motiviert sind, verdeutlichen die Ergebnisse die breite Reichweite und Vielseitigkeit resonatorbasierter quantenoptischer Experimente mit Farbzentren in Diamant.

Contents

1. Introduction 1

2. Color centers in diamond 9
2.1. The nitrogen–vacancy center 9
2.1.1. Optical properties 10
2.2. The tin–vacancy center 13
2.2.1. Inversion symmetry of group-IV color centers 14
2.2.2. Optical properties 15
2.2.3. Temperature requirements 18
2.2.4. Coherent spin control 20

3. Light–matter interaction in optical Fabry–Pérot resonators 23
3.1. Optical Fabry–Pérot resonators 23
3.1.1. Geometry and resonance condition 23
3.1.2. Finesse, linewidth and quality factor 24
3.1.3. Transverse mode profile and mode volume 25
3.2. Light–matter interaction: a dipole in a Fabry–Pérot cavity 27
3.2.1. Jaynes–Cummings Hamiltonian with external drive 27
3.2.2. Cavity and emitter damping 28
3.2.3. Heisenberg–Langevin equations 29
3.2.4. The Purcell effect 31
3.2.5. Transmission, reflection and scattering of a weak drive 32
3.2.6. Saturation 36
3.2.7. Real-world degradations 38
3.3. Collective effects in Fabry–Pérot cavities 41
3.3.1. Tavis–Cummings Hamiltonian and Master equation 41
3.3.2. Bad cavity limit and identical emitters 42
3.3.3. Collective Dicke basis 43
3.3.4. Collective emission rate: coherent vs. incoherent 44
3.3.5. Photon statistics 46

4. A cryogenic cavity QED platform for solid-state quantum optics 49
4.1. Fiber-based Fabry-Pérot microcavities 49
4.1.1. Mirror fabrication 51
4.2. Qlibri microcavity platform 54
4.2.1. Description of the main parts 54
4.2.2. Typical operation 57

4.3. Integration of the Qlibri microcavity platform into the Qinu dilution refrigerator . . . 61
4.3.1. Cavity thermalization and cryogenic cooldown . . . 62
4.3.2. Mechanical stability . . . 63
4.4. Superconducting magnetic field coil . . . 71
4.4.1. Integration into cavity and cryostat . . . 72
4.4.2. Simulation . . . 73
4.5. Conclusion and Outlook . . . 74

5. Tin-vacancy centers in diamond membranes integrated into open microcavities 77
5.1. From bulk diamond to cavity-integrated SnV membranes . . . 77
5.1.1. Raw material and surface polish . . . 77
5.1.2. SnV center formation . . . 79
5.1.3. Optical and spectroscopic pre-characterization . . . 81
5.1.4. Cavity integration . . . 84
5.2. A hybrid diamond–air cavity . . . 87
5.2.1. Electric field distribution . . . 87
5.2.2. Cavity linewidth, effective cavity length, and Purcell factor . . . 89
5.2.3. Absorption and scattering loss . . . 92
5.2.4. Mode dispersion . . . 94
5.2.5. Experimental performance of the hybrid cavity . . . 95
5.3. Conclusion and Outlook . . . 99

6. An efficient spin-photon interface for tin-vacancy centers in diamond . . . 101
6.1. Experimental setup . . . 101
6.2. Purcell-enhanced emission of single SnV centers . . . 103
6.2.1. SnV detection via cavity dispersion scans . . . 103
6.2.2. Hyperspectral fluorescence maps . . . 105
6.2.3. Cavity-enhanced ZPL count rate . . . 108
6.2.4. Purcell-effect of single SnV centers . . . 110
6.3. Cooperative coupling of a single SnV center and a microcavity . . . 116
6.3.1. Extinction signal in the cavity transmission profile . . . 117
6.3.2. Charge stability . . . 122
6.3.3. Zeeman splitting . . . 124
6.4. Spin-selective cavity transmission: analysis and outlook . . . 128

7. Cavity-mediated collective emission from few emitters in a diamond membrane 133
7.1. Experimental platform . . . 134
7.2. Cavity-enhanced ensemble fluorescence . . . 137
7.3. Photon statistics . . . 139
7.3.1. Few-emitter (anti-)bunching . . . 140
7.3.2. Collective bunching . . . 144
7.4. Numerical analysis . . . 145
7.4.1. Superlinear power dependence . . . 146
7.4.2. Photon statistics . . . 148

7.5. Conclusion and outlook 149

8. Conclusion and outlook 151

A. Appendix 157
A.1. Useful dissipator relations 157
A.2. Purcell rate starting from the hybridized decay rates 157
A.3. Transmission and reflection 158
A.4. Noise spectra of the Qinu gas handling system 159
A.5. Detailed data on Stuttgart samples 160
A.6. End-to-end detection efficiency 162
A.7. Three more SnVs showing extinction 164
A.8. Charge stability in terms of photon budget 164
A.9. List of symbols 167
A.10. List of abbreviations 170

List of Figures 173

List of Tables 175

Bibliography 177

1. Introduction

More than a century ago, quantum mechanics was developed as a fundamental theory of nature to resolve some of the most puzzling contradictions in physics at the time [1, 2, 3, 4]. Many of its core concepts, such as the intrinsic randomness of measurement outcomes and quantum entanglement, appeared highly counterintuitive and abstract. Over time, however, quantum mechanics became the foundation of many modern technologies, enabling developments such as lasers, nuclear magnetic resonance imaging, and semiconductor devices, which are now routinely used in everyday applications. These technologies rely on the macroscopic behavior of large ensembles of quantum systems, where individual quantum effects are effectively averaged over many particles.

Advances in fabrication, cryogenics, and control techniques, driven by decades of technological progress, have made it possible to prepare, manipulate, and measure individual quantum systems. This capability allows not only the use of ensemble-based quantum technologies, but also the controlled exploitation of quantum properties at the level of individual systems, most notably entanglement [5]. Prominent platforms for such single-system control include trapped ions and neutral atoms, superconducting qubits, and solid-state spin qubits such as quantum dots and color centers in solids.

The ability to control individual quantum systems enables a range of emerging technologies, including quantum simulation [6], quantum sensing [7], quantum communication [8, 9], and quantum computation [10]. Among these, the realization of scalable quantum computers is one of the most technologically challenging goals in modern physics and engineering. While major challenges remain, in particular with respect to scaling and error correction, recent progress across different experimental platforms [11, 12, 13] indicates that useful quantum processors may eventually complement classical high-performance computing infrastructures, promising substantial advantages for specific tasks and algorithms [14].

The development of large-scale quantum computers would, however, have consequences that extend beyond computation itself. In particular, many widely used public-key cryptographic schemes rely on the assumed computational hardness of certain mathematical problems—an assumption that cannot be expected to remain valid over long timescales [15, 16]. Since information encrypted today may need to remain confidential for decades, this motivates cryptographic approaches that remain secure even in the presence of future advances in computational power. This consideration resulted in strong interest in communication protocols whose security does not rely on computational complexity, but is instead guaranteed by fundamental physical principles.

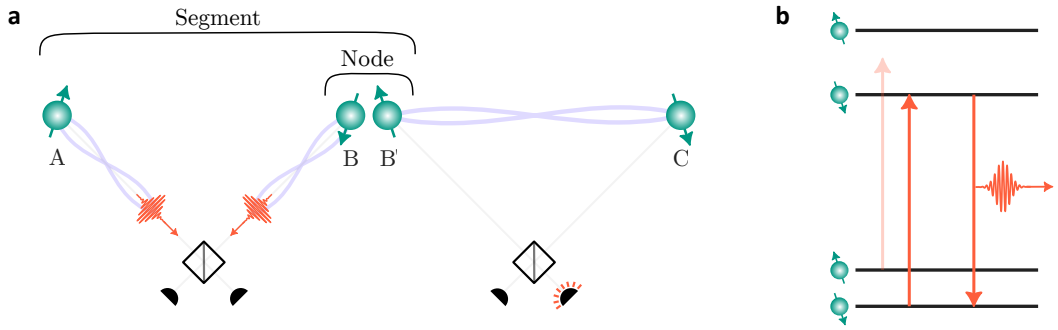

Figure 1.1: Quantum repeater scheme. (a) The quantum channel between the end nodes A and C is divided into two segments. Within each segment, local spin–photon entanglement is generated and converted into spin–spin entanglement via two-photon interference and heralded detection. A joint measurement of the two stationary qubits B and B' at the intermediate node performs entanglement swapping, thereby transferring the entanglement originally shared between A–B and B'–C onto the distant end nodes A and C. **(b)** Spin–photon entanglement is generated via spin-dependent optical transitions, where resonant excitation addresses only one spin state, resulting in an emission-based spin–photon entangled state.

In this context, quantum mechanics presents both the challenge and the solution: while it enables new forms of cryptographic attacks, it also provides the basis for quantum key distribution (QKD), which offers information-theoretic security and long-term confidentiality [17, 18]. Based on fundamental principles of quantum mechanics, and in particular the no-cloning theorem, QKD exploits the fact that any attempt to eavesdrop on a quantum channel necessarily disturbs the transmitted quantum states and leaves a detectable signature. QKD systems are already commercially available and are deployed in applications requiring long-term data confidentiality.

However, photon loss in optical fibers increases exponentially with distance, even at telecommunication wavelengths, which fundamentally limits the range of direct quantum communication. For this reason, QKD is currently implemented either over relatively short fiber links or, for long distances, using free-space satellite links [19, 20]. While satellite quantum communication allows QKD over intercontinental distances [21, 22], such approaches typically rely on trusted nodes and therefore do not provide end-to-end security. Overcoming this limitation, and enabling end-to-end security over long distances, requires a different approach, commonly referred to as a quantum repeater (QR). Although here motivated by security considerations, the quantum repeater, and more generally the infrastructure often referred to as the quantum internet [8], also enables further applications, such as distributed and blind quantum computing [23, 24] and distributed quantum sensing [25, 26].

Quantum repeaters and spin–photon interfaces. While point-to-point quantum communication protocols such as quantum key distribution can be implemented without entanglement, extending quantum communication to long distances fundamentally relies

on shared entanglement. Rather than transmitting fragile quantum states directly across a lossy channel, quantum repeaters distribute quantum information by establishing entanglement between distant stationary quantum memories, which serves as a resource to distribute quantum information.

To make this idea more concrete, we introduce the main building blocks of quantum repeaters and outline the physical concept of entanglement distribution via emission-based, heralded entanglement generation, as illustrated in Fig. 1.1a. For a general overview on the variety of QR architectures, we refer to [27].

(i) The **spin–photon interface** maps the quantum state of a stationary qubit (spin) onto a photonic degree of freedom (flying qubit), thereby generating spin–photon entanglement. The stationary qubit simultaneously acts as a quantum memory, enabling asynchronous operation across different network segments.

(ii) Spin–photon entanglement is projected onto spin–spin entanglement by a **projective measurement** at a central station, where interference of photons erases which-path information and detection events provide a heralding signal.

(iii) Entanglement across individual repeater segments is extended via **entanglement swapping**, performed through local joint measurements on stationary qubits at repeater nodes.

(iv) A **classical communication channel** distributes measurement outcomes between nodes, enabling heralded operation and correction for global phase shifts.

We now focus on the creation of spin–photon and, subsequently, spin–spin entanglement to illustrate the underlying physical principles of node-sends-photon quantum repeater protocols. Two spatially separated nodes, labeled A and B, each host a stationary qubit. The stationary spins are locally prepared in coherent superposition states,

$$|\psi_A\rangle = \frac{1}{\sqrt{2}}\left(|\uparrow\rangle_A + |\downarrow\rangle_A\right), \qquad |\psi_B\rangle = \frac{1}{\sqrt{2}}\left(|\uparrow\rangle_B + |\downarrow\rangle_B\right), \tag{1.0.1}$$

where $|\uparrow\rangle$ and $|\downarrow\rangle$ denote the spin states of the stationary qubit. If the stationary qubit exhibits spin-dependent optical transitions, this superposition can be coherently mapped onto a joint spin–photon state, thereby generating spin–photon entanglement as illustrated in Fig. 1.1b. The photonic qubit may be encoded, for example, in time bins, polarization, or photon number, resulting in the local entangled states

$$|\Psi\rangle_A = \frac{1}{\sqrt{2}}\left(|\uparrow\rangle_A |0\rangle_a + |\downarrow\rangle_A |1\rangle_a\right), \qquad |\Psi\rangle_B = \frac{1}{\sqrt{2}}\left(|\uparrow\rangle_B |0\rangle_b + |\downarrow\rangle_B |1\rangle_b\right), \tag{1.0.2}$$

where the subscripts a and b label the photonic modes emitted from nodes A and B, respectively, with $|0\rangle$ and $|1\rangle$ denoting photon-number states. The photonic modes propagate to a central station, where they interfere on a beam splitter and are subsequently detected, erasing which-path information. Conditioned on a successful single-photon detection

event, where the origin of the detected photon is fundamentally indistinguishable, the combined spin–photon state is projected onto a spin–spin entangled state of the form

$$|\Psi_{\text{spin}}\rangle = \frac{1}{\sqrt{2}} \left(|\uparrow_A \downarrow_B\rangle \pm |\downarrow_A \uparrow_B\rangle \right), \tag{1.0.3}$$

Unwanted two-photon events, which would project onto separable states such as $|\uparrow_A \uparrow_B\rangle$, are suppressed or filtered depending on the specific entanglement-generation protocol.

The entanglement established between stationary qubits at neighboring nodes can be extended to non-neighbouring nodes by local joint measurements, known as entanglement swapping, and sequentially propagated along the full quantum channel. In this way, long-distance quantum correlations are created without directly transmitting fragile quantum states over the entire channel. Depending on the achieved entanglement fidelities and the number of repeater segments, this strategy can outperform direct transmission in terms of loss scaling and achievable rates, a regime commonly referred to as quantum repeater superiority.

Quantum networks based on color centers in diamond. Across a range of material platforms, major milestones toward quantum networks have been demonstrated, including loophole-free Bell tests, spin–photon entanglement, and photon-mediated remote spin–spin entanglement. In particular, trapped neutral atoms [28, 29, 30], trapped ions [31, 32, 33], semiconductor quantum dots [34, 35, 36], rare-earth ions [37, 38, 39], and color centers in diamond [40, 41, 42, 43] have each demonstrated key primitives relevant for quantum communication and repeater architectures, and are actively pursued as candidate platforms for quantum networks.

The various platforms differ in their achievable coherence and memory times, in the quality of their optical interfaces, including the indistinguishability and collection efficiency of coherently emitted photons, and in their prospects for scaling and experimental complexity. Atomic systems offer excellent coherence and control, but typically rely on sophisticated trapping infrastructure, whereas solid-state approaches are more readily compatible with nanophotonic integration and on-chip architectures.

Within this landscape, color centers in diamond, and in particular the nitrogen-vacancy (NV) center, have enabled some of the most advanced quantum network demonstrations to date, including entanglement distribution across three spatially separated nodes [44]. A key enabling factor is the combination of an optically addressable electronic spin with nearby nuclear-spin memories, which provide long storage times together with high-fidelity optical readout and coherent control [45, 46, 47, 48]. This architecture allows multiple networking primitives to be implemented within a single experimental platform. In the reported three-node network experiment, the achieved heralded entanglement rate between distant quantum memories was approximately $1/(40\,\text{s})$, which currently limits scaling to larger networks. This rate is primarily constrained by the collection efficiency of coherently emitted NV photons, a limitation that can be addressed through the use of optical cavities and/or alternative color centers with a higher fraction of coherent photon

emission. For a general overview of achievements and challenges in color-center-based quantum networks, we refer to Refs. [49, 50].

Towards efficient photonic interfaces for scalable color-center-based quantum networks

The collection efficiency of coherently emitted photons from NV centers under resonant excitation is limited to the level of $\sim 10^{-3}$, which constitutes a major bottleneck for scaling few-node demonstrations toward larger quantum networks. Overcoming this limitation requires both efficient photonic interfaces that enhance light–matter interaction and photon collection, and emitter systems that intrinsically provide a high fraction of indistinguishable photons. In the context of color-center-based quantum networks, this challenge is addressed through the combination of optical cavities and group-IV color centers in diamond.

Photonic cavities are a central tool for enhancing light–matter interaction at the level of single quantum emitters. By modifying the local optical density of states, a cavity introduces an additional radiative decay channel that accelerates photon emission into a well-defined cavity mode via the Purcell effect [51]. This enhancement increases both the fraction of coherently emitted photons and their collection efficiency, and enables efficient interfacing with waveguides or optical fibers for quantum networking applications. More generally, optical cavities allow access to regimes of coherent light–matter interaction that are not available in free space. In cavity quantum electrodynamics (cQED), sufficiently strong emitter–photon coupling leads to deterministic dynamics between single photons and quantum emitters [52], and in the strong coupling regime to a reversible exchange of excitations and the formation of hybrid light–matter states [53, 54]. A wide range of cavity architectures has been developed and studied in this context, with nanophotonic cavities and open-access microcavities being the most prominent platforms for color centers in diamond. Nanophotonic architectures offer ultrasmall mode volumes, often well below a cubic optical wavelength, enabling large light–matter coupling strengths [55]. In contrast, open-access microcavities provide spectral and spatial tunability as well as flexible emitter integration, while still enabling substantial Purcell enhancement through high cavity finesse [56]. Both approaches have demonstrated promising performance for cavity QED with solid-state quantum emitters.

In parallel, **group-IV color centers** in diamond have been identified as promising alternatives to the NV center due to their superior optical properties, in particular a larger fraction of coherently emitted photons and improved suitability for cavity integration. These advantages arise from their inversion symmetry and the resulting vanishing permanent electric dipole moment, which strongly suppresses spectral diffusion and leads to a higher degree of photon indistinguishability. As a consequence, group-IV color centers are well suited for cavity QED experiments and quantum networking applications, where efficient light–matter coupling enabled by cavity integration is essential to achieve high performance.

A prominent example of this combined approach is provided by silicon-vacancy (SiV) centers integrated into nanophotonic cavities, which have demonstrated collection and

detection efficiencies of cavity-reflected photons exceeding 10 % in the high-cooperativity regime [57]. These capabilities have enabled scalable memory-assisted quantum communication [42] as well as efficient entanglement generation between two SiV electron spins in a metropolitan-scale quantum network [43].

While SiV centers require operation at millikelvin temperatures and thus the use of dilution refrigeration, heavier group-IV color centers such as germanium-, tin-, and lead-vacancy centers can be operated at temperatures above 1 K, relaxing the cryogenic requirements. More importantly, these defects combine long-lived electron and nuclear spin qubits with favorable optical properties for cavity integration, making them promising candidates for efficient spin–photon interfaces.

Motivated by these considerations, this thesis focuses on tin-vacancy (SnV) centers coupled to an open microcavity platform as a route toward efficient spin–photon interfaces for color-center-based quantum networks. Related cavity-integrated approaches employing heavier group-IV color centers are being pursued in parallel by several groups [58, 59, 60, 61].

Outline of this thesis. In **Chapter 2**, color centers in diamond, and in particular the nitrogen-vacancy (NV) and tin-vacancy (SnV) centers, are introduced with a focus on their optical properties relevant for the discussion and understanding of the cavity-integrated results presented in this thesis.

Motivated by the limited collection efficiency of solid-state defects, the fundamentals of cavity quantum electrodynamics (cQED) are discussed in **Chapter 3**, with a focus on the transmission and reflection properties of weakly probed cavity–emitter systems in the high-cooperativity regime. In addition to the single-emitter treatment, the previously derived model is extended to the case of multiple emitters, thereby introducing collective effects. This naturally leads to the fundamentals of superradiant behavior in ensembles of cavity-coupled emitters, which is relevant for the final chapter of the thesis.

The experimental platform of a fiber-based open microcavity integrated into a dilution refrigerator is introduced in **Chapter 4**. The unique functionality and performance of open microcavity platforms are highlighted, in particular their exceptional mechanical stability, which is required for high-finesse cavity operation at temperatures as low as 1 K. This platform is therefore well suited for cavity-enhanced spin–photon interfaces based on group-IV color centers in diamond.

The integration of tin-vacancy centers hosted in diamond membranes into open microcavities is the subject of **Chapter 5** and comprises two central aspects. First, the sample preparation process is discussed, transforming diamond plates into cavity-integrated membranes hosting tin-vacancy centers. Second, the physical subtleties arising from the inclusion of a second refractive-index material of variable thickness into an otherwise air-filled cavity are addressed. This leads to the concept of hybrid diamond–air cavities and its implications for the cooperativities that can be achieved.

Finally, the unique experimental capabilities of the cryogenic microcavity platform combined with efficiently integrated, tin-vacancy-hosting diamond membranes enable the investigation of spin–photon interface capabilities in **Chapter 6**. High cooperativities, observed as a significant shortening of the excited-state lifetime of single tin-vacancy centers, allow for resonant probing of the cavity–emitter system with a weak coherent probe. Emitter-induced extinction in the cavity transmission is observed, and Zeeman splitting of the transmission is demonstrated using a superconducting magnet, marking a significant step toward spin–photon interfaces based on tin-vacancy centers in an open microcavity platform.

In contrast to the single-emitter cavity QED regime emphasized throughout much of this thesis, **Chapter 7** explores cavity QED with an ensemble of emitters collectively coupled to a common optical mode. By integrating an ensemble of NV centers into the cavity, this chapter examines collective light–matter effects mediated by a shared radiation field and reports experimental signatures of superfluorescence. Although this regime is not directly motivated by quantum-network applications based on spin–photon interfaces, it illustrates the broader scope of cavity QED phenomena accessible with cavity-integrated color centers in diamond.

The thesis concludes with an overview of the achieved results and an outlook on the next steps involved in realizing an efficient spin–photon interface using microcavity-integrated SnV centers in diamond in **Chapter 8**.

2. Color centers in diamond

Color centers in diamond arise from point defects in the sp^3-bonded carbon lattice, such as vacancies and substitutional or interstitial impurities. These defects locally break the crystal symmetry and introduce discrete electronic states within the band gap. Their localized electronic transitions render them optically active quantum emitters. Diamond provides a favorable host material for such emitters: its wide 5.5 eV band gap ensures optical transparency over a broad spectral range, while its mechanical rigidity and chemical inertness provide a stable and long-term environment.

Among the various color centers, the nitrogen–vacancy (NV) center plays a central role in solid-state quantum optics. It is briefly introduced here to provide the background needed for the discussion of cavity-mediated collective emission from NV centers in Chapter 7. Comprehensive descriptions of its formation, optical properties, and spin dynamics can be found in previous theses from this group [62, 63] and in related works [64, 65].

The NV center emits only a small fraction of coherent photons and suffers from spectral diffusion due to its non-inversion-symmetric structure. Over the past decade, inversion-symmetric group-IV color centers have gained significant attention, as they exhibit a larger fraction of coherently emitted photons and remarkable spectral stability, even in nanostructured environments. In the second part of this chapter, we focus on the tin–vacancy (SnV) center—the main experimental platform of this work—and discuss its optical and spin properties relevant to the study of cavity-coupled SnV centers in Chapter 6.

2.1. The nitrogen–vacancy center

The NV center consists of a substitutional nitrogen atom adjacent to a lattice vacancy (see Fig. 2.1a). In its neutral charge state (NV^0), the defect hosts five electrons originating from the dangling bonds of the surrounding carbon and nitrogen atoms. In this work, however, we focus primarily on the negatively charged state (NV^-), which contains one additional electron donated by a nearby charge donor. Unless stated otherwise, the term NV center refers to this negative charge state.

The nitrogen-vacancy (NV) center is one of the most extensively studied solid-state quantum emitters, primarily owing to its excellent spin properties combined with optical addressability. In particular, its exceptional spin stability, even at room temperature, to-

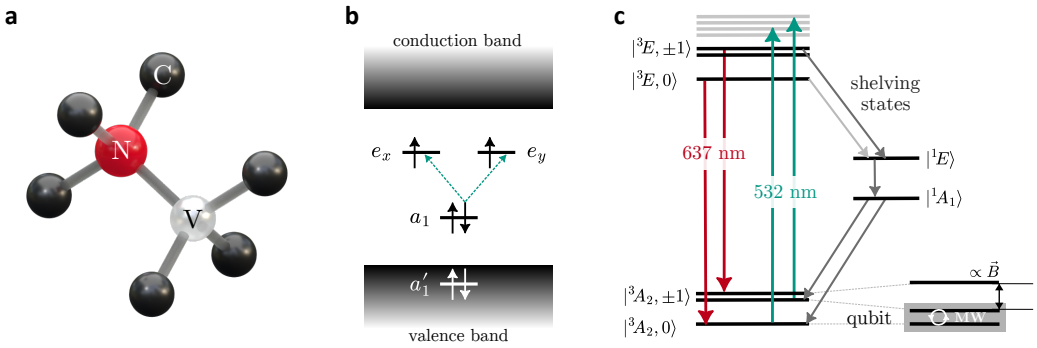

Figure 2.1: Nitrogen–vacancy center level structure. (a) Atomic configuration of the NV center, illustrating a substitutional nitrogen atom adjacent to a lattice vacancy. **(b)** Molecular orbitals of the defect for the negatively charged state, occupied by six electrons. The teal arrow indicates optical excitation from the ground state by promoting one electron from the a_1 orbital to the degenerate e_x/e_y orbitals. **(c)** Resulting electronic level structure with the ground (excited) state triplet $|^3A_2, m_s\rangle$ ($|^3E, m_s\rangle$) and intermediate singlet states $|^1E\rangle$ and $|^1A_1\rangle$. Green arrows schematically denote off-resonant optical excitation into the phonon sideband, red arrows zero-phonon-line emission, and gray arrows indicate relaxation via the singlet manifold. The spin qubit is typically realized within the ground-state manifold between the $m_s = 0$ and $m_s = -1$ sublevels, driven by microwave fields and read out optically.

gether with sufficiently robust optical transitions, has enabled a wide range of experiments and applications. The high natural abundance of nitrogen in both natural and synthetic diamond has further facilitated early experimental studies, following the first optical detection and spin readout of individual defects in the 1990s [66]. These properties have enabled numerous applications, particularly in quantum sensing of magnetic fields [67, 68] and in quantum networks [41, 69, 44].

2.1.1. Optical properties

Electronic level structure. The molecular orbitals of the NV center, shown in Fig. 2.1b, are obtained from linear combinations of the atomic orbitals of the three carbon and one nitrogen dangling bonds, while accounting for the C_{3v} symmetry of the defect. According to Hund's rules, the ground-state electronic configuration for the negatively charged state is $a_1'^2 a_1^2 e^2$. Upon optical excitation, one of the a_1 electrons is promoted into the degenerate e_x or e_y orbitals. Because the unpaired electrons in both the ground and excited states are well localized deep within the wide band gap of diamond, the NV center exhibits atom-like coherence properties despite being embedded in a solid-state host.

The two unpaired electrons couple to form either a spin triplet or a spin singlet state. Together with the occupation of the molecular orbitals, this gives rise to the electronic states labeled by their symmetry, as shown in Fig. 2.1c. The ground-state triplet $|^3A_2, m_s\rangle$ and the excited-state triplet $|^3E, m_s\rangle$ are separated by a transition energy corresponding

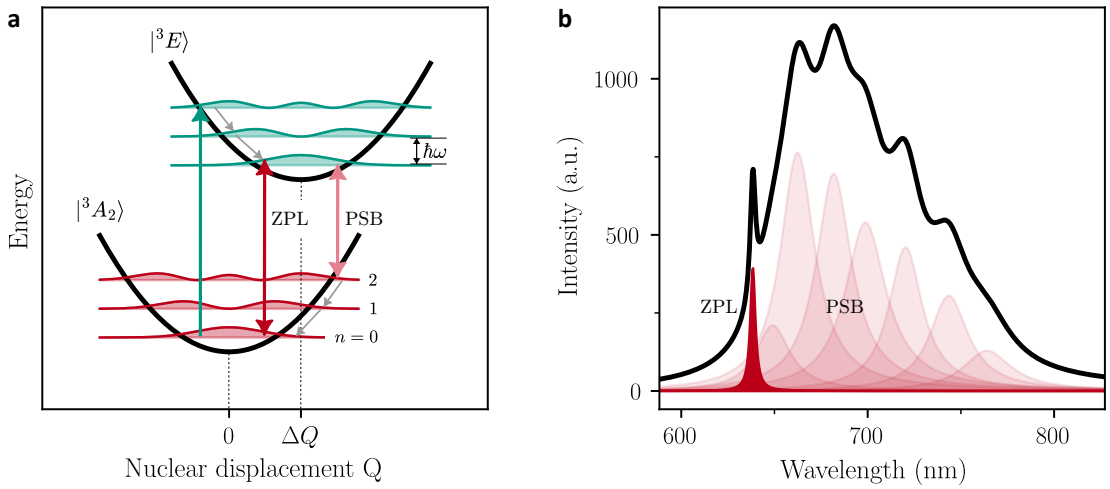

Figure 2.2: Vibronic broadening of the NV center ZPL. (a) Configuration-coordinate diagram illustrating the Huang–Rhys model for the NV center. Optical excitation and relaxation occur vertically, in accordance with the Franck–Condon principle, between the ground-state ($^3A_2$) and excited-state (^3E) potential energy surfaces, separated by a nuclear displacement ΔQ. The overlap of vibrational wavefunctions gives rise to phonon-assisted transitions (phonon sideband, PSB) in addition to the purely electronic zero-phonon line (ZPL). **(b)** Measured and fitted photoluminescence spectrum (black line) showing the ZPL at 637 nm and vibrationally broadened PSB contributions (shaded), reproduced with permission from Ref. [72].

to a photon wavelength of $\lambda_0 = 637\,\text{nm}$. The excited state decays radiatively with a characteristic lifetime $\tau_0 = 12\,\text{ns}$ [70]. The intermediate singlet states $|^1E\rangle$ and $|^1A_1\rangle$ lie between the triplet manifolds and are referred to as shelving or dark states, owing to their comparatively long lifetime of about 219 ns [71] and relaxation pathways via infrared emission and vibronic processes.

Zero phonon line and phonon sideband. The electronic transitions of color centers in diamond are almost invariably accompanied by coupling to vibrational modes of the solid-state environment. This modification of the absorption and emission spectra is described by the Huang–Rhys model, which treats the ground and excited states of the defect as quantum harmonic oscillators. The model is illustrated in Fig. 2.2a. The relevant vibrational mode occurs along the NV axis and is described by the nuclear displacement Q from the equilibrium position, with quantized energies $\hbar\omega$ (neglecting small differences in eigenfrequencies between the ground and excited states). The lack of inversion symmetry in the NV center leads to distinct charge distributions in the ground and excited states, resulting in a comparatively large displacement ΔQ between their equilibrium positions. Within the Born–Oppenheimer approximation, the electronic and nuclear motions are separated, giving rise to distinct potential energy surfaces for the ground and excited states [73]. According to the Franck–Condon principle, optical transitions occur on timescales much shorter than nuclear motion, such that excitation and relaxation processes

take place without a change in nuclear configuration, i.e., vertically in Fig. 2.2a, with probabilities determined by the overlap of the corresponding vibrational wavefunctions [74, 75].

The large displacement ΔQ therefore favors phonon-assisted emission, corresponding to radiative processes involving multiple phonons (phonon sideband, PSB) instead of purely electronic transitions (zero-phonon line, ZPL). As a consequence, NV centers can be efficiently excited off-resonantly at wavelengths blue-shifted from the ZPL, typically at 532 nm. Vibrational excitations relax nonradiatively into the surrounding lattice on timescales orders of magnitude shorter than the radiative lifetime [76] and, owing to diamond's large Debye temperature, are not thermally populated under equilibrium conditions. Consequently, the NV center can always be assumed to be in its vibrational ground state.

The resulting photoluminescence spectrum, shown in Fig. 2.2b (black line), consists of a zero-phonon line accompanied by a vibrationally broadened sideband. The individual PSB components and the resulting total spectrum are reproduced from Ref. [72]. The fraction of emission into the ZPL, known as the Debye–Waller factor, is $\beta_{\mathrm{DW}} = 0.03$ for NV centers [77].

Line broadening. Efficient entanglement between distant quantum memories relies on high interference contrast of the emitted photons in Hong–Ou–Mandel (HOM)–type experiments. Any deviation of the optical transition linewidth from the lifetime limit of 13 MHz (for NV centers) reduces this contrast. Two primary mechanisms cause such broadening: thermal broadening arising from the dynamic Jahn–Teller effect, and spectral diffusion induced by charge or electric-field fluctuations.

Thermal broadening of the NV^- optical line arises from phonon-induced mixing between the two degenerate excited-state orbitals, e_x and e_y. Lattice vibrations drive continuous transitions between these orbitals via a two-phonon Raman process, leading to fluctuations in the transition energy. The resulting fluctuations randomize the optical phase during emission, leading to a loss of optical coherence and a linewidth that typically scales with T^5 [78].

In addition to phonon-induced broadening, fluctuations in the local electric environment give rise to spectral diffusion. The absence of inversion symmetry in the NV center leads to non-centrosymmetric charge distributions and thus finite, permanent dipole moments that differ between the ground ($^3A_2$) and excited (^3E) states. Local electric-field fluctuations, for instance due to the (de)charging of nearby traps, shift the optical transition energy proportionally to the difference between these dipole moments. As the local charge configuration varies over time, the zero-phonon line frequency correspondingly fluctuates, giving rise to spectral diffusion [79, 80].

Both effects degrade the HOM interference contrast and thereby limit achievable entanglement rates. They also impede the formation of a collective dipole in ensembles of emitters,

complicating the observation of superradiance in solid-state defects, as discussed in Chapter 7. By employing a high-finesse cavity, we mitigate these limitations and enforce phase synchronization between the emitters, enabling the observation of collective emission from a small number of NV centers in diamond.

Optical pathways and three-level dynamics. So far, the role of the intermediate singlet (shelving) states—essential for optical spin initialization and readout—has not been discussed. Under off-resonant excitation through vibronic sidebands, the optical transition itself is spin-conserving. However, the subsequent decay pathways are spin-selective: relaxation through the singlet manifold is non–spin-conserving and occurs preferentially for the $m_s = \pm 1$ sublevels [81]. As a result, repeated optical excitation and decay cycles accumulate population in the $m_s = 0$ ground-state sublevel, thereby enabling efficient optical spin initialization. Under continuous off-resonant excitation and in the absence of external spin driving, the multi-level structure can be approximated by an effective three-level system, with the spin predominantly residing in the $m_s = 0$ sublevel. This simplification underlies the numerical model used in Chapter 7 to describe collective dynamics. The resulting three-level dynamics, derived from coupled rate equations and reflected in characteristic features of the NV fluorescence photon statistics, are described in detail in Refs. [82, 63].

Beyond spin initialization, the singlet states also enable optical spin readout. The relaxation pathways differ in their detected photon yield: direct decay from the excited triplet emits a ZPL or PSB photon, whereas relaxation via the singlet manifold involves a combination of non-radiative decay and infrared emission that is typically not detected in standard experiments and therefore appears intrinsically darker. Consequently, population in the $m_s = \pm 1$ sublevels yields reduced fluorescence compared to $m_s = 0$ under off-resonant excitation, forming the basis of optically detected magnetic resonance (ODMR). Applying a resonant microwave field that drives transitions between the spin sublevels transfers population from the bright $m_s = 0$ to the dark $m_s = \pm 1$ states, resulting in a measurable drop in fluorescence intensity. An external magnetic field lifts the degeneracy of the $m_s = \pm 1$ sublevels via the Zeeman effect, allowing the NV center—when combined with optical excitation, microwave driving, and photon detection—to function as a highly sensitive magnetometer [67, 68].

2.2. The tin–vacancy center

The SnV center consists of a substitutional tin atom located between two missing carbon atoms, forming a split-vacancy configuration (see Fig. 2.3a). In its neutral charge state (SnV^0), the defect hosts ten electrons originating from the dangling bonds of the surrounding tin and carbon atoms. Similar to the NV center discussed above, we focus primarily on the negatively charged state (SnV^-), which contains one additional electron donated by a

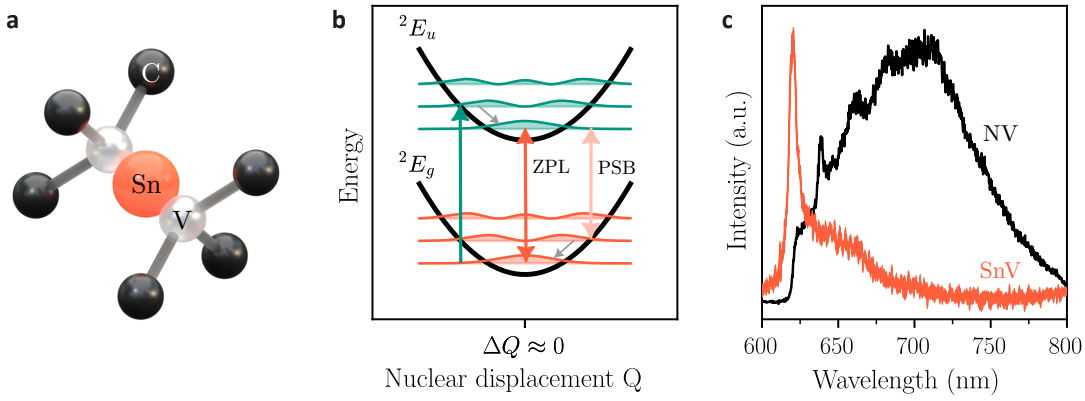

Figure 2.3: Inversion symmetry of the SnV center. (a) Atomic structure of the SnV center, showing a substitutional tin atom positioned between two lattice vacancies. **(b)** Configuration–coordinate diagram illustrating the Huang–Rhys model for the SnV center. Owing to its inversion symmetry, the SnV center exhibits only a very small nuclear displacement ($\Delta Q \approx 0$), resulting in a large overlap between the vibrational ground states of the electronic ground (^2E_g) and excited (^2E_u) manifolds, and thus a strong ZPL. Optical excitation and decay via the PSB remain possible but are significantly reduced compared to the NV center. **(c)** Experimental photoluminescence spectra of NV (black) and SnV (orange) centers, highlighting the higher Debye–Waller factor of the inversion-symmetric SnV.

nearby charge donor. Unless stated otherwise, the term SnV center refers to this negative charge state.

2.2.1. Inversion symmetry of group-IV color centers

All group-IV color centers share a D_{3d}-symmetric crystallographic configuration characterized by an inversion symmetry about the group-IV atom. This structural symmetry provides two key advantages compared to the non-centrosymmetric NV center: (i) reduced electron–phonon coupling, leading to larger Debye–Waller factors, and (ii) absence of a linear Stark effect arising from vanishing permanent electric dipole moments, resulting in reduced spectral diffusion.

Debye–Waller factor The inversion symmetry of group-IV color centers results in centrosymmetric charge distributions of all electronic orbitals. As a result, the equilibrium nuclear position of the substitutional atom remains nearly identical in the optical ground and excited states, leading to a strong overlap of the corresponding vibrational ground-state wavefunctions, as illustrated in Fig. 2.3b. Consequently, purely electronic transitions without phonon involvement are highly probable, giving rise to a strong ZPL. While off-resonant excitation of the SnV center is still possible, it is much less efficient than in the NV center and occurs at longer wavelengths. A comparison of the corresponding

photoluminescence spectra in Fig. 2.3c shows that the SnV center exhibits a much more pronounced ZPL than the NV center. This is reflected in a much larger Debye–Waller factor of $\beta_{\mathrm{DW}} = 0.57$ [83], compared to $\beta_{\mathrm{DW}} = 0.03$ for the NV center [77].

Spectral diffusion In the previous subsection, we discussed how spectral diffusion in NV centers arises from the difference in dipole moments between the ground and excited states, leading to a linear Stark effect. In contrast, the centrosymmetric charge distribution of group-IV defects yields vanishing permanent dipole moments in both ground and excited states, rendering them immune to first-order Stark shifts. Residual spectral drifts are therefore attributed either to local strain or to the finite polarizability of the defect, giving rise to a quadratic Stark effect. Studies show that both the difference in dipole moment and the polarizability between the ground and excited states are about four orders of magnitude smaller than those of NV centers [84, 85, 86]. This renders group-IV color centers more suitable for integration into nanoscale devices [42, 60, 87], where surface charge noise poses a major challenge for coherent NV-center applications [88, 89]. Nevertheless, SnV centers—and especially the heavier group-IV defects—can still exhibit spectral diffusion due to the aggressive ion implantation processes required for their creation, which introduce significant lattice damage in the surrounding crystal. This damage creates charge traps near the defect, often manifested as discrete spectral jumps—consistent with the shorter interaction range of the quadratic Stark effect [90]. The resulting loss of spectral stability can typically be mitigated by high-temperature annealing, which repairs lattice damage and restores the emitters' optical coherence [91, 83].

2.2.2. Optical properties

Electronic level structure. Similar to the NV center, the electronic level structure of the SnV center is governed by the D_{3d} symmetry of the defect and the hybridization of the dangling bonds of the constituent atoms. Although we focus here on the negatively charged SnV center, the same description applies to all group-IV vacancy centers, with only the magnitude of the level splittings differing between the various substitutional atoms. A detailed group-theoretical derivation of the resulting states, carried out for the negatively charged silicon–vacancy center (SiV), can be found in the doctoral thesis of C. Hepp [92].

Four molecular orbitals arise from symmetry-adapted linear combinations of the atomic orbitals: two non-degenerate orbitals (a_{1g} and a_{2u}) and two double-degenerate orbitals (e_u and e_g). These orbitals are occupied by eleven electrons: six from the neighboring carbon atoms, four from the tin atom, and one additional electron, provided by a nearby charge donor, resulting in a negatively charged defect. The energetic ordering of the orbitals can be obtained from density-functional theory (DFT) calculations [93] and is illustrated in Fig. 2.4a. The two lower orbitals (a_{1g} and a_{2u}) lie within the valence band, while the upper two (e_u and e_g) reside in the band gap. Because one electron is missing for complete filling, the defect can be described as having a single hole residing in the

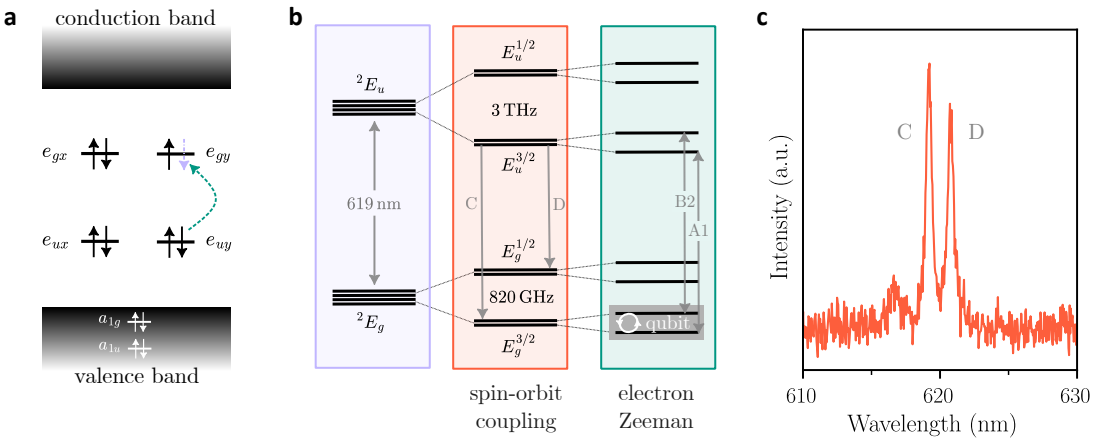

Figure 2.4: Tin–vacancy center level structure. (a) Molecular orbitals of the defect, occupied by eleven electrons. The teal arrow indicates optical excitation by promoting one electron from the degenerate e_u to the e_g orbitals. The resulting configuration can be described by an effective hole (purple) with spin $S = 1/2$. **(b)** Energy-level diagram of the SnV center in an external magnetic field. The fourfold-degenerate ground and excited states are separated by an energy corresponding to a photon wavelength of 619 nm. Neglecting strain and Jahn–Teller effects, spin–orbit coupling splits these into double-degenerate states, which are further separated by the Zeeman effect in an external magnetic field. The lowest ground-state doublet serves as the qubit manifold. **(c)** At cryogenic temperatures, the ZPL splits into the C- and D-transitions, corresponding to optical decay from the lowest excited spin–orbit state to the two ground states.

e_g orbital in the ground state and in the e_u orbital in the optically excited state. The electronic states are therefore labeled ^2E_g and ^2E_u, where the subscript denotes the orbital symmetry of the unoccupied (hole) state. The energy difference between ground and excited state corresponds to a photon wavelength of 619 nm. Spin–orbit coupling further splits the fourfold-degenerate states into double-degenerate spin–orbit eigenstates $E_g^{3/2}$, $E_g^{1/2}$, $E_u^{3/2}$, and $E_u^{1/2}$, with splittings of 820 GHz and 3 THz in the ground and excited states, respectively, as illustrated in Fig. 2.4b. The effects of strain and the Jahn–Teller interaction on the fine structure and spin-driving properties are neglected here and discussed in more detail in Refs. [92, 94, 95, 96, 97]. At cryogenic temperatures, the photoluminescence spectrum (Fig. 2.4c) exhibits two dominant lines, the C- and D-transitions, corresponding to optical decay from the lower excited spin–orbit branch $E_u^{3/2}$ to the two ground states. Transitions from the upper excited branch are typically weak, as population relaxes non-radiatively via phonon-mediated processes into the lower excited state before radiative decay. The relative contribution of the C transition to the total fluorescence is quantified by the branching ratio $\beta_{\mathrm{C/D}} \approx 0.8$ [60, 98].

The C-transition is the strongest and most relevant optical transition at cryogenic temperatures, as it connects the lowest orbital states of the ground and excited manifolds. In contrast to the NV center, where the emission dipole lies in the plane perpendicular to the defect's symmetry axis ($\langle 111 \rangle$), the emission dipole associated with the SnV C-transition is aligned with the symmetry axis, while the D-transition is polarized perpendicular to

it. This has been predicted and verified in [94, 83, 99] and becomes relevant for the polarization overlap of cavity-enhanced light–matter coupling.

An external magnetic field lifts the double degeneracy of the spin–orbit eigenstates via the Zeeman effect. Owing to the unequal Zeeman splittings of the ground- and excited-state spin sublevels, the C-transition splits into four optical transitions. While the spin-conserving transitions A1 and B2 are allowed, the nominally forbidden spin-flipping transitions A2 and B1 require an off-axis magnetic field. Depending on the applied magnetic field, the spin-conserving transitions can be selectively addressed optically, enabling optical spin readout. This capability enables the SnV center to serve as a spin–photon interface, with the spin qubit encoded in the lowest spin–orbit branch. The electron spin can be coherently driven either optically [100] or via microwave [96, 95, 97] fields and read out through its optical response, which is discussed in more detail in Sec. 2.2.4. The magnetic-field-dependent splitting of the C-transition is discussed in more detail in Sec. 4.4.

Charge dynamics The charge stability of the negatively charged SnV^- center is crucial for all envisioned applications. Blinking and the resulting spectral diffusion, caused by fluctuating charge environments, reduce both photon emission rates and optical coherence. Under resonant excitation, the optically active SnV^- can be converted into a dark charge state. As demonstrated in Ref. [101], illumination with a blue laser (445 nm) restores the negative charge state, presumably via photoionization processes involving nearby defect states; however, the exact microscopic mechanism underlying this process remains under debate. The overall charge stability and the efficiency of this repumping process depend sensitively on material properties such as defect depth, trap-state density, and surface termination. For shallow SnV centers (within a few tens of nanometers from the surface), surface electrostatics dominate the local Fermi level, making careful surface engineering essential.

Insights from the NV center provide guidance for achieving charge stability. For NV centers, oxygen-terminated, high–electron-affinity surfaces are known to stabilize the negatively charged NV^- state, whereas hydrogen termination induces hole accumulation and destabilizes it [102, 103]. While direct surface-termination studies for group-IV color centers remain limited, voltage-dependent photoluminescence measurements on single SnV centers [104] provide useful insight. Electron-rich conditions—realized by applying a negative bias—enhance the SnV^--related fluorescence at 620 nm, whereas electron depletion suppresses it, indicating a transition to a neutral charge state. Although explicit surface-treatment data are still lacking, these results strongly suggest that oxygen-rich, high–electron-affinity surfaces also stabilize the negative charge state of shallow SnV centers, analogous to the behavior of the NV center. Accordingly, surface oxidation via Piranha acid boiling or oxygen plasma treatment remains the standard preparation step prior to optical spectroscopy. It should be noted that bonding the diamond to other substrates, as discussed in Sec. 5.1.4, may alter near-surface electrostatics and shift the local Fermi level. The influence of such hybrid interfaces on the charge stability of SnV centers has not yet been systematically investigated.

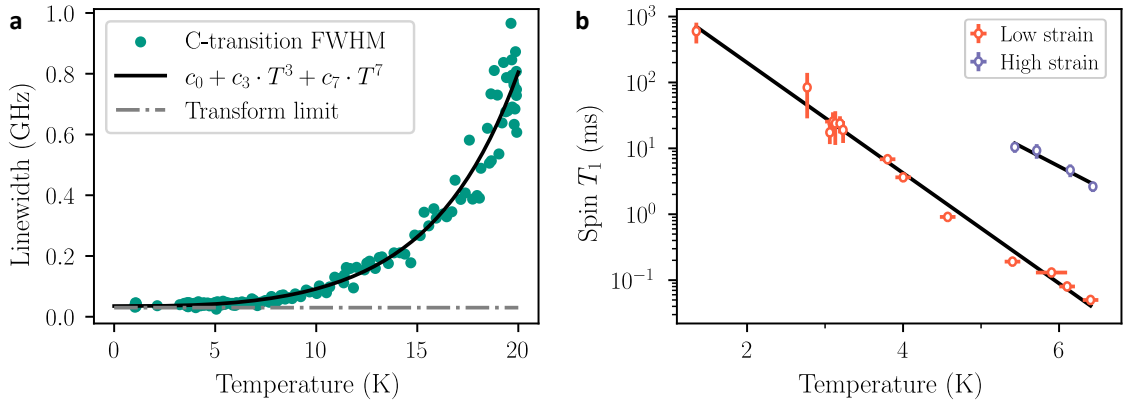

Figure 2.5: Phonon-induced optical and spin decoherence. (a) Full-width at half-maximum (FWHM) linewidth of the C-transition as a function of temperature, based on unpublished data provided by I. Karapatzakis. The linewidth saturates close to the transform limit of $\gamma_0/2\pi \approx 30\,\mathrm{MHz}$ at roughly 5 K. **(b)** Spin relaxation time T_1 as a function of temperature for low- and high-strain emitters, adapted from Ref. [97] (licensed under CC BY 4.0).

2.2.3. Temperature requirements

Phonon-related scattering processes limit both the optical and spin coherence of group-IV defects and therefore impose temperature constraints on experimental operation. The optimal temperature range depends on whether optical or spin coherence is targeted. We briefly summarize the main mechanisms of optical line broadening ($\gamma^\star$) as well as spin relaxation (T_1) and dephasing (T_2), and outline the corresponding temperature requirements.

Thermal line broadening. The optical linewidth increases with temperature due to electron–phonon interactions that dephase the optical transition in the excited state. At low temperatures, only acoustic phonons are thermally populated, and the linewidth is governed by their temperature-dependent coupling to the orbital states. For non-degenerate electronic states, phonons couple only in second order, leading to a linewidth scaling of $\gamma^\star \propto T^7$ [105]. In contrast, for degenerate states, the dynamic Jahn–Teller effect enables first-order phonon coupling between sublevels, resulting in a $\gamma^\star \propto T^5$ dependence as observed for NV centers [78]. However, this scaling has been rarely observed for group-IV defects, appearing only in a few studies on SiV centers [106, 107]. Most studies of group-IV centers report a dominant $\gamma^\star \propto T^3$ contribution to the pure dephasing, which Hizhnyakov *et al.* [108, 109, 110] attributed to an anomalous temperature dependence. This reduced exponent arises from a softening of elastic bonds—local lattice instabilities—that increase the density of low-frequency phonon modes in the excited state. These modes modulate the local strain or potential around the defect, leading to fluctuations of the transition

energy. Consequently, the temperature dependence of the linewidth in group-IV centers such as the SnV is typically described by

$$\gamma = \gamma^{T=0} + aT^3 + bT^7, \tag{2.2.1}$$

where $\gamma^{T=0}$ denotes the intrinsic linewidth[1], and the coefficients a and b reflect the relative strength of anomalous low-energy and intrinsic phonon-scattering processes.

Fig. 2.5a shows the temperature-dependent linewidth of the SnV C-transition, measured by I. Karapatzakis and adapted here with permission. The linewidth decreases with cooling and, below 5 K, saturates close to the lifetime limit of $\gamma_0/2\pi \approx 30$ MHz [111], indicating that phonon-induced dephasing is strongly suppressed at liquid-helium temperatures. This behavior is representative of group-IV color centers in general, allowing for transform-limited emission under cryogenic conditions at 4 K [112, 113, 114, 115]. Such narrow optical transitions are crucial for achieving indistinguishable photon emission and coherent light–matter interaction. As discussed in Chapter 3, Purcell-induced lifetime shortening can further relax the coherence requirements by increasing the natural linewidth, making the optical emission more resilient to residual dephasing.

Phonon-related spin relaxation and dephasing. Phonons drive spin relaxation through several temperature-dependent mechanisms. A complete description includes single-phonon (direct) transitions, resonant two-phonon (Orbach) processes, and off-resonant two-phonon (Raman) scattering [113, 116]. At intermediate temperatures, the dominant process is phonon-driven excitation into the upper orbital branch separated by Δ_g, followed by relaxation back into the ground state accompanied by a spin flip—the resonant two-phonon Orbach process [117]. In the absence of an off-axis magnetic field $B_\perp$, spin-flip transitions are forbidden because phonons couple only to the orbital degree of freedom and are intrinsically spin-conserving. An off-axis magnetic field mixes spin and orbital components, making spin-flip transitions partially allowed. The corresponding Orbach transition rate follows [116]

$$\Gamma_{\text{Orbach}}(T) \propto B_\perp^2 \, \Delta_g \left[\exp\left(\frac{h\Delta_g}{k_B T}\right) - 1\right]^{-1}. \tag{2.2.2}$$

Figure 2.5b shows the temperature dependence of the spin-relaxation time T_1 for two SnV centers: one low-strain and one high-strain defect. Because strain increases the ground-state orbital splitting Δ_g, it reduces phonon-induced spin flips at a given temperature and phonon occupation. Consequently, the highly strained emitter reaches T_1 times of about 1 ms at 5–6 K, whereas the low-strain emitter exceeds this value only at 3–4 K [97].

Phonon-mediated coupling through the orbital branches directly determines the temperature requirements of the various group-IV color centers. For small spin–orbit coupling, as in the silicon-vacancy (SiV) center, the orbital splitting Δ_g is sufficiently small that thermal

[1] Ideally, this equals the lifetime limit, but it can be further broadened by fast spectral diffusion or other dynamic effects.

phonons at relatively low temperatures can bridge this gap. Consequently, sub-kelvin temperatures—and thus dilution cryostats—are required to freeze out these phonons and maintain spin coherence. Heavier centers such as germanium-vacancy (GeV), tin-vacancy (SnV), and lead-vacancy (PbV) exhibit increasingly larger spin–orbit splittings and therefore operate under less stringent cryogenic conditions. Alternatively, lighter color centers can be operated in highly strained environments, where strain artificially increases the ground-state orbital splitting and thus suppresses phonon-induced spin relaxation [118, 119, 120, 121].

The spin-relaxation time T_1 also sets an upper bound for the spin-coherence time T_2, given by

$$T_2^{-1} = (2T_1)^{-1} + T_\Phi^{-1}, \tag{2.2.3}$$

where T_Φ accounts for additional pure dephasing processes. These are mainly caused by magnetic noise from the surrounding spin bath, which leads to fluctuations of the local magnetic field and, consequently, of the qubit frequency. Further details can be found in Refs. [122, 96, 123, 97].

Therefore, the SnV center must be operated at cryogenic temperatures to suppress thermally induced optical and spin decoherence. The optical linewidth becomes transform limited below approximately 5 K, so a 4 K liquid-helium cryostat suffices for optical coherence, whereas spin requirements depend on the experimental configuration—particularly the off-axis magnetic field $B_\perp$ and any static strain that modifies Δ_g. A survey of reported electron-spin T_1 values for SnV centers [96, 95, 97], together with quantum-networking targets of $T_2 \gtrsim 10$–100 ms [49], indicates that operation in the 1–4 K range is sufficient in practice.

2.2.4. Coherent spin control

As discussed previously, stronger spin–orbit coupling in the heavier group-IV color centers relaxes the temperature requirements by suppressing phonon-induced spin transitions. However, the same spin–orbit interaction complicates efficient spin driving, since the two spin sublevels are associated with orthogonal orbital states. As a result, direct spin transitions are forbidden by magnetic-dipole selection rules in unstrained emitters. Strain relaxes these selection rules by admixing the orbital branches, thereby making spin transitions partially allowed. For heavier group-IV defects, however, stronger spin–orbit coupling requires either larger strain, significant off-axis magnetic fields, or higher microwave driving powers to overcome the intrinsic limitation of inefficient spin control.

Applying off-axis magnetic fields is a feasible way to enable spin driving, but it introduces a fundamental trade-off. As discussed previously, such fields enhance phonon-mediated relaxation, reducing spin-coherence times and necessitating lower temperatures or more advanced cryogenic setups. Moreover, because the spin–orbit coupling strengths differ between the ground and excited states, their respective spin quantization axes become misaligned under an off-axis field. This misalignment introduces spin-flip probabilities

during optical relaxation, degrading optical cycling fidelity. Overcoming the spin-driving limitation through strain, rather than off-axis fields, is therefore generally more desirable.

Recent studies have demonstrated full coherent microwave control of the SnV electron spin in strained environments. Rabi driving frequencies of several MHz have been observed [95, 96, 97], and randomized benchmarking yields single-qubit gate fidelities above 99 % [95]. Hahn-echo coherence times reach $T_2 = 430\,\mu s$ and can be extended to $T_2 = 10\,ms$ by dynamical-decoupling (DD) sequences, establishing the SnV as a viable spin qubit for quantum-networking experiments [97]. While high microwave powers can cause local heating and increased dephasing—especially for long DD sequences—the use of superconducting coplanar waveguides minimizes heating and enables fast, coherent spin control even for extended DD pulse trains [97].

Quantum-network nodes require long-lived storage qubits to buffer entanglement across multiple network links. In the SnV center, two natural candidates fulfill this role: the host nuclear spin of a spin-bearing tin isotope (such as ^{117}Sn) and nearby ^{13}C nuclear spins in the diamond lattice. The host nuclear spin is strongly and intrinsically coupled to the electron spin, producing a hyperfine splitting of 452 MHz—more than an order of magnitude larger than the optical linewidth. This strong coupling enables purely optical nuclear-spin initialization with 98.6 % fidelity and single-shot readout at 80 % fidelity [124]. Beyond optical control, coherent microwave manipulation of the ^{117}Sn nuclear spin has been demonstrated, achieving Clifford-gate fidelities of 98.4 % and coherence times of 2.5 ms using two decoupling pulses [125]. Complementary to this intrinsic approach, a nearby ^{13}C nuclear spin provides an exceptionally long-lived quantum memory. Using a strongly coupled ^{13}C, Resch *et al.* [126] demonstrated joint electron–nuclear initialization with 99.7 % fidelity, dynamical-decoupling coherence times of $T_2 = 1.35\,s$, and single-qubit Clifford gate fidelities of 99.9 %, enabled by superconducting coplanar waveguides for efficient RF and microwave delivery. Together, these results highlight that both intrinsic and extrinsic nuclear spins in the SnV system constitute powerful and complementary routes toward high-fidelity, long-lived quantum memories for future quantum-network applications.

The excellent electron- and nuclear-spin coherence properties, combined with efficient and fast driving schemes, make SnV centers promising candidates for memory-assisted quantum networking. Optically—and particularly in comparison to NV centers—SnV and other group-IV defects benefit greatly from their inversion symmetry, resulting in a much higher Debye–Waller factor and therefore a stronger zero-phonon line. Nevertheless, optical excitation and detection efficiencies, as well as overall light–matter coupling, remain limiting factors for entanglement generation, since photons spontaneously emitted by color centers in bulk diamond are difficult to collect. Consequently, integration into photonic environments is essential, and enhancing the light–matter interaction through coupling to optical cavities will be the focus of the next chapter.

3. Light–matter interaction in optical Fabry–Pérot resonators

In Chapter 1, we motivated the necessity of optical cavities to enhance light–matter interaction and thereby improve the efficiency with which optically addressable spin qubits can be used to share entanglement between distant nodes. We saw that current quantum-network demonstrations are mainly limited by the limited collection efficiency of coherent photons and by how efficiently stationary qubits are interfaced with photons and photonic links. The present chapter introduces the basic concepts of light–matter interaction, beginning with a brief introduction to optical Fabry–Pérot resonators, followed by a discussion of light–matter interaction in the single-emitter regime and its extension to ensembles of emitters coupled to a common radiation field.

3.1. Optical Fabry–Pérot resonators

We start by briefly introducing the fundamental properties of optical Fabry–Pérot resonators, which provide the foundation for the subsequent discussion of cavity-enhanced light–matter interactions. A more detailed discussion can be found in previous doctoral theses [62, 127] or in several textbooks [128, 129].

3.1.1. Geometry and resonance condition

We consider a Fabry–Pérot resonator formed by two planar, partially reflecting mirrors with reflectivities R_1 and R_2, separated by an adjustable distance L, as shown in Fig. 3.1. The mirrors are aligned in parallel, so that light entering the cavity through one mirror undergoes multiple reflections before eventually leaking out. Unless stated otherwise, the cavity is assumed to be filled with air, a homogeneous medium with refractive index $n = 1$. The non-trivial consequences of introducing a second refractive-index material in the form of a diamond membrane will be discussed in Chapter 5. A macroscopic cavity field of wavelength λ builds up when the light undergoes constructive interference after each round trip. This condition is met when the accumulated round-trip phase ϕ satisfies

$$\phi = \frac{4\pi nL}{\lambda} = 2\pi q, \tag{3.1.1}$$

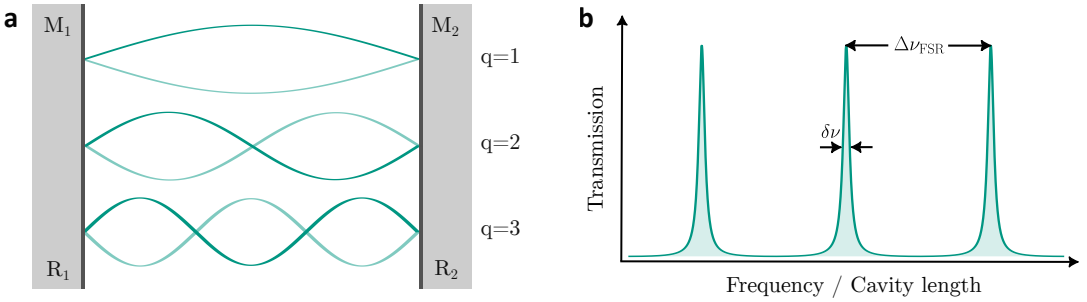

Figure 3.1: Fabry–Pérot cavity. **(a)** Standing-wave field patterns in a resonator formed by two mirrors $M_{1,2}$ separated by a distance L, shown for longitudinal mode indices $q = 1, 2, 3$. **(b)** Corresponding transmission peaks as a function of frequency (or cavity length), separated by the free spectral range $\Delta\nu_{\mathrm{FSR}} = c/(2nL)$. The resonance linewidth $\delta\nu_{\mathrm{cav}}$ is set by the mirror reflectivities $R_{1,2}$.

which is the case when the cavity length L corresponds to an integer multiple q of half wavelengths. For a fixed cavity length, the resonances are separated in frequency by

$$\Delta\nu_{\mathrm{FSR}} = \nu_{q+1} - \nu_q = \frac{c}{2nL}, \tag{3.1.2}$$

which is referred to as the free spectral range (FSR) of the cavity.

3.1.2. Finesse, linewidth and quality factor

Light entering the cavity interferes constructively when the round-trip phase satisfies the resonance condition. In the following, we introduce several key metrics for cavity-enhanced light–matter interaction by examining the transmission through the cavity when light enters through one of the mirrors. In the limit of small round-trip losses, the cavity transmission T_c in the vicinity of a resonance at phase ϕ_0 can be described by a Lorentzian lineshape,

$$T_c(\phi) = T_{c,\max} \frac{\left(\pi/\mathcal{F}\right)^2}{\left(\pi/\mathcal{F}\right)^2 + \left(\phi - \phi_0\right)^2}, \tag{3.1.3}$$

where $T_{c,\max}$ is the maximum transmission and $\mathcal{F}$ denotes the cavity finesse. The finesse is determined by the total round-trip losses,

$$\mathcal{F} = \frac{2\pi}{\mathcal{L}_{\mathrm{tot}}} = \frac{2\pi}{T_1 + T_2 + \mathcal{L}_{\mathrm{add}}}, \tag{3.1.4}$$

where $\mathcal{L}_{\mathrm{tot}}$ is the sum of all round-trip losses, $T_{1,2} = 1 - R_{1,2}$ are the mirror transmission coefficients, and $\mathcal{L}_{\mathrm{add}}$ accounts for additional losses such as scattering or absorption. The finesse can be viewed as quantifying the average number of photon round trips within the resonator prior to loss. As such, it constitutes a central parameter in cavity–enhanced

light–matter interaction, as the repeated round trips directly translate into an increased interaction strength between light and matter.

Using the relation between round-trip phase and frequency (see Eq. (3.1.1)), the transmission can equivalently be written as a function of frequency,

$$T_c(\nu) = T_{c,\max} \frac{\left(\frac{\delta\nu_{\mathrm{cav}}}{2}\right)^2}{\left(\frac{\delta\nu_{\mathrm{cav}}}{2}\right)^2 + (\nu - \nu_0)^2}, \tag{3.1.5}$$

where ν_0 is the resonance frequency and $\delta\nu_{\mathrm{cav}}$ is the full width at half maximum (FWHM) of the cavity resonance. The linewidth is related to the finesse and the free spectral range $\Delta\nu_{\mathrm{FSR}}$ via

$$\delta\nu_{\mathrm{cav}} = \frac{\Delta\nu_{\mathrm{FSR}}}{\mathcal{F}}. \tag{3.1.6}$$

The cavity linewidth can equivalently be expressed in terms of the intensity decay (damping) rate $\kappa = 2\pi\delta\nu_{\mathrm{cav}}$, which corresponds to a cavity ringdown time (photon lifetime) of $\tau_{\mathrm{cav}} = 1/\kappa$.

A more universal figure of merit, applicable not only to optical but also to mechanical or electrical resonators, is the quality factor Q. It is defined as the ratio of the resonance frequency to the linewidth,

$$Q = \frac{\nu_0}{\delta\nu_{\mathrm{cav}}} = 2\pi\nu_0\tau_{\mathrm{cav}} = q\mathcal{F}, \tag{3.1.7}$$

and thus is a universal measure of how efficiently a resonator stores energy. Because the quality factor scales with the longitudinal mode order q, it increases linearly with the cavity length L. In contrast, the finesse ideally remains independent of L, making it the more natural figure of merit for assessing Fabry–Pérot cavities, as discussed in Section 3.2.

3.1.3. Transverse mode profile and mode volume

So far, based on the longitudinal resonance condition for plane waves (Eq. (3.1.1)), we have described the spectral behavior of a Fabry–Pérot resonator with planar, perfectly parallel mirrors. In practice, however, finite mirror apertures together with slight angular misalignment cause clipping losses, which reduce the finesse and may lead to unstable cavity modes. For this reason, cavities are typically operated with at least one concave mirror that provides refocusing. The spherical curvature of the mirror enforces a curved intracavity wavefront that matches the mirror surface. In this case, the appropriate solutions of the scalar paraxial wave equation, consistent with the boundary conditions imposed by the mirrors, are Gaussian beams. Solving for the Gaussian mode that reproduces itself after one round trip between a plane mirror and a concave mirror of radius of curvature R_c (our cavity configuration) leads to the following properties, stated here without derivation (see Ref. [130] for details):

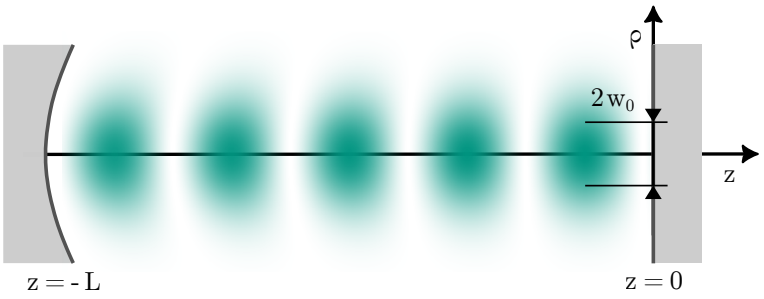

Figure 3.2: Gaussian mode in a plano–concave cavity. Illustration of the fundamental TEM_{00} mode in a cavity of length L with a curved mirror at $z = -L$ and a planar mirror at $z = 0$. The beam waist of radius w_0 is located at the planar mirror. The transverse coordinate is denoted by ρ, and the mode diameter is $2w_0$. The Gaussian field envelope broadens towards the concave mirror according to the cavity geometry.

- The stability range within which the Gaussian mode can reproduce itself upon reflection is given by
$$0 \leq \left(1 - \frac{L}{R_c}\right) \leq 1. \tag{3.1.8}$$
- A plane mirror at $z = 0$ requires a planar wavefront at its surface. For a Gaussian beam, this condition is only fulfilled at the beam waist, such that $w(z = 0) = w_0$.
- The radius of curvature of the concave mirror together with the cavity length determines the waist size (for an air-filled cavity),
$$w_0 = \sqrt{\frac{\lambda L}{\pi}\sqrt{\frac{R_c}{L} - 1}}. \tag{3.1.9}$$
The waist approaches zero ($w_0 \to 0$) at the stability edges $L \to 0$ and $L \to R_c$.

Note that both the mode waist and the stability range are modified when an additional material of refractive index different from air is introduced into the cavity, which will be discussed in Chapter 4. Knowing both the longitudinal and transverse dimensions of the cavity mode allows one to calculate the mode volume V_m, which quantifies the spatial confinement of the cavity field, and is defined as

$$V_m = \frac{\int \varepsilon(\mathbf{r})\,|E(\mathbf{r})|^2\,\mathrm{d}^3 r}{\max\left(\varepsilon(\mathbf{r})\,|E(\mathbf{r})|^2\right)}. \tag{3.1.10}$$

For a standing wave with a Gaussian envelope in an air-filled cavity, the integral reduces to $V_m = \frac{\pi}{4} w_0^2 L$.

3.2. Light–matter interaction: a dipole in a Fabry–Pérot cavity

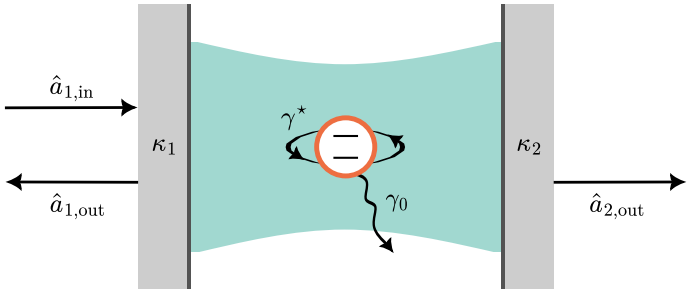

Figure 3.3: Cavity–emitter coupling model. An optical cavity with leakage rates κ_1, κ_2 is coupled with strength g to a two-level system characterized by spontaneous emission rate γ_0 and pure dephasing rate $\gamma^\star$. The system is driven by a weak coherent input field $\hat{a}_{1,\mathrm{in}}$, while cavity reflection and transmission are described by the output fields $\hat{a}_{1,\mathrm{out}}$ and $\hat{a}_{2,\mathrm{out}}$.

3.2.1. Jaynes–Cummings Hamiltonian with external drive

In the rotating frame at the drive frequency ω_l, the coupled system of a cavity mode, a two-level emitter, and a coherent drive is described by the Jaynes–Cummings Hamiltonian [131]

$$H_{\mathrm{JC}} = \underbrace{-\hbar\Delta_c\,\hat{a}^\dagger\hat{a}}_{\text{cavity detuning}} - \underbrace{\hbar\Delta_a\,\hat{\sigma}_+\hat{\sigma}_-}_{\text{emitter detuning}} + \underbrace{\hbar g\left(\hat{a}^\dagger\hat{\sigma}_- + \hat{a}\hat{\sigma}_+\right)}_{\text{light–matter coupling}} + \underbrace{i\hbar\chi\left(\hat{a}^\dagger - \hat{a}\right)}_{\text{drive}}. \tag{3.2.1}$$

Explanation of terms and notation.

- $\hat{a}^\dagger$, $\hat{a}$: creation and annihilation operators of the cavity mode, $[\hat{a}, \hat{a}^\dagger] = 1$.
- $\hat{\sigma}_- = |g\rangle\langle e|$, $\hat{\sigma}_+ = |e\rangle\langle g|$: lowering and raising operators of the emitter.
- $\Delta_c = \omega_l - \omega_c$: detuning between the drive frequency ω_l and the cavity resonance ω_c.
- $\Delta_a = \omega_l - \omega_a$: detuning between the drive frequency ω_l and the emitter transition ω_a.
- g: vacuum Rabi frequency, i.e. the coherent coupling strength between the emitter and the cavity mode.
- χ: drive amplitude, proportional to the square root of the input photon flux, $\chi = \sqrt{2P\kappa_1/(\hbar\omega_l)}$, where P is the incident laser power coupled into input port 1 of the cavity.

3.2.2. Cavity and emitter damping

The cavity and the emitter are coupled to a continuum of bath modes, which gives rise to dissipation. For the cavity, the field decay happens at rate $\kappa/2$, while the emitter polarization spontaneously decays at rate $\gamma_0/2$ and loses coherence at the pure dephasing rate $\gamma^\star$ (here κ and γ_0 denote the corresponding intensity decay rates, so that the field or polarization amplitudes decay at half these values). To describe the dissipation between the system operators $\hat{a}, \hat{\sigma}_-$ and the bath modes, one uses the Lindblad master equation in the form [132]

$$\frac{d\rho}{dt} = -\frac{i}{\hbar}[H, \rho] + \sum_k \left(L_k \rho L_k^\dagger - \frac{1}{2}\{L_k^\dagger L_k, \rho\} \right). \tag{3.2.2}$$

Here, ρ denotes the density operator of the system, and H the system Hamiltonian, describing the coherent time evolution. The operators L_k are Lindblad, or jump, operators, each representing a distinct dissipative channel. The anticommutator is defined as $\{A, B\} = AB + BA$. The associated Hamiltonian and jump operators for the coupled cavity-emitter system are:

- Hamiltonian: $H = H_{\mathrm{JC}}$.
- Cavity damping: $L_\kappa = \sqrt{\kappa}\,\hat{a}$.
- Emitter spontaneous emission: $L_{\gamma_0} = \sqrt{\gamma_0}\,\hat{\sigma}_-$.
- Emitter dephasing: $L_{\gamma^\star} = \sqrt{\gamma^\star/2}\,\hat{\sigma}_z$.

3.2.3. Heisenberg–Langevin equations

Starting from the Lindblad master equation (3.2.2), we obtain the equations of motion for operator expectation values:

$$\langle \dot{O} \rangle = \mathrm{Tr}\big(O\,\dot{\rho}\big) = \frac{i}{\hbar}\,\langle [H, O] \rangle + \sum_j \langle \mathcal{D}^\dagger[L_j]\,O \rangle, \tag{3.2.3}$$

with the adjoint action of the dissipator on an operator O

$$\mathcal{D}^\dagger[L]\,O = L^\dagger O L - \tfrac{1}{2}\big(L^\dagger L\,O + O\,L^\dagger L\big). \tag{3.2.4}$$

By inserting the Jaynes–Cummings Hamiltonian of Eq. (3.2.1) into the Lindblad master equation for operator expectation values (cf. Eq. (3.2.3)), one obtains the following equations of motion[2] [131]

$$\langle \dot{a} \rangle = -\left(\tfrac{\kappa}{2} - i\Delta_c\right)\langle a \rangle - ig\,\langle \sigma_- \rangle + \chi, \tag{3.2.5a}$$

$$\langle \dot{\sigma_-} \rangle = -\left(\tfrac{\gamma_0}{2} + \gamma^\star - i\Delta_a\right)\langle \sigma_- \rangle + ig\,\langle a\,\sigma_z \rangle, \tag{3.2.5b}$$

$$\langle \dot{\sigma_z} \rangle = -\gamma_0\big(\langle \sigma_z \rangle + 1\big) + 2ig\big(\langle a^\dagger \sigma_- \rangle - \langle a\,\sigma_+ \rangle\big). \tag{3.2.5c}$$

These coupled equations describe the temporal evolution of the intracavity field $\langle a \rangle$, the emitter polarization $\langle \sigma_- \rangle$, and the population inversion $\langle \sigma_z \rangle$. They form the basis for describing phenomena such as the Purcell effect, as well as the transmission and reflection spectra, in regimes ranging from high cooperativity to strong coupling.

Hybridized modes and strong coupling. In the limit of weak excitation (linear response), the emitter remains predominantly in the ground state, such that $\langle \sigma_z \rangle \approx -1$, allowing us to decouple the first two equations for the intracavity field $\langle \dot{a} \rangle$ and emitter polarization $\langle \dot{\sigma_-} \rangle$. We can write the coupled Heisenberg–Langevin equations in matrix form as [131]

$$\frac{\mathrm{d}}{\mathrm{d}t}\begin{pmatrix} \langle a \rangle \\ \langle \sigma_- \rangle \end{pmatrix} = \underbrace{\begin{pmatrix} i\Delta_{ca} - \frac{\kappa}{2} & -ig \\ -ig & -\gamma_\perp \end{pmatrix}}_{M}\begin{pmatrix} \langle a \rangle \\ \langle \sigma_- \rangle \end{pmatrix}, \tag{3.2.6}$$

where $\Delta_{ca} = \omega_c - \omega_a$ is the cavity–emitter detuning and $\gamma_\perp = \gamma_0/2 + \gamma^\star$ the transverse atomic decoherence rate. The general solution of Eq. (3.2.6) is a linear combination of the eigenmodes of M:

$$\begin{pmatrix} \langle a \rangle(t) \\ \langle \sigma_- \rangle(t) \end{pmatrix} = c_+\,\mathbf{u}_+\,e^{-\lambda_+ t} + c_-\,\mathbf{u}_-\,e^{-\lambda_- t}, \tag{3.2.7}$$

[2] See Appendix A.1 for relations that simplify the commutators and anticommutators involving the operators $a, a^\dagger, \sigma_-, \sigma_+, \sigma_z$.

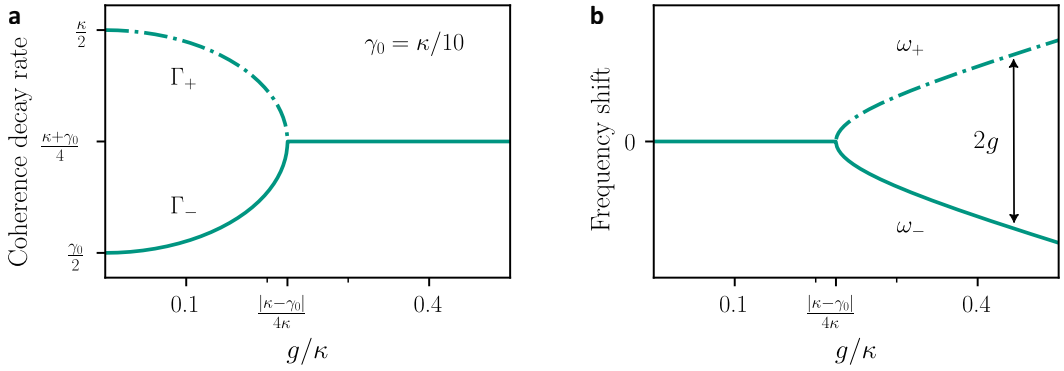

Figure 3.4: Hybridized cavity–emitter modes. **(a)** Hybrid polarization decay rates and **(b)** hybrid frequencies as a function of the coupling g. Strong coupling emerges when $g = |\kappa - \gamma_0|/4$. In the weak-coupling regime, the Purcell effect manifests as a modification of the polarization decay rate of the emitter-like mode, $\Gamma_- \propto g^2/\kappa$.

where $\lambda_\pm$ are the eigenvalues of M, $\mathbf{u}_\pm$ the corresponding eigenvectors, and $c_\pm$ are set by the initial conditions. The eigenvalues are

$$\lambda_\pm = \frac{\gamma_\perp + \frac{\kappa}{2} - i\Delta_{ca}}{2} \pm \frac{1}{2}\sqrt{\left(\frac{\kappa}{2} - \gamma_\perp - i\Delta_{ca}\right)^2 - 4g^2}\,. \tag{3.2.8}$$

The real and imaginary parts of the eigenvalues correspond to hybrid decay rates $\Gamma_\pm$ and frequency shifts $\omega_\pm$, respectively. Under resonant conditions ($\Delta_{ca} = 0$) with zero pure dephasing ($\gamma_\perp = \gamma_0/2$), we can write

$$\Gamma_\pm = \frac{\gamma_0 + \kappa}{4} \pm \mathrm{Re}\left\{\sqrt{\left(\frac{\kappa - \gamma_0}{4}\right)^2 - g^2}\right\}, \tag{3.2.9a}$$

$$\omega_\pm = \mathrm{Im}\left\{\sqrt{\left(\frac{\kappa - \gamma_0}{4}\right)^2 - g^2}\right\}. \tag{3.2.9b}$$

The evolution of the hybridized mode decay rates and frequencies is illustrated in Fig. 3.4. For zero coupling ($g = 0$), the two branches reduce to the bare cavity field and emitter coherence decay rates, $\kappa/2$ and $\gamma_0/2$. As the coupling strength g increases, the two rates approach each other and merge at the onset of strong coupling, $g = |\kappa - \gamma_0|/4$, where both hybridized modes share the same decay rate $\Gamma_\pm = (\kappa + \gamma_0)/4$ (Fig. 3.4a). In contrast, at zero detuning the mode frequencies remain degenerate up to this point. Beyond this point, they split symmetrically, approaching $\pm g$ in the ideal case without losses, reflecting the formation of two distinct normal modes (Fig. 3.4b). Many experiments beautifully demonstrate strong-coupling cavity QED in platforms such as atoms [53, 133], quantum dots [134, 135], and defect centers in diamond [136]. By contrast, our platform operates outside the strong-coupling regime, in the bad cavity (Purcell) limit ($\kappa \gg \gamma_\perp, g$), where the cavity significantly accelerates photon emission and modifies its transmission and reflection properties.

Bad cavity regime. Figure 3.4a shows that the decay rate Γ_- of the emitter-like hybridized mode increases quadratically with g, reflecting an accelerated population decay. This enhanced decay is quantified by the cooperativity C_0, defined from the deviation of the coherence decay rate Γ_- from the free-space value $\gamma_0/2$. Expanding the square root in the limit $\kappa \gg \gamma_\perp, g$, and noting that the population decay rate γ_c is twice the coherence decay Γ_-, one finds

$$\gamma_c \approx \gamma_0 + \frac{4g^2}{\kappa} = \gamma_0 (1 + C_0), \quad C_0 = \frac{\gamma_c}{\gamma_0} - 1 = \frac{\tau_0}{\tau_c} - 1 = \frac{4g^2}{\kappa \gamma_0}, \tag{3.2.10}$$

with $\tau_0 = 1/\gamma_0$ the free-space lifetime and $\tau_c = 1/\gamma_c$ the cavity-enhanced lifetime. A detailed derivation is provided in Appendix A.2. Experimentally, the cooperativity can be inferred from the ratio of the radiative lifetimes in free space (τ_0) and inside the cavity (τ_c).

3.2.4. The Purcell effect

It is not immediately obvious how the cooperativity C_0 relates to cavity parameters such as the quality factor and the mode volume, since the cavity–emitter coupling g was introduced without further specification. We therefore recall the standard relations. The coupling rate depends on the cavity mode volume. While the general mode volume V_m was defined in Sec. 3.1.3, for coupling to a specific emitter one introduces an effective mode volume V_{eff}, normalized at the emitter position rather than at a field antinode. The coupling rate between a cavity mode of volume V_{eff} and a dipolar transition with dipole moment μ_{12} at frequency $\omega = \omega_c = \omega_a$ depends on the orientation of the dipole relative to the cavity field. We quantify this by the projection factor $\xi = |\vec{\mu} \cdot \vec{E}|/(|\vec{\mu}|\,|\vec{E}|)$, such that $\xi = 1$ corresponds to perfect alignment. The coupling rate is then given by [128, 131]

$$g = \mu_{12} \sqrt{\frac{\omega}{2\epsilon_0 \hbar V_{\text{eff}}}}\, \xi, \tag{3.2.11}$$

while the corresponding free-space decay rate reads

$$\gamma_{12} = \frac{\omega^3 \mu_{12}^2}{3\pi\epsilon_0 \hbar (c/n)^3}. \tag{3.2.12}$$

The decay rate γ_{12} does not necessarily equal the spontaneous emission rate γ_0 if there are multiple transitions (radiative or non-radiative) contributing to the total decay rate γ_0. Introducing the branching ratio $\beta_{\text{tot}} = \gamma_{12}/\gamma_0$, and inserting the above relations for g and γ_{12} into the definition of C_0 from Eq. (3.2.10), we obtain

$$C_0 = \beta_{\text{tot}} \cdot \xi^2 \frac{3}{4\pi^2} \left(\frac{\lambda}{n}\right)^3 \frac{Q}{V_{\text{eff}}} \equiv \beta_{\text{tot}} \cdot F_P, \tag{3.2.13}$$

where $\kappa = \omega/Q$, $\lambda = 2\pi c/\omega$, and F_P is the single-mode, on-resonance Purcell factor, first introduced by Purcell in 1946 [51]. In its original definition, the Purcell factor F_P is

determined solely by the photonic environment (Q, V_m, λ, n) and quantifies how strongly a single cavity mode can enhance the spontaneous emission rate of a transition under the assumption of perfect dipole alignment at a field antinode. In practice, however, both the spatial overlap of the emitter with the cavity field (through the use of an effective mode volume V_{eff}) and the dipole orientation (through a factor ξ^2) are usually absorbed into the Purcell factor, so that F_P directly quantifies the enhancement experienced by the transition of interest.

For a Fabry–Pérot cavity, it is often convenient to express the Purcell factor in terms of the cavity finesse $\mathcal{F}$ and the beam waist w_0. Using $Q = \mathcal{F}\frac{2L}{\lambda/n}$ and $V_{\text{eff}} = \frac{\pi}{4}w_0^2 L$ (assuming the emitter is located at a field antinode), one obtains

$$F_P = \xi^2 \frac{3}{4\pi^2}\left(\frac{\lambda}{n}\right)^3 \frac{Q}{V_{\text{eff}}} = \xi^2 \frac{6}{\pi^3}\left(\frac{\lambda}{n}\right)^2 \frac{\mathcal{F}}{w_0^2}. \tag{3.2.14}$$

We will use this relation to predict and compare the expected Purcell factors for hybrid diamond–air Fabry–Pérot cavities in Sec. 5.2. A detailed derivation of the Purcell factor based on Fermi's golden rule can be found in Ref. [128].

In contrast to the Purcell factor F_P, the cooperativity C_0 quantifies the strength of the coherent interaction between a specific emitter transition and the cavity mode, normalized to the relevant dissipative rates. Since only the fraction of spontaneous emission that couples to the considered transition contributes, C_0 depends not only on the cavity parameters but also on the emitter properties through the branching ratio, with $C_0 = \beta_{\text{tot}} \cdot F_P$. It is often referred to as the effective Purcell factor, as it reflects not just the enhancement of a single decay channel, but the actual modification of the emitter's total spontaneous emission rate and, consequently, its excited-state lifetime.

3.2.5. Transmission, reflection and scattering of a weak drive

In the previous discussion, we derived the Purcell-enhanced emitter decay rate by analyzing the equations of motion for the cavity field and the emitter polarization in the bad-cavity limit. While this describes the modified spontaneous emission dynamics following excitation, we now turn to the coherent response of the coupled cavity–emitter system under weak driving, focusing on the steady-state transmission, reflection, and scattering properties.

Assuming steady state, we set the derivatives in Eqs. (3.2.5)a,b to zero, and assuming a weak drive (linear response), we set the inversion $\langle\sigma_z\rangle \approx -1$. Thus we obtain the steady-state intracavity field $\langle a\rangle$ and emitter dipole $\langle\sigma_-\rangle$

$$\langle a\rangle = \frac{\chi}{\frac{\kappa}{2} - i\Delta_c + g^2/(\frac{\gamma_0}{2} + \gamma^\star - i\Delta_a)}, \tag{3.2.15a}$$

$$\langle\sigma_-\rangle = \frac{-ig\chi}{\frac{\gamma_0}{2} + \gamma^\star - i\Delta_a}\langle a\rangle. \tag{3.2.15b}$$

We use the symmetric input–output boundary conditions at the two cavity mirrors (cf. Fig. 3.3) [137, 138]

$$\hat{a}_{1,\mathrm{in}} + \hat{a}_{1,\mathrm{out}} = \sqrt{\kappa_1}\,\hat{a}, \tag{3.2.16a}$$

$$\hat{a}_{2,\mathrm{out}} = \sqrt{\kappa_2}\,\hat{a}, \qquad (\hat{a}_{2,\mathrm{in}} = 0), \tag{3.2.16b}$$

and drive the system only through mirror 1, identifying $\hat{a}_{1,\mathrm{in}} = \chi/\sqrt{\kappa_1}$. With the steady-state intracavity amplitude $\langle a\rangle$ from the linearized solution, the complex amplitude transmission and reflection coefficients are

$$t_c(\omega_l) \equiv \frac{\langle \hat{a}_{2,\mathrm{out}}\rangle}{\langle \hat{a}_{1,\mathrm{in}}\rangle} = \frac{\sqrt{\kappa_1\kappa_2}}{\chi}\,\langle a\rangle, \tag{3.2.17a}$$

$$r_c(\omega_l) \equiv \frac{\langle \hat{a}_{1,\mathrm{out}}\rangle}{\langle \hat{a}_{1,\mathrm{in}}\rangle} = \frac{\kappa_1}{\chi}\,\langle a\rangle - 1 = \sqrt{\frac{\kappa_1}{\kappa_2}}\,t_c(\omega_l) - 1. \tag{3.2.17b}$$

The transmitted (T_c), reflected (R_c), and scattered (S_c) intensities are then given by

$$T_c(\omega_l) = |t_c(\omega_l)|^2, \qquad R_c(\omega_l) = |r_c(\omega_l)|^2, \qquad S_c(\omega_l) = 1 - T_c(\omega_l) - R_c(\omega_l). \tag{3.2.18}$$

Empty cavity and residual losses. As a consistency check, we derive the cavity transmission T_c for an empty cavity by setting the coupling to zero ($g = 0$). In this case, the transmission is given by

$$T_c(\Delta_c) = \frac{\kappa_1\kappa_2}{(\kappa/2)^2 + \Delta_c^2}, \tag{3.2.19}$$

which coincides with the expression in Eq. (3.1.5) when using the relations $\delta\nu_{\mathrm{cav}} = \frac{\kappa}{2\pi}$ and $T_{c,\max}^{g=0} = 4\kappa_1\kappa_2/\kappa^2$. For a lossless symmetric cavity with $\kappa_1 = \kappa_2 = \kappa/2$, the transmission reaches unity at resonance, while the reflection vanishes.

If an additional decay channel with rate κ_l that does not contribute to either reflection or transmission is present — such as scattering or absorption — then the transmitted and reflected intensities no longer add up to one ($T_c(\Delta_c) + R_c(\Delta_c) < 1$, hence $S_c(\Delta_c) > 0$), and scattering[3] becomes relevant. A full reflection contrast can still be reached in the case of an impedance-matched cavity, where the incoupling loss equals all other combined losses ($\kappa_1 = \kappa_2 + \kappa_l$). This directly follows from the reflectivity at zero detuning,

$$R_c(0) = \left(\frac{-\kappa_1 + (\kappa_2 + \kappa_l)}{\kappa_1 + \kappa_2 + \kappa_l}\right)^2 \equiv \left(r_{\min}^{g=0}\right)^2, \tag{3.2.20}$$

which vanishes under the impedance-matching condition.

[3] The scattering intensity S_c as used here includes residual cavity losses such as scattering, absorption, and clipping. For non-zero cavity–emitter couplings g, it also accounts for spontaneous emission into free-space modes outside the cavity.

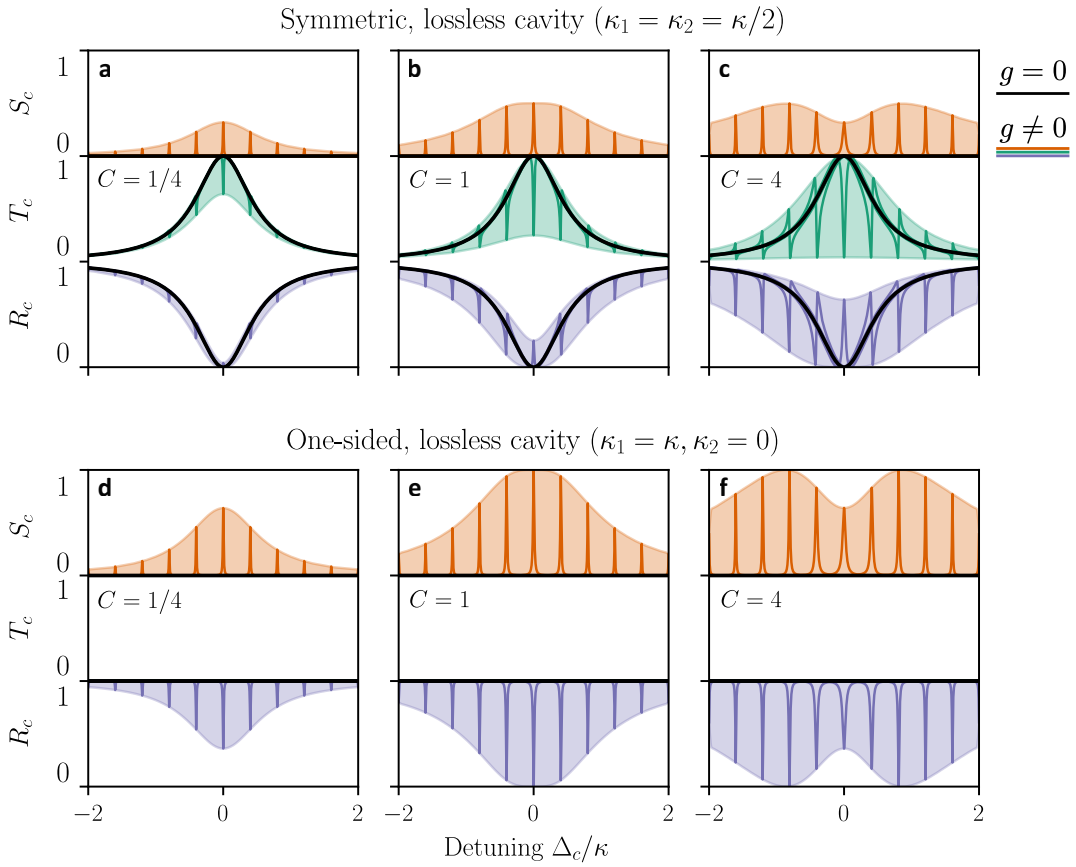

Figure 3.5: Cavity transmission T_c, reflection R_c, and scattering S_c spectra. Shown versus cavity detuning Δ_c/κ for three cooperativities $C = 1/4,\ 1,\ 4$ (corresponding to $g = \kappa/20,\ \kappa/10,\ \kappa/5$) at fixed atomic decay $\gamma_0 = \kappa/100$ and no pure dephasing ($\gamma^\star = 0$). Top row **(a–c)**: symmetric cavity ($\kappa_1 = \kappa_2 = \kappa/2$). Bottom row **(d–f)**: one-sided cavity ($\kappa_1 = \kappa,\ \kappa_2 = 0$). For each cooperativity, the shaded regions indicate the variation with emitter detuning Δ_a, bounded by the bare cavity response (black). Comparing the two geometries highlights how cavity symmetry modifies the interplay of transmission, reflection, and scattering in the coupled cavity–emitter system.

Resonant extinction and coherent cooperativity. We now examine how a coupled emitter ($g \neq 0$) modifies the cavity transmission and reflection spectra. At zero detuning ($\Delta_c = \Delta_a = 0$), the contrasts take the form

$$R_c(0) = \frac{\left(r_{\min}^{g=0} + C\right)^2}{(1+C)^2}, \tag{3.2.21a}$$

$$T_c(0) = \frac{T_{c,\max}^{g=0}}{(1+C)^2}, \tag{3.2.21b}$$

$$S_c(0) = \frac{\frac{4\kappa_1}{\kappa_1+\kappa_2} C}{(1+C)^2}, \tag{3.2.21c}$$

with the coherent cooperativity $C = 4g^2/\kappa(\gamma_0 + 2\gamma^\star)$. Equation (3.2.21a) can be recast as

$$R_c(0) = \frac{\left(-\kappa_1 + (\kappa_2 + \kappa_l + \kappa_e)\right)^2}{\left(\kappa_1 + \kappa_2 + \kappa_l + \kappa_e\right)^2},$$

where $\kappa = \kappa_1 + \kappa_2 + \kappa_l$ and $\kappa_e = 4g^2/(\gamma_0 + 2\gamma^\star) = C\kappa$. Written in this form, the effect of the emitter enters identically to an additional contribution to the effective cavity decay rate on resonance. In this sense, the presence of the emitter suggests an adapted impedance-matching condition, $\kappa_1 = \kappa_2 + \kappa_l + \kappa_e$, in analogy to the empty-cavity case.

For two important limiting cases the expressions simplify to

$$\text{Symmetric cavity } (\kappa_1 = \kappa_2): \quad \begin{cases} R_c(0) = \dfrac{C^2}{(1+C)^2}, \\ T_c(0) = \dfrac{1}{(1+C)^2}, \\ S_c(0) = \dfrac{2C}{(1+C)^2}. \end{cases} \tag{3.2.22}$$

$$\text{One-sided cavity } (\kappa_2 = 0): \quad \begin{cases} R_c(0) = \dfrac{(C-1)^2}{(1+C)^2}, \\ T_c(0) = 0, \\ S_c(0) = \dfrac{4C}{(1+C)^2}. \end{cases} \tag{3.2.23}$$

Figure 3.5 shows the frequency dependence of reflection, transmission, and scattering for three representative cooperativities ($C = 1/4,\ 1,\ 4$) in symmetric and one-sided lossless cavities. The shaded regions highlight the achievable contrast compared to the empty-cavity response (solid black line) as the emitter is detuned. The two cavity configurations not only allow for compact analytical expressions at zero detuning, but also reflect typical experimental situations where either transmission (symmetric cavity) or reflection (one-sided cavity) is the relevant observable.

In the symmetric case (see Fig. 3.5a–c), the reflection and transmission contrast at zero detuning is maximized and grows monotonically with cooperativity, as the emitter increasingly acts like a mirror. The scattered intensity peaks at 50% for $C = 1$, reflecting the balance between the cavity and emitter decay channels. For finite emitter detuning, the spectra exhibit Fano-like asymmetries due to interference between the direct cavity path and the emitter-mediated path; these become more pronounced at larger cooperativity. Importantly, the normalized transmission contrast depends only on the cooperativity and on the empty-cavity transmission $T_{c,\max}^{g=0}$. Since a symmetric cavity maximizes the bare transmission, it also maximizes the achievable contrast.

In the one-sided case (see Fig. 3.5d–f), the empty cavity fully reflects and shows no scattering. Coupling to the emitter opens a tunable loss channel, quantified by the effective rate κ_e, that scatters photons into free space. At zero detuning the reflection reduces to

$$R(0) = \left(\frac{C-1}{C+1}\right)^2 = \left(\frac{\kappa_e - \kappa_1}{\kappa_e + \kappa_1}\right)^2. \tag{3.2.24}$$

The impedance-matching condition $\kappa_e = \kappa_1 = \kappa$ ($C = 1$) produces destructive interference between the directly reflected and cavity-leaked fields, such that reflection vanishes and all incident photons are lost into free-space modes. For $C \geq 1$, full contrast can also be obtained by reducing the effective coupling via cavity detuning.

3.2.6. Saturation

So far, the derivation of the emitter-modified transmission and reflection spectra has assumed a weak coherent drive, such that the emitter remains predominantly in its ground state and the inversion is fixed to $\langle\sigma_z\rangle \approx -1$. We now relax this assumption and allow for a variable inversion,

$$\langle\sigma_z\rangle = -\frac{1}{1+s}, \tag{3.2.25}$$

which accounts for saturation of the two-level emitter.

We follow the derivation of Refs. [139, 140], where the saturation parameter is obtained as

$$s = \frac{4\beta_C^2}{C\gamma_0} |\langle a_{1,\mathrm{in}}\rangle|^2, \tag{3.2.26}$$

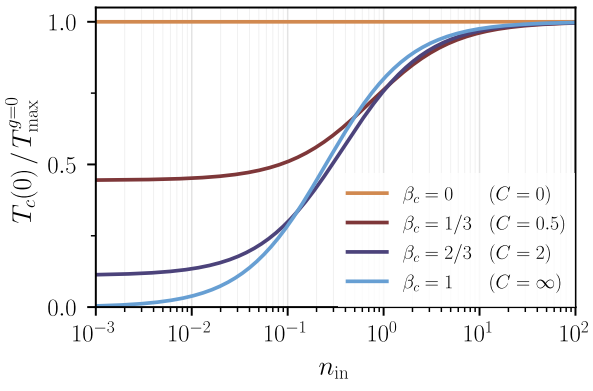

Figure 3.6: Saturation of the extinction contrast in transmission. On-resonant transmission as a function of the input photon number n_{in} for four coherent β_C factors, $\beta_C = 0$, 1/3, 2/3, and 1, corresponding to coherent cooperativities $C = 0$, 0.5, 2, and ∞, respectively. Increasing drive strength saturates the emitter, leading to a progressive reduction of the extinction contrast and a recovery of the bare-cavity transmission.

with the coherent β-factor defined as $\beta_C = C/(C+1)$. This quantity characterizes the probability for a resonant cavity photon to interact coherently with the emitter. Equation (3.2.26) can be rewritten in a more intuitive form,

$$s = \frac{n_{\text{in}}}{n_{\text{crit}}}, \tag{3.2.27}$$

by introducing the input photon number per Purcell-enhanced lifetime,

$$n_{\text{in}} = \frac{|\langle a_{1,\text{in}}\rangle|^2}{(C+1)\gamma_0}, \tag{3.2.28}$$

and the critical photon number,

$$n_{\text{crit}} = \frac{1}{4\beta_C}. \tag{3.2.29}$$

Here, $\langle a_{1,\text{in}}\rangle$ denotes the coherent amplitude of the input field in the input–output formalism and is normalized such that $|\langle a_{1,\text{in}}\rangle|^2$ equals the photon flux incident in the cavity input channel (in units of photons/s). Experimentally, it is obtained from the incident laser power as $|\langle a_{1,\text{in}}\rangle|^2 = \chi_{\text{in}} P_{\text{laser}}/(\hbar\omega)$, where χ_{in} accounts for mode-matching and the finite input coupling fraction.

The saturation model of Refs. [139, 140] is derived for a symmetric, lossless two-sided cavity, for which the intracavity photon number corresponding to a given incident photon flux is fixed by equal input–output coupling rates. For a general cavity with asymmetric mirror couplings and additional loss, the steady-state intracavity photon number for a given input field amplitude $\langle a_{1,\text{in}}\rangle$ is modified by a factor $2\kappa_1/\kappa$, where $\kappa = \kappa_1 + \kappa_2 + \kappa_{\text{loss}}$. We account for this by rescaling the saturation parameter accordingly, which shifts the effective input photon number required to reach saturation depending on the cavity asymmetry and loss.

For a perfectly coupled emitter ($C \gg 1$, corresponding to $\beta_C \to 1$), the system reaches saturation, characterized by an inversion $\langle \sigma_z \rangle \approx -1/2$, already at an average intracavity photon number of $n_{\text{in}} = 1/4$ per emitter lifetime. Since a two-level system can coherently interact with at most a single photon at a time, saturation suppresses the coherent light–matter interaction, leading to a reduction of the extinction contrast as excess photons are transmitted through the cavity. In Refs. [139, 140], the on-resonant transmitted intensity in the presence of saturation is derived as

$$T_c(0) = T_{c,\max}^{g=0}\left[\left(1 - \frac{\beta_C}{1+s}\right)^2 + \beta_C^2 \frac{s}{(1+s)^2}\right]. \tag{3.2.30}$$

This saturation-induced recovery of the bare-cavity transmission is illustrated in Fig. 3.6.

3.2.7. Real-world degradations

In the weak-drive limit, the ideal reflection, transmission, and scattering spectra follow directly from the input–output model. In practice, several additional mechanisms reduce the effective cooperativity

$$C = \frac{4g^2}{\kappa\,(\gamma_0 + 2\gamma^\star)}, \tag{3.2.31}$$

or lower the observable contrast.

Residual cavity loss κ_{loss}. The total linewidth can be written as $\kappa = \kappa_1 + \kappa_2 + \kappa_{\mathrm{loss}}$, where κ_1 and κ_2 are the designed port couplings and κ_{loss} accounts for absorption or scattering at the mirrors. Such residual losses increase the cavity decay rate without contributing to useful ports, thereby lowering the cooperativity, reducing the maximum achievable extinction, and shifting the empty-cavity baseline that defines the attainable contrast.

Mode matching. An imperfect spatial and polarization overlap between the probe/collection modes and the cavity mode reduces the effective coupling efficiency η_{mm}. In our setup, the probe field is delivered to the cavity through a single-mode fiber and therefore exhibits only a finite spatial overlap with the intracavity mode. In contrast, the transmitted signal is collected into free space, where the detection mode can be adapted to maximize collection efficiency. Assuming perfect angular alignment and optimal positioning of the fiber core relative to the cavity mode, the maximum achievable spatial mode-matching efficiency can be estimated following Ref. [56] as

$$\eta_{\mathrm{mm}} = \frac{4}{\left(\frac{w_f}{w_m} + \frac{w_m}{w_f}\right)^2 + \left(\frac{\pi\, n_f\, w_f w_m}{\lambda\, R}\right)^2}, \tag{3.2.32}$$

where w_f denotes the fiber mode waist, w_m the cavity mode waist at the fiber mirror, n_f the refractive index of the fiber, and R the radius of curvature of the fiber mirror (see Chapter 4.1.1 for further details).

The reflected spectrum is then a weighted sum of the ideal cavity response and an uncoupled background,

$$R_{\mathrm{obs}}(\Delta) = \eta_{\mathrm{mm}}\, R_{\mathrm{ideal}}(\Delta) + (1 - \eta_{\mathrm{mm}}), \tag{3.2.33}$$

which directly lowers the observed contrast.

Spatial/polarization mismatch. If the emitter is not positioned at a field antinode or its dipole is misaligned with the cavity polarization, the coherent coupling is reduced. A convenient parametrization is

$$g = \xi \sqrt{\tfrac{V_{\mathrm{m}}}{V_{\mathrm{eff}}}}\, g_{\mathrm{ideal}}, \tag{3.2.34}$$

with $0 \leq \xi, V_m/V_{\text{eff}} \leq 1$. Here, ξ quantifies polarization mismatch, while the ratio V_m/V_{eff} captures spatial mismatch via the effective mode volume at the emitter's position. The term g_{ideal} denotes the coupling rate for perfect alignment at a field antinode. In our open microcavity geometry, the lateral overlap can be tuned experimentally, whereas the longitudinal positioning with respect to a field antinode is largely fixed by the implantation depth of the color center and the reflection phase of the planar mirror. The polarization overlap, in turn, is set by the crystallographic dipole axes of the emitter and the polarization eigenmodes of the cavity, and is therefore essentially non-adjustable in practice[4].

Mechanical stability. Cavity-length fluctuations shift the cavity resonance, $\Delta_c \to \Delta_c + \delta_c(t)$. If the correlation time of $\delta_c(t)$ is short compared to the acquisition time, the recorded spectrum corresponds to the convolution of the ideal response with the cavity-detuning distribution $p_c(\delta)$, i.e., the cavity resonance is broadened (for Gaussian jitter the lineshape is Voigt with Lorentzian width κ and Gaussian width σ_c). This effectively enlarges the cavity linewidth and reduces cooperativity via $C = 4g_{\text{eff}}^2/(\kappa_{\text{eff}}\gamma_0)$. Slower drifts appear as scan-to-scan shifts of the cavity peak.

Pure dephasing. Fast environmental fluctuations (e.g. phonons, charge noise) that occur on timescales shorter than the emitter's coherence time act as an additional homogeneous broadening channel. Pure dephasing enters the transverse coherence rate as $\gamma_\perp = \gamma_0/2 + \gamma^\star$, thereby reducing the effective cooperativity and washing out interference.

Spectral diffusion. For solid-state emitters such as color centers, fluctuations of the optical transition frequency can occur on a wide range of timescales. If their correlation time is long compared to the emitter coherence time but short compared to the experimental integration time, the resonance performs a random walk during the measurement, and the recorded spectrum appears inhomogeneously broadened. In contrast, fluctuations slower than the integration time do not reduce spectral contrast but show up as discrete spectral jumps between successive scans.

Charge dynamics / blinking. Very slow dynamics, such as switching between charge or metastable states, make the emitter intermittently dark or detuned for durations much longer than a typical measurement of the coherent response. For fast blinking (compared to the detector integration time), the spectrum is a weighted mixture of bright and dark responses,

$$S_{\text{obs}}(\Delta) = p_b\, S_{\text{bright}}(\Delta) + (1 - p_b)\, S_{\text{dark}},$$

[4] In principle, one could choose a different crystal surface cut to alter the dipole orientation relative to the cavity polarization, but such substrates are generally not available as standard products.

with bright fraction p_b, which reduces the effective cooperativity to $p_\mathrm{b}\,C$. The relevant timescales of blinking and spectral diffusion can be identified from bunching features in the intensity autocorrelation function $g^{(2)}(\tau)$.

Although all of the above mechanisms reduce the observed contrast, their origin can usually be distinguished. Cavity-related effects such as loss, mode matching, or mechanical instability also appear in empty-cavity measurements and can be identified independently through linewidth, reflection contrast, or stability tests. Non-ideal polarization and spatial overlap manifest in lifetime measurements, lowering the bare cooperativity C_0. In contrast, emitter-related processes such as pure dephasing or spectral diffusion (as long as the spectral fluctuations remain small compared to the cavity linewidth) are only revealed in resonant measurements. Overall, these signatures allow one to disentangle the different contributions.

3.3. Collective effects in Fabry–Pérot cavities

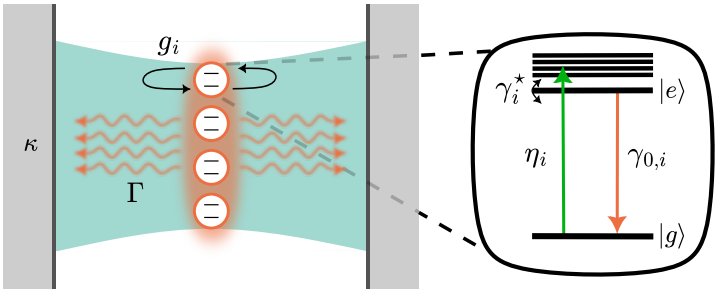

Figure 3.7: Collective cavity–emitter coupling model. An optical cavity with leakage rate κ couples with strength g_i to N two-level emitters. Each emitter is incoherently pumped at rate η_i, undergoes spontaneous emission at rate $\gamma_{0,i}$, and experiences pure dephasing at rate $\gamma_i^\star$. After adiabatic elimination of the cavity mode, the ensemble dipole decays collectively through the cavity channel at an effective rate Γ.

3.3.1. Tavis–Cummings Hamiltonian and Master equation

We now consider an ensemble of N emitters, each coupled to the same cavity mode. The system in its most general form is described by the Tavis–Cummings Hamiltonian [141, 142]

$$H_{\mathrm{TC}} = \underbrace{\hbar\omega_c\,\hat{a}^\dagger\hat{a}}_{\text{cavity}} + \underbrace{\hbar\sum_{i=1}^{N}\frac{\omega_{a,i}}{2}\hat{\sigma}_{z,i}}_{\text{emitters}} + \underbrace{\hbar\sum_{i=1}^{N} g_i\left(\hat{\sigma}_{+,i}\,\hat{a} + \hat{a}^\dagger\hat{\sigma}_{-,i}\right)}_{\text{cavity–emitter coupling}}. \tag{3.3.1}$$

Explanation of terms and notation.

- $\hat{a}^\dagger$, $\hat{a}$: creation and annihilation operators of the cavity mode, $[\hat{a}, \hat{a}^\dagger] = 1$.
- $\hat{\sigma}_{z,i} = |e\rangle_i\langle e| - |g\rangle_i\langle g|$: Pauli operator of emitter i with eigenstates $|e\rangle_i$ and $|g\rangle_i$.
- $\hat{\sigma}_{-,i} = |g\rangle_i\langle e|$, $\hat{\sigma}_{+,i} = |e\rangle_i\langle g|$: lowering and raising operators of emitter i.
- ω_c: cavity resonance frequency.
- $\omega_{a,i}$: optical transition frequency of emitter i (allows for inhomogeneous broadening).
- g_i: single-photon vacuum Rabi coupling rate between emitter i and the cavity mode.

The dynamics are governed by the Lindblad master equation (3.2.2) with the associated Hamiltonian and jump operators for the incoherently pumped cavity–ensemble system [142]:

- Hamiltonian: $H = H_{\mathrm{TC}}$.
- Cavity damping: $L_\kappa = \sqrt{\kappa}\,\hat{a}$.
- Emitter spontaneous emission: $L_{\gamma_{0,i}} = \sqrt{\gamma_{0,i}}\,\hat{\sigma}_{-,i}$.
- Emitter pure dephasing: $L_{\gamma^\star,i} = \sqrt{\frac{\gamma_i^\star}{2}}\,\hat{\sigma}_{z,i}$.
- Incoherent pumping: $L_{\eta,i} = \sqrt{\eta_i}\,\hat{\sigma}_{+,i}$.

In contrast to the weakly, resonantly driven single emitter (compare Eq. (3.2.1)), here we consider an incoherently pumped ensemble with independent pumping rates η_i. The incoherent drive thus enters via the dissipators rather than through the Hamiltonian.

3.3.2. Bad cavity limit and identical emitters

For N identical emitters with frequency ω_a and identical coupling g to a cavity of frequency ω_c, we define the detuning $\Delta = \omega_c - \omega_a$ and work in the rotating frame of the emitters at frequency ω_a. In the limit where the cavity field relaxes on the fastest timescale, the cavity can be adiabatically eliminated. This requires that the cavity decay rate dominates over the collective emitter–cavity coupling strength [142],

$$\kappa \gg g\sqrt{N}, \tag{3.3.2}$$

or, equivalently, that the cavity relaxes much faster than any emitter-induced dynamics. Under this assumption, the effective Hamiltonian of the emitters reads [143, 144]

$$H_{\mathrm{TC,eff}} = \hbar\,\frac{\delta\omega}{2}\sum_{i=1}^{N}\hat{\sigma}_{z,i} = \hbar\,\delta\omega\,\hat{J}_z, \tag{3.3.3}$$

with collective operators $\hat{J}_\pm = \sum_{i=1}^{N}\hat{\sigma}_{\pm,i}$ and $\hat{J}_z = \frac{1}{2}\sum_{i=1}^{N}\hat{\sigma}_{z,i}$. The cavity induces both an energy (Lamb) shift and an effective collective decay channel, with rates

$$\delta\omega = \frac{2g^2\,\Delta}{\Delta^2 + \left(\frac{\kappa+\eta+\gamma_0}{2} + \gamma^\star\right)^2}, \tag{3.3.4}$$

$$\Gamma = \frac{g^2\,\kappa}{\Delta^2 + \left(\frac{\kappa+\eta+\gamma_0}{2} + \gamma^\star\right)^2}. \tag{3.3.5}$$

On resonance ($\Delta = 0$), the Hamiltonian reduces to $H_{\mathrm{TC,eff}} = 0$, so the dynamics are governed purely by the collective decay channel with rate $\Gamma = 4g^2/\kappa = C_0\gamma_0$, in addition to the individual dissipators. This expression holds in the bad-cavity limit $\kappa \gg \gamma_0,\ \gamma^\star,\ \eta$, where cavity losses dominate over all other incoherent processes.

The master equation retains the emitter-local channels and replaces the cavity loss by a collective channel. The dynamics are again given by the Lindblad master equation (3.2.2) with the following ingredients:

- Hamiltonian: $H = H_{\mathrm{TC,eff}}$.
- Collective cavity-mediated decay: $L_{\mathrm{coll}} = \sqrt{\Gamma}\,\hat{J}_-$.
- Emitter spontaneous emission (unchanged): $L_{\gamma_0,i} = \sqrt{\gamma_{0,i}}\,\hat{\sigma}_{-,i}$.
- Emitter pure dephasing (unchanged): $L_{\gamma^\star,i} = \sqrt{\gamma_i^\star/2}\,\hat{\sigma}_{z,i}$.
- Incoherent pumping (unchanged): $L_{\eta,i} = \sqrt{\eta_i}\,\hat{\sigma}_{+,i}$.

For a detailed derivation and refinements such as emitter-induced broadening, see [143, 144].

3.3.3. Collective Dicke basis

It is often convenient to rewrite the dynamics in the basis of collective Dicke states $|J, M\rangle$, which are simultaneous eigenstates of $\hat{J}^2$ and $\hat{J}_z$:

$$\hat{J}^2|J,M\rangle = J(J+1)\,|J,M\rangle, \tag{3.3.6}$$

$$\hat{J}_z|J,M\rangle = M\,|J,M\rangle. \tag{3.3.7}$$

The quantum number M directly fixes the number of excitations in the ensemble,

$$n_{\mathrm{exc}} = \tfrac{N}{2} + M, \tag{3.3.8}$$

ranging from 0 (all emitters in the ground state, $M = -N/2$) to N (all emitters excited, $M = +N/2$). The quantum number J quantifies the strength of the collective dipole: the fully symmetric case $J = N/2$ corresponds to all emitters radiating in phase, maximizing the dipole moment and the coupling to the cavity. Smaller J values correspond to states with reduced permutation symmetry, leading to partial cancellation of dipoles and hence weaker collective coupling. Each Dicke state is a coherent superposition of all emitter configurations with the same number of excitations, constructed such that it carries a definite dipole strength (i.e. a definite J). The multiplicity of states in each J sector follows from combinatorics. Importantly, the number of states decreases with increasing J, so most states reside in lower-symmetry subradiant manifolds.

The action of the collective operators on these states makes the connection to cooperative emission explicit:

$$\hat{J}_\pm|J,M\rangle = \sqrt{(J \mp M)(J \pm M + 1)}\,|J, M \pm 1\rangle. \tag{3.3.9}$$

Accordingly, the cavity-mediated dissipator $L_{\mathrm{coll}} = \sqrt{\Gamma}\,\hat{J}_-$ induces transitions $|J,M\rangle \to |J,M-1\rangle$ with rates enhanced by the factor $(J+M)(J-M+1)$. In the symmetric manifold $J = N/2$, this enhancement produces the familiar superradiant burst, whose peak collective decay rate scales as $N\Gamma$.

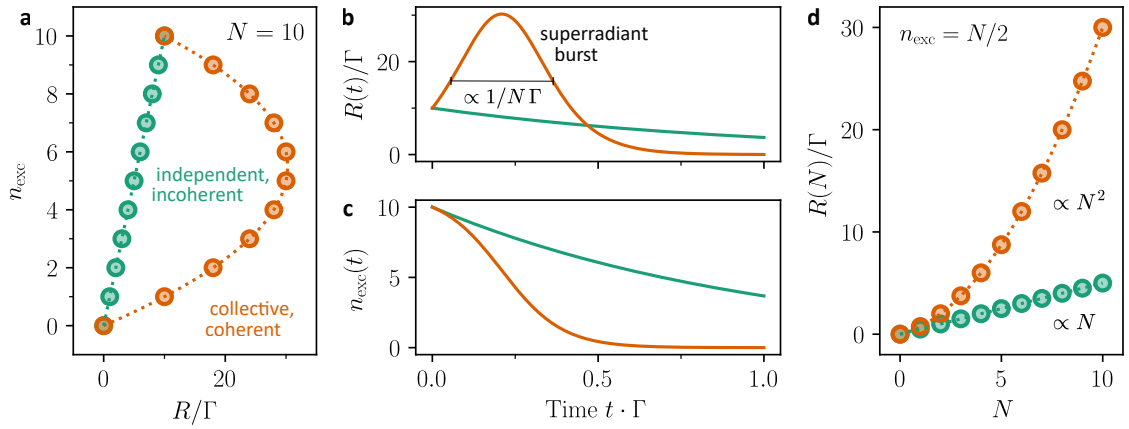

Figure 3.8: Emission dynamics for the coherent (Dicke) and incoherent ensemble. (a) Emission rate R/Γ versus excitation number n_{exc} for $N = 10$ emitters shows quadratic scaling in the collective (orange) case compared to the linear trend for independent decay (green). **(b,c)** Time evolution of the emission rate and excited-state population for a fully inverted ensemble, where Dicke superradiance produces a burst-like peak and accelerated depletion relative to the smooth exponential decay of incoherent emission. **(d)** Scaling of the emission rate at half inversion ($n_{\mathrm{exc}} = N/2$) with emitter number N, highlighting the quadratic growth of the collective channel versus the linear scaling of the independent one.

In contrast, the individual local dissipators $(L_{\gamma_0,i}, L_{\gamma^\star,i}, L_{\eta,i})$ break permutation symmetry and couple different Dicke manifolds J. Thus, the dynamics reflect a competition between collective superradiant decay and individual incoherent processes, which redistribute population across Dicke manifolds.

3.3.4. Collective emission rate: coherent vs. incoherent

The photon emission rate into the cavity mode is determined by the collective jump operator $L_{\mathrm{coll}} = \sqrt{\Gamma}\,\hat{J}_-$, hence

$$R = \left\langle L_{\mathrm{coll}}^\dagger L_{\mathrm{coll}} \right\rangle = \Gamma \left\langle J_+ J_- \right\rangle, \tag{3.3.10}$$

with the emitted intensity $I \propto R$. Expanding the collective dipoles separates independent and collective contributions

$$R = \Gamma \left(\sum_{i=1}^{N} \langle \sigma_{+,i}\sigma_{-,i} \rangle + \sum_{i \neq j} \langle \sigma_{+,i}\sigma_{-,j} \rangle \right), \tag{3.3.11}$$

where the first term counts the excited population (individual emission) and the second term encodes inter-emitter coherences responsible for the collective enhancement.

Coherent (Dicke) limit. If the ensemble occupies a Dicke state $|J, M\rangle$ one finds

$$R(J, M) = \Gamma\,(J + M)(J - M + 1) = \Gamma |A^-_{J,M}|^2. \tag{3.3.12}$$

In the fully symmetric manifold $J = N/2$, this depends only on the number of excitations $n_{\mathrm{exc}} = N/2 + M$:

$$R_{\mathrm{coh}}(n_{\mathrm{exc}}) = \Gamma\, n_{\mathrm{exc}} \left(N - n_{\mathrm{exc}} + 1\right). \tag{3.3.13}$$

This parabolic dependence rises linearly for $n_{\mathrm{exc}} \ll N$, peaks near half inversion with $R_{\max} \approx \Gamma N^2/4$, and vanishes at full inversion (compare Fig. 3.8a). The corresponding time dynamics (see Fig. 3.8b,c) show the delayed superradiant burst and rapid depletion of the excited-state population. The quadratic scaling with emitter number at half inversion as depicted in Fig. 3.8d is the hallmark of superradiant emission.

Incoherent (independent) limit. If inter-emitter coherences are destroyed, i.e. the pair term $\sum_{i\neq j}\langle\sigma_{+,i}\sigma_{-,j}\rangle$ vanishes due to strong dephasing or inhomogeneous broadening, one obtains

$$R_{\mathrm{inc}}(n_{\mathrm{exc}}) = \Gamma\, n_{\mathrm{exc}}, \tag{3.3.14}$$

which grows linearly with excitation number and emitter count, reaching $R = \Gamma N$ at full inversion. This linear law appears in Fig. 3.8a,c,d, in sharp contrast to the cooperative case.

Superlinearity under incoherent pumping. When emitters are driven off-resonantly by an incoherent pump with rate η, excitations are created stochastically and largely uncorrelated. The independent part of the emission therefore scales linearly with η, while the collective contribution arises only once at least two atoms are simultaneously excited. Since the probability of such coincidences grows quadratically with the excitation probability, the corresponding pair correlations $\langle\sigma_{+,i}\sigma_{-,j}\rangle$ enter as a term $\propto \eta^2$. The resulting emission rate can thus be written schematically as

$$R \;\approx\; A\,\eta \;+\; B\,\eta^2, \tag{3.3.15}$$

where the linear part reflects independent spontaneous decay and the quadratic part captures the cooperative enhancement. Which of these behaviors dominates in practice depends on the competition between the collective emission rate $\sim N\Gamma$ and the relevant decoherence processes. If the cooperative emission rate exceeds dephasing and inhomogeneous broadening, macroscopic polarization can develop and cooperative emission emerges; otherwise, the dynamics reduce to an incoherent emission law.

Previous works on steady-state superradiance [145, 146] have explored regimes of idealized ensembles and intermediate pump powers, in which the emission rate $R(\eta)$ closely follows the Dicke parabola as a function of excitation number, with a maximum near half inversion. The exact scaling, however, depends sensitively on the number of emitters, the pump regime, dephasing, and inhomogeneous broadening, and must therefore be modeled accordingly. In realistic solid-state ensembles, strong disorder would naively suggest that only incoherent emission is accessible; however, a central result of this work is that the cavity provides a collective decay channel capable of preserving superradiant signatures even in the presence of substantial inhomogeneity. As we will demonstrate in Chapter 7,

this results in a distinct superlinear scaling of the emitted intensity with pump power in the NV-based ensemble studied here.

3.3.5. Photon statistics

Another key manifestation of collective effects in cavities lies in the temporal photon correlations of the leaked cavity field $\hat{a}$. Experimentally, these are measured in a Hanbury Brown and Twiss (HBT) setup, which records the second-order intensity autocorrelation $g^{(2)}(\tau)$ as a function of temporal delay τ. For the cavity output channel after adiabatic elimination (A.E.), one finds

$$g^{(2)}(\tau) = \frac{\langle \hat{a}^\dagger(0)\,\hat{a}^\dagger(\tau)\,\hat{a}(\tau)\,\hat{a}(0)\rangle}{\langle \hat{a}^\dagger(0)\,\hat{a}(0)\rangle^2} \overset{\text{A.E.}}{\approx} \frac{\langle \hat{J}_+(0)\,\hat{J}_+(\tau)\,\hat{J}_-(\tau)\,\hat{J}_-(0)\rangle}{\langle \hat{J}_+(0)\,\hat{J}_-(0)\rangle^2}. \tag{3.3.16}$$

Collective (Dicke) regime. In the coherent Dicke regime, emitters share a common phase and form a macroscopic dipole. Successive emission events then add constructively, producing fluctuations stronger than thermal light: superradiant bursts yield strongly bunched statistics with $g^{(2)}(0) > 2$. Unlike the case of independent emitters, however, there is no general closed-form expression for $g^{(2)}(\tau)$. Its temporal profile depends sensitively on excitation conditions, dephasing, and inhomogeneous broadening, and is typically obtained by numerically solving the master equation. Analytic solutions exist only in special limits, but the generic feature is a narrow, high bunching peak at $\tau = 0$, reflecting the cooperative character of the emission.

Independent (uncorrelated) regime. When emitters radiate independently, the steady state can be approximated as a factorized state in the product basis[5] and the collective operators reduce to $\hat{J}_\pm = \sum_i \hat{\sigma}_{\pm,i}$.

This yields the expression [142]

$$g^{(2)}(\tau) = \frac{\sum_i I_i^2\, g_i^{(2)}(\tau) + \sum_{i\neq k} I_i I_k \big(1 + g_i^{(1)}(\tau) g_k^{(1)*}(\tau)\big)}{\big(\sum_i I_i\big)^2}, \tag{3.3.17}$$

where I_i denotes the emission intensity of emitter i, and $g_i^{(1)}(\tau)$ and $g_i^{(2)}(\tau)$ are the corresponding normalized first- and second-order correlation functions, defined as

$$I_i = \langle \hat{\sigma}_{+,i}(0)\hat{\sigma}_{-,i}(0)\rangle, \quad g_i^{(1)}(\tau) = \frac{\langle \hat{\sigma}_{+,i}(\tau)\hat{\sigma}_{-,i}(0)\rangle}{I_i}, \quad g_i^{(2)}(\tau) = \frac{\langle \hat{\sigma}_{+,i}(0)\hat{\sigma}_{+,i}(\tau)\hat{\sigma}_{-,i}(\tau)\hat{\sigma}_{-,i}(0)\rangle}{I_i^2}.$$

At zero delay this reproduces the thermal-like scaling

$$g^{(2)}(0) = 2\big(1 - \tfrac{1}{N}\big), \tag{3.3.18}$$

[5] That is, in the tensor product of individual emitter states $\{\,|g\rangle_1 \otimes |g\rangle_2 \otimes \cdots,\ |e\rangle_i \otimes |g\rangle_j \cdots\}$, as opposed to the collective Dicke basis.

reflecting the interference of uncorrelated photons. In the opposite limit of strong dephasing, where all first-order coherences vanish within the detection window, one obtains

$$g^{(2)}(0) \simeq 1 - \tfrac{1}{N}. \tag{3.3.19}$$

This reduces to single-emitter antibunching for $N = 1$ and approaches unity, corresponding to Poissonian photon statistics, in the limit $N \to \infty$.

4. A cryogenic cavity QED platform for solid-state quantum optics

In Chapter 2, we have seen that quantum network applications based on color centers in diamond require efficient optical interfaces to link solid-state quantum emitters with photonic channels. In Chapter 3, we introduced a theoretical framework describing how Fabry–Pérot cavities can enhance light–matter interaction via the Purcell effect, thereby enabling efficient coupling of emitters to their optical environment. In the following chapter, we describe the experimental platform of a fiber-based Fabry–Pérot microcavity integrated into a dilution refrigerator, providing a versatile and efficient system for solid-state quantum optics with exceptional mechanical stability at operating temperatures of about 1 K.

4.1. Fiber-based Fabry-Pérot microcavities

Our approach in the context of different cavity architectures. Strong light–matter interaction is a key requirement for realizing multi-node quantum networks in cavity quantum electrodynamics (cQED). As discussed in Chapter 3, a central figure of merit in this context is the Purcell factor $F_P \propto Q/V_m$, highlighting the need to simultaneously optimize the spectral (Q) and geometrical (V_m) properties of the cavity. This requirement has led to the development of a variety of optical resonator architectures, whose suitability depends on the integrated quantum emitter or host material. The main cavity geometries and representative experiments are summarized in Fig. 4.1 with their respective quality factors and mode volumes.

For isolated quantum systems such as atoms or ions, side optical access is required for trapping and manipulation. Consequently, open-access Fabry–Pérot cavities are commonly used for these qubit platforms [147, 148, 149]. The side access comes at the price of a large mode volume, $V_m \sim 10^4 - 10^6 (\lambda/n)^3$, which must be compensated by a high finesse, $\mathcal{F} \sim 10^4 - 10^5$, and corresponding quality factors of $Q \sim 10^7 - 10^9$.

In contrast, solid-state quantum emitters do not require trapping and can be integrated into a variety of cavity platforms. Semiconductor quantum dots can be directly grown into cavity structures such as micropillars or whispering-gallery-mode (WGM) resonators, which feature mode volumes of only a few wavelengths cubed [134, 150, 151]. Photonic crystal cavities offer an alternative platform with ultra-small mode volumes below $V \lesssim (\lambda/n)^3$,

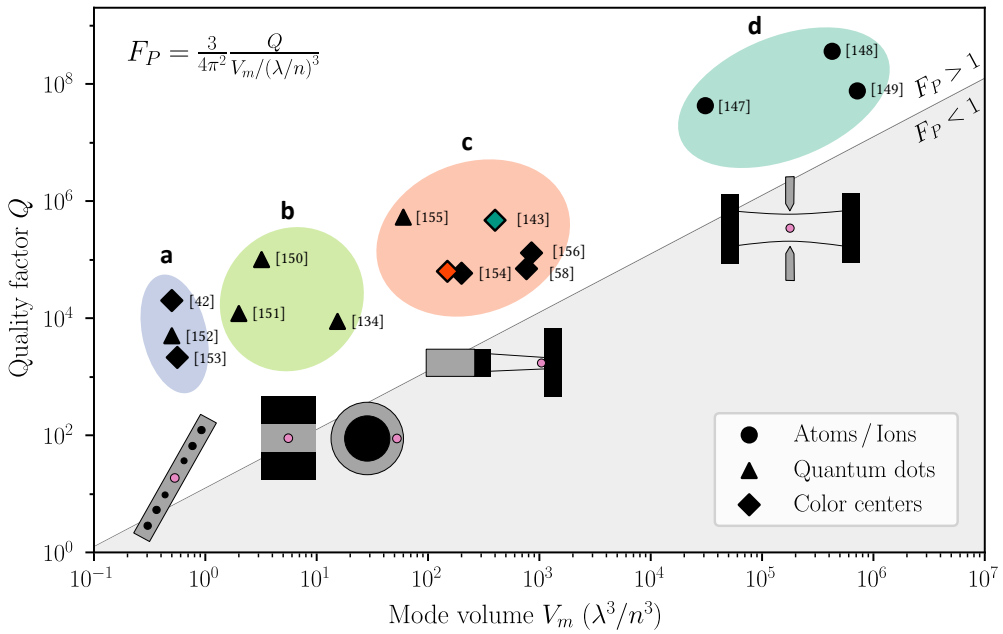

Figure 4.1: Quality factor and mode volume across different cavity platforms. Cavity QED experiments are grouped according to cavity geometry: **(a)** nanophotonic cavities, **(b)** semiconductor microcavities, including micropillars and whispering-gallery-mode resonators, **(c)** tunable Fabry–Pérot microcavities, including fiber-based implementations, and **(d)** open-access Fabry–Pérot cavities. The diagonal line indicates the boundary between Purcell factors above and below unity, assuming perfect branching ratio as well as spectral, polarization, and spatial mode overlap. The orange and teal data points highlight the experimental results presented in Chapters 6 (SnV) and 7 (NV), respectively. For some literature data points, the mode volume and/or quality factor were not explicitly reported and were therefore estimated or calculated.

achieved through periodic dielectric structures that tightly confine light within the emitter host material. This approach is compatible with quantum dots [152] as well as color centers in diamond [42, 153]. However, realizing high-quality diamond-based integrated resonators remains challenging: the hardness and chemical inertness of diamond complicate the precise etching, masking, and surface finishing required for high-performance optical cavities. Furthermore, only a small fraction of color centers in a given sample exhibit suitable optical properties, necessitating spatial screening of the diamond chip. Since nanophotonic cavities are spatially non-tunable, large-scale fabrication is required to obtain a few usable devices with desirable color centers centered in the cavity's field maximum. Nevertheless, the combination of extremely low mode volumes and high quality factors enables highly efficient nodes for quantum networks, as demonstrated in Refs. [42, 43, 59].

Fabry–Pérot microcavities represent a trade-off between their macroscopic counterparts and fully integrated nano- or micro-resonators. They combine wide spectral tunability via adjustable mirror spacing with moderately small mode volumes and high quality

factors [154, 155, 156, 63, 58]. The exact geometry depends on the target application; using optical fibers as one or both mirrors enables further miniaturization and integration.

Our approach. Our cavity geometry is based on a Fabry–Pérot microcavity, in which a macroscopic (half-inch) mirror serves as the sample surface, while the second mirror is formed by the coated end facet of a single-mode optical fiber, as illustrated in Fig. 4.2. Fine cavity tuning is provided by piezoelectric actuators that translate the fiber along the cavity axis and laterally position the sample mirror, while coarse positioning over typically a few millimeters in all spatial directions is realized with stepper motors. This setup enables extensive sample scanning and compensates thermal drifts during cooldown. The open geometry of such microcavities provides exceptional spectral and spatial tunability but also makes them highly susceptible to mechanical noise. Consequently, sophisticated engineering of all cavity components is required to minimize vibrations and ensure mechanical stability, as discussed in Sec. 4.3.2.

This design offers several advantages over cavities formed by two macroscopic mirrors. First, the small lateral cross-section of the fiber tip—often further reduced by laser ablation—allows the mirrors to be brought within a few micrometers of each other, overcoming geometric constraints that otherwise limit achievable cavity lengths and mode volumes. Second, optical excitation and detection are inherently fiber-coupled: light can be launched directly into the cavity through the fiber, without the need for free-space alignment or mode-matching optics, which greatly simplifies operation inside a cryostat. Third, the overlap between the guided fiber mode and the cavity field is fixed by design, ensuring robust and efficient coupling. Finally, when the cavity and fiber modes are well matched, photons are collected through the same fiber, forming a fully fiber-integrated interface ideal for quantum-networking experiments. Despite these advantages, cavities formed by two macroscopic mirrors remain a robust and well-established architecture, and can achieve small mode volumes when aligned with sufficient angular precision, as demonstrated in Refs. [154, 157, 158, 159].

4.1.1. Mirror fabrication

Machining of fiber mirror profiles As discussed in Chapter 3, a Fabry–Pérot resonator requires at least one concave mirror surface to support a stable optical mode. Integrating macroscopic membranes into the cavity requires an extremely flat surface, which is why the curved profile can only be produced on the opposing fiber mirror.

There are two common techniques for structuring the end facet of an optical fiber. Focused ion beam (FIB) milling can produce arbitrary profiles with sub-micrometer depth and lateral resolution. This enabled the realization of a variety of light-shaping [160, 161] and resonant structures [162] in glass fibers. However, FIB milling is a slow process that does not allow for mass production and, more importantly, results in defect-rich and rough surfaces ($\sigma_{\mathrm{RMS}} > 1\,\mathrm{nm}$) that require further processing to achieve low-loss cavities [163].

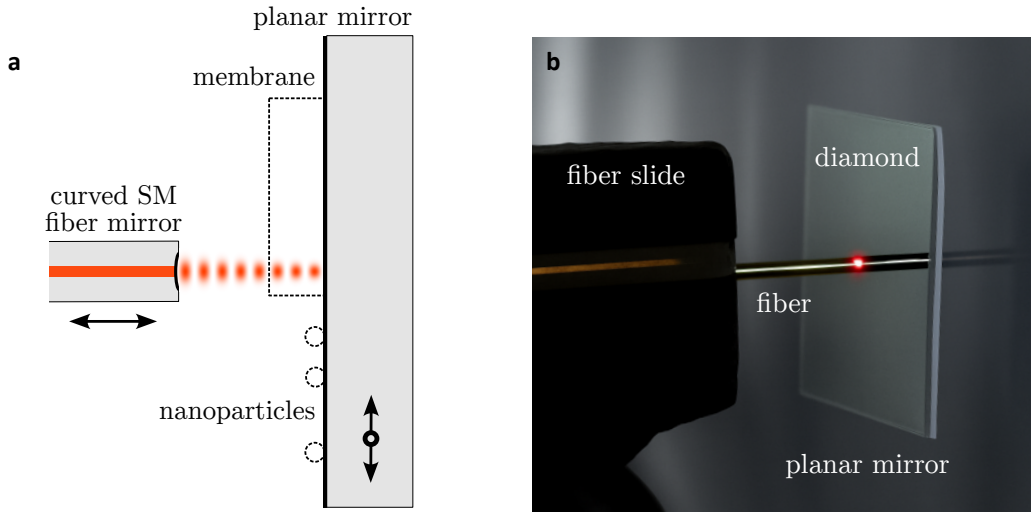

Figure 4.2: A fiber-based Fabry–Pérot microcavity. (a) Schematic of the resonator consisting of a longitudinally tunable concave fiber tip and a laterally tunable macroscopic mirror (dimensions not to scale). The macroscopic mirror typically serves as the sample mirror, here illustrated with either a solid-state membrane or nanoparticles. **(b)** Photograph of the corresponding cavity configuration, digitally enhanced for clarity and contrast while preserving the original appearance. The fiber protrusion is intentionally larger than in typical operation to improve visual clarity.

Our approach uses a tightly focused CO_2 laser pulse to locally melt, evaporate and reflow the glass surface into a circular or elliptical concave mirror profile. Surface tension during reflow results in a smooth surface ($\sigma_{\mathrm{RMS}} \sim 0.2\,\mathrm{nm}$) enabling fiber Fabry–Pérot cavities with high finesse [56]. Figure 4.3a shows a representative fiber end facet used in this work. The depression created by the CO_2 laser shot was characterized using a white-light interferometer (WLI). The resulting reconstructed depth profile is shown in Fig. 4.3b and resembles, to first order, the intensity distribution of the laser focus, which follows a Gaussian profile. The corresponding 2D Gaussian fit is shown as contour lines (black) together with the extracted principal axes (gray). From the depth of the profile t and the standard deviations σ_x, σ_y, one can deduce the radii of curvature $\mathrm{ROC}_{x,y}$ according to

$$\mathrm{ROC}_{x,y} = \frac{\sigma_{x,y}^2}{8t}. \tag{4.1.1}$$

The detailed fabrication procedure is summarized in Refs. [164, 62, 143]. The fibers used in the experiments presented in this work were fabricated by Jonathan Körber for the SnV project and by Maximilian Pallmann for the NV project, with mirror radii of curvature in the range of 15 µm to 35 µm.

Distributed Bragg reflector coating To make the structured fibers suitable for high-finesse optical cavities, the end facets are coated with highly reflective multilayers. Throughout this work, Distributed Bragg Reflectors (DBRs) were used to transform both the fiber

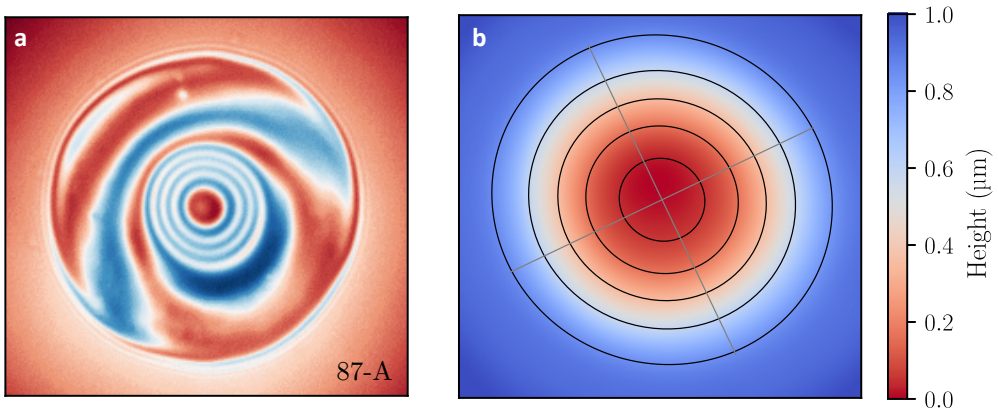

Figure 4.3: Fiber mirror. (a) White-light interferometry image of the fiber end facet after a single CO_2 laser pulse. **(b)** Reconstructed depth profile and corresponding 2D Gaussian fit (black contours, gray principal axes).

end facets and planar glass substrates into cavity mirrors. DBRs consist of alternating layers of high- (Ta_2O_5, $n_H = 2.12$) and low-refractive-index (SiO_2, $n_L = 1.46$) materials, each of thickness $d = \lambda/(4n)$. The thickness is chosen such that partial waves reflected at each refractive-index interface interfere constructively in reflection and destructively in transmission. A stack of N $\lambda/4$-pairs with refractive indices n_H and n_L on a substrate with refractive index n_S, terminated by an external medium of refractive index n_0, yields a minimal reflectivity at the design wavelength λ of [165]

$$R_{\min} = \left(\frac{n_0 n_L^N - n_S n_H^N}{n_0 n_L^N + n_S n_H^N} \right)^2, \tag{4.1.2}$$

and a stopband width given approximately by [166]

$$\frac{\Delta f_{\mathrm{DBR}}}{f} \approx \frac{4}{\pi} \frac{n_H - n_L}{n_H + n_L}, \tag{4.1.3}$$

where $f = c/\lambda$ denotes the optical frequency corresponding to the design wavelength.

Highly reflective DBRs require many alternating layers to effectively suppress transmission of the electromagnetic field. However, because of the finite refractive-index contrast, the optical field can penetrate significantly into the dielectric stack. In contrast to metallic mirrors, where reflection arises from the interaction between the optical field and free electrons within tens of nanometers, dielectric DBRs exhibit penetration depths of several hundred nanometers in the visible range. Depending on the physical gap between the two mirrors and on the depth of the fiber profile, this can substantially limit the minimum achievable cavity length.

In regimes where the overall quality factor of the emitter–cavity system is limited by the emitter rather than by the cavity itself (the bad-emitter limit), additional mirror losses can be tolerated. Under these conditions, the achievable Purcell enhancement can be improved

only by minimizing the cavity mode volume. It can therefore be advantageous to use metal-coated mirrors instead of dielectric DBRs, which introduce higher transmission losses but significantly reduce the optical field penetration depth [167]. In the present work, dielectric distributed Bragg reflectors (DBRs) were selected because they provide high finesse and thereby enable strong light–matter coupling. Ultrashort cavity lengths are not required here, as the finite thickness of the integrated diamond membrane sets a lower bound on the achievable mode volume.

4.2. Qlibri microcavity platform

The Qlibri microcavity platform originated from developments in the groups of Theodor W. Hänsch, Alexander Högele, and David Hunger, where fiber-based Fabry–Pérot microcavities were advanced into a reliable tool for cavity quantum optics. Building on the expertise gained in these projects, former members of the groups[6] founded the company Qlibri GmbH to refine and commercialize the technology. In parallel, our group developed cryogenic-compatible cavity platforms based on the same underlying concept, which were used to obtain the experimental results presented in Chapter 7 and published in Ref. [143]. Since then, we have adopted the Qlibri system as the basis for most cavity experiments presented in this thesis, benefiting from its robust mechanical design and straightforward integration.

4.2.1. Description of the main parts

A schematic and two photographs of the Qlibri cavity platform are shown in Fig. 4.4. In the following, we briefly describe the working principle of the platform by outlining its main mechanical components.

Scanning unit. The planar mirror and sample are mounted inside the xy-scanning unit, which provides fine positioning via two piezo actuators[7]. The scanning mechanism is based on a monolithic flexure design, commonly employed in atomic force microscopy [168] and in commercial cryogenic nanopositioning systems [169, 170, 171]. The mechanism operates without friction, exhibits high mechanical stiffness and large resonance frequencies (resulting in excellent vibration robustness), and requires no lubricants, making it ideally suited for vacuum and cryogenic environments. At room temperature, the xy-scanning range of the Qlibri scanner amounts to approximately $100 \times 100\ \mu m^2$, which decreases to about $10 \times 10\ \mu m^2$ under cryogenic conditions due to the strong temperature dependence of the piezoelectric effect in commonly used actuator materials. The large scanning range,

[6] Thomas Hümmer, Jonathan Noé, Michael Förg, and Manuel Nutz

[7] xy-capacitances at RT: $C_x^{\mathrm{RT}} \approx C_y^{\mathrm{RT}} \approx 1\,800$ nF; capacitances at 4 K: $C_x^{LT} \approx C_y^{LT} \approx$ 70–80 nF.

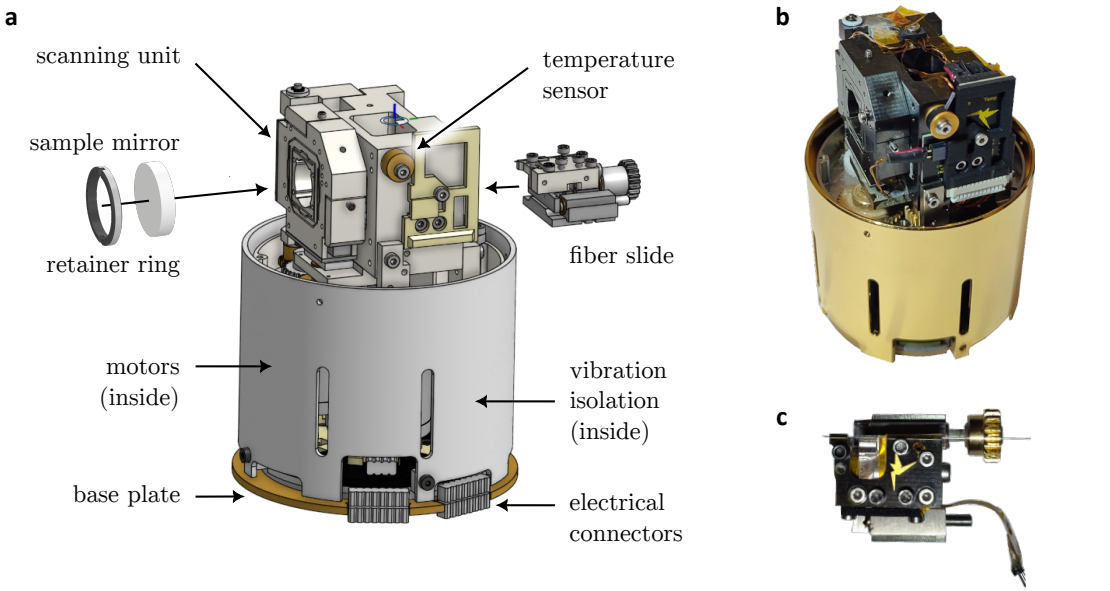

Figure 4.4: Qlibri microcavity platform. (a) Rendered model of the Qlibri microcavity platform with the main mechanical and electrical components labeled. Details are provided in the main text. The model was provided by Qlibri GmbH and adapted for illustration. **(b)** Photograph of the assembled platform. **(c)** Photograph of the fiber slide with an aluminum-coated fiber inserted.

even under cryogenic conditions, facilitates and accelerates the search for color centers, as will be discussed in Chapter 6. The 12.7 mm diameter sample mirror is mounted in the circular SM05-threaded aperture of the xy-scanning unit and secured with a retainer ring[8], providing a rigid mechanical connection between the mirror and the scanner.

In previous home-built cavity implementations, xy-scanning was achieved by mechanically bending a metallic ferrule into which the fiber was glued [172]. In contrast, the present approach—realizing xy-scanning via the sample mirror—offers a significant advantage: the optical axis defined by the fiber micromirror remains fixed while the sample is scanned. As a result, the cavity mode propagating into free space does not shift laterally when accessing different sample positions. This feature is particularly beneficial when coupling the cavity emission into small-aperture detectors, such as through single-mode fiber coupling.

Fiber slide. The fiber mirror is clamped with screws onto the fiber slide (see Fig. 4.4c) in one of two available V-grooves such that the fiber end facet protrudes by approximately 1 mm. The fiber slide is then inserted into the resonator block and secured with the corresponding fixing screws. It incorporates two stacked piezoelectric actuators[9] for cavity-length tuning. These can be controlled independently: the modulation piezo provides a large travel range and allows scanning over several free spectral ranges (FSRs) even at

[8] Thorlabs, SM05RR

[9] z-capacitances at room temperature: $C_{\text{mod}}^{\text{RT}} \approx 390$ nF, $C_{\text{off}}^{\text{RT}} \approx 230$ nF; at 4 K: $C_{\text{mod}}^{\text{LT}} \approx C_{\text{off}}^{\text{LT}} \approx 10$–$20$ nF.

cryogenic temperatures, while the offset piezo enables fine positioning with a cryogenic travel range of a few hundred nanometers. This configuration covers a large dynamic range—from a few picometers up to several micrometers—sufficient to place the cavity resonance with sub-linewidth precision (tens of picometers) and to scan across multiple FSRs separated by a few hundred nanometers.

The fiber slide incorporating the micromirror is mounted onto the main block by sliding it into place and securing it with the designated fixing screws. Electrical contact to the cavity controller is provided via the pin connectors visible in Fig. 4.4c, which mate with the printed circuit board attached to the main block. In combination with the flexible slide design, the fiber clamping mechanism enables fast and reliable exchange of cavity fibers, replacing previously used glued assemblies that required substantially more effort and time for replacement [172].

Motors. Coarse positioning of both the sample and the cavity length over a few millimeters is realized using three cryo-compatible stepper motors. These allow scanning across the entire diamond sample, typically 2×2 mm^2 in size, and enable controlled approach and retraction of the fiber mirror relative to the sample mirror—particularly useful for compensating thermal drifts during cooldown. The rotational motion of each stepper motor is converted into linear displacement via a gear mechanism, providing xy-translation of the scanner unit and z-axis motion of the fiber slide. The motors are driven by a dedicated controller and operated through custom control software, providing sub-micrometer positioning precision. The required drive currents are on the order of a few hundred milliamperes, which leads to noticeable cryostat heating, which further emphasizes the importance of the large piezo-controlled tuning range that minimizes the need for coarse actuation by the stepper motors.

Cavity controller and control software. The cavity is operated with the provided cavity controller and Python-based control software, which includes pre-defined standard measurement and analysis modules and is easily extendable with custom hardware modules such as spectrometers, laser control, or time-to-digital converters. The software communicates with the cavity controller, which provides four piezo-control outputs for xy-scanning and cavity-length modulation, and reads in a photodiode voltage during standard cavity operation, where the cavity transmission signal of a narrow-linewidth laser is detected on an avalanche photodiode (APD), as illustrated in Fig. 4.5a.

The FPGA-based cavity controller provides fast, precise control of the cavity parameters. Its output voltages can be selectively filtered and amplified depending on the operating mode. At cryogenic temperatures, the amplification stage enables access to the full xyz-positioning range, whereas such large amplitudes are typically unnecessary during room-temperature operation. An adjustable low-pass filter, implemented via a digitally controlled potentiometer, allows flexible trade-offs between bandwidth and noise: a low cutoff frequency ensures low-noise steady-state operation (e.g., during cavity locking or passive resonance stabilization), while the filter can be fully bypassed for fast scanning. In

the following, we briefly introduce the most common measurement procedures employed for cavity characterization. These include the controlled approach of the fiber mirror before operation, determination of the cavity finesse, transmission scans for sample characterization, and measurements of the platform's mechanical stability.

4.2.2. Typical operation

To characterize the cavity and perform basic sample measurements, the cavity is operated by probing it with a laser coupled through the fiber mirror, while the transmitted intensity is detected on an APD (see Fig. 4.5a). This configuration allows for a controlled approach of the fiber and planar mirrors, enables finesse measurements, and facilitates scanning cavity microscopy under z-piezo modulation (cf. Figs. 4.5b–d). In addition, the mechanical stability can be assessed either at constant or drift-compensated z-piezo voltage (cf. Fig. 4.5e). The following sections describe these fundamental measurement procedures—relevant for all subsequent experiments—and illustrate the general operating principles of the Qlibri microcavity platform.

Approaching the fiber. After inserting the fiber slide—or after a warm-up or cool-down cycle—the fiber is typically retracted by a few hundred micrometers, placing the cavity outside its stability range for wavelengths within the coating stopband. In this situation, it is most convenient to use a low-finesse ($\mathcal{F} \approx 1$) laser at a wavelength outside the stopband, where the coating is predominantly transmissive and therefore only weakly modulates the transmitted signal. This configuration allows continuous monitoring of the cavity modulation while approaching the fiber toward the planar mirror. Figure 4.5b shows two exemplary transmission traces recorded with a 532 nm laser during cavity modulation. As the fiber is moved closer to the planar mirror via the stepper motors of the coarse-positioning stage, the resonances shift toward lower piezo voltages (to the left in the figure) until contact between the two mirrors is reached. Upon contact, the FSR increases because the same z-piezo voltage corresponds to a smaller modulation length. Physical contact should be avoided if there is a risk of picking up dirt or particles with the fiber, as this may introduce a permanent scatterer into the fiber dimple, degrading cavity finesse. For solid-state membranes, brief contact is generally safe as long as the fiber is not further approached or laterally moved while in contact, since this could cause spalling of the DBR coating or even break the fiber. Once the contact position is identified, the fiber can be safely retracted by a few FSR to operate the cavity in an open configuration at small mirror separations.

Finesse measurement. Close to the contact position, the mirror separation lies within the stability range of the cavity, and a laser with wavelength λ inside the coating stopband can be used. If no local scatterer is present on the sample, sharp resonances spaced by the FSR $= \lambda/2$ appear, together with higher-order transverse modes. The finesse can be determined by finely sampling the cavity transmission with sufficient amplitude

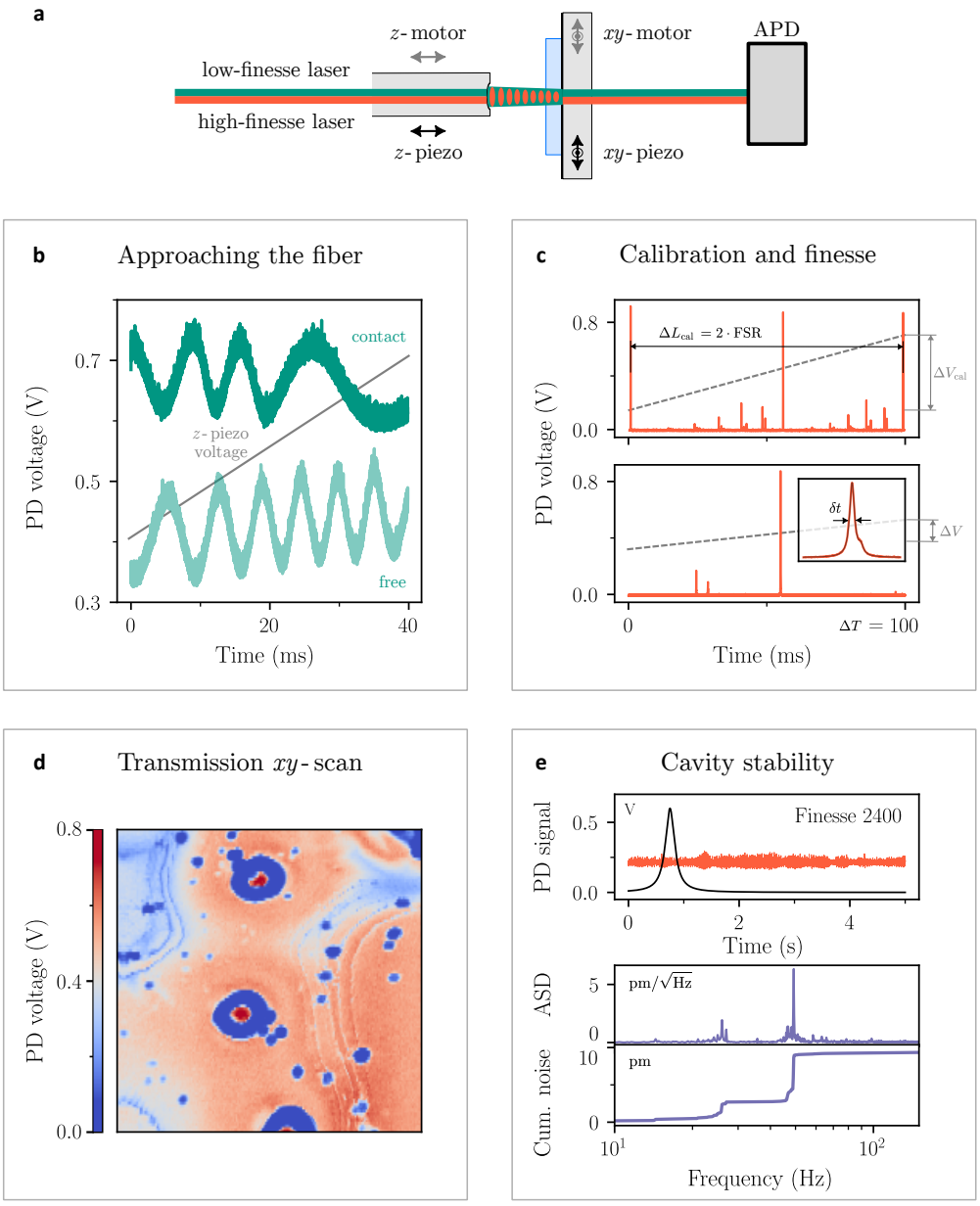

Figure 4.5: Qlibri cavity operation. **(a)** Schematic of the experimental setup. The cavity is probed via the fiber mirror using a low-finesse ($\mathcal{F} \approx 1$, teal) and a high-finesse ($\mathcal{F} \approx 10^3$, orange) laser, with the transmitted signal detected on an APD. **(b)** The fiber is approached toward the planar sample mirror using the low-finesse laser under cavity modulation. The FSR increases as the mirrors come into contact. **(c)** The z-piezo voltage is calibrated into a modulation length via the relation FSR $= \lambda/2$ (upper panel). After calibration, the finesse is extracted from a Lorentzian fit of a single resonance (lower panel). **(d)** The transmission peak height across a full lateral scan reveals surface-induced variations of the sample, providing indirect information on the surface topography as well as localized scattering sites. **(e)** The cavity stability is characterized by monitoring the APD signal at constant (or drift-compensated) z-piezo voltage and evaluating the corresponding noise spectrum via the amplitude spectral density (ASD) or the cumulative noise contribution. All data shown are illustrative and representative for typical Qlibri cavity operation.

and resolution to resolve both the FSR and the cavity linewidth. Owing to the linear relation between scanning time, z-piezo voltage, and cavity length, the ratio of FSR to linewidth can be directly evaluated in the time domain without calibration, neglecting piezo nonlinearities. Precise measurement of high finesses requires high oscilloscope sampling rates, which makes data transfer and evaluation slow. For faster finesse measurements, the Qlibri software therefore performs a one-time calibration of the z-piezo voltage to the cavity length modulation. This calibration can then be used to determine the finesse within a reduced scanning range, focusing on the cavity resonance of interest rather than scanning over multiple FSRs.

The calibration procedure is illustrated in Fig. 4.5c. The length-modulation range is set to a voltage ΔV_{cal} that corresponds to an integer number N of FSR in length, $\Delta L_{\mathrm{cal}} = N \cdot \mathrm{FSR} = N \cdot (\lambda/2)$. This defines the voltage-to-length calibration factor $c_{\mathrm{cal}} = \Delta L_{\mathrm{cal}}/\Delta V_{\mathrm{cal}}$, allowing any cavity length change to be calculated as $\Delta L = c_{\mathrm{cal}}\,\Delta V$. For a fast finesse measurement, the modulation range is reduced to focus on a single cavity resonance (see Fig. 4.5c, lower panel). Fitting the transmission signal with a Lorentzian (Fig. 4.5c, inset) in the time domain yields a linewidth δt, which can be converted into voltage via $\delta V = (\Delta V/\Delta T)\,\delta t$ and into length via $\delta L = c_{\mathrm{cal}}\,\delta V = c_{\mathrm{cal}}\,(\Delta V/\Delta T)\,\delta t$. Since $\Delta L = c_{\mathrm{cal}}\,\Delta V$, this simplifies to $\delta L = \Delta L\,(\delta t/\Delta T)$, directly relating the measured temporal linewidth to the cavity linewidth in length units assuming a linear relation between the piezo voltage and the length change. Apparent nonlinearities—visible as unequal spacing between adjacent FSRs in Fig. 4.5c—introduce uncertainty into the measured finesse unless the nonlinear elongation of the piezo is properly calibrated. Slower scans without low-pass filtering minimize nonlinearities caused by the finite RC response of the piezo and driver electronics. In this regime, residual deviations predominantly originate from the intrinsic material nonlinearity of the piezo itself. Extracting the finesse from the central cavity resonance within the calibrated scan range averages nonlinear deviations above and below the resonance, yielding a more accurate estimate. The remaining deviation constitutes the dominant systematic uncertainty and limits the accuracy of the extracted finesse to approximately 10%.

Cavity transmission scan. A rapid sample characterization within the xy-piezo scanning range can be performed by recording the transmitted cavity resonance height on an xy grid, as illustrated in Fig. 4.5d. The resonance peak amplitude depends on the reflectivities of both mirrors and on residual intracavity losses.

For a bare planar mirror, only the residual losses—such as scattering and absorption—vary across the surface. Hence, lateral scans enable detection of localized scatterers or absorbers whose effective cross-sections are enhanced by the cavity finesse. This principle forms the basis of scanning cavity microscopy, which enables the detection of extremely weakly absorbing nanosystems with sensitivity increased by several orders of magnitude [127, 173].

In the present setup, the planar mirror carries a diamond membrane with spatially varying thickness placed on top of the DBR. The measured transmission signal is therefore

primarily used to infer the membrane topography [174]. As discussed in Chapter 5, the transmission properties and residual losses depend strongly on the local diamond thickness, since the membrane effectively acts as an additional cavity layer with refractive index $n_\mathrm{d} = 2.41$. This modifies both the cavity finesse and the intracavity field distribution, with important implications for light–matter coupling as discussed in Sec. 5.2. Hence, the observed transmission contrast reflects spatial variations in the effective finesse of the hybrid membrane–air cavity and provides a first indication of the underlying spatial mode composition.

Stability measurement. When the cavity is tuned into resonance with the laser, the time-dependent transmitted intensity can be used to characterize the mechanical stability of the microcavity platform—an essential figure of merit for efficient light–matter coupling, as discussed in Sec. 4.3.2. The intensity signal can be converted into a cavity length deviation by $\Delta z(t) = K\,\Delta I(t)$, using the linearized slope of the Lorentzian cavity resonance with amplitude I_0, setpoint I_stp, and previously measured finesse $\mathcal{F}$:

$$K = \frac{8\mathcal{F} I_\mathrm{stp}^2}{\lambda I_0}\sqrt{\frac{I_0}{I_\mathrm{stp}} - 1}. \tag{4.2.1}$$

In a thermally stable environment, e.g. after full thermalization under cryogenic conditions, the cavity resonance can be passively kept resonant with the laser. Otherwise, the passive stability is typically assessed under drift-compensated conditions—i.e. side-of-fringe locking with zero proportional gain and minimal integral feedback (see Refs. [172, 175] for details).

The resulting time trace (Fig. 4.5e, upper panel) is converted into a cavity length jitter via Eq. (4.2.1) and analyzed in the frequency domain. The Fast Fourier Transform (FFT) of the zero-mean signal yields the power spectral density (PSD) $S_z(f)$ in units of $[\mathrm{m}^2/\mathrm{Hz}]$, from which the amplitude spectral density (ASD) is obtained as $A_z(f) = \sqrt{S_z(f)}$ in units of $[\mathrm{m}/\sqrt{\mathrm{Hz}}]$. The cumulative noise $\sigma_{z,\mathrm{cum}}(f)$ is then determined by integrating the squared ASD over a frequency range up to f:

$$\sigma_{z,\mathrm{cum}}(f) = \left(\int_0^f A_z(f')^2\,\mathrm{d}f'\right)^{1/2}. \tag{4.2.2}$$

The lower panels of Fig. 4.5e show the spectral analysis of an exemplary drift-compensated time trace. When integrated over the full measurement bandwidth, $\sigma_{z,\mathrm{cum}}(f)$ equals the root-mean-square (RMS) cavity length jitter, here $\sigma_z \approx 10\,\mathrm{pm}$. The measurement shown is illustrative, recorded at room temperature in a relatively noisy environment without acoustic shielding; the cryogenic stability of the Qlibri platform is discussed later in Sec. 4.3.2.

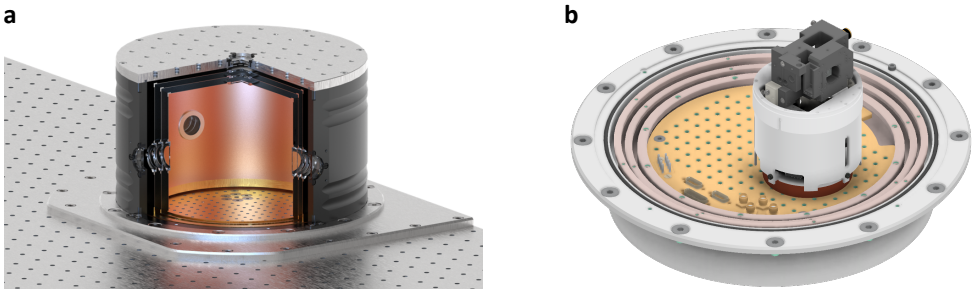

Figure 4.6: Integration of a Qlibri microcavity platform into a Qinu dilution refrigerator. **(a)** Rendered view of the table-top cryostat experimental chamber (image reproduced from Qinu GmbH [176]). **(b)** Rendered view of the Qlibri microcavity platform mounted on the cryostat cold plate.

4.3. Integration of the Qlibri microcavity platform into the Qinu dilution refrigerator

The cavity platform is integrated into a dilution refrigerator developed by Qinu GmbH, a startup founded by Marcel Schrodin that originated from Wolfgang Wernsdorfer's research group at our institute. The cryostat provides optical and electrical access specifically designed to meet the requirements of the Qlibri microcavity platform. As one of the first users of both systems, we highlight here the capabilities of the combined setup, which unites an ultrastable microcavity with a low-vibration dilution refrigerator. In the following, we briefly introduce the cryostat and then assess the joint performance of the two devices in terms of mechanical stability and achievable sample temperature—two key parameters for operating a high-finesse cavity with strong light–matter coupling and for meeting the sub-4 K temperature requirements of group-IV color centers.

Qinu dilution refrigerator. The compact, table-top dilution refrigerator used in the following experiments is based on an inverted design originally developed by A. Benoit and W. Wernsdorfer, where the coldest component—the mK plate—is positioned at the top, in contrast to conventional dilution refrigerators. This geometry is particularly well suited for optical experiments, as the cryostat can be mounted directly onto an optical table, providing optical access through windows at standard beam height.

The system employs a remotely located Gifford–McMahon (GM) cryocooler as the primary cooling engine, which circulates liquid helium through the cryostat to precool and maintain the intermediate temperature stages at approximately 100 K, 20 K, and 4 K. The GM cryocooler, installed in a separate room for vibration isolation, thus provides the cooling power of a liquid-helium bath while avoiding direct mechanical coupling to the cryostat. The 4 K plate is directly accessible within the experimental chamber of the cryostat and hosts components that do not require millikelvin temperatures, such as the supercon-

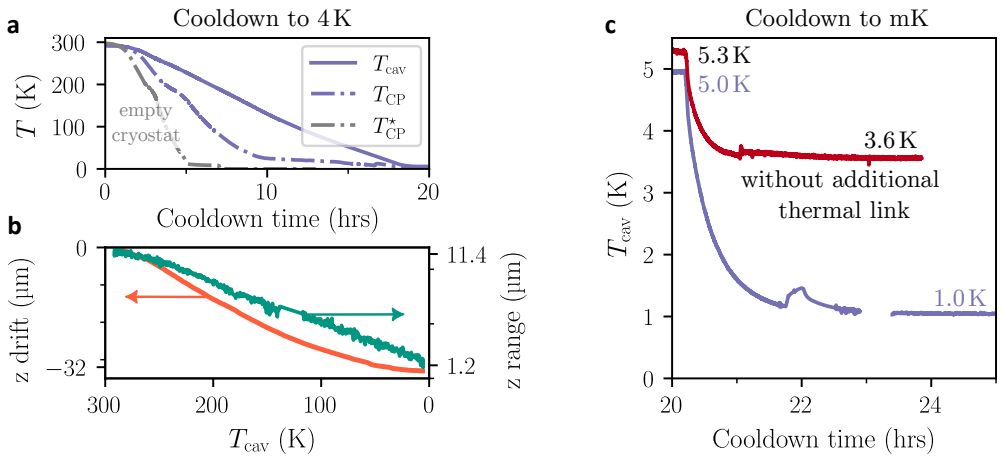

Figure 4.7: Cooldown and thermalization of the Qlibri microcavity platform inside the Qinu dilution refrigerator. (a) Cooldown of the cavity platform (blue) and cold plate (gray, CP) from room temperature to 4 K. The presence of the cavity platform introduces a significant thermal mass, extending the cooldown time to approximately 20 h compared to the empty cryostat (dash-dotted line). **(b)** Simultaneous measurement of the longitudinal cavity drift (green) and z-piezo scanning range (orange) during cooldown as a function of the interpolated cavity temperature. The cavity contracts by about 32 µm, while the piezo range decreases from 11.4 µm to 1.2 µm. **(c)** Further cooling to the millikelvin regime illustrates the effect of improved thermal anchoring: adding an additional thermal link between the main cavity block and the mixing chamber reduces the final cavity temperature from 3.6 K to 1.0 K, at cold-plate temperatures of 250 mK and 140 mK, respectively.

ducting magnet used in our experiments. The ^{3}He/^{4}He mixture is counter-circulated and precooled by the ^{4}He circuit, before reaching the mixing chamber, which is thermally anchored to the mK plate where the cavity platform is mounted. Depending on the operational mode, the cryostat can be run either at liquid-helium temperatures (4 K mode) or at millikelvin temperatures (mK mode) once the mixture is condensed. A detailed description of the working principle and design of such systems is provided in Ref. [177].

The Qinu cryostat offers short cooldown times (approximately 6 hours for an empty cryostat), optical windows for free-space and fiber-coupled optical access, comprehensive DC and RF electrical connectivity, and interfaces for the integration of superconducting magnets.

4.3.1. Cavity thermalization and cryogenic cooldown

Thermalization and final temperature. The Qlibri microcavity platform is mounted to the cold plate via a copper adapter plate, which aligns the optical axis with the cryostat window. The Qlibri base plate (see Fig. 4.4a) is thermally connected to the cavity main block via a

copper braid, thereby transferring cooling power to the cavity. A temperature sensor[10] is attached to this block to monitor the cavity temperature. An exemplary cooldown to 4 K is shown in Fig. 4.7a, displaying the temperatures of both the cavity and the cold plate over time. For an empty cryostat (gray dash-dotted line), the cooldown to millikelvin temperatures typically requires 5–10 h. When the cavity platform is installed its substantial thermal mass extends the cooldown duration to about 20 h. Imperfect thermal coupling is evident from a transient temperature difference exceeding 100 K between the cavity and the cold plate during cooldown.

The original Qlibri base plate was made of aluminum, to which the thermal link to the cavity main block is attached. Since aluminum becomes superconducting below approximately 1.2 K, its electronic contribution to the thermal conductivity—the dominant channel at low temperatures—vanishes, thereby impeding efficient thermalization. Consequently, the original configuration was not suitable for operation in the millikelvin regime. This limitation is illustrated in Fig. 4.7c, where the cavity temperature (red curve) reaches only 3.6 K while the cold plate cools to 250 mK. To overcome this limitation, an additional copper braid was installed to directly connect the cold plate to the main cavity block, bypassing the superconducting aluminum section. This modification enabled the cavity to cool to $T_{\mathrm{cav}} = 1.0\,\mathrm{K}$ at a cold-plate temperature of 140 mK. The benefit of the improved thermal link is already noticeable in the 4 K operation mode, where the equilibrium temperature decreases from 5.3 K to 5.0 K, but becomes particularly significant below the superconducting transition of aluminum. In subsequent iterations, Qlibri replaced the aluminum base plate with a copper version in all cryogenic platforms, eliminating the need for additional thermal links.

Thermal contraction and scanning range. During cooldown, the longitudinal cavity drift and the z-piezo scanning range were monitored by tracking several free spectral ranges (FSRs) of a low-finesse laser. Because of the differing thermal expansion coefficients of the materials comprising the microcavity platform, the cavity length contracts by approximately 30 µm during cooldown. Consequently, the initial cavity length must be adjusted to a slightly larger value at room temperature to prevent the fiber from crashing into the mirror at low temperature. As discussed in Sec. 4.2, the z-piezo scanning range decreases strongly with temperature due to the pronounced temperature dependence of the piezoelectric effect—from slightly above 11 µm at room temperature to about 1 µm at cryogenic temperatures, as shown in Fig. 4.7b.

4.3.2. Mechanical stability

The importance of mechanical stability. The performance of cavity-based quantum interfaces critically depends on mechanical stability, as vibrations translate directly into resonance-frequency jitter. In Sec. 3.2.4, we introduced the Purcell factor for ideal spectral

[10] Lake Shore, CX-1050-CU-HT-1.4L.

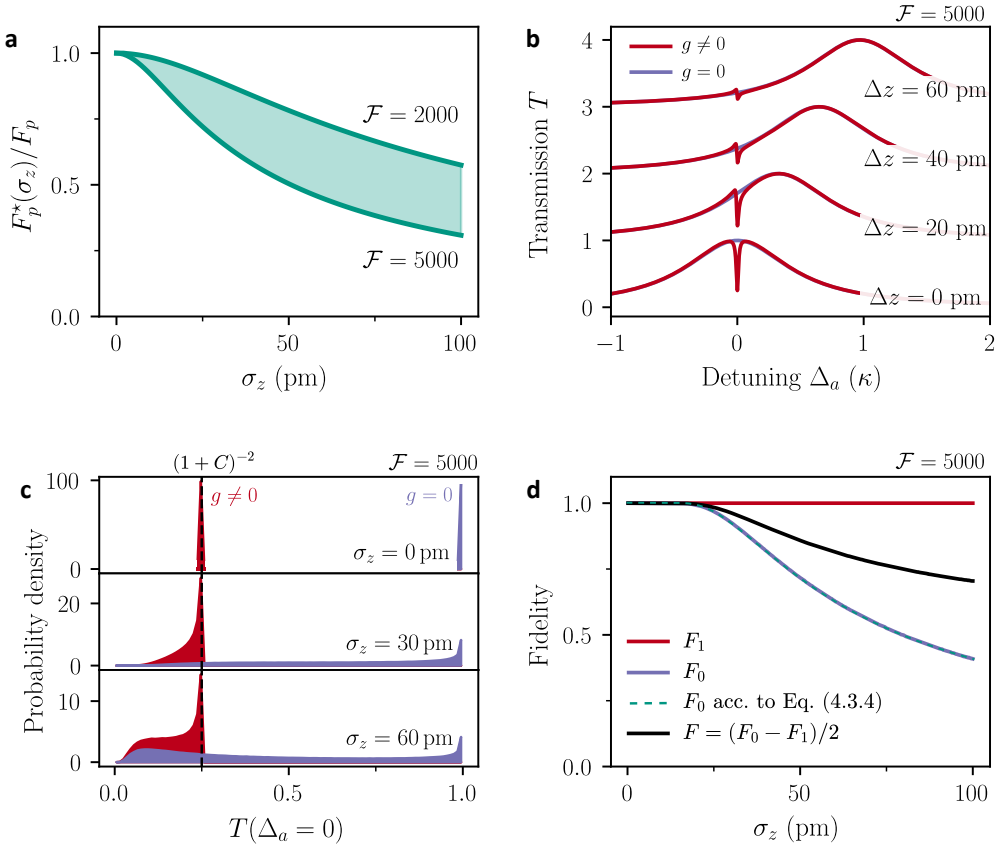

Figure 4.8: Cavity stability requirements. All simulations are evaluated at a wavelength of $\lambda = 620\,\text{nm}$, which allows converting cavity-length fluctuations into spectral jitter via $\sigma_\nu/\delta\nu_{\text{cav}} = \sigma_z/\delta L$, where $\delta L = \lambda/(2\mathcal{F})$ is the FWHM linewidth in length. **(a)** Reduction of the ideal Purcell factor F_P due to vibrational cavity-length jitter σ_z. **(b)** Simulated transmission spectra for four cavity-length detunings at a cooperativity of $C = 1$ and finesse $\mathcal{F} = 5\,000$. **(c)** Simulated transmission histograms at zero emitter detuning ($\Delta_a = 0$) for an empty (purple) and emitter-coupled (red) cavity at three vibration levels. **(d)** Readout fidelities extracted from the histograms using a threshold of $1/(1+C)^2$. The dotted teal line illustrates the agreement between the analytical expression for F_0 given in Eq. (4.3.4) and the simulation.

overlap (Eq. (3.2.14)). In practice, finite spectral detuning between emitter and cavity leads to a vibration-induced reduction of the Purcell factor given by [178]

$$F_P^\star(\sigma_z) = F_P \sqrt{\frac{\pi}{8}} \frac{\delta L}{\sigma_z} \exp\left(\frac{\delta L^2}{8\sigma_z^2}\right) \left[1 - \text{erf}\left(\frac{\delta L}{2\sqrt{2}\sigma_z}\right)\right], \tag{4.3.1}$$

where σ_z denotes the RMS cavity-length jitter, and $\text{erf}(\cdot)$ is the Gaussian error function. The normalized reduction $F_P^\star/F_P$ is shown in Fig. 4.8a for the typical finesse range of the upcoming measurements, $\mathcal{F} = 2\,000$–$5\,000$, corresponding to cavity-length linewidths of $\delta L = 155$–$62\,\text{pm}$ at $\lambda = 620\,\text{nm}$.

To further quantify the effect of mechanical vibrations on the coupled cavity–emitter system and its transmission response to a weak coherent drive, we consider length fluctu-

ations that shift the cavity resonance as $\Delta_c \to \Delta_c + \delta_c(t)$. If the correlation time of $\delta_c(t)$[11] is long compared to the acquisition time, each measurement effectively probes a static detuning $\delta_c(t)$, corresponding to a cavity-length offset Δz. Simulated transmission spectra for $\Delta z = 0, 20, 40, 60\,\mathrm{pm}$ are shown in Fig. 4.8b, with the empty-cavity baseline (purple) and the coupled system (red) at $C = 1$ and $\mathcal{F} = 5000$. Such spectra would be obtained by sweeping the laser frequency across the cavity resonance. While the integration time of an individual data point is typically shorter than the correlation time of the cavity-length jitter, the duration of a full frequency sweep—usually several seconds—is much longer. This mismatch complicates detecting weak extinction features, as cavity resonance jitter can imprint characteristic fluctuations onto the recorded signal, partially masking the extinction contrast. A practical way to mitigate this effect is to average over multiple scans, which smooths out slow frequency drifts and amplitude variations caused by mechanical noise.

When probing continuously at the emitter frequency ($\Delta_a = 0$), as in spin-readout or entanglement protocols, the transmission histograms for three vibration levels, $\sigma_z = 0, 30$, and 60 pm, are depicted in Fig. 4.8c. For a symmetric, lossless cavity without jitter, the empty-cavity transmission is unity, while emitter coupling reduces it to $T_{c,\max}^{g\neq 0} = 1/(1 + C)^2$ (see Eq. (3.2.22)). Increasing vibration amplitude reduces the mean transmission for both cases and increases the probability that even the empty cavity transmits below the cooperative contrast. This degradation is reflected in Fig. 4.8d, which shows the readout fidelities using a fixed threshold at $T_{c,\max}^{g\neq 0}$. For $\sigma_z < 25\,\mathrm{pm}$, the likelihood of false classification is negligible, yielding fidelities close to unity. We define the total readout fidelity as $F = (F_1 + F_0)/2$, where F_1 (F_0) denotes the probability of correctly identifying the presence (absence) of an emitter. Beyond $\sigma_z \approx 25\,\mathrm{pm}$, the fidelity drops toward 0.5, corresponding to random discrimination, as both distributions merge near zero transmission.

An analytical estimate for this limit can be derived from the probability that the empty-cavity transmission falls below the threshold, since the filled-cavity fidelity F_1 remains unity:

$$T_c^{g=0} < T_{c,\max}^{g\neq 0} \;\Rightarrow\; |\Delta z| > \frac{\delta L}{2}\sqrt{\frac{1}{T_{c,\max}^{g\neq 0}} - 1} = \frac{\delta L}{2}\sqrt{C(2+C)} \equiv a. \tag{4.3.2}$$

Assuming normally distributed cavity-length detuning, $\Delta z \sim \mathcal{N}(0, \sigma_z^2)$, the corresponding tail probability becomes

$$P(|\Delta z| > a) = \mathrm{erfc}\left(\frac{a}{\sqrt{2}\,\sigma_z}\right) \Rightarrow P(T_c^{g=0} < T_{c,\max}^{g\neq 0}) = \mathrm{erfc}\left(\frac{\delta L}{2\sqrt{2}\,\sigma_z}\sqrt{C(2+C)}\right). \tag{4.3.3}$$

Accordingly, the empty-cavity fidelity is

$$F_0 = 1 - P(T_c^{g=0} < T_{c,\max}^{g\neq 0}). \tag{4.3.4}$$

[11] The correlation time can be inferred from the vibration spectrum of the cavity. Dominant mechanical frequencies of 20–100 Hz correspond to correlation times of 10–50 ms.

The characteristic bend observed in the fidelity curve of Fig. 4.8d occurs when the argument of the complementary error function approaches unity. Solving for the corresponding vibration level yields the requirement

$$\sigma_z^{\mathrm{req}} = \frac{\delta L}{2\sqrt{2}}\sqrt{C(2+C)}. \tag{4.3.5}$$

Inserting $\mathcal{F} = 5\,000$ and $C = 1$ results in a required mechanical stability of $\sigma_z^{\mathrm{req}} = 38\,\mathrm{pm}$. This expression intuitively shows that stronger coupling (larger C) leads to a deeper extinction, thereby allowing larger tolerable vibration amplitudes before the readout fidelity degrades. In this idealized picture, sufficiently high cooperativities can, in principle, relax the stability requirements entirely; however, in practice, background fluorescence and detector dark counts ultimately limit the achievable contrast.

While the analysis above is derived for transmission-based state readout fidelity, the same physical mechanism applies more generally to cavity-based protocols that rely on a clear distinction between on- and off-resonant optical responses, such as those associated with spectrally distinct spin states. Cavity-length fluctuations detune the cavity from the probe, thereby reducing the effective cooperativity. As a result, the ideally resonant state exhibits a reduced contrast due to weakened interaction, while the off-resonant state experiences a reduction of the bare cavity transmission. Both effects drive the bright and dark responses toward each other, reducing their separability and hence the achievable fidelity. For entanglement protocols, the qualitative impact is analogous, although the quantitative scaling of the fidelity with vibration amplitude depends on the specific scheme and is not derived here.

Passive, drift-compensated, and actively locked stability. We experimentally analyze the amplitude and spectral characteristics of the cavity-length fluctuations using the stability measurement introduced in Sec. 4.2.2. The cavity stability is characterized under three different stabilization modes: (i) *passive stability*, where the cavity resonance is manually aligned to the narrow-linewidth laser; (ii) *drift-compensated stability*, where a side-of-fringe feedback loop with only minimal integral control compensates for low-frequency drifts; and (iii) *active stability*, where both proportional and integral gains are optimized to achieve the best possible suppression of cavity-length noise.

The stability results for the three modes in the 4 K operation mode at a cavity temperature of $T_{\mathrm{cav}} = 5.3\,\mathrm{K}$ are shown in Fig. 4.9a,c and summarized in Table 4.1. The dominant noise components for the passive and drift-compensated configurations lie within the frequency range $\Delta f = 20\text{–}100\,\mathrm{Hz}$. In the drift-compensated case, the feedback loop effectively suppresses noise contributions below 30 Hz, as indicated by the absence of the 20 Hz peak. Apart from this low-frequency suppression, both spectra and their corresponding RMS noise levels remain comparable.

Hence, the passive cavity stability discussed in the following is represented by the drift-compensated time traces, as they provide equivalent noise performance without requiring manual adjustment of the z-piezo voltage. In the following, we refer to this stability simply

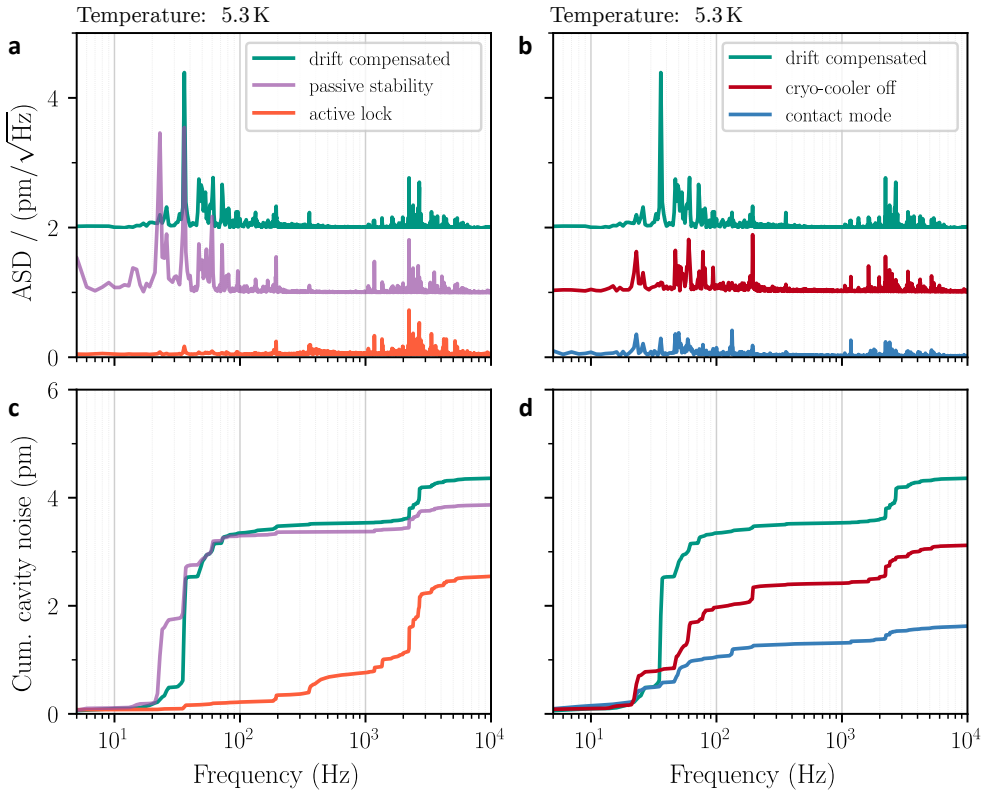

Figure 4.9: Cavity stability at 5 K. The amplitude spectral density (ASD) and cumulative cavity noise are shown for different stabilization modes and operating conditions. **(a,b)** ASD of the cavity length fluctuations. **(a)** Comparison of active, passive, and drift-compensated stabilization at $T_{\mathrm{cav}} = 5.3\,\mathrm{K}$. The passive and drift-compensated spectra exhibit dominant noise components between 20–100 Hz, while the active lock suppresses low-frequency noise up to 100 Hz but amplifies components above 1 kHz. **(b)** Effect of practical noise-mitigation measures. Turning off the cryocooler (red) reduces the low-frequency vibration peak near 36 Hz, and bringing the fiber mirror into contact with the planar mirror (blue) further enhances mechanical rigidity and suppresses differential mirror motion. **(c,d)** Cumulative noise plots showing the integrated RMS displacement up to each frequency, illustrating overall stability improvements from several picometers in open mode to below 2 pm in contact.

as *passive*. Active feedback further suppresses the main low-frequency components below 100 Hz, while high-frequency components above 1 kHz are amplified due to the phase lag beyond the servo bandwidth. Although further optimization of the proportional–integral–derivative (PID) parameters of the digital locking scheme could improve the actively locked stability, this was not pursued, as all experiments presented in this work relied on the high passive stability achieved without active locking.

Table 4.1: Overview of cavity stability measurements at various temperatures and operating conditions. The *Mode* refers to the stabilization scheme applied to the cavity: *Drift*-compensated (slowest integral feedback), *Passive* (no feedback), or *Active* (actively locked feedback). *GM* specifies whether the GM cryocooler was running, while *Contact* indicates whether the fiber and planar mirror were in contact. The cumulative root-mean-square displacement $\sigma_{z,\mathrm{cum}}$ (integrated up to 10 kHz, as shown in Fig. 4.9 & 4.10) and the fully integrated (100 kHz bandwidth) standard deviation σ_z quantify the mechanical noise of the cavity length. The last column refers to the respective figure panels where the data are plotted.

T_{cav} (K)	Mode	GM	Contact	$\mathcal{F}$	I_0 (V)	I_{stp} (V)	$\sigma_{z,\mathrm{cum}}$ (pm)	σ_z (pm)	Figure
5.3	Drift	on	no	2350	0.86	0.4	4.4	4.5	4.9a-d (teal)
5.3	Passive	on	no	2350	0.86	0.4	3.9	4.0	4.9a,c (purple)
5.3	Active	on	no	2350	0.86	0.4	2.5	2.9	4.9a,c (orange)
5.3	Drift	on	yes	~2350	0.66	0.3	1.6	1.9	4.9b,d (blue)
5.3	Drift	off	no	2350	0.86	0.4	3.1	3.3	4.9b,d (red)
5.3	Drift	on	no	2350	0.86	0.4	4.4	4.5	4.10a,c (teal)
293	Drift	off	no	4800	0.40	0.2	1.5	1.8	4.10a,c (red)
3.6	Drift	on	no	2400	0.65	0.3	3.9	4.0	4.10a,c (blue)
1.0	Drift	on	no	4800	0.56	0.3	9.9	10.0	4.10a,c (purple)
1.0	Drift	off	no	4800	0.56	0.3	5.1	5.2	–
1.0	Drift	on	yes	~5200	0.50	0.2	0.4	0.6	4.10b,d

Practical measures to suppress mechanical noise. Two practical measures can improve passive stability without interrupting cryogenic operation: (i) The cryocooler can be temporarily shut off for several hours, as the cryostat contains a liquid helium reservoir that maintains base temperature during this time. In the absence of mechanical vibrations transmitted from the cryocooler to the sample stage, the stability improves from 4.5 pm to 3.3 pm (see Fig. 4.9b,d). This improvement is primarily visible as the disappearance of the ASD peak near 36 Hz. Accelerometer measurements on components of the gas-handling system (see Appendix A.4) confirmed this assignment, revealing a vibration at 37 Hz.

(ii) The fiber and planar sample mirror can be brought into physical contact, as typically done when approaching the fiber (see Sec. 4.2.2 and Ref. [63]). The resulting monolithic contact substantially enhances the mechanical rigidity of the cavity and suppresses differential mirror motion. The finesse of the contact mode, required to evaluate mechanical stability, cannot be determined using the method described in Sec. 4.2.2, since the cavity-length variation during a piezo voltage scan is highly nonlinear. Therefore, we use the finesse measured for the resonances immediately prior to contact and assume that the contact mode exhibits a similar value. This assumption is verified by comparing the linewidths of the last open and first contact mode, which show no significant difference.

The magnitude of improvement between the open and contact mode, however, varies notably between measurements—from a moderate enhancement of stability from 4.5 pm

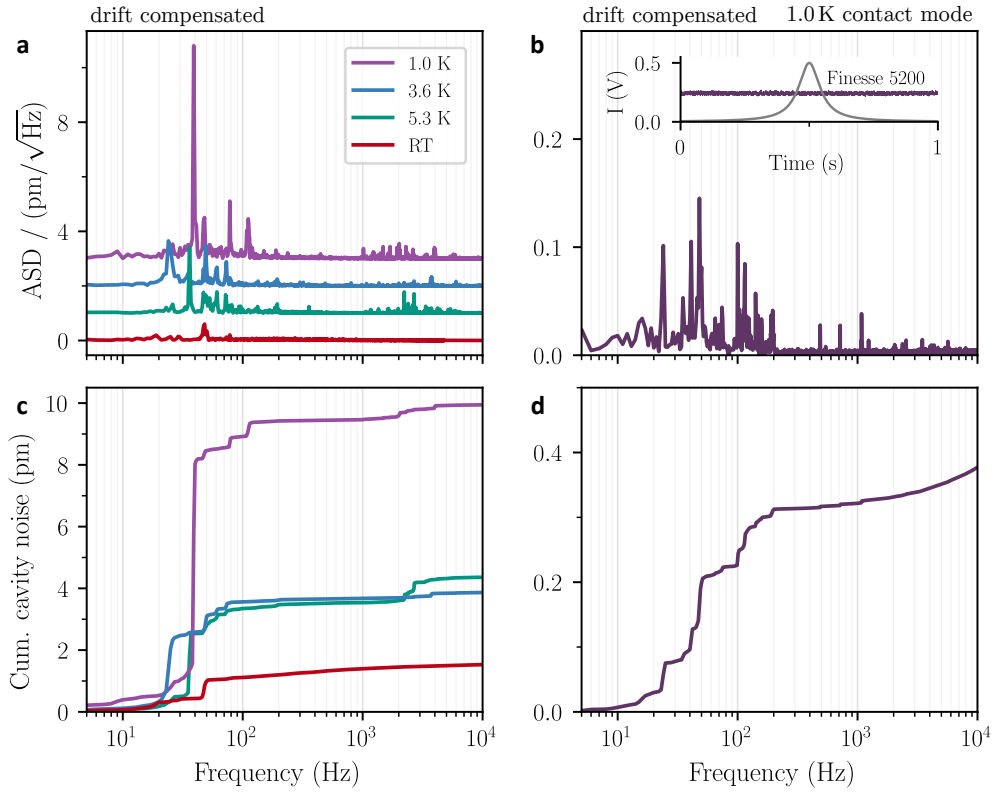

Figure 4.10: Cavity stability at different temperatures. Amplitude spectral density (ASD) and cumulative cavity noise recorded at room temperature and under cryogenic conditions. **(a,c)** Drift-compensated stability for $T_{\mathrm{cav}} = 1.0\,\mathrm{K}$ (purple), 3.6 K (blue), 5.3 K (teal), and room temperature (red). Introducing an additional thermal link to reach 1.0 K increases the overall noise level, while the room-temperature trace shows the lowest spectral amplitude owing to the absence of cryostat vibrations. **(b,d)** Stability in contact mode at $T_{\mathrm{cav}} = 1.0\,\mathrm{K}$, demonstrating record mechanical stability with $\sigma_{z,\mathrm{cum}} = 0.4\,\mathrm{pm}$ at a finesse of $\mathcal{F} = 5\,200$. The inset in (b) shows the resulting nearly noise-free time trace of a cavity resonance.

to 1.9 pm (Fig. 4.9b,d) to a pronounced reduction from 10.0 pm to 0.6 pm (Fig. 4.10). We attribute this variation to differences in how far the fiber must be pushed into contact to reach optical resonance, which depend on the local thickness of the diamond membrane. Thicker regions shift the cavity resonance and therefore require stronger fiber indentation, altering the mechanical coupling and consequently the noise suppression. Although operating in contact mode may appear to be a straightforward way to improve stability, it is generally preferable to avoid it, as contact introduces a risk of particle contamination and prevents lateral repositioning. Moreover, contact may adversely affect the defect's coherence properties by modifying its local electric environment and by increasing the local sample temperature due to imperfect thermalization of the fiber within the cryostat.

An ultrastable microcavity platform at 1 K. Up to this point, we have discussed different stabilization schemes and measures to improve stability, exemplified for datasets recorded in the 4-K operation mode of the cryostat, yielding a cavity temperature of $T_{\mathrm{cav}} = 5.3\,\mathrm{K}$. However, addressing the electron spin requires substantially lower temperatures, making the stability in the condensation (millikelvin) mode of the cryostat more relevant. As discussed in Sec. 4.3.1, the lowest temperature reached at the xy-scanner of the cavity is about 1.0 K, achieved by adding an additional copper thermal link directly connecting the main cavity block to the mK plate of the cryostat. Without this link, the temperature settles at 3.6 K.

This configuration allows a direct comparison of the cavity stability in the 4 K and millikelvin operation modes for the same thermal-link configuration (blue and teal curves in Fig. 4.10a,c), which yield comparable RMS length jitters of 4.5 pm and 4.0 pm, respectively. For reference, the room-temperature stability (red curve in Fig. 4.10a,c) exceeds that obtained under cryogenic conditions, exhibiting lower vibration amplitudes as expected when all cryostat components are turned off and internal damping of the cavity materials is increased.

Introducing an additional cold link, however, degraded the stability: the added mechanical connection to the main cavity block resulted in a jitter of 10.0 pm, with a dominant noise component at 39 Hz, close to the 37 Hz vibration peak of the cryocooler. Comparable stability to the original configuration was recovered when the cryocooler was turned off, as the 39 Hz peak vanished (see Table 4.1). Optimization of the geometry and stiffness of the thermal copper link could further mitigate this noise coupling, but this was not pursued in the present work.

Nevertheless, a record mechanical stability was achieved at $T_{\mathrm{cav}} = 1.0\,\mathrm{K}$ in contact mode, reaching $\sigma_z = 0.6\,\mathrm{pm}$ ($\sigma_{z,\mathrm{cum}} = 0.4\,\mathrm{pm}$ over a 10 kHz bandwidth) at a finesse of $\mathcal{F} = 5\,200$, corresponding to a cavity-length jitter of only about 1% of the cavity FWHM linewidth. The nearly noise-free time trace shown in the inset of Fig. 4.10b directly illustrates this exceptional stability.

Comparison of passive stabilities across cryogenic microcavity systems. The development of open and tunable microcavity platforms with high passive stability under cryogenic conditions has been pursued by several research groups in recent years, using diverse vibration-damping and nanopositioning approaches in both liquid-helium bath and closed-cycle cryostats. Table 4.2 summarizes the reported mechanical stabilities and operating temperatures from Refs. [179, 178, 180, 172]. Further efforts toward optimizing the mechanical performance of tunable microcavity systems can be found in Refs. [181, 182, 183], although these works have not demonstrated substantially improved passive stability compared to the values listed in the table.

The highest reported passive mechanical stabilities to date have been achieved in liquid-helium bath cryostats at 4 K ($\sigma_z = 4.3\,\mathrm{pm}$ [179]) and 10 K ($\sigma_z = 5\,\mathrm{pm}$ [172]), benefiting from the inherently low mechanical noise of bath cryogenic environments. In contrast,

Table 4.2: Reported passive stabilities of cryogenic open-access microcavities. Comparison of mechanical length stabilities achieved with macroscopic and fiber-based concave–planar mirror geometries operated in different cryostat types and at various cavity or sample temperatures. The value marked with ⋆ was obtained by time-filtering during a mechanically quiet phase of the cryostat.

	Greuter *et al.* [179]	Fontana *et al.* [178]	Herrmann *et al.* [180]	Pallmann *et al.* [172]	**This work**
Cavity type	Concave–planar	Fiber–planar	Fiber–planar	Fiber–planar	Fiber–planar
Cryostat	Bath	Closed-cycle	Closed-cycle	Closed-cycle / Bath	Dilution
T_{cav} (K)	4	11	8	10 / 10	5.3 / 1.0
σ_z open (pm)	4.3	16⋆	25	15 / 5	4.5 / 10
σ_z contact (pm)	–	–	–	2.4 / 0.8	1.9 / 0.6

implementations in closed-cycle cryostats generally exhibit larger vibration amplitudes, resulting in reduced passive stabilities of $\sigma_z = 16\,\mathrm{pm}$ [178] (time-filtered during the quiet phase of the cryostat), $\sigma_z = 25\,\mathrm{pm}$ [180], and $\sigma_z = 15\,\mathrm{pm}$ [172], respectively. In these systems, the cavity temperature often remains above 4 K, typically stabilizing near 10 K, due to imperfect thermalization between the cryocooler cold head and the comparatively large thermal mass of the cavity assembly.

In the present work, the combination of a carefully engineered, passively vibration-damped cavity platform with a dilution refrigerator—where the cryocooler and pumps are effectively isolated from the cryostat chamber—yields a cavity quantum optics setup with outstanding passive stability. The achieved performance surpasses that of closed-cycle liquid-helium cryostats and reaches a stability comparable to the best bath-cryostat implementations operating around 5 K. Moreover, the dilution refrigerator enables operation of the cavity platform at temperatures down to 1 K, with further potential for improvement through more efficient thermalization of the cavity assembly. In this regime, we achieve a passive stability of $\sigma_z = 10\,\mathrm{pm}$ in open mode and an exceptional $\sigma_z = 600\,\mathrm{fm}$ in contact mode. This level of mechanical stability would permit cavity operation at a finesse of $\mathcal{F} \approx 10^5$ (for $\lambda = 619\,\mathrm{nm}$), thereby bringing the system within reach of the strong-coupling regime for SnV centers in diamond.

4.4. Superconducting magnetic field coil

Accessing the electron spin of the SnV center requires an external magnetic field to lift the degeneracy of the spin sublevels $m_s = \pm\frac{1}{2}$. The spin-conserving optical transitions, labeled A1 and B2 in Fig. 2.4b, connect the orbital ground states of the optical ground ($E_g^{3/2}$) and excited ($E_u^{3/2}$) manifolds. Due to the different Zeeman splittings in the ground and excited states, the two spin-conserving transitions can be resolved optically once the magnetic-field-dependent splitting $\Delta\nu_{\mathrm{spin}} \equiv \mathrm{A1} - \mathrm{B2}$ exceeds the Purcell-broadened optical

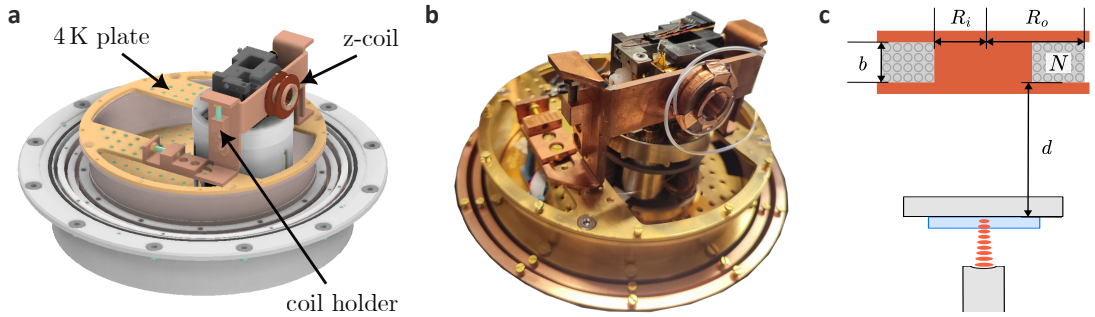

Figure 4.11: Integration of a superconducting magnetic coil. **(a,b)** Rendered model and photograph of the cryostat and cavity platform with the magnetic coil assembly mounted and thermally anchored to the 4 K plate of the cryostat. **(c)** Schematic top view illustrating the key parameters of the cavity magnet assembly: the inner (R_i) and outer (R_o) coil radii, the coil length b, and the distance d between the coil and the sample.

linewidth $\Gamma_c = (C_0 + 1)\gamma_0 + \gamma^\star$. As an estimate of the line splitting, we use the zero-strain results from Ref. [97]:

$$\Delta\nu_{\text{spin}}(B_\parallel) = 2\,B_\parallel\left(f^u_{3/2} - f^g_{3/2}\right)\gamma_l \approx 6\,\text{GHz}\,\text{T}^{-1}\cdot B_\parallel, \tag{4.4.1}$$

where $B_\parallel$ denotes the projection of the magnetic field onto the SnV symmetry axis. For a magnetic coil aligned with the optical axis—and thus with the (100)-surface normal of the diamond membrane—the projection is $B_\parallel = B\cos(54.7^\circ)$.

4.4.1. Integration into cavity and cryostat

The magnetic coil design, shown in Fig. 4.11a, consists of a z-coil mounted on a copper assembly that is rigidly fixed and thermally anchored to the 4 K plate of the cryostat. It is thermally isolated from both the cold plate and the cavity platform. The magnet is positioned as close as possible to the diamond sample to maximize the magnetic field at the color center. The coil holder includes an SM05-threaded aperture to accommodate a collimating lens in close proximity to the microcavity. The holder is designed such that the lens (and thus the coil) can be adjusted in x, y, and z to achieve optimal alignment. A photograph of the final assembly is shown in Fig. 4.11b.

Coil parameters. Assuming optimal alignment between the optical and coil axes, the magnetic field at the sample is determined by the coil geometry—specifically, the number of windings N, the current I through the superconducting wire, and the distance d between the coil and the sample. In the following, we first estimate the maximum achievable number of turns from geometrical considerations and then compare this value to the experimentally realized winding number, which is used in the field calibration.

The number of windings is constrained by the wire diameter d_w, the coil length b, and the inner (R_i) and outer (R_o) winding radii. A simple geometric estimate for the maximum number of turns that can be accommodated within the available volume is obtained from the ratio of the coil cross section to the wire cross section, multiplied by a filling factor f that accounts for imperfect packing:

$$N = \frac{(R_o - R_i)\, b}{\pi (d_w/2)^2}\, f. \tag{4.4.2}$$

The filling factor is bounded by the densest two-dimensional hexagonal packing, $f_{\text{hex}} = \pi/(2\sqrt{3}) \approx 0.91$. In practice, deviations from ideal packing reduce the achievable density. We therefore introduce an empirical correction factor f_{exp}, estimated from previous coil-winding results by Marcel Schrödin, and use an effective filling factor $f = f_{\text{exp}} f_{\text{hex}}$ with $f_{\text{exp}} \approx 0.8$.

The geometrical parameters of the superconducting coil used in our experiments are

$$b = 8\,\text{mm}, \quad R_i = 9.25\,\text{mm}, \quad R_o = 15\,\text{mm}, \quad d_w = 152\,\mu\text{m}^{12}. \tag{4.4.3}$$

With these parameters, the geometric estimate yields a maximum winding number of $N_{\text{theo}} \approx 1800$.

Experimentally, the number of turns is determined directly by monitoring the winding process, yielding $N_{\text{exp}} = 1680$. This value is used in the following to estimate the magnetic field at the sample, while the close agreement with N_{theo} confirms the consistency of the winding geometry.

4.4.2. Simulation

To estimate the magnetic field at the sample position, we simulated the magnetic flux density B in the vicinity of the coil using a finite-element method (FEM) solver[13]. The model assumes $N_{\text{exp}} = 1680$ windings carrying a current of $I = 10\,\text{A}$, distributed over the coil volume defined by the geometrical parameters in Eq. (4.4.3). This current corresponds to the maximum output of the employed current source. The simulated field distribution in the xz-plane is shown in Fig. 4.12a. From the symmetry axis ($x = 0$), we extract the axial magnetic field $B_z(z)$ as a function of distance from the coil center, plotted in Fig. 4.12b. At the sample position, located 12–18 mm from the coil center, the calculated field magnitude lies in the range $B_z = 0.09$–$0.19\,\text{T}$.

For comparison, the axial magnetic field can be approximated analytically by the expression for a finite solenoid with midpoint at $z = b/2$ [184]:

$$B(z) = \frac{\mu_0 N I}{2b}\left[\frac{z}{\sqrt{R^2 + z^2}} - \frac{z - b}{\sqrt{R^2 + (z-b)^2}}\right], \tag{4.4.4}$$

[12] Supercon 54S43
[13] Comsol Multiphysics

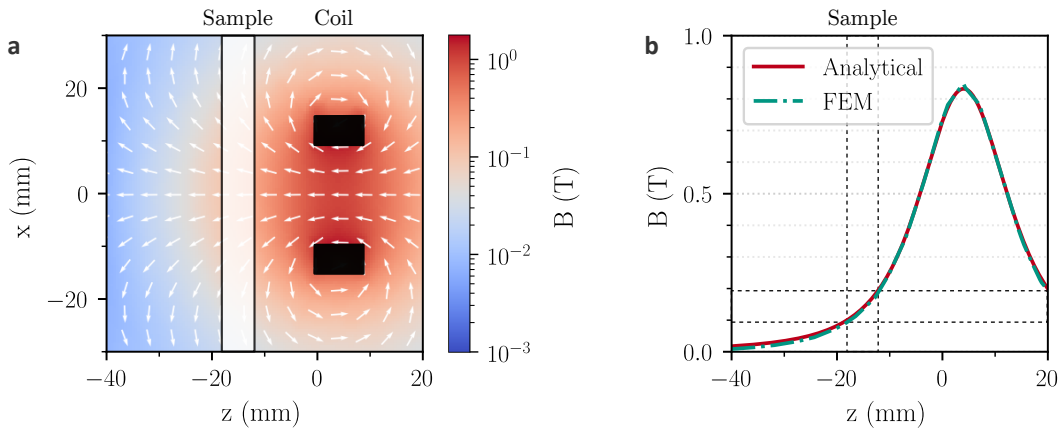

Figure 4.12: Finite-element simulation of the magnetic field generated by the coil. (a) Simulated magnetic flux density B in the xz-plane for a current of $I = 10\,\mathrm{A}$, displayed on a logarithmic color scale. **(b)** Magnetic field along the symmetry axis ($x = 0$), extracted from the 3D field map (dots), compared with the analytical expression of Eq. (4.4.4) (solid line).

where $R = (R_i + R_o)/2$ is the effective coil radius. This analytical model reproduces the FEM results with excellent agreement, as shown in Fig. 4.12b.

The highest magnetic field amplitudes occur near the inner boundary of the coil ($r \approx R_i$), where the local field reaches approximately $B|_{r=R_i} \approx 1.5\,\mathrm{T}$. The employed superconducting wire is specified for a critical magnetic field of $B_{\mathrm{crit}} = 3\,\mathrm{T}$ at a current of 10 A, ensuring stable operation well below the critical limit even at the maximum drive current.

Inserting the simulated magnetic-field range into the magnetic-field-dependent optical spin splitting of Eq. (4.4.1), we obtain an expected optical splitting of $\Delta\nu_{\mathrm{spin}} = 320\text{–}670\,\mathrm{MHz}$. This value exceeds the natural optical linewidth of $\gamma_0/2\pi \approx 30\,\mathrm{MHz}$ [111] by more than an order of magnitude, enabling optical spin readout even under conditions of high cooperativity and Purcell-broadened emission.

4.5. Conclusion and Outlook

In this chapter, we introduced a cryogenic cQED platform for solid-state quantum optics experiments, establishing the foundation for the studies presented in the following chapters. The combination of a Qlibri microcavity platform with a Qinu dilution refrigerator equipped with a superconducting magnetic field coil represents a novel experimental approach, enabling operation at temperatures down to 1.0 K. This regime allows for spin-resolved spectroscopy of group-IV color centers in open microcavities.

Importantly, the platform maintains exceptional mechanical stability under these cryogenic conditions, permitting cavity operation at high finesse. The simultaneous achievement of

temperatures around 1.0 K and high mechanical stability represents a key advance, paving the way toward high-cooperativity emitter–cavity coupling and spin-based cQED with group-IV defects, as will be demonstrated in Chapter 6.

5. Tin-vacancy centers in diamond membranes integrated into open microcavities

In the previous chapter, we demonstrated the integration of a microcavity platform with a dilution cryostat, establishing a mechanically stable system that operates at record-low temperatures for an open optical microcavity, thereby providing a quiet and stable environment for cavity-based quantum-optics experiments at about 1 K. Although these measurements were performed with a diamond membrane already integrated into the cavity, the membrane's properties were not relevant to the discussion of the technical aspects of the cavity platform.

Building on that work, we first describe how a bare cavity and a bulk diamond plate are converted into a cavity-integrated diamond membrane hosting tin–vacancy (SnV) centers. We then analyze how this integration affects the optical properties of the cavity—such as the quality factor, finesse, and mode volume—which in turn determine the achievable Purcell enhancement.

5.1. From bulk diamond to cavity-integrated SnV membranes

Transforming commercially available diamond substrates into cavity-integrated diamond membranes hosting tin-vacancy centers requires a multi-step fabrication process, much of which was carried out in collaboration with partners at the Universities of Stuttgart, Kassel, Leipzig, and Ulm within the joint projects QR.X and QR.N. The contributions of the individuals involved are acknowledged at the relevant sample-preparation stages described in the following sections.

5.1.1. Raw material and surface polish

As starting material, we use high-purity, single-crystal, electronic-grade, chemical-vapor-deposition-grown (CVD-grown) diamond plates obtained from *ElementSix*, supplied in two formats: $4.0 \times 4.0 \times 0.5\,\mathrm{mm}^3$ (plate A) and $2.0 \times 2.0 \times 0.5\,\mathrm{mm}^3$ (plate B). This material represents one of the purest commercially available diamond materials, with extremely

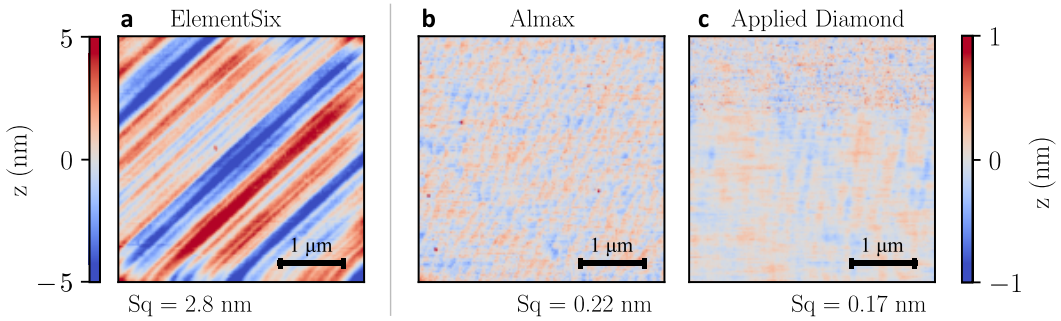

Figure 5.1: AFM topographies of different surface polishes. **(a)** As-received *ElementSix* diamond plates: Sq = 2.8 nm rms, with visible polishing scratches. **(b,c)** Surface quality after two different commercial polishing processes: **(b)** *Almax easyLab*, Sq = 0.22 nm rms; **(c)** *Applied Diamond, Inc.*, Sq = 0.17 nm rms.

low defect and impurity concentrations, making it ideal for quantum-optical applications. According to the manufacturer, the as-received plates exhibit a surface roughness below 5 nm, confirmed by atomic force microscopy (AFM) measurements shown in Fig. 5.1a. All AFM measurements were conducted by our collaborators at the University of Kassel[14]. A surface roughness of Sq = 2.8 nm rms was measured over an area of $4.0 \times 4.0\ \mu m^2$. However, this surface quality is insufficient for direct cavity integration: optical scattering losses would be excessive, and van der Waals bonding would not be feasible. Further surface processing is therefore required.

Plate A was laser-cut into three slices and polished by *Almax easyLab* to a final thickness of 0.04 mm ($4.0 \times 4.0 \times 0.04\ mm^3$). The manufacturer specifies a surface roughness below 1 nm and reduced subsurface damage achieved by a soft scaife polishing technique. AFM measurements confirmed a surface roughness of Sq = 0.22 nm rms (Fig. 5.1b). Each polished slice was then cut into quarters, yielding twelve $2.0 \times 2.0 \times 0.04\ mm^3$ pieces for further processing.

Plate B was processed by *Applied Diamond, Inc.*, laser-cut into three slices and polished down to 0.04 mm thickness using a standard scaife polish followed by a subsequent chemical etch to remove subsurface damage. The resulting surface roughness was Sq = 0.17 nm rms (Fig. 5.1c).

Mechanical polishing techniques such as the conventional scaife method can introduce surface and subsurface crystal damage, such as microcracks and stress fields, extending several micrometers into the bulk diamond [185, 186, 187]. These local defects can act as charge traps, causing spectral diffusion or blinking of defect centers. It is therefore advantageous either to employ a less aggressive polishing process (as done by *Almax*

[14] Philipp Graßhoff, Julia Heupel, Cyril Popov

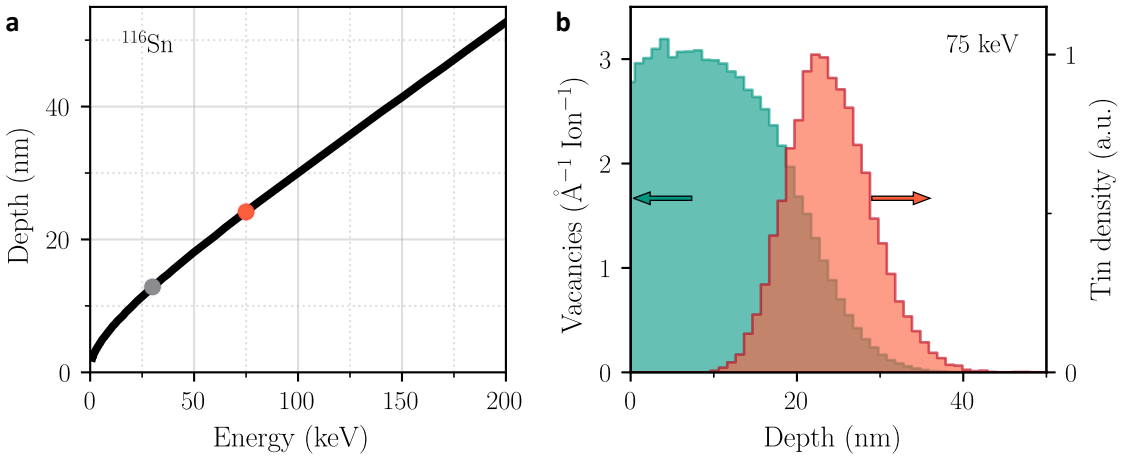

Figure 5.2: SRIM simulation of tin implantation in diamond. (a) Projected implantation depth in diamond versus implantation energy for ^{116}Sn. The two energies used in this work are indicated by markers. **(b)** At 75 keV, the ion depth distribution (right axis, arbitrary units; red) and the nuclear damage profile (left axis, vacancies per unit path length per ion; teal) are shown.

easyLab) or to remove the damaged surface layer by etching (as in the case of *Applied Diamond, Inc.*), similar to strain-relief etching procedures reported in Ref. [188].

5.1.2. SnV center formation

Implantation. Tin is not naturally present in CVD diamond at measurable concentrations, so we introduce it by ion implantation. We studied three samples—DDK1, AB2, and CA1—prepared from two source plates (A and B). A concise overview of sample processing parameters is given in Table 5.1. Samples DDK1 (plate B) and AB2 (plate A) were implanted at the University of Leipzig[15] with ^{116}Sn ions at a kinetic energy of $E_{\mathrm{kin}} = 75\,\mathrm{keV}$ and doses of $1 \cdot 10^{9}\,\mathrm{cm}^{-2}$ and $1 \cdot 10^{10}\,\mathrm{cm}^{-2}$, respectively, at nominally normal incidence (0°). Sample CA1 (plate A) was implanted at the University of Stuttgart[16] with $E_{\mathrm{kin}} = 30\,\mathrm{keV}$ ^{116}Sn ions at a dose of $4 \cdot 10^{10}\,\mathrm{cm}^{-2}$, also at 0°. While the actual angle for DDK1 and AB2 may deviate by a few degrees due to the Leipzig mounting geometry, we expect CA1 to be closer to normal incidence because of the more constrained alignment of the Stuttgart setup. Although X-ray diffraction–based alignment was not yet implemented for the implantation runs discussed here, the Stuttgart setup has since been upgraded to allow precise alignment of the sample mount with the crystalline axes.

In the simplest case, assuming an amorphous-like target material, the ion penetration depth is governed only by the ion's kinetic energy and the target density and can be simulated using SRIM (Stopping and Range of Ions in Matter), a Monte Carlo–based code

[15] Dominic Reinhardt, Michael Kieschnick, Jan Meijer
[16] Vladislav Bushmakin, Jörg Wrachtrup

that models ion trajectories and energy loss via elastic (nuclear) and inelastic (electronic) scattering [189, 190]. In this approximation, the depth is insensitive to the crystallographic orientation or alignment with high-symmetry axes. The resulting projected range as a function of energy is shown in Fig. 5.2a. At $E_{\mathrm{kin}} = 75\,\mathrm{keV}$, ^{116}Sn ions are stopped on average at a depth of approximately 24 nm, which was chosen to roughly match the position of the cavity field antinode, located around 20 nm below the mirror surface according to the mirror coating design. The corresponding depth distribution and vacancy production rate are plotted in Fig. 5.2b. Near the peak of the damage profile, the vacancy yield reaches approximately $1\,\mathrm{Å}^{-1}\,\mathrm{ion}^{-1}$, indicating a highly damaged, locally near-amorphous environment around the tin ion's stopping region.

Channeling. Up to this point, the crystalline nature of the diamond lattice has been neglected. In a single crystal, ions incident close to major symmetry axes can undergo channeling, i.e. they avoid large-angle nuclear collisions and therefore penetrate significantly deeper into the crystal. This effect can be modeled using Crystal Transport of Ions in Matter (Crystal–TRIM) [191], which accounts for lattice order. Channeling is extremely sensitive to the incidence angle and any amorphous or damaged surface layer. For $E_{\mathrm{kin}} = 75\,\mathrm{keV}$ ^{116}Sn ions along the (100) axis at perfect normal incidence, Crystal–TRIM predicts a long channeling tail extending beyond 100 nm. Even a small angular misalignment sharply reduces this tail, causing the distribution to approach the amorphous-like SRIM profile (Fig. 5.3a). Likewise, adding an amorphous top layer—introduced here to illustrate the effect of a highly damaged surface, for example resulting from aggressive scaife polishing—suppresses channeling by randomizing ion trajectories before they enter the crystal (Fig. 5.3b). Because channeled ions stop farther from the surface—and hence farther from the peak of implantation damage—normal-incidence implantation can be advantageous for creating charge- and spectrally-stable defect centers. Systematic optical studies comparing channeled and non-channeled SnV centers, however, remain an open topic.

High-temperature annealing. As introduced in Chapter 2, the SnV center consists of a tin atom positioned between two vacant carbon sites in the diamond lattice. After ion implantation, the heavy tin atoms are typically surrounded by implantation-induced lattice damage, which must be repaired through high-temperature annealing [91]. At temperatures above 600 °C, vacancies become mobile and diffuse through the lattice until reaching energetically more favorable configurations, such as vacancy–interstitial annihilation (healing), clustering of vacancies [192], or the formation of color centers. Increasing the annealing temperature increases the vacancy diffusion rate, allowing even stable defect complexes such as divacancies to dissociate and anneal out. Therefore, lattice recovery and color-center formation are typically performed by annealing at 1 200–1 500 °C under high vacuum [83, 193], or at 2 100 °C under high-pressure conditions to prevent surface graphitization [91].

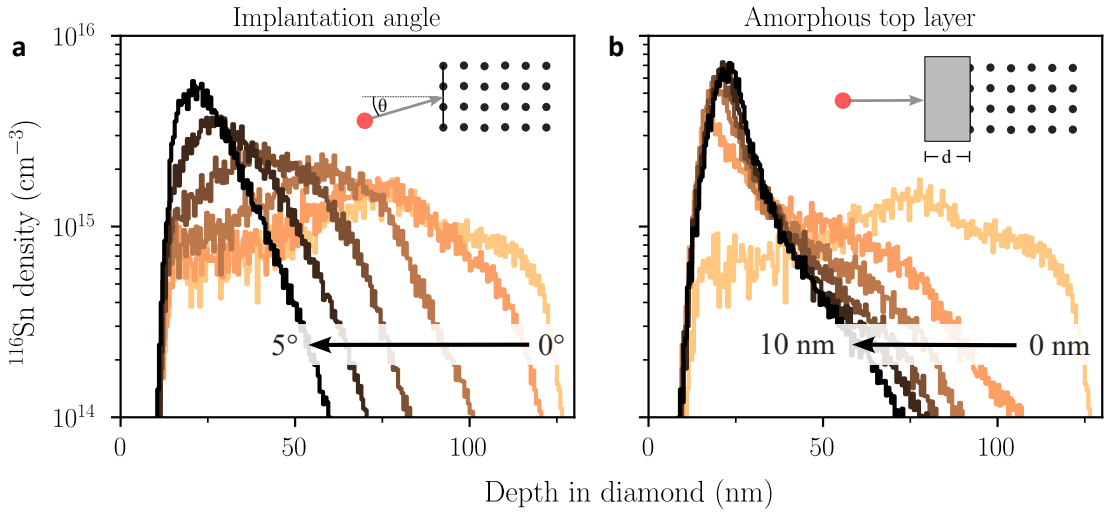

Figure 5.3: Crystal–TRIM simulation of tin implantation in diamond. (a) Simulated implantation profiles for different incidence angles, illustrating the suppression of channeling at oblique angles. **(b)** Simulated effect of an amorphous surface layer of increasing thickness on the reduction of the channeling tail.

The samples used in this work were annealed at 1 200 °C for 4 h (DDK1, AB2) by our collaborators at the University of Ulm[17], or at 1 450 °C for 2 h (CA1), respectively, by our collaborators at the University of Stuttgart[18]. Afterwards, the samples were cleaned using a tri-acid boiling process[19] to remove residual graphitic surface contamination.

Following annealing and surface cleaning, the samples were optically characterized to confirm successful SnV center activation and to evaluate their optical quality prior to membrane fabrication and cavity integration.

5.1.3. Optical and spectroscopic pre-characterization

In the following, we summarize the key results from the pre-characterization of the three SnV-activated diamond membranes, including room-temperature confocal microscopy, photoluminescence (PL) spectroscopy, as well as cryogenic photoluminescence excitation (PLE) experiments. The extent of pre-characterization varies among the samples, as resonant cryogenic measurements to assess spectral and charge stability were only performed on sample CA1 due to the unavailability of a cryogenic confocal setup at the time when samples DDK1 and AB2 were received.

[17] Jens Fuhrmann, Fedor Jelezko
[18] Vladislav Bushmakin, Jörg Wrachtrup
[19] Equal parts nitric acid (HNO_3), sulfuric acid (H_2SO_4), and perchloric acid ($HClO_4$) in a 1:1:1 volume ratio. Typical cleaning involves heating to 390 °C for 30–60 minutes under a reflux condenser.

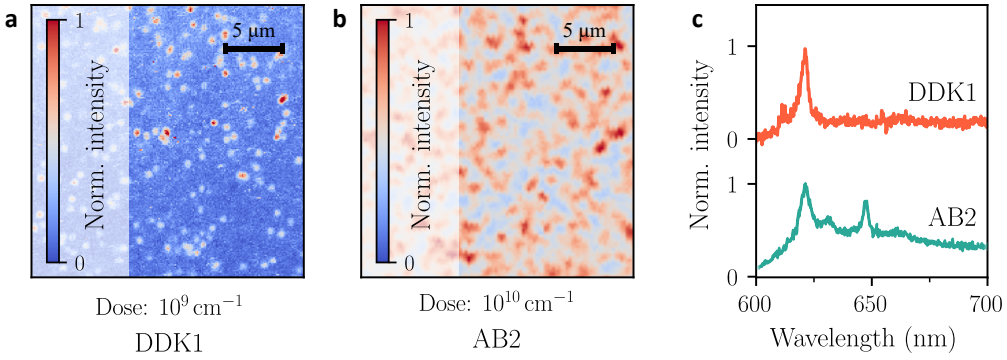

Figure 5.4: Room-temperature confocal microscopy of samples DDK1 and AB2. (a) Confocal image of the low-dose sample DDK1 ($1 \cdot 10^9$ cm^{-2}) showing spatially isolated single emitters. **(b)** Confocal image of the medium-dose sample AB2 ($1 \cdot 10^{10}$ cm^{-2}) exhibiting a higher emitter density, with bright clusters rather than individually resolvable centers. **(c)** Representative room-temperature PL spectra for both samples: the DDK1 single-emitter spectrum (orange) shows the characteristic SnV$^-$ zero-phonon line (ZPL) at 619 nm, whereas the ensemble spectrum from AB2 (teal) features additional lines at approximately 630 nm and 646 nm.

Samples DDK1 and AB2. Both DDK1 and AB2 underwent identical SnV activation treatments, differing only in implantation dose (see Table 5.1). Room-temperature confocal PL maps for the two doses ($1 \cdot 10^9$ cm^{-2} and $1 \cdot 10^{10}$ cm^{-2}) are shown in Figs. 5.4a,b, respectively. At the lower dose, individual SnV centers are clearly resolved, whereas the higher-dose sample exhibits dense regions of overlapping emission. The PL spectra in Fig. 5.4c illustrate the difference between these regimes. The single-defect emission from DDK1 reveals the characteristic SnV$^-$ ZPL at 619 nm, whereas the AB2 ensemble emission exhibits multiple peaks. Although these features were initially attributed to the neutral charge state SnV^0, charge-state control experiments in Ref. [104] have ruled out this assignment. Instead, the additional spectral components likely originate from perturbed SnV$^-$ centers residing in a damaged or vacancy-rich lattice environment, which anneal out at temperatures above 1 500 °C [91].

Sample CA1. This sample was implanted at the lowest energy and highest dose, and annealed at the highest temperature, making its processing conditions markedly different from those of DDK1 and AB2. The same cryogenic confocal microscope setup as described in Ref. [97] was used to characterize the spectral and charge stability under resonant excitation prior to bonding the membrane onto a cavity mirror. The cryogenic measurements were performed by Jeremias Resch.

A series of resonant confocal scans was performed using an excitation power of 10 nW and laser frequency steps of approximately 0.4 GHz, covering a total spectral width of about 100 GHz. Fluorescence was detected in the SnV phonon sideband (PSB) to suppress

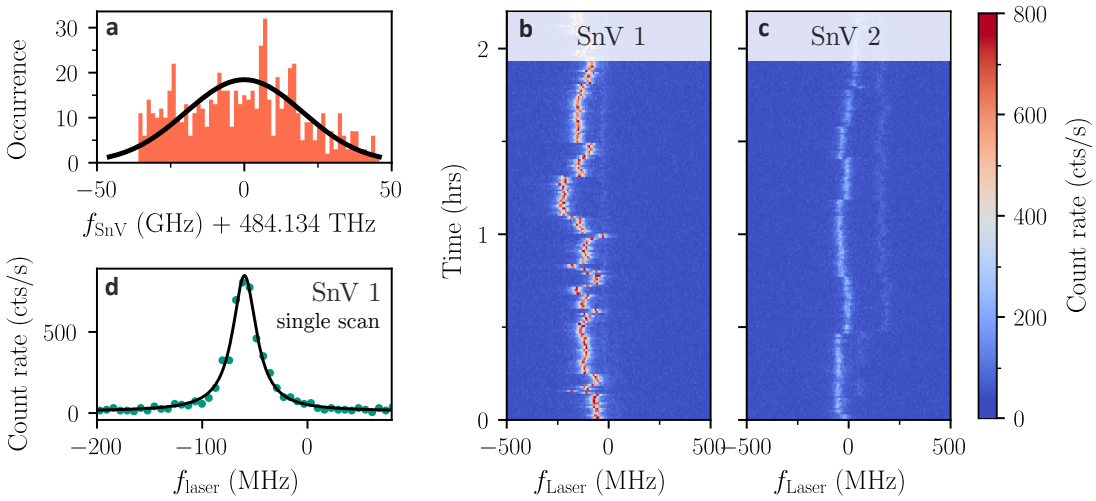

Figure 5.5: Cryogenic resonant characterization of sample CA1. (a) Histogram of the ZPL frequencies of several hundred SnV centers measured within the confocal field of view. **(b,c)** PLE spectra of two emitters identified in the same region, demonstrating charge stability over several hours without repumping and spectral stability over tens of minutes. **(d)** Exemplary single scan resonance with a Lorentzian FWHM linewidth of $\gamma/2\pi = 27$ MHz.

residual excitation light, using a 633 nm long-pass filter[20]. This allowed us to determine the spectral positions of the ZPL C-transitions around the nominal unstrained frequency of $f^0_{\mathrm{SnV}} \approx 484.13$ THz [111].

Using a two-dimensional peak-finding algorithm and evaluating all 246 confocal maps, we detected 653 SnV centers within a scan area of $22 \times 22\,\mu\mathrm{m}^2$ and a frequency window of 100 GHz. This corresponds to a combined spatial and spectral density of resonantly detectable SnV centers of $\rho^{\mathrm{conf}}_{\mathrm{SnV}} \approx 10^{-2}\,\mathrm{GHz}^{-1}\,\mu\mathrm{m}^{-2}$. From the distribution of SnV resonance frequencies, we extract a central ensemble frequency of $f_{\mathrm{CA1}} = 484.134(20)$ THz.

To assess spectral stability, charge stability, and optical linewidths, PLE scans were performed on three randomly selected emitters, two of which are shown in Fig. 5.5b,c. In PLE spectroscopy, a frequency-tunable laser resonantly addresses the optical transition while the resulting fluorescence is detected in the phonon sideband, such that the excitation spectrum directly reflects the homogeneous linewidth and spectral dynamics of the emitter. The laser frequency was scanned across the respective SnV transition using an excitation power of 2 nW. In both scans, two faint additional ZPLs are visible, likely originating from nearby defect centers. Owing to limited measurement time, only a small number of emitters was investigated in detail. All identified defect centers exhibited stable charge states under resonant excitation without requiring a repumping laser.

Emitter SnV 1 (Fig. 5.5b) shows a central peak position distribution with a FWHM of $\delta f_{\mathrm{SnV1}} = 105$ MHz and a single-scan linewidth of $\gamma_{\mathrm{SnV1}}/2\pi = 26(4)$ MHz. Emitter SnV 2

[20] *Semrock*, LP01-633R-25

(Fig. 5.5c) exhibits a central peak position distribution with $\delta f_{\mathrm{SnV2}} = 75\,\mathrm{MHz}$, predominantly in a tri-stable configuration over several tens of minutes, and a single-scan linewidth of $\gamma_{\mathrm{SnV2}}/2\pi = 25(8)\,\mathrm{MHz}$ (see Appendix A.5 and Fig. A.2 for details). In addition to these two emitters, two further faint SnV-related lines are visible within the same spectral window. While not characterized in detail, their presence suggests a non-negligible density of optically addressable SnV centers with comparable spectral properties. Taken together, these observations indicate that this sample is likely to host multiple spectrally stable SnV centers, making it a promising candidate for cavity integration, as discussed in Chapter 6.

A second diamond plate was partially implanted under identical conditions: one half at 60 keV and the other at 100 keV, and subsequently characterized in the same cryogenic confocal setup. The resulting zero-phonon-line (ZPL) distributions, charge and spectral stability, and single-scan linewidths were comparable to those of the 30 keV implantation presented here (see Appendix A.5 and Figs. A.3 & A.4 for details).

5.1.4. Cavity integration

Van der Waals bonding. The diamond plates ($2.0 \times 2.0 \times 0.04\,\mathrm{mm}^3$) hosting SnV centers are integrated into the cavity via a van der Waals bond between the sample and the planar cavity mirror. A van der Waals bond relies on intermolecular forces to provide adhesion between two surfaces without an intermediate layer. The process requires extreme flatness, sub-nanometer surface roughness, and excellent cleanliness. The bonding procedure is described in detail in Refs. [188, 63] and illustrated in Fig. 5.6a. Both the mirror and the sample are cleaned using Piranha solution[21] and rinsed multiple times with double-distilled water. The mirror is additionally treated with a mild oxygen plasma to further clean the surface and to make it hydrophilic for the bonding step. During this process, the sample is lifted from the water surface by a vacuum tweezer and placed onto the dielectric mirror. A thin residual water film mediates the initial contact between the surfaces, allowing the bond to form gradually as the water evaporates. As the water evaporates, the interference fringes vanish, indicating that no air gap remains between the diamond and the mirror—an optical signature of a successful bond (Fig. 5.6b). Without any additional treatment, both surface polishes (*Almax easyLab* and *Applied Diamond, Inc.*) were reliably bonded with a 100% success rate.

Etching to micrometer-thick membranes. To achieve small cavity mode volumes, maintain cavity lengths within the fiber mirror's stability range, and minimize absorption in the diamond, the 40 µm-thick plates were thinned to a few micrometers. This was accomplished by inductively coupled plasma reactive ion etching (ICP-RIE) performed

[21] 2:1 H_2SO_4[98%] : H_2O_2[35%]

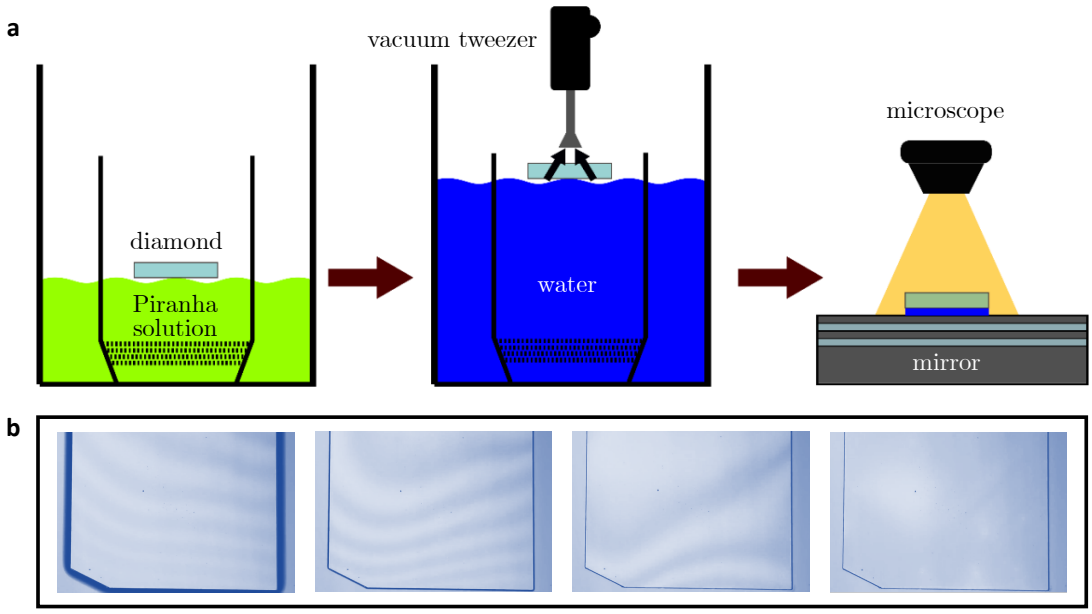

Figure 5.6: Van der Waals bonding procedure. (a) The process involves cleaning both the planar mirror and the diamond plate in Piranha solution, rinsing the diamond in double-distilled water, and lifting it from the water surface onto the planar mirror. Adapted from Ref. [188] (licensed under CC BY 4.0). **(b)** Microscope images showing a successful bond: the interference fringes, and thus the gap between the diamond and mirror, gradually disappear as the bond forms.

by our collaborators at the University of Kassel[22], following the procedure described in Ref. [188].

The resulting membrane properties were characterized by their final thickness t_d, measured using white-light interferometry, and surface roughness, determined via AFM. The measured values for all three samples are summarized in Table 5.1, showing surface roughness values of Sq = 0.2–0.3 nm and final thicknesses ranging from t_d = 0.8–4.0 µm, depending on the sample and the local position on the membrane.

[22] Philipp Graßhoff, Julia Heupel, Cyril Popov

Table 5.1: Summary of cavity-integrated diamond samples and processing conditions. * Subsurface-damage etch performed by Applied Diamond. ** Strain-relief etch carried out by P. Graßhoff (University of Kassel).

Sample	Plate	Polish	Strain relief	E_{kin} (keV)	Dose (cm^{-2})	Annealing	t_d (µm)	Sq (nm)
DDK1	B	App. Dia.	yes*	75	$1 \cdot 10^9$	1200 °C, 4 h	3.5–4.0	0.2–0.3
AB2	A	Almax	yes**	75	$1 \cdot 10^{10}$	1200 °C, 4 h	1.5–2.0	0.2–0.3
CA1	A	Almax	no	30	$4 \cdot 10^{10}$	1450 °C, 2 h	0.8–2.1	0.2–0.3

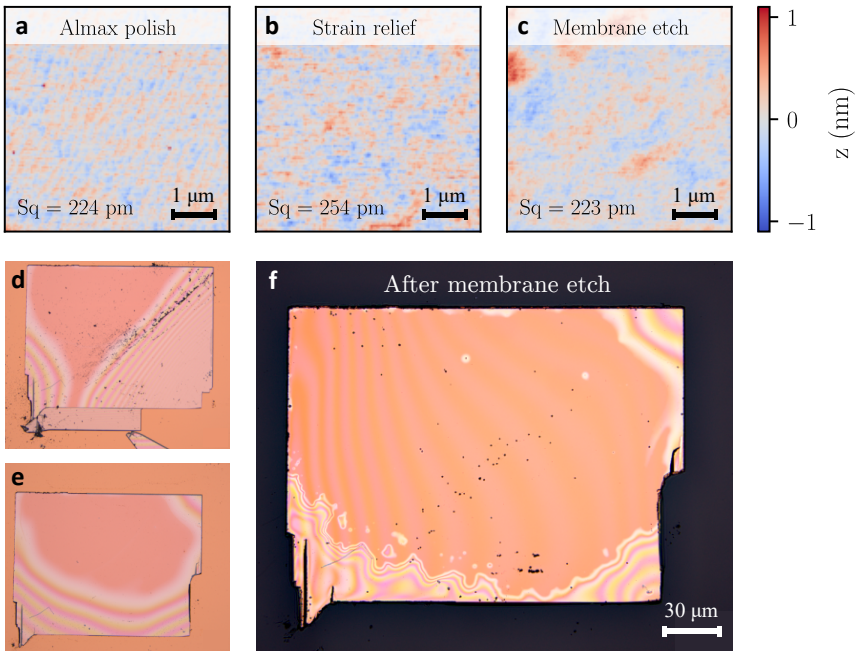

Figure 5.7: Surface roughness, bonding, and etching of sample AB2. (a–c) Atomic force microscopy (AFM) images showing the surface roughness after the commercial Almax polish, after strain-relief etching, and after the membrane etch, respectively. **(d,e)** Microscope images illustrating the improvement of the bond by manually removing non-bonded diamond areas. **(f)** Microscope image of the final cavity mirror after etching the membrane to a thickness of 1–2 µm.

Sample AB2 underwent a slightly modified treatment and is therefore discussed in more detail below. To reduce subsurface damage from the scaife polishing process, AB2 was subjected to an additional strain-relief etch prior to implantation and bonding. Both the strain-relief etch on the bonding surface and the subsequent membrane etch on the diamond–air interface preserved the surface roughness, as shown in Fig. 5.7a–c. Despite this, the strain-relief etch introduced edge artifacts that impeded bonding, as visible in Fig. 5.7d,e. The remaining interference fringes disappeared only after the non-bonded regions of the diamond plate were manually removed using a scalpel.

The final bonded and thinned diamond membrane, shown in Fig. 5.7f, exhibits a thickness of $t_\mathrm{d} = 1.5–2.0\,\mu\mathrm{m}$ in its central region. Thickness variations appear as interference fringes arising from constructive and destructive interference of broadband light reflected within the thin diamond membrane. As the local thickness changes, different wavelengths satisfy the interference condition, producing the characteristic color variations. The same mechanism will lead to the air-like and diamond-like cavity mode character for a fixed wavelength discussed below.

5.2. A hybrid diamond–air cavity

Adding a dielectric layer with a refractive index different from air into an otherwise air-filled cavity significantly alters the optical properties of the system. The finesse, linewidth, mode volume, and—most importantly—the expected Purcell enhancement are all affected. The extent of this influence depends primarily on the refractive index and thickness of the inserted layer, which in our case is a diamond membrane with refractive index $n_\mathrm{d} = 2.41$ and thickness t_d of a few micrometers.

The hybrid diamond–air cavity can be described from two equivalent perspectives. In the first, and more intuitive, picture, the diamond membrane is treated as an additional layer of the distributed Bragg reflector (DBR) stack, while the air gap serves as the reference region for defining field amplitudes and round trips. This description is particularly convenient for analyzing the cavity finesse as measured from an air-gap scan. Alternatively, the system can be viewed—less intuitively—as a diamond-filled cavity in which the air gap acts as an additional DBR layer. This perspective is advantageous because the emitter is hosted inside the diamond membrane. In this case, the reference field is defined within the diamond, and the losses per round trip as well as the effective cavity length are adjusted accordingly. As a result, this description is the natural choice for analyzing the local field at the emitter and the resulting Purcell factor. Both descriptions are physically equivalent but emphasize different aspects of the hybrid mode structure and energy distribution.

In the first picture, the system is treated as a DBR stack with an additional diamond layer terminated by air, revealing that the reflectivity of the membrane–mirror system varies with the diamond thickness due to interference between fields partially reflected at the air–diamond interface. In the extreme case of destructive interference within the diamond layer, the configuration is termed *air-like*, where the optical field is concentrated in the air gap and the reflectivity increases while transmission decreases. Conversely, for constructive interference, the configuration is *diamond-like*, with the field—and thus the stored energy—concentrated within the diamond membrane. In this case, more light couples into the membrane, resulting in a lower effective reflectivity and hence higher transmission.

From this qualitative reasoning, it is evident that the diamond thickness strongly affects the cavity finesse (losses per round trip), linewidth (quality factor), mode volume (energy distribution), and therefore the Purcell factor. A quantitative assessment of these quantities will be presented in the following sections.

5.2.1. Electric field distribution

In the previous paragraph, we introduced the two limiting mode characters—air-like and diamond-like. We now analyze them more rigorously by calculating the electric-field distribution inside the hybrid cavity. The cavity consists of two DBRs, an air gap, and a

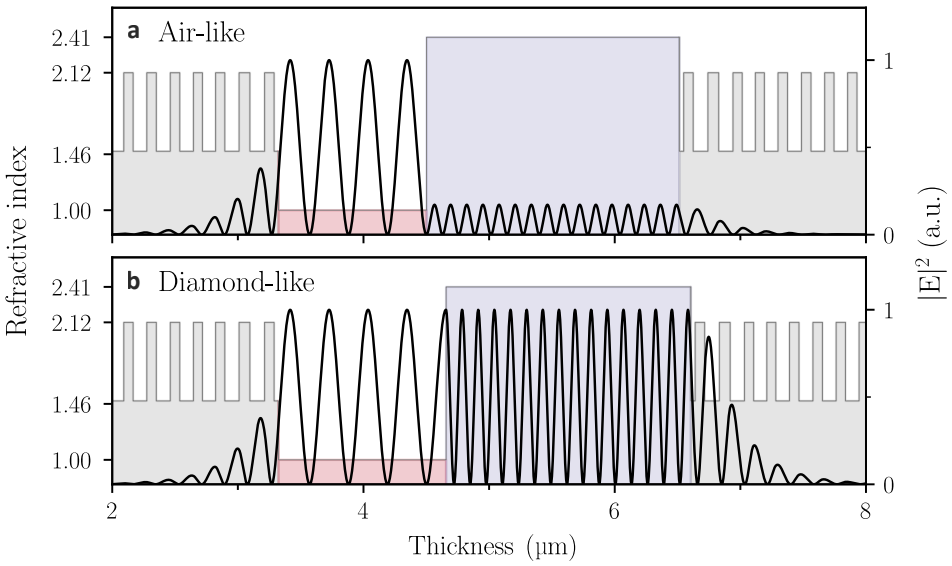

Figure 5.8: Electric-field distributions for air-like and diamond-like modes. Refractive index profile and normalized electric-field intensity $|E|^2$ for the hybrid cavity modes with **(a)** air-like and **(b)** diamond-like character. The air gap and diamond membrane are indicated in red and blue, respectively.

diamond membrane of variable thickness, modeled using a transfer-matrix approach [194], as illustrated in Fig. 5.8.

The corresponding resonance condition for the field in the diamond layer is given by

$$t_\mathrm{d} = N \cdot \frac{\lambda_n}{4} + \frac{\Phi - \pi}{2\pi} \cdot \frac{\lambda_n}{2}, \tag{5.2.1}$$

where N is an even (odd) integer for air-like (diamond-like) modes, $\lambda_n = \lambda_0/n_\mathrm{d}$ is the wavelength in diamond, and Φ is the reflection phase of the DBR. For a standard $\lambda/4$ stack with a high-index termination, $\Phi = \pi$, Eq. (5.2.1) simplifies to $t_\mathrm{d} = N\lambda_n/4$. Because the reflection phase is fixed for a given DBR, the interference condition also determines the field phase and amplitude at the air–diamond interface, leading to a field node (antinode) for the air-like (diamond-like) mode.

This distinction has important consequences for scattering losses at the diamond surface, which scale with the local field intensity. In the air-like case, the field amplitude vanishes at the surface, minimizing scattering losses, whereas in the diamond-like case, the field is maximized at the surface, increasing the potential for scattering. This effect will be discussed in more detail in Sec. 5.2.3.

Applying the continuity condition of the electric field at the diamond–air interface together with the resonance condition of the hybrid cavity yields the ratio of field intensities in the air and diamond regions on resonance, which quantifies the mode character [195]:

$$\mathcal{I}_{A/D} \equiv \frac{E^2_{\mathrm{max,a}}}{n_{\mathrm{d}} E^2_{\mathrm{max,d}}} = \frac{1}{n_{\mathrm{d}}} \sin^2\left(\frac{2\pi t_{\mathrm{d}}}{\lambda_n} - \frac{\Phi - \pi}{2}\right) + n_{\mathrm{d}} \cos^2\left(\frac{2\pi t_{\mathrm{d}}}{\lambda_n} - \frac{\Phi - \pi}{2}\right). \tag{5.2.2}$$

For the air-like condition (N even in Eq. (5.2.1)), the energy density $n^2|E|^2$ is uniform across the air and diamond regions. In contrast, the diamond-like mode confines most of the energy within the diamond layer, where it is enhanced by a factor of n_{d}^2. The expression in Eq. (5.2.2) will be used in the following to calculate the effective losses, cavity lengths, and, ultimately, the Purcell factor.

5.2.2. Cavity linewidth, effective cavity length, and Purcell factor

As discussed in Sec. 3.1.2, the cavity linewidth $\delta\nu_{\mathrm{cav}}$ is determined by the intensity decay rate of the intracavity field, $\delta\nu_{\mathrm{cav}} = \kappa/(2\pi)$. For a purely air-filled Fabry–Pérot cavity, it can be expressed as

$$\delta\nu_{\mathrm{cav}} = \frac{1}{2\pi} \frac{\text{losses per round trip}}{\text{round-trip duration}} = \frac{1}{2\pi} \frac{\mathcal{L}}{2nL/c} = \frac{c/(2nL)}{2\pi/\mathcal{L}} = \frac{\Delta\nu_{\mathrm{FSR}}}{\mathcal{F}}, \tag{5.2.3}$$

where $\mathcal{L}$ denotes the total intensity loss per round trip, L is the physical cavity length, n the refractive index of the intracavity medium, $\Delta\nu_{\mathrm{FSR}} = c/(2nL)$ the free spectral range, and $\mathcal{F}$ the finesse.

For a hybrid cavity, however, the intuitive picture of a photon simply bouncing between two mirrors no longer holds, since the electric field E, the intensity ($\propto n|E|^2$), and the energy density ($\propto n^2|E|^2$) are no longer uniform across the cavity. To capture these effects, one redefines the effective round-trip duration and loss by accounting for the spatially varying field distribution.

This definition is not unique, as the round-trip loss and duration can be referenced either to the air region or to the diamond region. These conventions lead to different effective finesses and cavity lengths. In the following, we adopt the convention of Ref. [195], where the losses and effective length are referenced to the field inside the diamond membrane. Although this convention may seem less intuitive in terms of finesse, it is advantageous for calculating the Purcell factor, since the mode volume—and therefore the coupling strength—is naturally referenced to the emitter position within the diamond layer.

Diamond gap as reference. This paragraph summarizes the results of Ref. [195]. When referencing the intracavity field to the diamond region, the effective round-trip time

is $c/(2n_\mathrm{d}L_\mathrm{eff})$, where c/n_d is the speed of light in the reference medium and L_eff is the effective cavity length. This length accounts for the diamond thickness t_d and the air-gap thickness t_a, each weighted by the local photon-energy density and normalized to the maximum energy density inside the diamond. Following the generalized definition of the energy-distribution length [179], we define

$$L_\mathrm{eff,d} = L_\mathrm{eff} = \frac{\int_\mathrm{cav} n^2 |E(z)|^2 \,\mathrm{d}z}{n_\mathrm{d}^2 |E_\mathrm{max,d}|^2/2}, \tag{5.2.4}$$

where the factor of $1/2$ accounts for the standing-wave field distribution in the cavity. This effective length also enters the definition of the optical mode volume V_eff used to evaluate the Purcell factor.

While the general expression for the mode volume in Eq. (3.1.10) involves a three-dimensional energy-density integral, here the mode profile is described in a reduced form. The transverse field distribution is characterized by the Gaussian waist w_0, while the longitudinal energy distribution is captured by L_eff. Using the standard normalization to the maximum energy density, the effective mode volume can then be written as

$$V_\mathrm{eff} = \frac{\pi w_0^2}{2} \frac{\int_\mathrm{cav} n^2 |E(z)|^2 \,\mathrm{d}z}{n_\mathrm{d}^2 |E_\mathrm{max,d}|^2} = \frac{\pi w_0^2}{4} L_\mathrm{eff}. \tag{5.2.5}$$

This diamond-referenced definition is therefore the natural choice when evaluating the Purcell enhancement.

The mirror losses per diamond-referenced round trip are

$$\mathcal{L}_\mathrm{M,eff,d} = \mathcal{I}_{A/D}\, \mathcal{L}_\mathrm{M,a} + \mathcal{L}_\mathrm{M,d} = \frac{2\pi}{\mathcal{F}_\mathrm{d}}, \tag{5.2.6}$$

where $\mathcal{L}_\mathrm{M,d}$ are the losses at the diamond-terminated mirror (encountered once per round trip) and $\mathcal{L}_\mathrm{M,a}$ those at the air-terminated mirror, weighted by the relative field intensity in the air region. Here, "diamond termination" means that the mirror transmission is calculated assuming a semi-infinite diamond medium, which differs from the standard air-terminated case used in common mirror simulations. The corresponding linewidth is

$$\delta\nu_\mathrm{cav,d} = \frac{c/(2n_\mathrm{d}L_\mathrm{eff,d})}{2\pi/\mathcal{L}_\mathrm{M,eff,d}} = \frac{c/(2n_\mathrm{d}L_\mathrm{eff,d})}{\mathcal{F}_\mathrm{d}}. \tag{5.2.7}$$

In the calculation of the Purcell factor, the effective cavity length cancels—just as in a homogeneous cavity—yielding the commonly used expression

$$F_P = \frac{6}{\pi^3} \left(\frac{\lambda}{n_\mathrm{d}}\right)^2 \frac{\mathcal{F}_\mathrm{d}}{w_0^2}, \tag{5.2.8}$$

with $\mathcal{F}_\mathrm{d} = 2\pi/\mathcal{L}_\mathrm{M,eff,d}$. In principle, $\mathcal{F}_\mathrm{d}$ could be measured by scanning the diamond thickness at a fixed air gap and extracting the linewidth and free spectral range—an

experiment that is practically infeasible. Therefore, we now introduce an experimentally accessible finesse—defined with respect to the air gap—from which the Purcell factor can be inferred.

Throughout this section, we assume the emitter to be located at the electric-field maximum within the diamond. Under these conditions, the effective mode volume can be evaluated at the field maximum, and the effective cavity length appearing in both the quality factor and the mode volume cancels out. Deviations from this idealized case can later be included through a multiplicative correction factor. Furthermore, we assume perfect polarization alignment between the emitter and the cavity mode, allowing us to omit the overlap factor ξ^2.

Air gap as reference. In this formulation, the air gap serves as the reference region for defining the effective cavity length and finesse, yielding experimentally accessible quantities that differ from those in the diamond-referenced description. The effective round-trip time is $c/(2L_{\mathrm{eff,a}})$, where c is the speed of light in vacuum and $L_{\mathrm{eff,a}}$ is the effective cavity length normalized to the energy density in the air gap, $|E_{\mathrm{max,a}}|^2$:

$$L_{\mathrm{eff,a}} = \frac{\int_{\mathrm{cav}} n^2 |E(z)|^2 \, \mathrm{d}z}{|E_{\mathrm{max,a}}|^2/2} = L_{\mathrm{eff,d}}\, n_{\mathrm{d}}\, \mathcal{I}_{A/D}^{-1}. \tag{5.2.9}$$

The losses at the diamond-terminated mirror are encountered once per round trip, while those at the air-terminated mirror are weighted by the corresponding field intensities:

$$\mathcal{L}_{\mathrm{M,eff,a}} = \mathcal{L}_{\mathrm{M,a}} + \mathcal{I}_{A/D}^{-1}\mathcal{L}_{\mathrm{M,d}} = \frac{2\pi}{\mathcal{F}_{\mathrm{a}}} = \mathcal{L}_{\mathrm{M,eff,d}} \cdot \mathcal{I}_{A/D}^{-1}. \tag{5.2.10}$$

The finesse $\mathcal{F}_{\mathrm{a}}$ defined in this way corresponds to the value measured in an air-gap scan, neglecting any additional loss channels.

The linewidth is identical to that of the diamond-referenced cavity in Eq. (5.2.7), because the weighting factors and refractive-index terms cancel:

$$\delta\nu_{\mathrm{cav,a}} = \frac{c/(2L_{\mathrm{eff,a}})}{2\pi/\mathcal{L}_{\mathrm{M,eff,a}}} = \frac{c/(2L_{\mathrm{eff,a}})}{\mathcal{F}_{\mathrm{a}}} = \frac{c/(2n_{\mathrm{d}}L_{\mathrm{eff,d}})}{\mathcal{F}_{\mathrm{d}}} = \delta\nu_{\mathrm{cav,d}} = \delta\nu_{\mathrm{cav}}. \tag{5.2.11}$$

For the Purcell factor, however, the mode volume remains referenced to the energy density in the diamond region, so the intensity weighting does not cancel. A residual intensity ratio $\mathcal{I}_{A/D}^{-1}$ remains, reflecting the hybrid mode character:

$$F_P = \frac{6}{\pi^3}\left(\frac{\lambda}{n_{\mathrm{d}}}\right)^2 \frac{\mathcal{F}_{\mathrm{a}}}{w_0^2}\, \mathcal{I}_{A/D}^{-1}. \tag{5.2.12}$$

This expression links the experimentally measured finesse $\mathcal{F}_{\mathrm{a}}$ to the effective Purcell enhancement, weighted by the field distribution between the air and diamond regions.

Air-like and diamond-like Purcell factors. The Purcell factor can be expressed in terms of the air-side mirror loss $\mathcal{L}_{\mathrm{M,a}}$ (fiber mirror), the diamond-side mirror loss $\mathcal{L}_{\mathrm{M,d}}$ (planar mirror), and the mode character $\mathcal{I}_{A/D}$. Using Eqs. (5.2.6) and (5.2.8), we obtain the following relations for a symmetric cavity and for the two limiting asymmetric cases:

- **Symmetric cavity**[23]: $\mathcal{L}_{\mathrm{M,a}} = \mathcal{L}_{\mathrm{M,d}} \Rightarrow F_{P,\text{diamond-like}} = F_{P,\text{air-like}} \cdot n_{\mathrm{d}}$,
- **Diamond-lossy cavity**: $\mathcal{L}_{\mathrm{M,a}} \ll \mathcal{L}_{\mathrm{M,d}} \Rightarrow F_{P,\text{diamond-like}} = F_{P,\text{air-like}}$,
- **Air-lossy cavity**: $\mathcal{L}_{\mathrm{M,a}} \gg \mathcal{L}_{\mathrm{M,d}} \Rightarrow F_{P,\text{diamond-like}} = F_{P,\text{air-like}} \cdot n_{\mathrm{d}}^2$.

Operating in the diamond-like mode is, in principle, advantageous for maximizing the Purcell factor, provided that mode-dependent or residual losses are negligible—an assumption that is often not fulfilled in practice. In addition, the diamond-like configuration offers practical benefits: the finesse $\mathcal{F}_a$ of this mode is reduced by approximately $1/n_{\mathrm{d}} \approx 0.41$ for a symmetric, lossless cavity, rendering it less sensitive to mechanical noise. Moreover, when collecting emission through the planar, diamond-sided mirror, higher directionality and improved collection efficiency are obtained due to the increased outcoupling losses of this mirror.

5.2.3. Absorption and scattering loss

So far, we have only considered intensity-weighted mirror losses when determining the expected Purcell factor and have neglected additional loss channels, of which absorption and scattering are the most relevant. In the previous section, we concluded that diamond-like operation is, in principle, advantageous for maximizing the Purcell factor—provided that mode-dependent losses are negligible. In this section, we examine how long this assumption remains valid in practice by identifying the dominant sources of such residual losses and by estimating their impact on the achievable Purcell enhancement. These additional losses contribute per effective round trip, which again depends on the chosen reference medium. Finally, we establish an experimentally motivated criterion that allows us to determine under which conditions operation in the diamond-like regime remains superior to the air-like configuration in realistic scenarios.

Absorption loss. The absorption loss per effective diamond round trip, $\mathcal{L}_{\mathrm{abs,d}}$, follows the Beer–Lambert law. Assuming that absorption occurs only within the diamond membrane and neglecting losses in air or vacuum, we obtain

$$\mathcal{L}_{\mathrm{abs,d}} = 1 - \exp(-2\alpha t_{\mathrm{d}}) \approx 2\alpha t_{\mathrm{d}}, \tag{5.2.13}$$

where α is the absorption coefficient of the diamond. It depends on the material's optical quality, which is determined by impurity and doping concentrations, as well as residual

[23] A symmetric cavity is not achieved merely by using identical mirror coatings on both sides; one must also account for the different optical terminations (air vs. diamond) and their reflection phases.

damage introduced during fabrication. For high-purity electronic-grade CVD diamond, α is typically 0.1–1 ppm µm^{-1} in the visible range, making absorption a negligible contribution at micrometer thicknesses [196]. Even for high-dose implantations, absorption is expected to be larger but remains negligible compared to scattering losses for the thin membranes considered here.

Scattering loss. Scattering losses arise from refractive-index discontinuities at interfaces that exhibit surface roughness σ_{rms} and scale with the local field intensity. In practice, only the two diamond interfaces contribute significantly, since mirror coatings typically exhibit sub-angstrom roughness and the intracavity field decays rapidly inside the multilayer stack becoming limiting only for ultra-high finesse cavities. For the diamond–air interface, the scattering loss per effective diamond round trip, $\mathcal{L}_{\mathrm{scat,eff,d}}$, was derived in Ref. [195] as

$$\begin{aligned}\mathcal{L}_{\mathrm{scat,a-d}} &= \mathcal{L}_{\mathrm{scat,DA}} + \mathcal{I}_{A/D}\,\mathcal{L}_{\mathrm{scat,AD}} \\ &\approx \sin^2\!\left(\frac{2\pi t_{\mathrm{d}}}{\lambda_n} - \frac{\Phi-\pi}{2}\right)\frac{n_{\mathrm{d}}+n_{\mathrm{a}}}{n_{\mathrm{d}}}\,(n_{\mathrm{d}}-n_{\mathrm{a}})^2\left(\frac{4\pi\sigma_{\mathrm{rms}}}{\lambda_0}\right)^2,\end{aligned} \tag{5.2.14}$$

where $\mathcal{L}_{\mathrm{scat,DA}}$ and $\mathcal{L}_{\mathrm{scat,AD}}$ denote the scattering losses for propagation from air to diamond and from diamond to air, respectively. The dependence on the sine term reflects the mode character of the hybrid cavity: scattering is minimal for air-like modes (field node at the surface) and maximal for diamond-like modes (field antinode).

At the diamond–mirror interface, additional scattering losses can occur, governed by the local field amplitude and the mirror reflection phase Φ. For $\Phi = \pi$ (high-index termination), the field has a node at the interface and the scattering contribution is negligible. As Φ deviates from π, the field amplitude increases and the scattering loss rises accordingly. We therefore include a correction term, $\mathcal{L}_{\mathrm{scat,d-m}}$, without explicit analytic form, yielding the total scattering loss per round trip:

$$\mathcal{L}_{\mathrm{scat,eff,d}} = \mathcal{L}_{\mathrm{scat,a-d}} + \mathcal{L}_{\mathrm{scat,d-m}}(n_{\mathrm{d}}, n_{\mathrm{s}}, \sigma_{\mathrm{rms}}, \lambda)\cos^2(\Phi/2), \tag{5.2.15}$$

where $\mathcal{L}_{\mathrm{scat,d-m}}$ is a constant scattering coefficient weighted by the field intensity at the mirror interface.

Total losses. The total loss per effective diamond round trip, $\mathcal{L}_{\mathrm{tot,d}}$, is obtained by summing the mirror, absorption, and scattering losses:

$$\mathcal{L}_{\mathrm{tot,d}} = \mathcal{L}_{\mathrm{M,eff,d}} + \mathcal{L}_{\mathrm{abs,d}} + \mathcal{L}_{\mathrm{scat,eff,d}} = \frac{2\pi}{\mathcal{F}_{\mathrm{tot,d}}}. \tag{5.2.16}$$

Because the losses per diamond round trip are not directly measurable, we also express the total losses per air round trip, $\mathcal{L}_{\mathrm{tot,a}}$, by rescaling Eq. (5.2.16) with the intensity ratio $\mathcal{I}_{A/D}$:

$$\begin{aligned}\mathcal{L}_{\mathrm{tot,a}} &= \mathcal{I}_{A/D}^{-1}\left(\mathcal{L}_{\mathrm{M,eff,d}} + \mathcal{L}_{\mathrm{abs,d}} + \mathcal{L}_{\mathrm{scat,eff,d}}\right) \\ &= \mathcal{L}_{\mathrm{M,eff,a}} + \mathcal{L}_{\mathrm{abs,a}} + \mathcal{L}_{\mathrm{scat,eff,a}} = \frac{2\pi}{\mathcal{F}_{\mathrm{tot,a}}}.\end{aligned} \tag{5.2.17}$$

Including all loss contributions, it is no longer straightforward to predict whether an air-like or a diamond-like mode yields the larger Purcell factor. To include all losses, we generalize the Purcell factor F_P of Eq. (5.2.12) by replacing $\mathcal{F}_\mathrm{a}$ with $\mathcal{F}_\mathrm{tot,a}$:

$$F_P = \frac{6}{\pi^3}\left(\frac{\lambda}{n_\mathrm{d}}\right)^2 \frac{\mathcal{F}_\mathrm{tot,a}}{w_0^2}\mathcal{I}_{A/D}^{-1}. \tag{5.2.18}$$

For a realistic cavity, the diamond-like mode remains advantageous as long as the reduction in finesse caused by residual absorption and scattering losses does not outweigh the intensity enhancement inside the diamond. In terms of the Purcell factor, this condition can be written as

$$F_P^\text{diamond-like} > F_P^\text{air-like} \quad \Leftrightarrow \quad n_\mathrm{d}^2\,\mathcal{F}_\mathrm{tot,a}^\text{diamond-like} > \mathcal{F}_\mathrm{tot,a}^\text{air-like}.$$

Experimentally, this relation can be verified by performing an air-gap scan and comparing the measured total finesses for both mode characters. As discussed below in Sec. 5.2.5, the residual losses under our experimental conditions increase the diamond-like cavity losses only marginally, such that the predicted Purcell factor remains higher for the diamond-like mode. This conclusion will be verified experimentally in Chapter 6 by comparing the cooperativity achieved for both mode characters. In many previously reported diamond-integrated open microcavity experiments, however, measurements are performed predominantly in the air-like regime, as diamond-like modes typically suffer from increased scattering losses [154, 156, 58, 61]. Achieving and maintaining sufficiently low diamond surface roughness is therefore a significant experimental challenge.

5.2.4. Mode dispersion

To predict or validate the Purcell factor for a given experimental configuration, it is essential to determine the mode character, i.e., the relative field intensity in the air and diamond regions. The methods introduced above, however, do not directly provide access to the intracavity energy distribution. Nevertheless, the different mode characters affect not only the mode volume, finesse, and linewidth, but also imprint a distinct signature on the cavity-mode dispersion, i.e., on how the resonance wavelength shifts with air-gap thickness.

This becomes clear when treating the hybrid cavity as two coupled resonators—an air-filled and a diamond-filled cavity—interacting through the finite refractive-index step at their interface. In the limit of an infinitely large membrane refractive index, the two resonators are uncoupled, with resonant wavelengths $\lambda_q = 2t_\mathrm{a}/q$ for the air cavity and $\lambda_u = 2n_\mathrm{mem}t_\mathrm{mem}/u$ for the diamond membrane, where q and u denote the respective longitudinal mode orders. When varying the air-gap thickness, the slopes of these resonances with respect to the air-gap thickness are $2/q$ for the air modes and zero for the membrane modes, as the membrane thickness remains fixed.

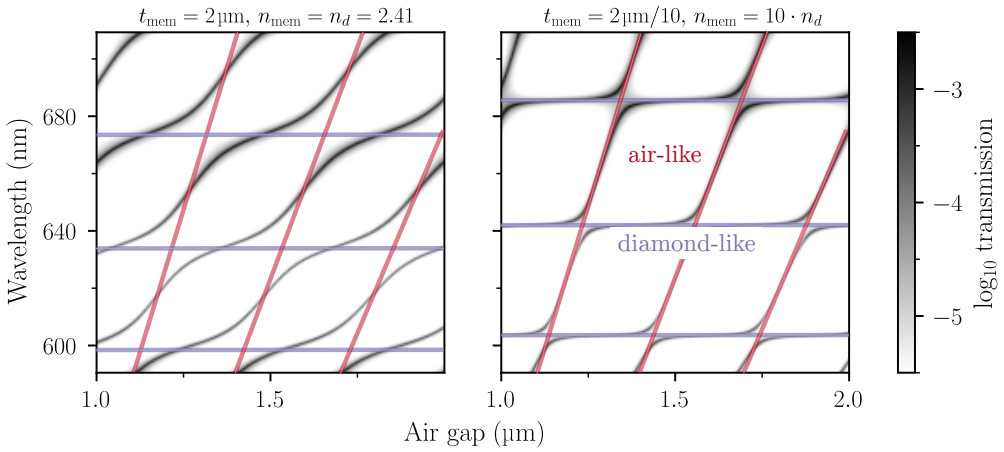

Figure 5.9: Hybrid cavity mode dispersion. (a) Mode dispersion of a realistic diamond–air cavity, with air-like and diamond-like modes indicated by straight lines. **(b)** Increasing the refractive-index contrast reduces the coupling between the two modes, making their distinct air- and diamond-like nature more evident. Here, an exaggerated membrane index of $n_{\mathrm{mem}} = 10n_{\mathrm{d}}$ is used to emphasize this distinction.

Introducing a finite refractive index ($n_{\mathrm{d}} = 2.41$) couples the two previously independent resonators, producing the characteristic avoided-crossing behavior in the dispersion relation. Air-like modes retain a steep dispersion, whereas diamond-like modes exhibit a shallower slope. Two representative dispersion curves are shown in Fig. 5.9. For a realistic diamond membrane with thickness $t_{\mathrm{d}} = 1\,\mu\mathrm{m}$ and $n_{\mathrm{mem}} = n_{\mathrm{d}} = 2.41$ (Fig. 5.9a), pronounced avoided crossings between air- and diamond-like modes are observed. Artificially increasing the membrane refractive index ($n_{\mathrm{mem}} = 10n_{\mathrm{d}}$) highlights the transition towards the uncoupled-resonator limit, as indicated by the much smaller gap at the crossings in Fig. 5.9b. To preserve the overall optical cavity length, the diamond thickness was reduced by a factor of ten in this simulation. In the following, we use the characteristic slope of measured cavity-dispersion scans to determine the mode character at specific cavity lengths and lateral positions, corresponding to different diamond thicknesses.

5.2.5. Experimental performance of the hybrid cavity

In the preceding sections, we discussed the conceptual implications and practical challenges of introducing a second refractive-index material into an otherwise air-filled Fabry–Pérot cavity. We now turn to the experimental implementation and estimate the Purcell enhancement expected for the cavity used in this work. To this end, we specify the dielectric mirror coatings, which largely determine the cavity parameters, and calculate the Purcell factor in an idealized scenario. The experimentally relevant Purcell enhancement is then inferred from finesse measurements for both air-like and diamond-like cavity modes, thereby capturing the impact of residual losses such as scattering and absorption.

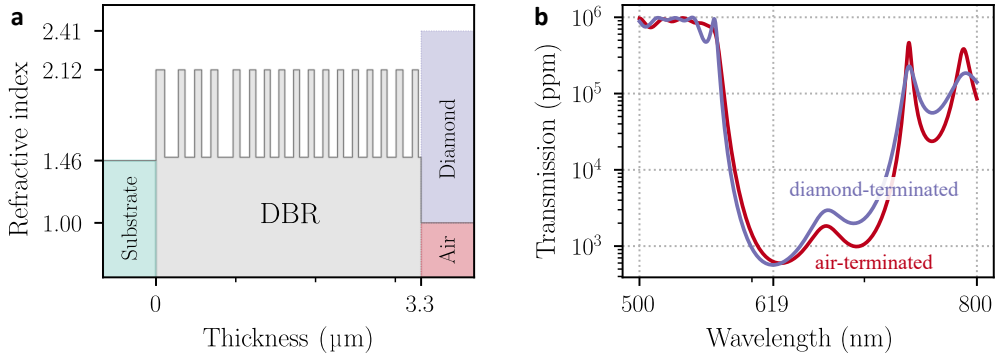

Figure 5.10: SnV mirror coating. **(a)** Layer structure of the mirror coating consisting of a glass substrate and alternating high- and low-refractive-index layers forming a distributed Bragg reflector (DBR), terminated with a low-index spacer layer that shifts the electric-field maximum to a depth of 21.5 nm. The outermost medium is either air (red) or diamond (purple). **(b)** Simulated wavelength-dependent transmission of the coating, calculated using the transfer-matrix method. The transmission differs for air- and diamond-terminated coatings, as shown in red and purple, respectively.

Coating design and expected Purcell factor. The target cooperativity of $C_0 = \beta_{\mathrm{tot}} \cdot F_P \gtrsim 1$ (see Eq. (3.2.13)) sets the required mirror transmission losses for achieving the desired light-matter coupling. The branching ratio β_{tot} for the SnVs C-transition can be explicitly decomposed into its components via

$$\beta_{\mathrm{tot}} = \beta_{\mathrm{QE}} \cdot \beta_{\mathrm{C/D}} \cdot \beta_{\mathrm{DW}} \approx 0.36, \tag{5.2.19}$$

with the quantum efficiency $\beta_{\mathrm{QE}} \approx 0.8$ [91], the C-transition branching (see Sec. 2.2.2) $\beta_{\mathrm{C/D}} \approx 0.8$ [60, 98], and the Debye–Waller factor $\beta_{\mathrm{DW}} \approx 0.57$ [83]. To ensure robust cavity performance even under elevated scattering and absorption losses, we design the cavity finesse to yield the desired Purcell factor for an air-like mode, thus enabling even higher cooperativities for diamond-like modes when losses are minimized. High Purcell factors are only achieved when the emitter is located at a field antinode of the cavity standing wave. The position of this antinode is determined by the reflection phase of the DBR stack, which can be tuned by adding a low-refractive-index spacer layer atop an otherwise high-index terminated mirror. For a reflection phase of $\Phi = 60°$ in diamond, the field antinode is located at a depth of 21.5 nm, close to the maximum of the non-channeled emitter distribution.

Both the fiber and sample mirrors employ an identical dielectric mirror coating (Fig. 5.10a), composed of alternating layers of high-index (Ta_2O_5) and low-index (SiO_2) materials. The layer thicknesses deviate from the conventional quarter-wave design to introduce an additional low-finesse stop band at $\lambda_0 = 690$ nm for a potential spectrally detuned cavity lock, and to maintain high transmission at $\lambda_0 = 532$ nm for efficient off-resonant excitation. The transmission losses for air and diamond termination at $\lambda_0 = 619$ nm are $\mathcal{L}_{\mathrm{M,a}} = 623$ ppm and $\mathcal{L}_{\mathrm{M,d}} = 566$ ppm, respectively.

From these transmission losses, the corresponding finesses for the diamond-like and air-like regions can be calculated using Eqs. (5.2.6) and (5.2.10), respectively. The expected Purcell factor then follows from Eq. (5.2.8), assuming a mode waist of $w_0 = 1.2\,\mu\text{m}$.[24] The exact mode waist varies between experiments due to differences in the radii of curvature of the used fibers and varying air and diamond thicknesses. The calculated values, neglecting residual cavity losses, are summarized in Table 5.2 for purely air-like ($F_P \lesssim 18$, $C_0 \lesssim 6.6$) and diamond-like ($F_P \lesssim 45$, $C_0 \lesssim 16.4$) mode characters, where we included the best possible polarization overlap $\xi^2 = 2/3$ between the SnV emission dipole for a (100) surface normal and the cavity electric field, and use Eq. (5.2.19) to calculate the cooperativity C_0. These values represent upper bounds and will be reduced in practice by non-ideal spectral, spatial (lateral or longitudinal), or in-plane polarization overlap.

Experimental finesse and realistic Purcell factor. In the following, we compare the experimentally measured cavity finesse with the expected values of $\mathcal{F}_a$ given in Table 5.2 for both air-like and diamond-like modes. To this end, we acquired finesse maps of sample AB2 over the full scanning range of the cavity stage at room temperature, at positions of low and high finesse. This was done by performing air-gap scans on a lateral grid from which we extracted the free spectral range and the linewidth at $\lambda_0 = 619\,\text{nm}$. The resulting maps are shown in Fig. 5.11, where the low-finesse map features a median finesse of $\mathcal{F}_a^{\text{low}} = 1700$ and the high-finesse map has a median finesse of $\mathcal{F}_a^{\text{high}} = 4830$.

To verify that the low- and high-finesse positions correspond to diamond-like and air-like modes, respectively, we acquired a dispersion map at a clean lateral position for each case as shown in Fig. 5.11c,d. This was achieved by illuminating the cavity with a 532 nm laser, generating broadband background fluorescence that is filtered by the cavity resonances and detected in a spectrometer. The dispersion exhibits a shallow slope around $\lambda_0 = 619\,\text{nm}$ for the low-finesse position, indicating a diamond-like mode. In contrast, the high-finesse position shows a steep slope, characteristic of an air-like mode. In addition to the broadband fluorescence, the same 619 nm laser used in the finesse measurement serves as a reference marker, appearing as a straight line in the dispersion map.

From the measured cavity dispersion, we can also deduce the thickness of the diamond membrane. This can be done either by fitting the measured dispersion with a transfer-matrix model, or by using the diamond-like wavelengths of two neighboring resonances according to $\lambda_u = 2nt_{\text{mem}}/u$, which yields

$$\lambda_u = \frac{2nt_{\text{mem}}}{u}, \qquad \lambda_{u+1} = \frac{2nt_{\text{mem}}}{u+1} \Rightarrow t_{\text{mem}} = \frac{\lambda_u \lambda_{u+1}}{2n(\lambda_{u+1} - \lambda_u)}. \tag{5.2.20}$$

For $\lambda_u \approx 620\,\text{nm}$ and $\lambda_{u+1} \approx 690\,\text{nm}$, this gives $t_{\text{mem}} \approx 1.3\,\mu\text{m}$, in good agreement with the transfer-matrix simulation and interferometric measurements from our collaborators in Kassel for sample AB2 (cf. Table 5.1).

[24] The mode waist in our experiments typically lies in the range $w_0 = 1.0$–$1.4\,\mu\text{m}$, depending on the air (1–2 µm) and diamond (1–4 µm) gap sizes and the fiber radii of curvature (16–36 µm).

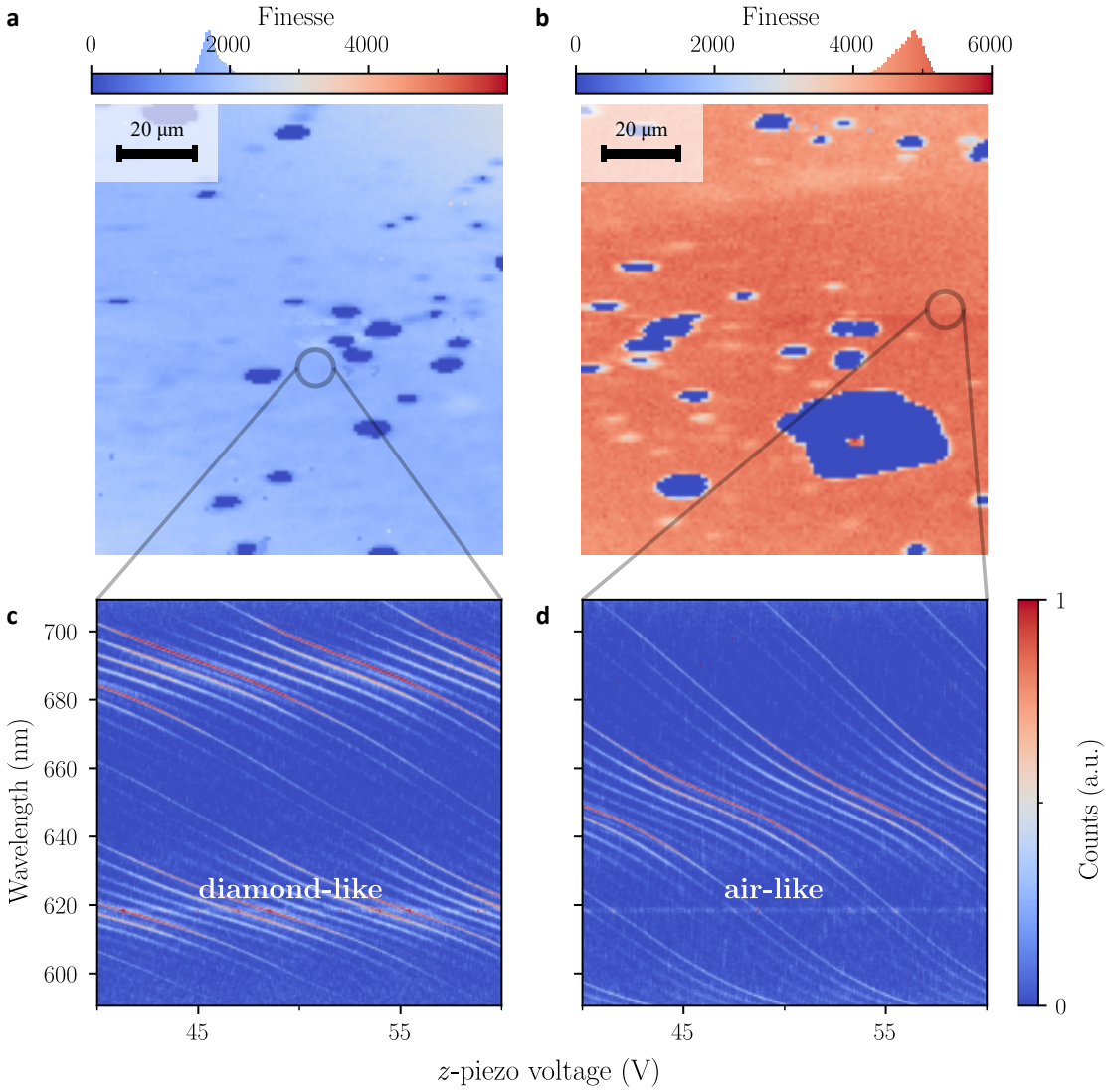

Figure 5.11: Air-like and diamond-like cavity finesse $\mathcal{F}_a$. (a,b) Room-temperature finesse maps of a diamond-like (**a**, left) and air-like (**b**, right) cavity region, showing median finesses of 1700 and 4830, respectively. **(c,d)** Corresponding cavity dispersion scans confirming the mode character: a nearly flat dispersion for the diamond-like mode (**c**) and a steeper dispersion for the air-like mode (**d**). Neglecting piezo nonlinearities, the z-piezo voltage is proportional to the cavity air-gap length, with larger voltages corresponding to shorter cavities. The horizontal line at $\lambda_0 = 619\,\text{nm}$ marks the wavelength at which the finesse was evaluated.

From the experimentally measured air-like and diamond-like finesse, we can deduce the expected Purcell factor including additional losses by calculating the finesse in diamond $\mathcal{F}_{\text{tot,d}}$ according to Eqs. (5.2.16) and (5.2.17), and the Purcell factor according to Eq. (5.2.12). The results are summarized in Table 5.2, yielding realistic expected Purcell factors of $F_P \lesssim 12$ ($C_0 \lesssim 4.3$) for an air-like mode and $F_P \lesssim 24$ ($C_0 \lesssim 8.8$) for a diamond-like mode. Although the measured finesse is significantly lower than the design value, we do not

observe drastic losses that would predominantly occur in the diamond-like mode, such as scattering. The ratio of diamond-like to air-like finesse in air length, $\mathcal{F}_a^{\text{diamond-like}}/\mathcal{F}_a^{\text{air-like}}$, decreases slightly from 0.43 for the designed coating to 0.35 for the experimentally determined value. This result is not surprising given the measured surface roughness of Sq = 0.22 nm, as determined in Fig. 5.7. For this roughness, the expected scattering losses for a diamond-like mode are only 55 ppm, which is negligible compared to the mirror losses. A comprehensive experimental determination and modeling of the different loss channels contributing to the measured cavity finesse would require a more thorough analysis of the mode-character–dependent finesse variation, as performed, for example, in Ref. [174, 197]. Nevertheless, the absence of large loss channels that predominantly affect diamond-like cavity modes is highly beneficial, as it enables operation in both air-like and diamond-like modes. The latter offer approximately twice the Purcell factor, which will be verified in Chapter 6.

The data shown were acquired using sample AB2. Similar behavior and comparable finesse values were observed for all three samples listed in Table 5.1, each exhibiting a diamond-like mode character associated with higher expected Purcell factors compared to the air-like mode.

5.3. Conclusion and Outlook

In this chapter, we described the complete process of fabricating diamond membranes from bulk diamond plates and integrating them into optical microcavities hosting SnV centers. Several samples were produced, three of which were discussed in detail. These samples form the basis for the results presented in the following chapter, where the light–matter coupling will be analyzed.

Table 5.2: Design and experimental finesse and expected Purcell factor. The design finesse in air and diamond lengths is calculated from the mirror losses $\mathcal{L}_{\text{M,a}} = 623$ ppm and $\mathcal{L}_{\text{M,d}} = 566$ ppm. The ideal Purcell factor F_P is calculated for a cavity mode waist of $w_0 = 1.2\,\mu\text{m}$ according to Eq. (5.2.8), assuming the best possible polarization overlap of $\xi^2 = 2/3$ and perfect spatial and spectral overlap. The cooperativity C_0 includes the branching ratio $\beta_{\text{C/D}} \approx 0.8$, the quantum efficiency $\beta_{\text{QE}} \approx 0.8$, and the Debye–Waller factor $\beta_{\text{DW}} = 0.57$ according to Eq. (5.2.19). The finesse in air length was determined experimentally. From this, one can calculate the expected Purcell factor including all loss mechanisms.

	Design		**Experimental**	
	Air-like	Diamond-like	Air-like	Diamond-like
$\mathcal{F}_a$	7320	3160	4830	1700
$\mathcal{F}_d$	3040	7620	2000	4090
$F_P\vert_{w_0=1.2\,\mu\text{m}}$	$\lesssim 18$	$\lesssim 45$	$\lesssim 12$	$\lesssim 24$
$C_0\vert_{w_0=1.2\,\mu\text{m}}$	$\lesssim 6.6$	$\lesssim 16.4$	$\lesssim 4.3$	$\lesssim 8.8$

Introducing a second material into an otherwise air-filled cavity has important implications for both the cavity performance and the expected Purcell factor. A correct understanding of these effects is crucial for evaluating the light–matter coupling discussed in Chapter 6. Thanks to careful sample preparation yielding low surface roughness, we were able to realize samples that enable efficient cavity operation at diamond-like lateral positions. This configuration offers significant advantages in terms of reduced mechanical stability requirements and achievable cooperativity, as will be demonstrated in Chapter 6.

6. An efficient spin-photon interface for tin-vacancy centers in diamond

In this chapter, a fiber-based microcavity platform operated in a dilution refrigerator is used to investigate spin–photon interface capabilities based on individual tin-vacancy (SnV) centers in diamond. By coupling single SnV centers embedded in a thin diamond membrane to an optical cavity, Purcell-enhanced emission and coherent light–matter interaction are observed. Resonant probing of the cavity–emitter system with a weak coherent field reveals emitter-induced extinction features in the cavity transmission, and Zeeman-split optical transitions are resolved under the application of a magnetic field. Together, these results establish the experimental basis for spin–photon interfaces using tin-vacancy centers in an open microcavity platform.

6.1. Experimental setup

This section describes the optical setup used to excite, probe, and detect cavity-coupled SnV centers, including the employed excitation lasers and detection instrumentation. Details on the microcavity platform integrated into a dilution refrigerator are provided in Chapter 4, while the fabrication and properties of the SnV-center-hosting diamond membranes are discussed in Chapter 5.

A continuous-wave (cw), diode-pumped solid-state laser at 532 nm[25] is used for identification and alignment of SnV centers to the cavity mode via off-resonant excitation. For excited-state lifetime measurements, we employ a pulsed supercontinuum laser together with an acousto-optical tunable filter stage[26], enabling narrowband wavelength selection for pulsed excitation. Cavity characterization and resonant probing of the cavity–emitter system are performed using a single-frequency, tunable cw laser based on optical parametric oscillation, operated at its frequency-doubled output near 619 nm[27]. The three excitation sources are combined using a dichroic mirror (DM) and a polarizing beam splitter (PBS), and are coupled into a single-mode fiber that is fusion-spliced inside the cryostat onto the cavity fiber mirror.

[25] Hübner Photonics, Cobolt Samba 532
[26] NKT Photonics, SuperK FIANIUM & SuperK Select
[27] HÜBNER Photonics, C-WAVE GTR

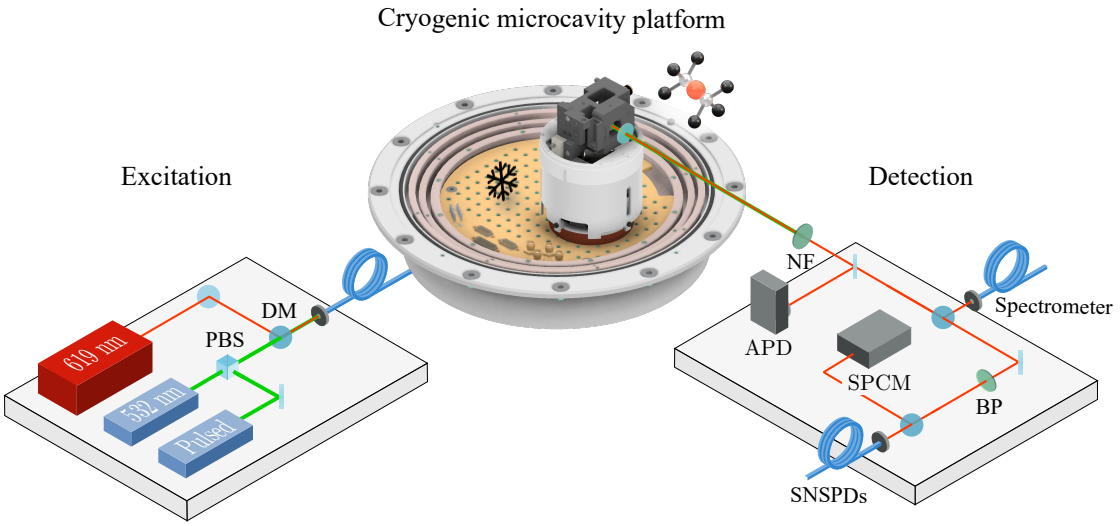

Figure 6.1: Cryogenic microcavity platform and optical setup. The microcavity platform is mounted on the millikelvin plate of the dilution refrigerator. Cavity-integrated SnV centers are excited off-resonantly or resonantly probed through the cavity fiber mirror. The emitted fluorescence or transmitted probe light exits through the free-space output mode of the cavity, where it is collimated inside the cryostat and guided out through an optical window. Outside the cryostat, the signal is spectrally filtered and detected using an avalanche photodiode (APD), a fiber-coupled spectrometer, a free-space single-photon counting module (SPCM), or fiber-coupled superconducting nanowire single-photon detectors (SNSPDs).

The fluorescence or transmitted probe signal leaves the cavity through its free-space output mode and is collimated inside the cryostat using an aspheric lens[28]. After passing through the optical windows of the cryostat, off-resonant 532 nm excitation light is suppressed using a 532 nm notch filter (NF). For measurements involving strong transmitted laser fields, such as cavity finesse or stability measurements, the signal is detected using an avalanche photodiode[29] (APD). For detection of fluorescence or weak transmitted probe signals, the light is sent either to a multimode fiber-coupled spectrometer[30] or, after a band-pass filter[31], to a free-space single-photon counting module[32] (SPCM) or to single-mode fiber-coupled superconducting nanowire single-photon detectors[33] (SNSPDs).

Single-mode fiber coupling significantly reduces background under off-resonant excitation by spatially filtering the emitted light. It efficiently couples only the fundamental cavity mode while strongly suppressing contributions from higher-order transverse modes and stray scattering. This is particularly beneficial because the large numerical aperture of the free-space SPCM would otherwise collect substantial background light. The overall collec-

[28] Without magnet assembly: Thorlabs AL1225-A; with magnet assembly: Asphericon AFL12-15-P-B-285
[29] Thorlabs, APD410A2/M
[30] Andor, Shamrock 750
[31] Semrock, FF01-620/14-25
[32] Excelitas, SPCM-AQRH-12-TR
[33] Single Quantum, Eos 2400 CS

tion efficiency into the single-mode fiber is limited to approximately 15–35 %, depending on alignment and thermal drifts that cause relative displacement between the collimation lens and the cavity output mode waist. Depending on the signal-to-background ratio of the respective measurement, either the SPCM or the SNSPDs were used. The limited fiber-coupling efficiency could potentially be mitigated by implementing a cryogenically tunable *xyz* stage inside the cryostat, allowing for in-situ optimization of the collimation alignment.

6.2. Purcell-enhanced emission of single SnV centers

This section discusses the detection and Purcell-enhanced emission of single SnV centers coupled to a tunable microcavity platform under off-resonant excitation. In this regime, the effective frequency resolution is limited by the cavity linewidth, which is on the order of several gigahertz. Consequently, the spectral and spatial emitter density must be sufficiently low for individual emitters to remain resolvable within a single cavity resonance. For this reason, the measurements presented here were performed on sample AB2. Its medium implantation dose and comparatively broad spectral distribution, resulting from the low annealing temperature (see Table 5.1), provide an optimal emitter density for off-resonant detection. By contrast, sample DDK1 exhibits too low a spatial density for efficient SnV identification, while sample CA1 shows too high a spectral density (see Fig. 5.5), preventing single-emitter discrimination under off-resonant excitation. When employing resonant detection schemes, as discussed in Section 6.3, where the spectral resolution is determined by the much narrower emitter linewidth, sample CA1 becomes ideally suited.

6.2.1. SnV detection via cavity dispersion scans

In the first set of measurements, cavity-coupled SnV centers were identified by performing dispersion scans under off-resonant excitation at cryogenic temperatures ($T_{\mathrm{cav}} \approx 5.3\,\mathrm{K}$), analogous to the room-temperature scans shown in Fig. 5.11c,d. The SnV centers integrated within the cavity were excited via the fiber using a cw 532 nm laser at a power of $P \approx 2\,\mathrm{mW}$ measured in free-space transmission, corresponding to $P_{\mathrm{laser}} \approx 8\,\mathrm{mW}$ before fiber coupling. This difference arises from residual reflectivities of the bare and diamond-terminated mirrors, as well as losses introduced by fiber coupling and splicing.

This comparatively high excitation power not only drives the SnV centers but also generates background fluorescence, originating predominantly from the fiber and the distributed Bragg reflector (DBR) mirror stack. As a result, the cavity-mode dispersion is visible even in the absence of resonant emitters, as illustrated in Fig. 6.2a. In the spectral window shown, five cavity modes are observed: the fundamental TEM_{00} mode and the two orthogonal first-order Hermite–Gaussian modes (TEM_{10} and TEM_{01}), each exhibiting polarization splitting. Polarization splitting is observed at nearly all lateral positions and is particularly

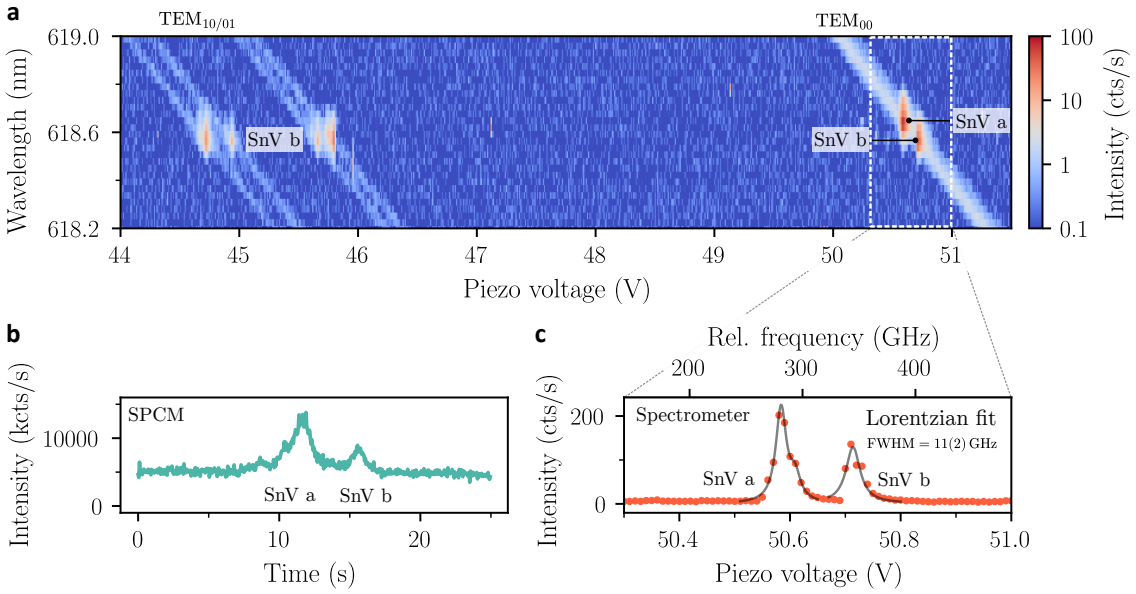

Figure 6.2: Cavity mode dispersion under off-resonant excitation. **(a)** Cavity-length–dependent fluorescence spectra measured on sample AB2 reveal the cavity-mode dispersion together with two SnV centers, labeled *SnV a* and *SnV b*. Both are visible in the fundamental cavity mode; however, *SnV a* does not couple to higher-order modes, indicating optimal spatial overlap with the fundamental mode. **(b)** The same two transitions are observed on an SPCM during a slow cavity scan of the fundamental mode across their zero-phonon-line (ZPL) wavelengths. **(c)** A zoom into the fundamental mode inside the dispersion scan highlights the spectral shape of the cavity-probed emitters. A Lorentzian fit yields a FWHM of 11(2) GHz, calibrated via the dispersion slope and consistent with the cavity linewidth inferred from the local finesse and cavity length.

prominent for diamond-like modes, consistent with local strain-induced birefringence introducing polarization-dependent frequency shifts.

When the cavity is tuned into resonance with the ZPL of a SnV center, the Purcell effect enhances emission into the cavity mode, producing a bright feature in the dispersion map. In Fig. 6.2, two such features are identified and attributed to two distinct SnV centers, *SnV a* ($\lambda_0 \approx 618.7$ nm) and *SnV b* ($\lambda_0 \approx 618.6$ nm), where λ_0 denotes the ZPL wavelength. Both emitters couple to the fundamental mode, whereas only *SnV b* shows coupling to the first-order modes. The absence of *SnV a* in these higher-order modes indicates optimal spatial overlap with the fundamental cavity mode and negligible overlap with odd-parity modes.

A zoom into the local dispersion of the fundamental mode near the two SnV transitions allows examination of the spectral shape of the cavity-enhanced fluorescence. The applied piezo voltage is converted into a cavity detuning using the slope extracted from the linear region of the dispersion. By integrating the fluorescence signal along the wavelength axis, two peaks are obtained that exhibit a polarization-split double-Lorentzian structure. This form directly reflects the polarization splitting of the cavity mode. Fitting the data with a double Lorentzian yields a full width at half maximum of 11(2) GHz, consistent

with the cavity linewidth expected from the local finesse and cavity length (see Sec. 6.2.2). This indicates that the observed spectral features are cavity-limited, implying that emitter spectral diffusion is significantly narrower than the cavity linewidth.

The fluorescence signal from the same two emitters was also recorded on an SPCM using the pulsed laser source at an excitation power of $P \approx 0.1\,\mathrm{mW}$. The resulting time trace, shown in Fig. 6.2b, reproduces their relative spectral positions but without providing detailed spectral information. Whereas a spectrometer-based dispersion map spanning a 4 nm window requires several minutes due to comparatively low count rates, the SPCM-based time trace can be acquired within seconds. In the following section, we introduce a rapid cavity-based method for lateral and spectral screening of the diamond sample to identify bright SnV emission.

6.2.2. Hyperspectral fluorescence maps

To efficiently locate bright SnV emission, we perform a dispersion scan similar to the procedure described previously, mapping the spectral information onto the time domain and detecting the fluorescence with an SPCM. The following measurements are all taken at an air-like lateral position of the cavity with a cavity finesse in the range of $\mathcal{F}_a \approx 4\,000$–$5\,000$.

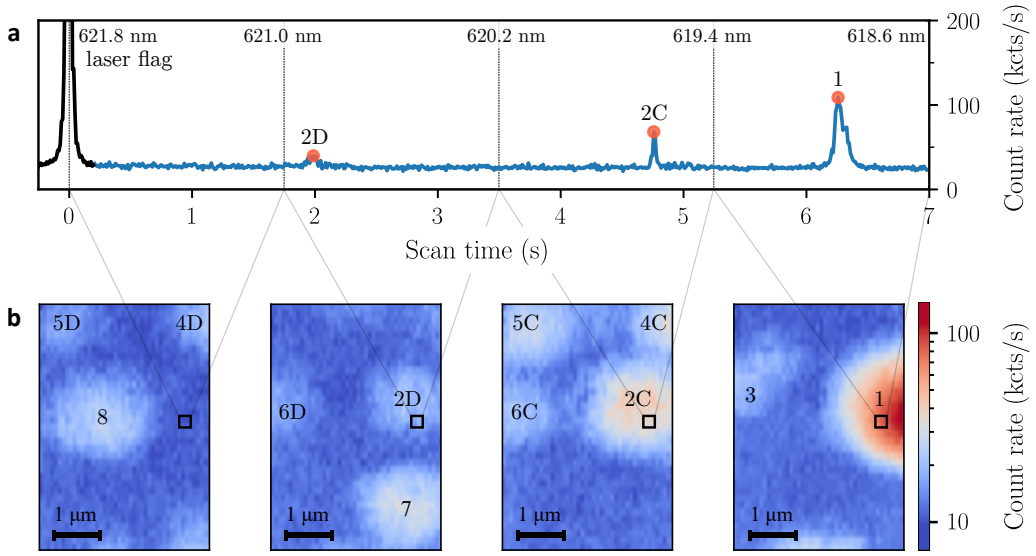

Figure 6.3: Hyperspectral fluorescence maps. (a) Exemplary fluorescence time trace obtained while tuning the cavity resonance from the laser flag at 621.8 nm toward 618.6 nm. Distinct peaks in the count rate correspond to three different zero-phonon lines (ZPLs), consistent with emission from two individual SnV centers. **(b)** The time trace is divided into four equal wavelength intervals. For each interval, the maximum fluorescence signal is plotted as a function of the lateral cavity position, yielding hyperspectral fluorescence maps. Emitters are labeled SnV 1–8, where spatially overlapping features are attributed to the C and D transitions of the same SnV center.

The cavity is illuminated through the fiber using both an off-resonant cw laser and a resonant laser at 622 nm, which serves as a wavelength flag in the fluorescence time trace and provides an absolute wavelength reference. This allows correction for slow longitudinal cavity drifts during the acquisition. As an independent absolute wavelength reference, we use the emission wavelength of a particular SnV center measured separately with the spectrometer.

An exemplary fluorescence time trace recorded at one lateral cavity position is shown in Fig. 6.3a. At time $t = 0\,\mathrm{s}$, the laser flag is detected. For $t > 0\,\mathrm{s}$, the cavity length is monotonically reduced, shifting its resonance to shorter wavelengths and into the range where SnV emission is expected. The scan has a total duration of 8 s. As a second absolute reference, the fluorescence of emitter 1 was recorded on a spectrometer, yielding $\lambda_{\mathrm{SnV1}} = 618.9\,\mathrm{nm}$.

The fluorescence time-trace measurement was repeated on a grid of lateral cavity positions. Plotting the maximum signal within each of the four wavelength windows yields the hyperspectral fluorescence maps shown in Fig. 6.3b. We identify eight distinct SnV emitters, labeled SnV 1–8. Weaker emitters, emitters that are not fully spatially separable, or emitters located at the boundaries of the scan region are omitted from further analysis. Spatially overlapping but spectrally distinct emission features are attributed to the C and D transitions of the same center. In several cases, only one transition is detected, likely

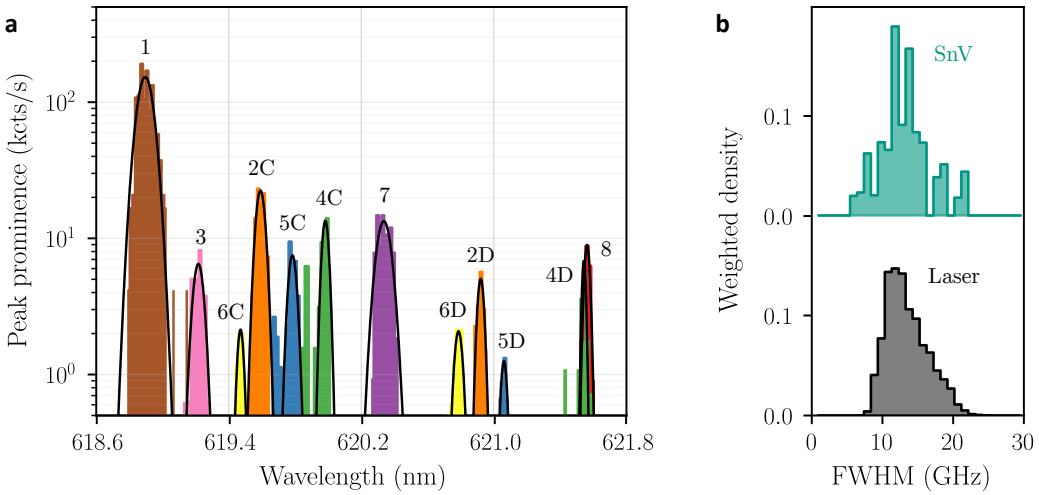

Figure 6.4: Spectral properties of detected SnV centers. (a) Spectral distribution of the detected peaks shown in Fig. 6.3b. The peak heights are scaled to correspond to the expected count rate under perfect spatial overlap with the cavity mode. Peaks that overlap spatially, and are therefore attributed to the C and D transitions of the same SnV center, are shown in matching colors. **(b)** Weighted distributions of the linewidths obtained from double-Lorentzian fits to the laser and SnV peaks. The weights correspond to the inverse of the relative fit uncertainty. The strong overlap between the two distributions indicates that the linewidths of both the laser and SnV peaks are limited by the cavity linewidth.

Table 6.1: Summary of the spectral distribution of the detected SnV zero-phonon lines. Overview of the SnV zero-phonon-line wavelengths detected in Fig. 6.3 and analyzed in Fig. 6.4. Where both C and D transitions were observed, the corresponding spectral splitting is reported as well.

SnV	1	2	3	4	5	6	7	8
C (nm)	618.90(5)	619.60(3)	619.22(3)	619.99(2)	619.79(3)	619.48(2)	620.34(4)	621.57(2)
D (nm)		620.93(2)		621.55(1)	621.07(2)	620.79(3)		
C–D (GHz)	—	1 036	—	1 215	995	1 027	—	—

due to spectral separation outside the scanned wavelength interval or insufficient signal strength.

The clear spatial separation of the emitters enables extraction and unique assignment of the spectral properties of each transition. From the detuning relative to the laser flag, we determine the wavelength distribution of the individual peaks, shown in Fig. 6.4a. The histograms follow the notation used in Fig. 6.3b, and their heights are scaled to reflect the measured peak prominence under conditions of perfect spatial overlap with the cavity mode.

The broad distribution of zero-phonon-line wavelengths spanning several nanometers is likely a consequence of the specific color-center creation parameters. These include shallow implantation at a depth of $\sim$ 20 nm, a possibly non-normal implantation angle which prevents efficient channeling, the relatively low annealing temperature (1 200 °C), and strain introduced during the van der Waals bonding process. Together, these factors result in SnV centers embedded in a highly strained and defect-rich environment, leading to the pronounced spectral inhomogeneity observed. Additional evidence for the strongly strained environment is provided by the spectral separation between the C and D transitions, observed for four emitters within the scanned region. These splittings range from 995 GHz (*SnV 5*) to 1 215 GHz (*SnV 4*), substantially larger than the ground-state splitting of unstrained SnV centers (820 GHz) [97]. The full results of the spectral analysis are summarized in Table 6.1.

The spectral width of each detected peak (laser flag and SnV fluorescence) provides access to both the spectral resolution of the cavity and, as discussed below, an upper bound on the inhomogeneous ZPL width. As in the dispersion scan shown in Fig. 6.2, each peak is fit with a double Lorentzian to account for polarization splitting. Because each peak contains only a limited number of samples, the relative fit uncertainty is typically on the order of 0.1–0.5. To suppress poorly constrained fits in the resulting linewidth distribution, the extracted FWHM values are weighted by the inverse relative uncertainty. The resulting distributions are shown in Fig. 6.4b: both the laser and SnV ZPLs exhibit nearly identical characteristic linewidths of 13(3) GHz and 13(4) GHz, respectively.

The observation of identical peak widths for the laser and the SnV ZPLs indicates that both are spectrally limited by the cavity. Because the intrinsic laser linewidth is orders of

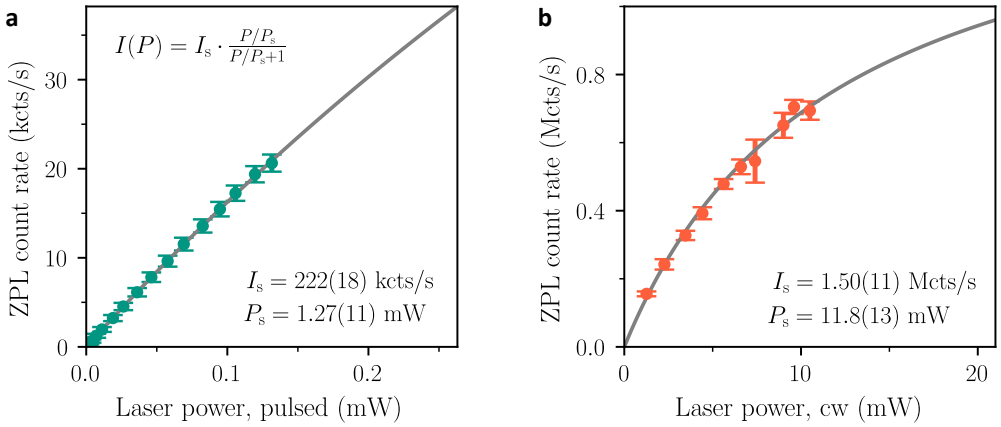

Figure 6.5: Saturation count rate of SnV 1. (a) Power-dependent ZPL count rate under pulsed off-resonant excitation, yielding a saturation count rate of $I_S^{\text{pulsed}} = 222(18)$ kcts/s and a saturation power of $P_S^{\text{pulsed}} = 1.27(11)$ mW. **(b)** Power-dependent ZPL count rate under cw off-resonant excitation, yielding a saturation count rate of $I_S^{\text{cw}} = 1.50(11)$ Mcts/s and a saturation power of $P_S^{\text{cw}} = 11.8(13)$ mW.

magnitude narrower than the cavity linewidth, the measured laser peak directly provides an estimate of the cavity's spectral resolution. The fact that the SnV peaks exhibit the same linewidth therefore implies that their intrinsic inhomogeneous broadening is significantly smaller than the cavity linewidth, ensuring substantial spectral overlap and enabling efficient Purcell enhancement.

The extracted linewidths are larger than the value obtained from a weak resonant laser-frequency scan of the cavity of 8(1) GHz. We attribute this difference to strong thermal cavity-length fluctuations present under off-resonant excitation, which broaden the apparent linewidth compared to the weakly driven resonant case.

6.2.3. Cavity-enhanced ZPL count rate

Saturation intensity for pulsed and cw excitation. We study the saturation behavior of *SnV 1*, the brightest detected emitter, by spatially tuning the cavity for maximum overlap and recording the ZPL count rate as a function of excitation power under both pulsed and cw off-resonant excitation at 532 nm (Fig. 6.5).

Both data sets follow the standard saturation model

$$I(P) = I_S \frac{P/P_S}{1 + P/P_S}, \tag{6.2.1}$$

where I_S is the saturation count rate and P_S the saturation power, defined via $I(P_S) = I_S/2$. For pulsed excitation at a repetition rate of $f_{\text{rep}} = 80$ MHz, we obtain $I_S^{\text{pulsed}} = 222(18)$ kcts/s and $P_S^{\text{pulsed}} = 1.27(11)$ mW. For cw excitation, the fit yields $I_S^{\text{cw}} = 1.50(11)$ Mcts/s and $P_S^{\text{cw}} = 11.8(13)$ mW.

The different saturation count rates follow directly from the maximal achievable emission rates in the two excitation schemes. In the cw case, the excitation rate can be made larger than the spontaneous decay rate, such that the emitter is repumped immediately after each emission event. The saturated count rate is then determined by the inverse excited-state lifetime τ_c and the overall detection efficiency η_{det}, yielding

$$I_{\mathrm{S}}^{\mathrm{cw}} = \eta_{\mathrm{det}}/\tau_c.$$

For pulsed excitation with a pulse duration much shorter than the excited-state lifetime, $t_{\mathrm{pulse}} \ll \tau_c$, at most one excitation can occur per laser pulse. In this case, the saturated count rate is given by

$$I_{\mathrm{S}}^{\mathrm{pulsed}} = \eta_{\mathrm{det}} f_{\mathrm{rep}},$$

where f_{rep} denotes the pulse repetition rate. The expected ratio of the two saturation count rates is therefore $I_{\mathrm{S}}^{\mathrm{pulsed}}/I_{\mathrm{S}}^{\mathrm{cw}} = f_{\mathrm{rep}}\tau_c \approx 0.17$ for the Purcell-enhanced lifetime $\tau_c \approx 2.1\,\mathrm{ns}$ (see Sec. 6.2.4), in good agreement with the experimentally observed ratio of $0.15(2)$.

The same reasoning explains the difference in saturation powers. Under cw excitation, saturation requires delivering one excitation per excited-state lifetime, whereas in the pulsed scheme one excitation per pulse suffices. The expected ratio is therefore $P_{\mathrm{S}}^{\mathrm{pulsed}}/P_{\mathrm{S}}^{\mathrm{cw}} = f_{\mathrm{rep}}\tau_c \approx 0.17$, in reasonable agreement with the measured value $0.11(2)$, noting that absolute power calibration and variations of the excitation spot contribute more strongly to the uncertainty in P_{S} than in the count-rate ratio.

Estimate of the overall detection efficiency. We take the pulsed saturation count rate $I_{\mathrm{S}}^{\mathrm{pulsed}} = 222(18)\,\mathrm{kcts/s}$ and compare it directly to the maximum possible detected count rate $I_{\mathrm{max}}^{\mathrm{pulsed}} = f_{\mathrm{rep}} = 80\,\mathrm{MHz}$, assuming unity end-to-end detection efficiency upon excitation.[34] Their ratio yields an experimental overall emitter-to-detector efficiency of $\eta_{\mathrm{det}} \approx 0.3\,\%$.

Several factors contribute to this efficiency. (i) For a cooperativity $C_0 \approx 1.8$ (see Sec. 6.2.4), the probability for emission of a ZPL photon into the cavity mode is $\beta_{C_0} = C_0/(1{+}C_0) \approx 0.64$. (ii) The fraction of cavity photons exiting into the free-space collection mode is given by the free-space cavity loss rate for an air-like mode, $\mathcal{L}_{\mathrm{M,d}}/n_d = 566\,\mathrm{ppm}/2.41 \approx 230\,\mathrm{ppm}$, relative to the total cavity losses $\mathcal{L}_{\mathrm{tot,a}} = 2\pi/\mathcal{F}_a \approx 1\,400\,\mathrm{ppm}$, yielding $\eta_{\mathrm{dir}} \approx 0.17$. (iii) The detection efficiency for a photon in the free-space collection path is given by the product of the detector quantum efficiency, $\eta_{\mathrm{SPCM}} \approx 0.75$, and the optical transmission to the detector. The latter includes losses from filters, lenses, and mirrors, as well as the focusing efficiency on the detector aperture. The overall optical detection efficiency of the free-space collection path was measured to be $\eta_{\mathrm{fs}} = 0.26$ (compare Appendix A.6).

Combining these contributions yields an expected emitter-to-detector efficiency of

$$\eta_{\mathrm{det}} = \beta_{C_0}\,\eta_{\mathrm{fs}}\,\eta_{\mathrm{dir}} \approx 1.7\,\%.$$

[34] An analogous estimate can be obtained from the cw saturation count rate by comparing to the maximum emission rate τ_{c}^{-1}.

Comparing this expected efficiency to the measured value reveals a remaining discrepancy of 0.3 %/1.7 % ≈ 1/6, which we attribute primarily to fast charge-state dynamics under off-resonant excitation. In this scenario, the SnV center spends most of the time in a dark charge state and only an effective fraction of order ∼ 18 % in the bright SnV^- state. This interpretation is consistent with the analysis of the Purcell enhancement, where no clear correlation between detected count rates and cooperativity is observed, indicating additional dynamics not captured by lifetime shortening alone, as discussed in the following section.

6.2.4. Purcell-effect of single SnV centers

We demonstrate Purcell-induced lifetime shortening of *SnV 1* and determine the cooperativity of the cavity–emitter system. We then compare all measured lifetimes for air-like and diamond-like cavity modes, highlighting the superior cooperativity achievable with diamond-like modes.

Lifetime shortening. To measure the lifetime shortening, the SnV center is excited using a pulsed off-resonant laser source, and the detected photons are histogrammed as a function of the delay time with respect to the laser pulses using time-correlated single-photon

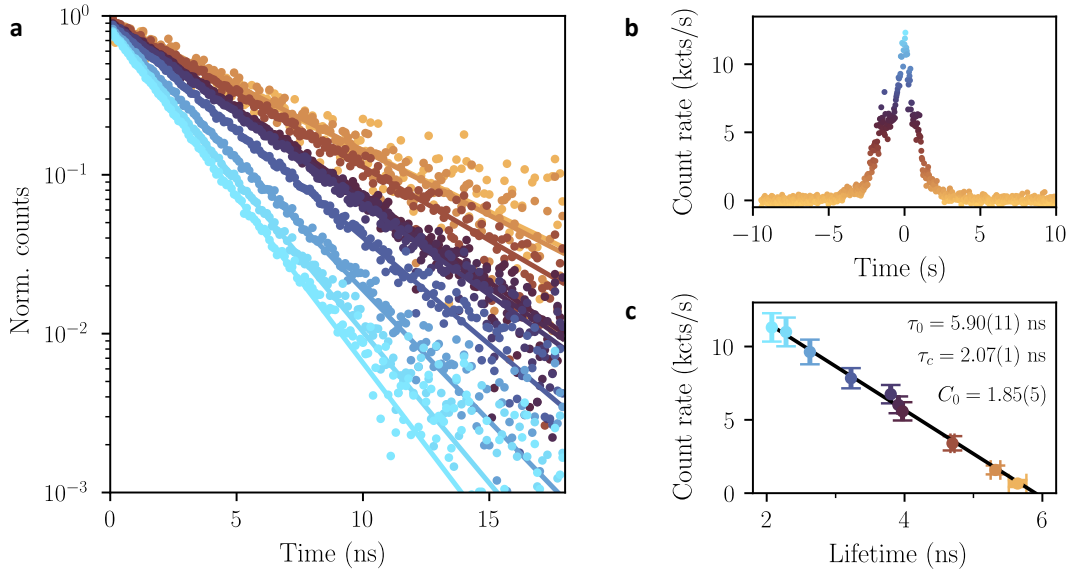

Figure 6.6: Lifetime shortening and Purcell factor. (a) TCSPC measurement of a cavity-coupled SnV center (*SnV 1*), showing a reduced lifetime when tuning the cavity and SnV ZPL into resonance (from brown to blue). **(b)** Corresponding SnV resonance as the cavity is tuned across the ZPL. The small bump on the left side arises from a polarization-split cavity mode. **(c)** Detected ZPL count rate plotted against the excited-state lifetime and fit by a linear model. From the fit we extract the free-space and cavity-enhanced lifetimes, from which the cooperativity $C_0^{\text{air}} = 1.85(5)$ is obtained.

counting (TCSPC). By acquiring histograms for different spectral cavity–emitter detunings, we extract the on- and off-resonance excited-state lifetimes, corresponding to the Purcell-enhanced and free-space decay, respectively. The decay curves are shown in Fig. 6.6a. As the cavity is tuned from far off-resonance (brown) to resonance (blue) with the SnV ZPL, the decay accelerates.

All histograms are background-corrected by subtracting a far-detuned reference trace (taken several cavity linewidths away), which removes background fluorescence and residual laser leakage that would otherwise introduce additional exponential components with different time constants. The corresponding SnV resonance as a function of cavity detuning is displayed in Fig. 6.6b.

The excited-state lifetime is obtained from a single-exponential fit to each histogram, while the corresponding count rate is determined by averaging the detected ZPL counts during the 60 s integration time. Figure 6.6c shows the detuning-dependent count rate plotted against the extracted lifetime. For pulsed excitation with a repetition period much longer than the excited-state lifetime, the detected count rate depends solely on the cavity collection efficiency for ZPL photons, which scales as

$$I(\tau_c) = I_0\,\beta_{C_0}(\tau_c) = I_0\frac{C_0(\tau_c)}{1+C_0(\tau_c)} = I_0\frac{\tau_0/\tau_c - 1}{\tau_0/\tau_c} = I_0\left(1-\frac{\tau_c}{\tau_0}\right), \tag{6.2.2}$$

where I_0 is the maximum count rate in the limit of infinite cooperativity C_0. A linear fit yields a free-space lifetime of $\tau_0 = 5.90(11)$ ns, a Purcell-reduced lifetime of $\tau_c = 2.07(1)$ ns, and a corresponding cooperativity of $C_0^{\mathrm{air}} = 1.85(5)$, where the superscript indicates that the emitter is located at a predominantly air-like lateral position. The larger uncertainty in the free-space lifetime arises from the extrapolation of the linear fit to zero count rate, whereas the uncertainty of the cavity-enhanced lifetime is determined solely by the monoexponential fit.

The linear relation between detected count rate and excited-state lifetime is valid for pulsed excitation with repetition periods much longer than the lifetime, or more generally for pulsed and cw excitation well below saturation. For completeness, we note that under saturated excitation the excitation rate becomes lifetime-dependent, and the count rate no longer scales linearly with the collection efficiency β_{C_0}.

Air-like and diamond-like cooperativity. In Sec. 5.2, we showed that a diamond-like hybrid cavity mode provides stronger light–matter coupling than an air-like mode, owing to the larger local electric field in the diamond-like configuration. This advantage holds as long as additional losses, such as scattering at the air–diamond interface, do not significantly degrade the diamond-like mode. Measured finesses confirm that the ratio of diamond-like to air-like finesses remains close to the designed values (Table 5.2). What remains is to verify that the cooperativity indeed reflects this expected advantage, which we do below.

We therefore measure the Purcell-enhanced lifetime shortening at lateral cavity positions exhibiting air-like and diamond-like mode characters, focusing on emitters for which

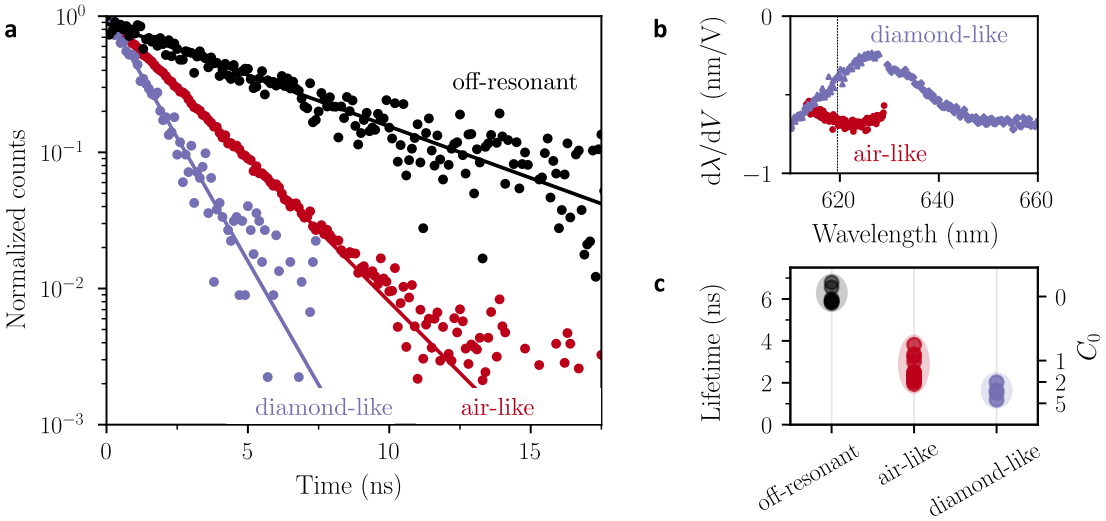

Figure 6.7: Lifetime shortening for air-like and diamond-like cavity modes. (a) Exemplary TCSPC decay curves recorded with the cavity tuned far off-resonance (black), for an SnV center near an air-like position (red), and near a diamond-like position (purple). The diamond-like mode yields the strongest lifetime reduction. **(b)** The mode character at the corresponding cavity positions is identified from the local cavity dispersion, extracted via the hybrid-mode slope. The purely diamond-like and air-like mode wavelengths are 627 nm and 623 nm, respectively, both within a few nanometers of the SnV ZPL at 619 nm. **(c)** Distribution of extracted lifetimes for all investigated SnV centers, grouped by dominant mode character. The off-resonant lifetime is obtained following the procedure of Fig. 6.6c. The secondary right axis indicates the corresponding cooperativity calculated using the average off-resonant lifetime $\tau_0 \approx 6.1$ ns.

the detected count rate was sufficiently high to enable reliable lifetime measurements, thereby preferentially selecting emitters with favorable cavity coupling. Representative TCSPC traces recorded at such positions are shown in Fig. 6.7a. Both the air-like (red) and diamond-like (purple) traces show clear lifetime reductions relative to the far-detuned decay (black). The air-like and off-resonant curves correspond to those presented in Fig. 6.6. The diamond-like decay is well described by a monoexponential fit, yielding a Purcell-enhanced lifetime of $\tau_c = 1.19(2)$ ns together with an off-resonant free-space lifetime of $\tau_0 = 5.85(30)$ ns, resulting in a cooperativity of $C_0^{\mathrm{dia}} = 3.9(3)$. The ratio between the two cooperativities, $C_0^{\mathrm{dia}}/C_0^{\mathrm{air}} = 2.09(16)$, is consistent with the relative diamond-like and air-like finesses $\mathcal{F}_{\mathrm{d}} = 4\,090$ and $2\,000$ (with diamond as a reference medium, see Table 5.2).

To confirm that the two lateral positions indeed correspond to predominantly air-like and diamond-like thicknesses, we perform cavity dispersion scans of the hybrid modes, similar to those in Fig. 5.11c,d. The slope of the fundamental cavity mode near the ZPL wavelength of 619 nm at both positions is shown in Fig. 6.7b. The air-like position shows its purely air-like mode (largest slope magnitude) at 623 nm, while the diamond-like position shows its purely diamond-like mode (smallest slope magnitude) at 627 nm. The air-like dispersion

was measured with a finer wavelength grid, which is why fewer points appear in the plot.

To show that the two example decays in Fig. 6.7a are representative, we compile all measured lifetimes and group them by dominant mode character, as shown in Fig. 6.7c. This classification uses finesse measurements as an indicator of mode character, as full dispersion scans are significantly more time-consuming. Accordingly, the air-like lifetimes correspond to finesses of $\mathcal{F}_\mathrm{a} = 4\,000–5\,000$, while the diamond-like lifetimes correspond to $\mathcal{F}_\mathrm{a} = 1\,700–2\,700$. A finesse measurement was not taken for every lifetime data point individually but for a representative position within the xy-scan range. Consequently, we do not attempt a point-by-point mapping between finesse and cooperativity here; such a study would require higher-accuracy finesse measurements and a larger dataset to reduce statistical scatter.

Nonetheless, the trend in Fig. 6.7c is clear: diamond-like mode characters yield substantially larger cooperativities, with $C_0^\mathrm{dia} \approx 2.0–4.1$, whereas air-like modes show $C_0^\mathrm{air} \approx 0.6–2.2$. Since full detuning-dependent lifetime scans were not performed for every emitter, we use the average off-resonant lifetime $\tau_0 \approx 6.1\,\mathrm{ns}$ as a reference for calculating this cooperativity range. Variations of the intrinsic lifetime between emitters are expected to be small compared to the observed Purcell-induced lifetime changes.

Monte–Carlo simulation of expected Purcell factors. We now compare the experimentally measured cooperativities, and the corresponding inferred Purcell factors, to the expected Purcell factors for air-like and diamond-like cavity modes. To this end, we employ two complementary Monte–Carlo approaches that rely on different experimentally accessible quantities. Using Eq. (3.2.13), $F_P \propto Q/V_\mathrm{eff}$, we determine the Purcell factor from the experimentally measured cavity linewidth together with a transfer-matrix–modeled cavity mode volume. Using Eq. (5.2.8), $F_P \propto \mathcal{F}_d/w_0^2$ with $\mathcal{F}_d = \mathcal{F}_a\,\mathcal{I}_{A/D}^{-1}$, we instead compute the Purcell factor from the measured cavity finesse and an estimate of the cavity mode waist.

For the first approach, calculating the cavity mode volume requires knowledge of the air gap thickness t_air, the diamond thickness t_d, and the cavity mode character. To avoid evaluating the full transfer-matrix model for every individual gap configuration, we calculate the mode volume once for an arbitrary pair of values $(t_\mathrm{air}, t_\mathrm{d})$ at both an air-like and a diamond-like mode. This allows us to extract the corresponding field penetration depths $t_\mathrm{pen}^\mathrm{air}$ and $t_\mathrm{pen}^\mathrm{dia}$, which are, to good approximation, independent of the longitudinal mode order and thus of the precise cavity geometry. From the transfer-matrix model, we obtain $t_\mathrm{pen}^\mathrm{air} = 0.70\,\mu\mathrm{m}$ and $t_\mathrm{pen}^\mathrm{dia} = 0.29\,\mu\mathrm{m}$. Using these results, the effective cavity length for arbitrary air and diamond gaps becomes

$$L_\mathrm{eff}^\mathrm{air} = t_\mathrm{d} + t_\mathrm{air} + t_\mathrm{pen}^\mathrm{air} \quad \text{(air-like)},$$

$$L_\mathrm{eff}^\mathrm{dia} = t_\mathrm{d} + \frac{t_\mathrm{air}}{n_d^2} + t_\mathrm{pen}^\mathrm{dia} \quad \text{(diamond-like)}.$$

The corresponding cavity mode volume is then approximated as $V_\mathrm{eff} = \pi w_0^2 L_\mathrm{eff}/4$.

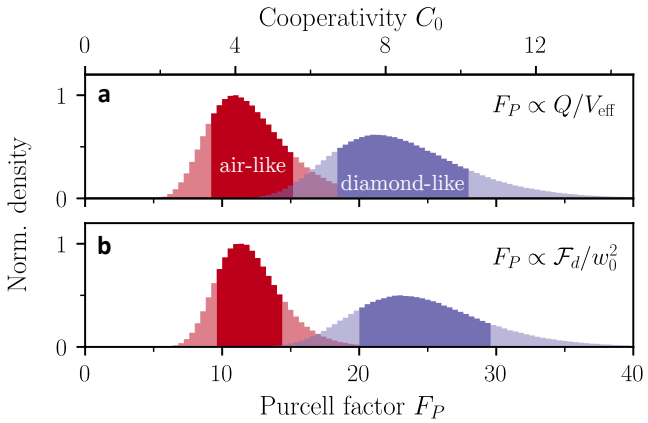

Figure 6.8: Monte–Carlo evaluation of expected Purcell factors. (a) Simulated Purcell-factor distributions obtained from the measured cavity linewidths and modeled cavity mode volumes using the relation $F_P \propto Q/V_{\text{eff}}$. **(b)** Corresponding distributions derived from the measured cavity finesses using $F_P \propto \mathcal{F}_\text{d}/w_0^2$, with $\mathcal{F}_\text{d} = \mathcal{F}_\text{a}\,\mathcal{I}_{A/D}^{-1}$. Both approaches yield consistent and overlapping distributions for air-like and diamond-like modes. The secondary horizontal axis indicates the corresponding cooperativity, $C_0 = \beta_\text{tot} F_P$ with $\beta_\text{tot} \approx 0.36$. Shaded regions denote the central 68% interval (one-sigma equivalent) of the simulated distributions. The underlying parameters and their uncertainties are summarized in Table 6.2.

The cavity linewidth is measured using a resonant laser scan. Specifically, we measure and average the linewidths of the first three longitudinal cavity modes above the contact mode at both an air-like and a diamond-like lateral position. This yields a typical air-like cavity linewidth of $\delta\nu_\text{cav}^\text{air} = 8.2(13)\,\text{GHz}$ and a diamond-like cavity linewidth of $\delta\nu_\text{cav}^\text{dia} = 7.5(6)\,\text{GHz}$. Inserting these values into the Purcell-factor expression and assuming a maximum polarization overlap of $\xi^2 = 2/3$ yields the distributions of expected Purcell factors shown in Fig. 6.8a. We obtain $F_P^\text{air} = 10.7^{+4.6}_{-1.4}$ ($C_0^\text{air} = 3.9^{+1.7}_{-0.5}$) and $F_P^\text{dia} = 21.6^{+6.4}_{-1.2}$ ($C_0^\text{dia} = 7.9^{+2.3}_{-1.2}$). The asymmetric uncertainties represent the central 68% interval (one-sigma equivalent) around the maximum-likelihood value of each simulated distribution.

For the second approach, based on the measured cavity finesse, we use the air- and diamond-like finesses $\mathcal{F}_\text{a}$ (air-referenced) of 4 830 and 1 700 respectively, as determined in Fig. 5.11. These values are converted into a diamond-referenced finesse $\mathcal{F}_\text{d}$ using the cavity mode character $\mathcal{I}_{A/D}^{-1}$. We assign a relative uncertainty of 10% to the measured finesse to account for experimental uncertainty and potential deviations from a purely air-like or purely diamond-like mode character. Using an expected cavity mode waist of $w_0 = 1.2(1)\,\mu\text{m}$ and inserting these values into Eq. (5.2.8) yields the Purcell-factor distributions shown in Fig. 6.8b. Notably, this independent approach yields Purcell-factor distributions that are numerically identical, within uncertainty, to those obtained from the linewidth-based method. The resulting values are $F_P^\text{air} = 10.7^{+4.6}_{-1.4}$ ($C_0^\text{air} = 3.9^{+1.7}_{-0.5}$) and

Table 6.2: Monte–Carlo input parameters for the Purcell-factor simulations. Summary of the parameters and associated uncertainties used in the two complementary Monte–Carlo approaches based on cavity linewidths and cavity finesses. Uniform distributions indicate parameters sampled within fixed bounds, while Gaussian distributions indicate normally distributed uncertainties.

Parameter	Symbol	Value / Range	Distribution
Shared parameter (both approaches)			
Mode waist	w_0	1.2(1) µm	Gaussian
Linewidth-based approach: $F_P \propto Q/V_{\mathrm{eff}}$			
Air gap thickness	t_{air}	1.0–2.0 µm	Uniform
Diamond thickness	t_{d}	1.3–2.0 µm	Uniform
Field penetration depth (air-like)	$t_{\mathrm{pen}}^{\mathrm{air}}$	0.70 µm	Fixed
Field penetration depth (diamond-like)	$t_{\mathrm{pen}}^{\mathrm{dia}}$	0.29 µm	Fixed
Cavity linewidth (air-like)	$\delta\nu_{\mathrm{cav}}^{\mathrm{air}}$	8.2(13) GHz	Gaussian
Cavity linewidth (diamond-like)	$\delta\nu_{\mathrm{cav}}^{\mathrm{dia}}$	7.5(6) GHz	Gaussian
Finesse-based approach: $F_P \propto \mathcal{F}_{\mathrm{d}}/w_0^2$			
Finesse (air-like, air-referenced)	$\mathcal{F}_{\mathrm{a}}^{\mathrm{air}}$	4830 ± 10%	Gaussian
Finesse (diamond-like, air-referenced)	$\mathcal{F}_{\mathrm{a}}^{\mathrm{dia}}$	1700 ± 10%	Gaussian
Mode character correction	$\mathcal{I}_{A/D}^{-1}$	$n_d = 2.41$	Fixed

$F_P^{\mathrm{dia}} = 21.6^{+6.4}_{-1.2}$ ($C_0^{\mathrm{dia}} = 7.9^{+2.3}_{-1.2}$)[35]. The parameters and associated uncertainties underlying both complementary Monte–Carlo approaches are summarized in Table 6.2.

We compare the experimentally measured air-like and diamond-like cooperativities, $C_0^{\mathrm{air}} = 1.85(5)$ and $C_0^{\mathrm{dia}} = 3.87(27)$ (Fig. 6.7a), to the expected values obtained from the Monte–Carlo simulation in Fig. 6.8. Both measured values are approximately a factor of two smaller than the predicted cooperativities and lie well outside the stated uncertainties. Several experimental effects that are not explicitly included in the Purcell-factor estimate can plausibly account for such a reduction; however, most of them are difficult to quantify precisely. The following contributions should therefore be regarded as order-of-magnitude estimates:

- **In-plane polarization mismatch.** While the out-of-plane dipole orientation is included via $\xi^2 = 2/3$, a polarization-split cavity mode introduces an additional reduction. In the ideal case, only one cavity eigenpolarization couples efficiently to the emitter; in the worst case, both couple equally, leading to up to a factor-of-two

[35] Note that these values differ slightly from those listed in Table 5.2, as the tabulated numbers are computed from nominal parameters without uncertainties. In contrast, the Monte–Carlo evaluation incorporates parameter uncertainties, and the nonlinearity of $F_P \propto \mathcal{F}_{\mathrm{d}}/w_0^2$ causes the maximum-likelihood value of the resulting distribution to shift toward slightly lower values.

reduction. The degree of polarization splitting can be inferred from the relative count rates obtained when tuning each polarization resonance across the ZPL (cf. Fig. 6.6).

- **Field–antinode mismatch.** If the SnV depth deviates from the designed field antinode position, for example due to implantation channeling, the local electric field strength is reduced, lowering the effective Purcell factor.
- **Lateral misalignment.** Even after optimizing the cavity position by maximizing fluorescence, a residual lateral misalignment between the emitter and the cavity mode is realistic. Such a misalignment reduces the local cavity field experienced by the emitter and can therefore lead to a reduced Purcell factor.
- **Cavity vibrations.** Mechanical vibrations with amplitudes on the order of 10 pm during the measurement are expected to reduce the Purcell factor by approximately 2% for diamond-like modes and up to 8% for air-like modes.
- **Spectral diffusion.** Spectral diffusion on the order of 1 GHz is expected under strong off-resonant excitation. A detuning jitter of about 10% of the cavity linewidth would, however, suppress the Purcell factor by less than 5%.

Taken together, the estimated polarization, spatial, and spectral misalignments can readily account for an overall reduction of the Purcell factor by approximately a factor of two. Nevertheless, it remains striking that none of the measured cooperativities—neither for air-like nor for diamond-like cavity modes—approach the predicted values. This raises the possibility that the effective branching ratio, quantum efficiency, or Debye–Waller factor of shallow SnV centers in a heavily damaged lattice may differ from commonly reported values, thereby reducing the achievable lifetime shortening.

6.3. Cooperative coupling of a single SnV center and a microcavity

In the previous section, we investigated the coupling of SnV centers to a tunable microcavity under off-resonant excitation. This enabled us to identify individual emitters in hyperspectral fluorescence maps and to evaluate their cavity coupling through saturation count rates and Purcell-induced lifetime shortening. Owing to the exceptionally low surface roughness of the diamond membranes, diamond-like cavity modes can be realized without introducing excessive scattering losses, enabling stronger light–matter interaction than for air-like modes. As a result, cooperativities in the range $C_0^{\mathrm{dia}} \approx 2.0$–$4.1$ are achieved. In this high-cooperativity regime, the SnV optical transition is expected to significantly modify the cavity transmission and reflection when probed with a weak resonant laser, as theoretically discussed in Sec. 3.2.5. The following section demonstrates these effects, including, to our knowledge, the first observation of an electron spin signature from cavity-coupled SnV centers.

6.3.1. Extinction signal in the cavity transmission profile

In contrast to the off-resonant measurements presented previously on sample AB2, the following results are obtained from sample CA1. Its higher spatial and spectral emitter density enables a faster resonant emitter search. Moreover, its excellent optical coherence as well as spectral and charge stability, characterized prior to cavity integration in a cryogenic confocal microscope (see Fig. 5.5), make it ideally suited for resonant cavity–emitter studies. Unless stated otherwise, the cryostat is operated in the 4 K mode, corresponding to a cavity temperature of $T_{\mathrm{cav}} \approx 4.5\,\mathrm{K}$.

Emitter search. To probe the coherent coupling between a SnV center and the cavity, we drive the cavity with a weak coherent field of 1–10 pW (before fiber coupling) and record the transmitted intensity on an SPCM while repeatedly scanning the laser frequency across the cavity resonance. We scan across the cavity resonance near the expected C-transition frequency, $f^0_{\mathrm{SnV}} = 484.134\,\mathrm{THz}$ (see Fig. 5.5), and identify SnV centers by extinction features, i.e. pronounced dips in the cavity transmission.

To avoid missing emitters that temporarily occupy a dark charge state, each scan is preceded by a 532 nm repump pulse with a duration of 10 ms and a power of 10 mW (before fiber coupling). To minimize spectral jumps following charge-state reinitialization, lower repump powers applied over longer durations are typically preferred. However, at this stage of the experiments, where the laser frequency is swept regardless, discrete spectral jumps after reinitialization are not critical. For this reason, comparatively high repump powers applied for short durations were used to maximally perturb the local charge configuration. The laser sweep spans approximately 25 GHz. Over multiple consecutive scans, the cavity resonance is positioned across the scanned frequency range to ensure full spectral coverage given the finite cavity linewidth (8–16 GHz). If the cavity exhibits significant polarization splitting—as is commonly observed when operated at a diamond-like lateral position—both polarization modes must be probed, since an emitter may couple predominantly to only one of them.

The same frequency scan range is used at multiple lateral positions within the piezo scan window ($10 \times 10\ \mu\mathrm{m}^2$). Subsequently, the laser scan range is shifted to screen the sample over a broader spectral window. If no emitter is observed within a 100–200 GHz band around the central frequency, the sample is coarsely repositioned using the cavity stepper motors.

Unless stated otherwise, all subsequent measurements were performed on a single emitter that exhibited the highest charge stability and the strongest extinction contrast. A comparison to additional emitters is provided in Appendix A.7. We attribute the overall difficulty in locating charge-stable and thus resonantly detectable SnV centers to the unfavorable charge environment experienced by shallow SnV centers (10–20 nm), likely introduced by the van der Waals bond and the nearby Bragg-mirror interface (see Sec. 6.3.2). Specifically, we detected approximately one extinction feature—and thus one

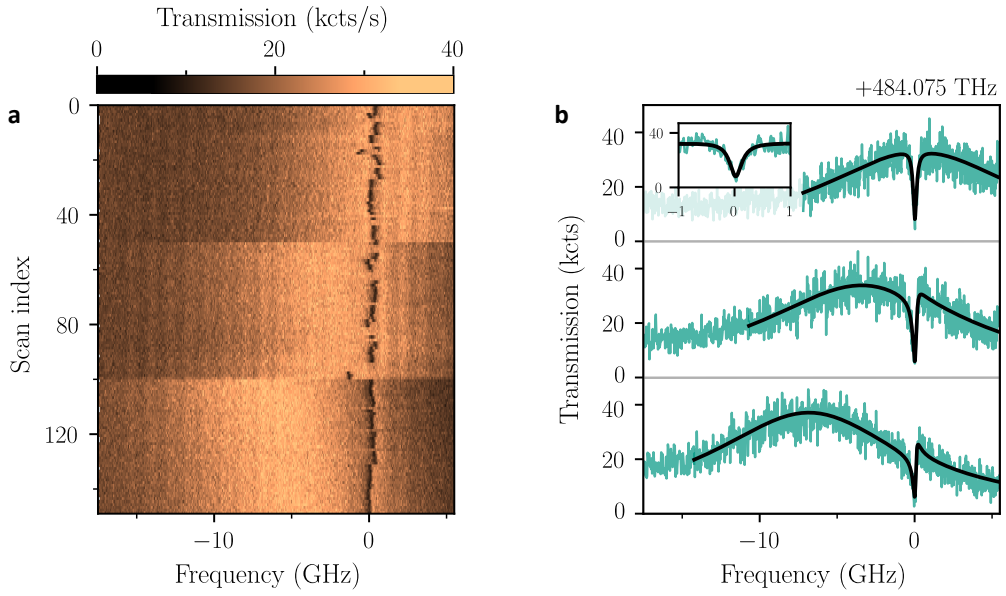

Figure 6.9: SnV-induced extinction in the cavity transmission profile. (a) Repeated laser-frequency scans across the cavity resonance showing an SnV-induced extinction feature at $f_{\mathrm{SnV}} \approx 484.075\,\mathrm{THz}$. The cavity is tuned to three different detunings with respect to the emitter, illustrating the on-resonance extinction as well as the asymmetric, Fano-like line shapes that occur under detuned conditions. Whenever the emitter switched into a dark charge state during acquisition, a manual repump pulse was applied to recover the optical transition. **(b)** Three representative background-corrected transmission traces corresponding to the detunings shown in (a). The black lines are fits to the response of the coupled emitter–cavity system, as discussed in the text. The inset shows a zoom into the resonance.

spectrally stable SnV center—per two to three lateral scan ranges over a spectral window of 100–200 GHz. This corresponds to a combined spectral and spatial density of $\rho_{\mathrm{SnV}}^{\mathrm{cav}} \approx (10^{-5}\text{–}10^{-4})\,\mathrm{GHz}^{-1}\,\mu\mathrm{m}^{-2}$, which is significantly lower than the density obtained prior to cavity integration, $\rho_{\mathrm{SnV}}^{\mathrm{conf}} \approx 10^{-2}\,\mathrm{GHz}^{-1}\,\mu\mathrm{m}^{-2}$.

Extinction signal and Fano resonances. A transmission scan in the vicinity of a SnV transition at $f_{\mathrm{SnV}} \approx 484.075\,\mathrm{THz}$ ($\lambda_{\mathrm{SnV}} \approx 619.31\,\mathrm{nm}$) is shown in Fig. 6.9a. The laser power before fiber coupling was set to $P_{\mathrm{laser}} \approx 4\,\mathrm{pW}$, resulting in approximately 30 kcts/s of transmitted and detected photons at the center of the cavity resonance (see Appendix A.6 for further details on the transmission and detection properties). During each frequency sweep, the laser power exhibits a drift and oscillation of roughly 20%. To compensate for this, we normalize the detected count rate by the continuously monitored laser power and rescale it to match the count level at the center of the scan. The frequency scan rate of the measurement is $10\,\mathrm{GHz\,s}^{-1}$, corresponding to a line acquisition time of approximately 2.5 s. Only the forward portion of the sawtooth frequency sweep is shown; the mirrored backward scan is omitted for clarity but is included in the evaluation of the cQED parameters extracted from the fit. On resonance, the SnV transition produces an extinction feature

with a contrast of about 80%, which is clearly visible in the transmission trace at the cavity resonance. Whenever the emitter switched into a dark charge state during acquisition, a repump pulse was manually applied at the beginning of the subsequent trace to recover the optical transition.

Three exemplary traces for approximately zero and two increasing cavity–emitter detunings are shown in Fig. 6.9b, illustrating the on-resonance extinction feature as well as the asymmetric, Fano-like line shapes that emerge under detuned conditions. This Fano response arises from the coherent interference between the narrow emitter-induced contribution and the broader cavity transmission channel. When the emitter is detuned from the cavity resonance, their relative phase leads to the characteristic asymmetric interference profile.

Fitting of the cQED parameters. Each individual time trace exhibiting an extinction feature is fitted according to Eqs. (3.2.15a), (3.2.17a), and (3.2.18). To accurately capture the full detected signal, the model includes the nearby orthogonally polarized cavity mode. This mode is frequency-split by $\Delta\nu_{\mathrm{pol}} \approx -38\,\mathrm{GHz}$, corresponding to a mode located on the low-frequency side of the main cavity resonance, and has an amplitude $A_{\mathrm{pol}} \approx 0.7\,A$, where A is the amplitude of the main cavity mode. Because the second mode is sufficiently close in frequency, its Lorentzian tail produces a small but frequency-dependent background $I_{\mathrm{bg,pol}}(\omega_l)$, which must be included in the fit to extract the true extinction contrast and cooperativity. In addition, detector background is taken into account by including a constant background level of $I_{\mathrm{bg,det}} = 500\,\mathrm{cts/s}$.[36]

The full fit function for the detected intensity is

$$I(\omega_l;\,\Theta) = I_{\mathrm{cQED}}(\omega_l;\,\Theta) + I_{\mathrm{bg,pol}}(\omega_l) + I_{\mathrm{bg,dc}}, \tag{6.3.1}$$

where $\Theta = \{A,\, g,\, \kappa,\, \gamma_{\mathrm{tot}},\, \omega_c,\, \omega_a\}$ collects all parameters varied in the fit.

The cavity-QED contribution is

$$I_{\mathrm{cQED}}(\omega_l) = A\,\frac{(\kappa/2)^2}{\left|\left(\frac{\kappa}{2} - i(\omega_l - \omega_c)\right) + \frac{g^2}{\left(\frac{\gamma_{\mathrm{tot}}}{2} - i(\omega_l - \omega_a)\right)}\right|^2}, \tag{6.3.2}$$

and the background from the orthogonal polarization mode is

$$I_{\mathrm{bg,pol}}(\omega_l) = A_{\mathrm{pol}}\,\frac{(\kappa/2)^2}{(\kappa/2)^2 + \left(\omega_l - \omega_c + \Delta\omega_{\mathrm{pol}}\right)^2}, \tag{6.3.3}$$

with fixed values of A_{pol} and $\Delta\omega_{\mathrm{pol}}$ determined independently and not varied during the fit. The constant offset $I_{\mathrm{bg,dc}}$ accounts for detector dark counts.

[36] The detector background comprises contributions from intrinsic dark counts (200 cts/s) and residual ambient illumination (300 cts/s).

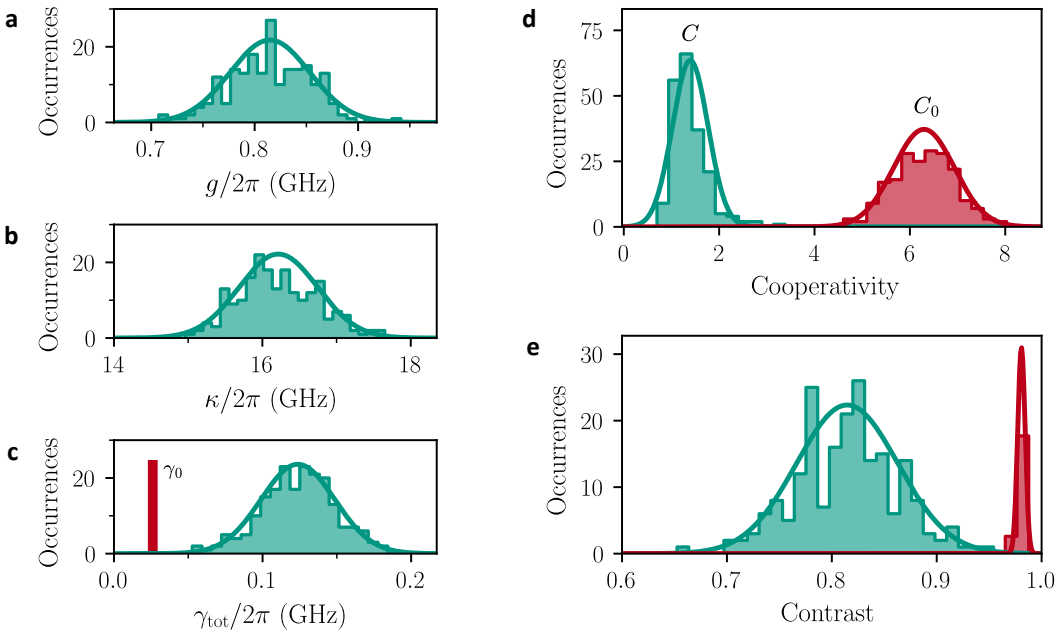

Figure 6.10: Distribution of the fitted cQED parameters. (a–c) Histograms of the fitted coupling rate g, cavity linewidth κ, and emitter linewidth γ_{tot}, together with Gaussian fits used to extract the mean and standard deviation of each distribution. The vertical red bar in (c) marks the transform-limited emitter linewidth $\gamma_0/2\pi \approx 26$ MHz. **(d)** Measured coherent cooperativity C (teal) and the corresponding ideal cooperativity C_0 obtained by replacing the dephased linewidth γ_{tot} with the transform-limited value γ_0 (red). **(e)** Inferred resonant extinction contrast (teal) and the ideal contrast expected for a transform-limited emitter (red; rescaled by a factor of 1/10 for visibility). All distributions are derived from individual fits to single-scan extinction spectra, with a sample size of $N = 203$.

Although the contribution of the second cavity mode at the center of the main extinction feature is only on the order of 2.5%, its Lorentzian tail becomes significant at detunings of several cavity linewidths. To avoid bias from imperfect knowledge of $\Delta\omega_{pol}$ or A_{pol}, the fit window on the side facing the second mode is therefore restricted to approximately one cavity FWHM, as indicated in Fig. 6.9b. This ensures that the fitting routine remains dominated by the true cQED resonance while still accounting for the slowly varying background from the orthogonal polarization mode.

We note that the contribution of this orthogonally polarized mode could, in principle, be reduced by optimizing the excitation and collection polarizations. In the present measurement series, however, such polarization filtering was not applied, resulting in weak but systematic residual coupling of the second mode into the detection path, which must therefore be included in both the model and the choice of fit window.

The 300 recorded line scans (50 for each of the three cavity detunings, in both scan directions) were first pre-screened using a peak-finding routine to detect the presence

of an extinction feature within the broader cavity resonance. Each candidate trace was subsequently inspected manually to ensure that the fit returned a reliable result; traces were discarded if the extinction feature jumped during the scan or if the peak-finding algorithm identified a peak not corresponding to an extinction feature. The distributions of the relevant fit parameters (g, κ, γ_{tot}) obtained from the remaining 203 successful fits are shown in Fig. 6.10a–c, along with Gaussian fits used to extract mean values and standard deviations. The resulting cQED parameter set is

$$\{g, \kappa, \gamma_{\mathrm{tot}}\}/2\pi = \{0.81(4),\ 16.2(5),\ 0.12(2)\}\ \mathrm{GHz}. \tag{6.3.4}$$

Two noteworthy observations arise from this analysis. (i) The measured cavity linewidth is approximately a factor of two larger than the value extracted in Sec. 6.2.4, $\delta\nu_{\mathrm{cav}}^{\mathrm{dia}} = 7.5(6)\,\mathrm{GHz}$. This broadening is consistent with a locally reduced cavity finesse at the diamond-like position, $\mathcal{F}_{\mathrm{a}} \approx 1200$, compared to the typical $\mathcal{F}_{\mathrm{a}} \approx 1700$. The reduced finesse is presumably caused by increased scattering losses, either due to enhanced surface roughness or the adsorption of scattering particles.[37] The measured cavity length noise of $\sigma_z \approx 13\,\mathrm{pm}$ contributes negligibly to the linewidth: this corresponds to only about 5 % of the cavity FWHM at the given finesse and results in merely a 1–2 % increase of the measured Voigt linewidth.

(ii) The extracted homogeneous linewidth is significantly larger than the transform-limited value of $\gamma_0/2\pi \approx 26\,\mathrm{MHz}$ (red marker in Fig. 6.10c), obtained from the far-detuned lifetime $\tau_0 \approx 6.1\,\mathrm{ns}$ (see Fig. 6.7c). We attribute the increased linewidth primarily to the shallow implantation depth of the emitters, which places them in close proximity to the surface and therefore in a noisy charge environment. Fast charge fluctuations in this region lead to rapid spectral diffusion of the zero-phonon line on the comparatively slow timescale of the probing of the transition (tens of milliseconds), resulting in an effectively broadened homogeneous line. Although locally elevated temperatures at the sample position cannot be entirely ruled out, we consider it unlikely: phonon broadening at the observed level would require temperatures above 10 K, far higher than the measured $T_{\mathrm{cav}} \approx 4.5\,\mathrm{K}$. Moreover, we observe transform-limited extinction features from other emitters in sample AB2 under similar experimental conditions (see Appendix A.7), which would be incompatible with a systematically elevated local temperature. We therefore attribute the excess linewidth mainly to fast charge-noise–induced spectral diffusion affecting these particular shallow emitters.

Even under the unfavourable conditions of increased cavity decay and emitter dephasing, we extract a coherent cooperativity of

$$C = \frac{4g^2}{\kappa\gamma_{\mathrm{tot}}} = \frac{4g^2}{\kappa(\gamma_0 + 2\gamma^\star)} = 1.4(4), \tag{6.3.5}$$

[37] These measurements were taken after several weeks of cryostat operation, during which significant water adsorption on the sample surface may have increased scattering losses.

corresponding to an on-resonant extinction contrast (see Eq. (3.2.21b)) of

$$C = 1 - \frac{1}{(C+1)^2} = 0.81(5). \tag{6.3.6}$$

Assuming a transform-limited emitter ($\gamma^\star = 0 \Rightarrow \gamma_{\mathrm{tot}} = \gamma_0$), the ideal cooperativity would be $C_0 = 6.3(6)$, yielding an extinction contrast of $C = 0.981(4)$. This ideal cooperativity can, in principle, be accessed directly via lifetime measurements, since it determines the Purcell enhancement through $\tau_0/\tau_c - 1 = C_0$.

In the present experiment, however, we were unable to obtain a reliable lifetime measurement. The resonant emitters did not exhibit sufficient count rate under pulsed off-resonant excitation to produce a clear zero-phonon-line signal. We attribute this to an unfavourable charge environment that drives the SnV centers predominantly into a dark charge state under such excitation conditions. In fact, we did not observe a single usable lifetime trace in sample CA1; the available count rates were substantially lower than in sample AB2, where the emitters were implanted approximately twice as deep, consistent with a more stable charge environment.

6.3.2. Charge stability

To assess charge stability under resonant probing, we perform cavity transmission scans at different probe powers, shown in Fig. 6.11a. The probe power is parameterized by the detected peak cavity transmission count rate A, extracted from fits using Eq. (6.3.1). The corresponding incident laser power before fiber coupling is related to this count rate via the calibration $P/A \approx 0.1\,\mathrm{pW/(kcts/s)}$.

With increasing probe power, we observe a pronounced reduction in charge stability, accompanied by enhanced spectral diffusion. To quantify this behavior, we extract the cooperativity and emitter linewidth from fits to individual frequency scans; the results are shown in Fig. 6.11b,c. While the cooperativity decreases slightly with increasing probe power, this trend can be attributed to a broadening of the emitter linewidth, consistent with power-induced spectral diffusion. The onset of this behavior occurs above a threshold peak cavity transmission rate of $A_{\mathrm{thresh}} \approx 30\text{–}40\,\mathrm{kcts/s}$.

We do not observe signatures of saturation-induced contrast reduction. This is consistent with the applied probe power levels. For the largest probe power used in the measurements shown, corresponding to a detected peak transmission rate of $A_{\mathrm{max}} = 168\,\mathrm{kcts/s}$, we estimate an input photon number per Purcell-enhanced lifetime of $n_{\mathrm{in}} \approx 0.003$ (see Eq. (A.6.2) in Appendix A.6). This value is far below the critical photon number $n_{\mathrm{crit}} \approx 0.43$ for the measured cooperativity $C = 1.4(4)$, corresponding to a saturation parameter $s = n_{\mathrm{in}}/n_{\mathrm{crit}} \approx 8 \times 10^{-3}$. We therefore conclude that the observed power-dependent behavior is not influenced by optical saturation.

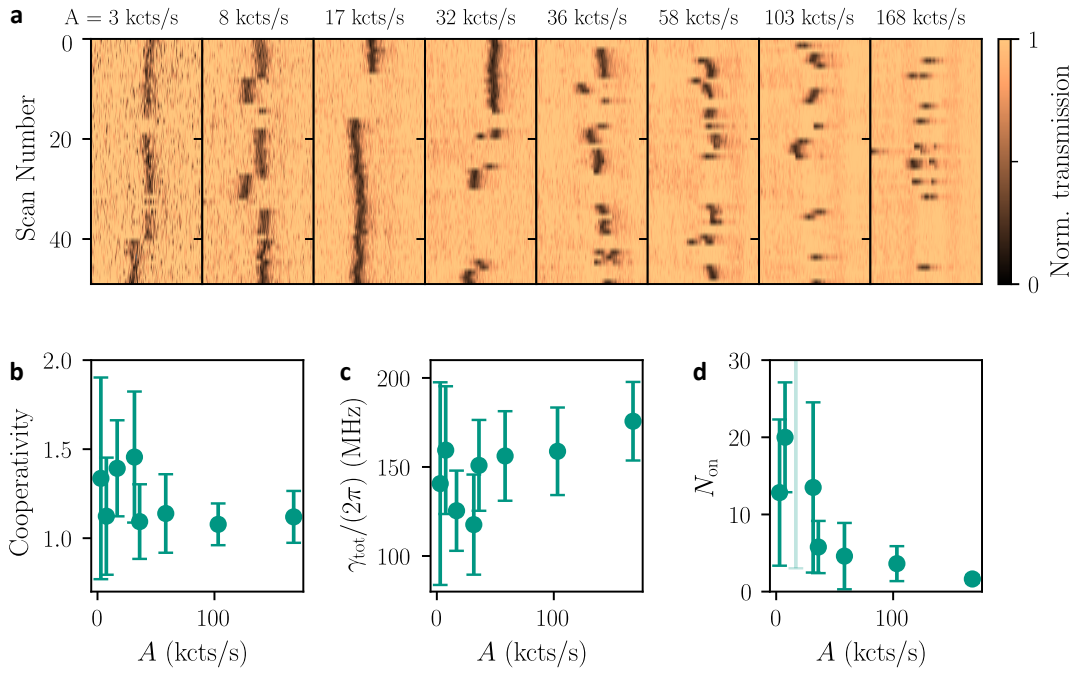

Figure 6.11: Power-dependent extinction properties. **(a)** Transmission scans acquired at increasing probe powers, parameterized by the detected peak cavity transmission count rate, revealing a progressive reduction in charge stability. **(b,c)** Extracted cooperativity and emitter linewidth as a function of the detected peak cavity transmission, showing a slight decrease in cooperativity attributable to power-induced spectral diffusion. **(d)** Average number of consecutive scans for which the SnV center remains in the bright state before switching dark.

The transition to charge instability at A_{thresh} is also reflected in Fig. 6.11d, which shows the average number N_{on} of consecutive scans during which the emitter remains in the bright charge state before switching dark. A clear reduction in N_{on} is observed beyond this threshold.[38] The data point at $A = 17\,\text{kcts/s}$ is shown transparently due to a large uncertainty arising from a statistical outlier within the limited number of recorded scans. A complementary perspective on this behavior is provided by the photon-budget analysis presented in Appendix A.8, which shows that once charge instability is reached, the transition to the dark charge state occurs after an approximately constant number of scattered photons of $N_{\text{ext}} \approx 6 \times 10^4$.

The threshold $A_{\text{thresh}} \approx 30\text{–}40\,\text{kcts/s}$ can be conveniently expressed in terms of the saturation parameter. The onset of charge instability during resonant cavity scans corresponds to $s \approx 1.6 \times 10^{-3}$, defined with respect to the Purcell-enhanced lifetime and the measured cooperativity. By comparison, confocal microscopy experiments on shallowly implanted SnV centers (20 nm) can operate under charge-stable conditions for

[38] Only one scan direction is shown, such that the plotted values are approximately twice those apparent in Fig. 6.11a.

hours during photoluminescence-excitation scans at saturation parameters as large as $s \approx 2 \times 10^{-2}$ [126].

As discussed in Sec. 2.2.2, the charge stability of shallow color centers depends sensitively on the near-surface electrostatics and the local defect environment, which can differ substantially between cavity-integrated and confocal geometries and likely underlie the observed difference in charge-stability thresholds. In the cavity-integrated geometry, bonding the diamond membrane to a dielectric Bragg mirror stack may modify the near-surface Fermi level and electrostatic landscape compared to a diamond–air interface, which could contribute to the reduced charge stability observed here. This interpretation is further supported by cryogenic photoluminescence-excitation measurements performed prior to bonding (Sec. 5.1.3), which demonstrated excellent charge stability for all investigated SnV centers.

In several cQED and nanophotonic implementations of diamond color centers, such interface-related effects are commonly mitigated by employing deeper implantation depths, typically in the range of 50–150 nm, which reduces the direct influence of the surface environment while maintaining efficient optical coupling [58, 61, 59]. Accordingly, pursuing deeper implantation depths instead of shallow SnV centers constitutes a natural next step for the present platform.

6.3.3. Zeeman splitting

A crucial step towards an efficient spin–photon interface is the magnetic lifting of the degeneracy between the $m_s = \pm 1/2$ spin sublevels, such that the single extinction feature in the cavity transmission profile is split into two non-degenerate, optically addressable transitions (cf. Eq. (4.4.1)). This splitting enables spin-selective transmission or reflection of individual photons. To this end, we employ the superconducting magnetic field coil described in Sec. 4.4 and record cavity transmission scans of the previously discussed SnV center for variable coil currents $I_{\mathrm{coil}} = 0\text{–}9\,\mathrm{A}$. The maximum current is limited by quenching of the superconductivity, which occurs at $I_{\mathrm{coil}} \approx 9.3\,\mathrm{A}$.

Figures 6.12a,b show two exemplary single-scan cavity transmission traces recorded at a cavity temperature of $T_{\mathrm{cav}} \approx 4.5\,\mathrm{K}$, without ($I_{\mathrm{coil}} = 0\,\mathrm{A}$) and with ($I_{\mathrm{coil}} = 9\,\mathrm{A}$) an applied magnetic field. Upon applying the magnetic field, we observe a pronounced broadening of the extinction feature together with a reduction in contrast, without a clear resolution of two distinct dips within a single scan.

Zeeman splitting determined via averaged transmission scans. To improve the signal quality, in particular for the broadened and reduced-contrast traces, we average over multiple individual scans. For this purpose, each scan is fitted with a single extinction feature (Eq. (6.3.1)). The extracted emitter resonance frequency ω_a is then used to align the scans in frequency prior to summation. The resulting averaged transmission spectra

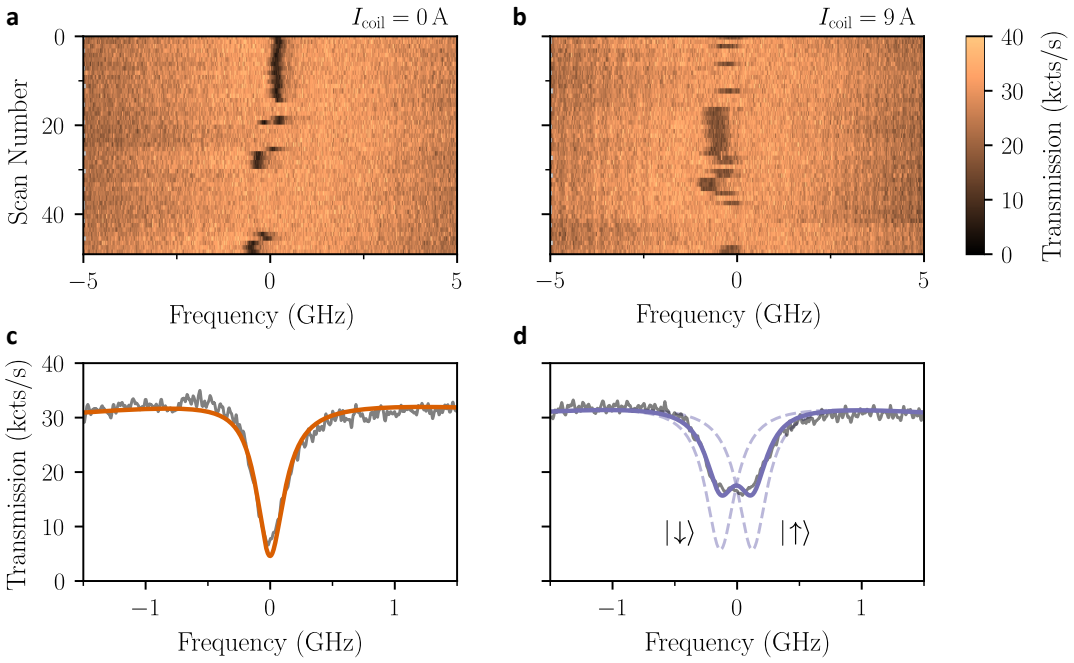

Figure 6.12: Cavity extinction with and without magnetic field. (a,b) Single-scan cavity transmission traces recorded without ($I_{coil} = 0$ A) and with ($I_{coil} = 9$ A) an applied magnetic field. **(c,d)** Corresponding averaged transmission spectra, obtained after aligning individual scans in frequency with respect to the emitter resonance. At zero field, the data exhibit a single extinction dip well described by a single-emitter cQED fit. At finite field, two spin-resolved extinction features contribute to the averaged spectrum, resulting in a double-dip response. The solid line shows the averaged cQED fit, while dashed curves indicate the individual spin-resolved contributions. The extracted effective splitting is $\Delta\nu_{spin}(I_{coil} = 9\,\text{A}) \approx 260$ MHz.

without and with magnetic field are shown in Figs. 6.12c,d. The zero-field data are well described by a single-emitter cavity-QED model, while the finite-field spectrum is captured by the averaged response of two emitter transitions split by an effective Zeeman splitting $\Delta\nu_{spin}$. From this analysis, we extract $\Delta\nu_{spin}(I_{coil} = 9\,\text{A}) \approx 260$ MHz.

The alignment procedure is not fully robust. The extinction features observed in single scans are typically asymmetric and not perfectly centered, which can lead to systematic errors in determining the zero-field emitter resonance frequency. In addition, slow drifts of the cavity resonance can give rise to asymmetric (Fano-like) line shapes, such that the averaged transmission spectrum reflects contributions from a distribution of emitter–cavity detunings. Consequently, neither the single-dip nor the split-dip model perfectly reproduces the averaged data.

The finite-field averaged trace comprises contributions from two spin-selective transitions that can only be resolved if the system is probed on timescales shorter than the electron spin relaxation time T_1, and if the number of scattered photons remains below the cyclicity of the transition to prevent spin initialization into the opposite state. While the relevant

timescales cannot be determined precisely without detailed knowledge of the local strain, temperature, and off-axis magnetic field at the emitter, the observed linewidth broadening and contrast reduction within a single scan (lasting a few tens of milliseconds) indicate that one or both of these processes occur on comparable or faster timescales. To illustrate the individual spin-resolved contributions, we plot both components separately together with the averaged fit in Fig. 6.12d, thereby indicating their full contrast. A detailed discussion of the relative contrast between the two spin contributions, as relevant for single-shot spin-state readout, is provided in Sec. 6.4.

Zeeman splitting inferred from effective linewidth broadening. A more robust determination of the Zeeman splitting is obtained by analyzing the statistics of single-resonance cQED fit parameters extracted from transmission scans recorded at different magnetic fields, following the procedure described in Sec. 6.3.1. For each coil current setting, we acquire 100 individual transmission traces and fit each trace with Eq. (6.3.1). Exemplary fits for $I_{\mathrm{coil}} = 0\,\mathrm{A}$ and $I_{\mathrm{coil}} = 9\,\mathrm{A}$ are shown in Fig. 6.13a, where a clear linewidth broadening and contrast reduction are observed at finite magnetic field.

For each current, the fitted linewidth γ_{fit} and extinction contrast $1-1/(C+1)^2$ are evaluated for all traces, and the corresponding mean values and standard deviations are extracted. These quantities are plotted as a function of coil current in Fig. 6.13b. With increasing magnetic field, the linewidth increases from $\gamma_{\mathrm{fit}}(I_{\mathrm{coil}} = 0\,\mathrm{A}) = \gamma_{\mathrm{tot}} \approx 120\,\mathrm{MHz}$ to $\gamma_{\mathrm{fit}}(I_{\mathrm{coil}} = 9\,\mathrm{A}) \approx 320\,\mathrm{MHz}$, while the extinction contrast decreases from 0.82 to 0.54.

The fitted linewidth provides a meaningful estimate only as long as the underlying splitting remains small compared to the intrinsic emitter linewidth γ_{tot}, in which case $\gamma_{\mathrm{fit}}^2 \approx \gamma_{\mathrm{tot}}^2 + (2\pi\Delta\nu_{\mathrm{spin}})^2$. Once the splitting becomes comparable to or larger than γ_{tot}, the single-dip fit no longer yields a reliable linewidth and cannot be directly used to infer the splitting.

To account for this effect, we model the extinction spectrum using the cQED parameters determined in Sec. 6.3.1 and introduce a controlled splitting $\Delta\nu_{\mathrm{spin}}$ by averaging over two spin-resolved contributions. Each modeled spectrum is then fitted with a single extinction feature, and the resulting fitted linewidth is extracted, as illustrated in the inset of Fig. 6.13c. The resulting relation between the fitted linewidth and the true splitting (Fig. 6.13c) is used to correct the experimentally measured linewidths and extract the Zeeman splitting as a function of coil current, shown in Fig. 6.13d. A linear fit yields a slope

$$\Delta\nu_{\mathrm{spin}}/I_{\mathrm{coil}} = 29.2(18)\,\mathrm{MHz\,A^{-1}}.$$

At a coil current of $I_{\mathrm{coil}} = 9\,\mathrm{A}$, the inferred splitting $\Delta\nu_{\mathrm{spin}} = 263(16)\,\mathrm{MHz}$ is in good agreement with the estimate obtained from the averaged double-extinction fit in Fig. 6.12d.

In Sec. 4.4, we estimated a magnetic field range of $B_z = 0.09$–$0.19\,\mathrm{T}$ at the sample position for a coil current of $I_{\mathrm{coil}} = 10\,\mathrm{A}$, arising from uncertainty in the coil–sample distance. For an unstrained SnV center, this field corresponds to an expected optical Zeeman splitting of $\Delta_{\mathrm{opt}}(I_{\mathrm{coil}} = 10\,\mathrm{A}) = 320$–$670\,\mathrm{MHz}$. Scaling this estimate to $I_{\mathrm{coil}} = 9\,\mathrm{A}$

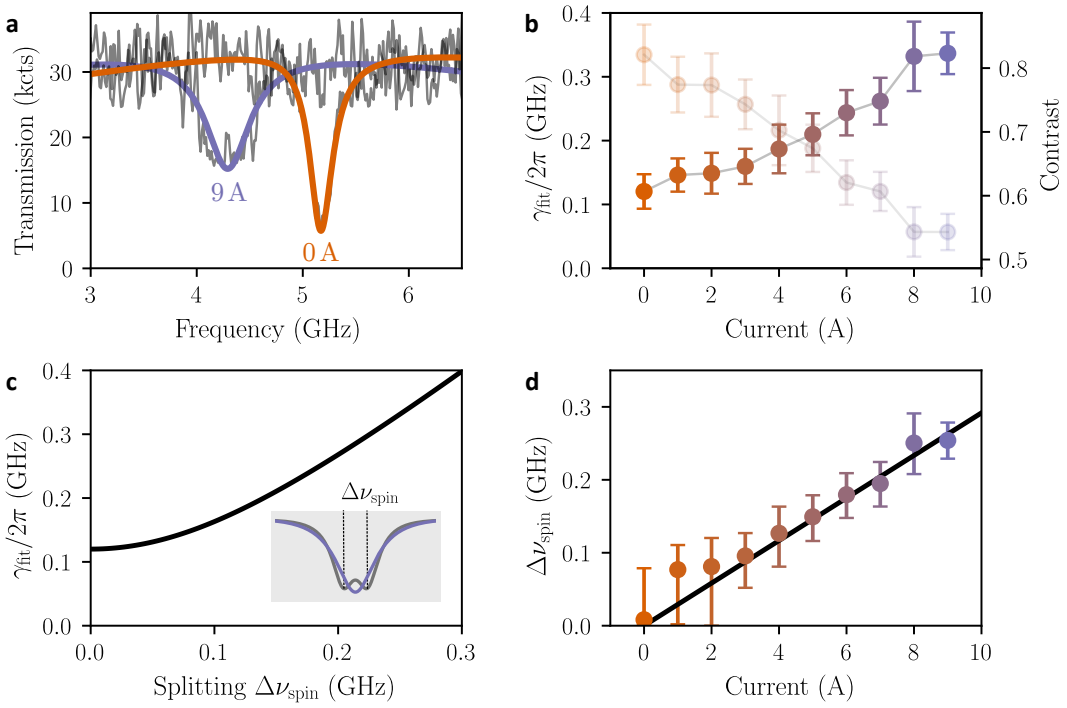

Figure 6.13: Evaluation of the Zeeman splitting. **(a)** Exemplary cavity transmission scans recorded without ($I_{\mathrm{coil}} = 0$ A) and with ($I_{\mathrm{coil}} = 9$ A) an applied magnetic field, together with single-dip cQED fits. **(b)** Extracted effective linewidth γ_{fit} (left axis) and extinction contrast (right axis) as a function of coil current. **(c)** Modeled effective single-dip linewidth γ_{fit} as a function of the underlying splitting $\Delta\nu_{\mathrm{spin}}$ for a zero-field linewidth $\gamma_{\mathrm{tot}} = 120$ MHz (inset). **(d)** Extracted Zeeman splitting $\Delta\nu_{\mathrm{spin}}$ as a function of coil current.

yields $\Delta_{\mathrm{opt}}(I_{\mathrm{coil}} = 9\,\mathrm{A}) = 290\text{–}600$ MHz, exceeding the experimentally measured value $\Delta\nu_{\mathrm{spin}} = 263(16)$ MHz.

To account for this discrepancy, we use the Hamiltonian derived in Ref. [97] to estimate the ground-state strain amplitude Υ_g required to reproduce the observed splitting within the estimated magnetic field range. In this model, the effective optical splitting between the two spin-orientation–resolved optical transitions depends on the local strain and is sensitive to the angular orientation between the applied magnetic field and the SnV symmetry axis, which can lead to reduced splittings for certain field orientations. Assuming an angle of 54.7° between the magnetic field and the SnV symmetry axis, we infer a ground-state strain amplitude of $\Upsilon_g = 110\text{–}250$ GHz.

For the same reasons that prevented a reliable measurement of the emitter lifetime, we were also unable to directly measure the ground-state splitting of the investigated SnV center. Nevertheless, the observed shift of the SnV transition frequency relative to the ideal unstrained value $f^0_{\mathrm{SnV}} = 484.134$ THz [111] by 59 GHz indicates a moderately strained

SnV center. This observation is consistent with the inferred ground-state strain amplitude and with the pronounced strain-induced polarization splitting of the cavity mode.

6.4. Spin-selective cavity transmission: analysis and outlook

We now evaluate the performance of the demonstrated cavity-based system as a potential spin–photon interface and discuss realistic routes for improvement. We first consider the experimental configuration employed in the preceding measurements, in which fiber-coupled photons probe the SnV electron spin via cavity transmission and are detected in the free-space output channel. Alternative readout and routing schemes are discussed subsequently.

The performance of such a spin–photon interface is primarily characterized by two quantities: the bare cavity transmission probability $\mathcal{P}_t$, which determines the probability for an incident fiber-coupled photon to be transmitted through the cavity and thus directly impacts the achievable entanglement rate, and the spin-dependent transmission contrast C_{spin}, which limits the fidelity of the generated spin–photon entangled state.

Current limitations. In the present configuration, we determine a transmission probability of

$$\mathcal{P}_t = \eta_{\text{mm}} T_{\text{c,max}} \approx 0.035 \times 0.12 = 0.0042,$$

which is primarily limited by non-optimized spatial mode matching as well as cavity asymmetry and residual intracavity losses. A detailed breakdown of the individual contributions is provided in Appendix A.6.

The achievable on-resonance spin contrast C_{spin} depends on the coherent cooperativity and on the spectral separation of the two spin-selective optical transitions. Consistent with the transmission contrast definition $C = (T_c^{g\neq 0} - T_c^{g=0})/T_c^{g=0}$ we define the spin contrast as

$$C_{\text{spin}} \equiv \frac{|T_{c,\uparrow} - T_{c,\downarrow}|}{T_c^{g=0}} = |C_\uparrow - C_\downarrow|. \tag{6.4.1}$$

In the limit of large Zeeman splitting and narrow homogeneous linewidths, the two spin states are spectrally well separated and the contrast approaches the single-transition, cooperativity-limited value $C_{\text{spin}} \to C = 1 - 1/(C+1)^2$. In the current regime, where the spin splitting is comparable to the homogeneous linewidth, both transitions contribute at the probe frequency, resulting in a reduced contrast.

Using the extracted cavity-QED parameters together with the measured magnetic-field splitting at the maximum coil current, $\Delta\nu_{\text{spin}}(I_{\text{coil}} = 9\,\text{A}) = 263\,\text{MHz}$, we obtain on-resonance transmission values of $T_{c,\uparrow} \approx 0.81$ and $T_{c,\downarrow} \approx 0.18$. This corresponds to an on-resonance spin contrast of

$$C_{\text{spin,res}} = 0.64,$$

which is reduced compared to the single-transition contrast ($C \approx 0.81$) due to the finite spectral separation of the spin transitions.

In the following, we discuss realistic strategies to improve both the transmission probability $\mathcal{P}_t$ and the spin contrast C_{spin}.

Improving the transmission probability. One contribution to the reduced transmission probability originates from deviations from the ideal symmetric cavity condition $\kappa_1 = \kappa_2 = \kappa/2$. With the symmetric mirror coatings employed here, operation on a diamond-like cavity mode inherently increases the transmission through the sample mirror, thereby introducing cavity asymmetry. Neglecting residual losses, this effect sets an upper bound of $T_{c,\text{max}} = 0.86$ for diamond-like operation with the present coating design. Reaching a fully symmetric cavity under diamond-like operation would therefore require either intentionally asymmetric mirror coatings or operation away from the diamond-like regime.

In the present experiment, however, the dominant limitation is not cavity asymmetry but residual intracavity losses. At the specific lateral position used here, these losses are particularly pronounced, resulting in a reduced finesse of $\mathcal{F}_a \approx 1200$, compared to more typical diamond-like positions on the same membrane ($\mathcal{F}_a \approx 1700$). Even at such representative positions, however, substantial residual losses remain, indicating that loss mechanisms beyond cavity asymmetry play a central role. As discussed in Sec. 5.2.5, similar deviations from the design finesse are observed across different diamond membranes and cavity fibers, suggesting a loss mechanism that is largely independent of both lateral position and cavity mode character. Identifying and mitigating these global loss channels would require dedicated measurements on bare cavities and detailed modeling of scattering and absorption processes, as explored in Refs. [174, 197]. Operating at a representative diamond-like position would nonetheless reduce the total loss rate and increase the maximum achievable transmission to $T_{c,\text{max}} \approx 0.25$, which already constitutes a substantial improvement over the presently measured value $T_{c,\text{max}} \approx 0.12$.

A more substantial limitation arises from the combined fiber incoupling and spatial mode-matching efficiency. In the current configuration, we estimate an overall mode-matching efficiency of $\eta_{\text{mm}} = 0.023$, dominated by imperfect spatial overlap between the fiber and cavity modes. For ideal alignment, the theoretical upper bound given by Eq. (3.2.32) yields $\eta_{\text{mm,max}} \approx 0.57$ for the experimentally relevant parameters.

The large discrepancy between the measured and ideal values is attributed primarily to a lateral offset between the fiber core and the fiber mirror profile, non-ideal fiber cleaves, and angular misalignment between the cavity fiber and the planar mirror. Accordingly, improving angular alignment and employing fibers with reduced cleave angles as well as a smaller offset between the fiber core and the fiber depression profile are expected to significantly enhance the transmission.

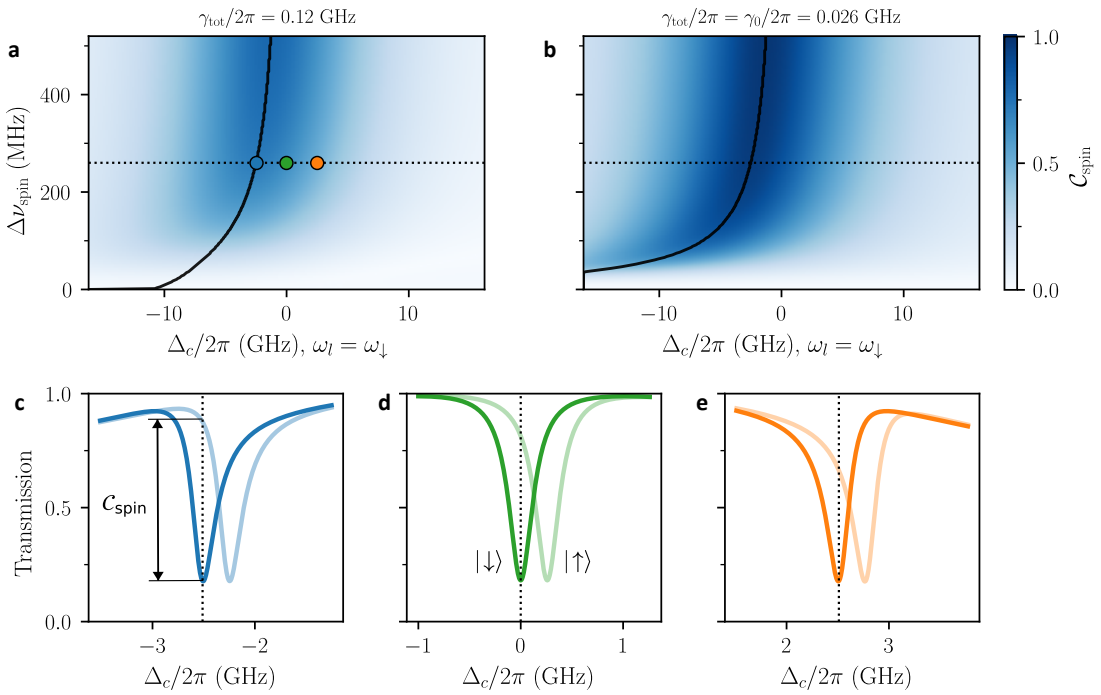

Figure 6.14: Spin contrast for variable cavity detuning and spin splitting. (a,b) Calculated spin contrast C_{spin} as a function of cavity detuning $\Delta_c = \omega_l - \omega_c$ and spin splitting $\Delta\nu_{\text{spin}}$, evaluated at the resonance of the spin-down transition for the measured homogeneous linewidth $\gamma_{\text{tot}}/2\pi = 120\,\text{MHz}$ **(a)** and for a lifetime-limited linewidth $\gamma_0/2\pi = 26\,\text{MHz}$ **(b)**. The dotted line indicates the experimentally achieved splitting $\Delta\nu_{\text{spin}} = 263\,\text{MHz}$, while the solid line marks the optimum detuning for each splitting. **(c–e)** Exemplary cavity transmission profiles at the optimum detuning **(c)**, zero detuning **(d)**, and negative optimum detuning **(e)**, illustrating the origin of the asymmetric contrast maps.

Overall, we expect that an end-to-end transmission probability of $\mathcal{P}_t \gtrsim 10\,\%$ is a realistic target when operating at lateral positions with reduced residual losses and after optimizing fiber–cavity mode matching. Further improvements may be achieved by identifying and mitigating the global scattering and absorption loss channels that currently limit the cavity finesse.

Improving the spin contrast. In the present experiment, the achievable spin contrast is limited by three main factors: the finite Zeeman splitting $\Delta\nu_{\text{spin}}$, the homogeneous linewidth γ_{tot}, and the detuning between the cavity resonance and the probed spin transition. While the first two determine the spectral overlap of the spin-selective transitions, the cavity detuning provides an additional degree of freedom that can be exploited to enhance the contrast by reducing Purcell-induced broadening and by leveraging the Fano-like asymmetry of the extinction features.

Fig. 6.14 illustrates the combined influence of these parameters. For a finite Zeeman splitting, operating at a nonzero cavity detuning yields a larger contrast than probing on resonance, as it reduces the effective linewidth and enhances the asymmetry of the transmission response. As the splitting increases, the optimum detuning shifts toward zero, and the maximum contrast approaches the cooperativity-limited value $C = 1 - 1/(C+1)^2$, as indicated by the solid curves in Fig. 6.14a,b. Due to the asymmetric line shape, it is also favorable to probe the spin transition that is further detuned from the cavity resonance, which explains the asymmetry of the contrast maps around zero cavity detuning.

For the current parameters ($\gamma_{\mathrm{tot}}/2\pi = 0.12\,\mathrm{GHz}$, $C = 1.4$, $\Delta\nu_{\mathrm{spin}} = 263\,\mathrm{MHz}$), the maximum achievable contrast is $C_{\mathrm{spin,det}} = 0.70$ at the optimum detuning, compared to the on-resonance value $C_{\mathrm{spin,res}} = 0.64$. In the limit of infinite splitting, the contrast approaches $C = 0.81$.

Assuming a lifetime-limited linewidth ($\gamma_{\mathrm{tot}}/2\pi = \gamma_0 = 0.026\,\mathrm{GHz}$), the maximum achievable contrast for the same magnetic field increases to $C_{\mathrm{spin,det}} = 0.95$, approaching the ideal value $C = 0.98$. Increasing the Zeeman splitting by a factor of two—for example by reducing the coil–sample distance, increasing the number of windings, and/or adjusting the field orientation—would further push the achievable contrast toward the cooperativity limit, yielding $C_{\mathrm{spin}} = 0.79$ (0.97) for $\gamma_{\mathrm{tot}}/2\pi = 0.12\,\mathrm{GHz}$ (0.026 GHz).

In summary, substantial improvements in spin–photon interface performance are feasible with comparatively minor adjustments to the existing experimental platform. Identifying lifetime-limited emitters would provide the most significant gain by reducing the homogeneous linewidth and increasing the coherent cooperativity. Such emitters may already be present in the current samples, as evidenced by lifetime-limited extinction features observed at other positions (Appendix A.7). In addition, operating at lateral positions with reduced cavity losses would further enhance the cooperativity. Finally, increasing the achievable Zeeman splitting, either through improved coil geometry or positioning, would relax the requirements on linewidth and detuning and enable near-ideal spin contrast.

Different configurations and readout schemes. The access from both sides of the cavity, through the fiber mirror and the free-space mirror, allows for four distinct configurations to resonantly probe the electron spin: in transmission, either from the fiber or from free space, and in reflection, from either side. The most common approach, particularly in nanophotonic cQED platforms developed jointly by the groups of Lukin and Lončar [198, 42, 43], relies on reflection from a one-sided cavity ($\kappa_1 \approx \kappa$) for spin readout and spin–photon entanglement generation. In this configuration, the emitter acts as a tunable loss channel and, for cooperativities $C \geq 1$, the impedance-matching condition can always be restored—for instance by detuning the emitter from resonance—allowing in principle for maximal extinction contrast even in the presence of intracavity loss as discussed in Sec. 3.2.5 and specified in Eq. (3.2.24). A crucial enabling factor for reflection-based readout in nanophotonic platforms is the near-unity spatial mode matching achieved by adiabatically interfacing a tapered single-mode fiber with the guided waveguide mode of the cavity. Such tapered fiber–waveguide interfaces have been demonstrated to enable

fiber–nanophotonic coupling efficiencies exceeding 90% [199, 200, 201], providing efficient and well-defined coupling between the fiber mode and the nanophotonic waveguide mode.

While this approach, probing the SnV centers in reflection, is in principle also applicable to our system, it critically relies on near-perfect spatial mode matching. In the present fiber Fabry–Pérot cavity configuration, the cavity mode is fixed by the fiber mirror geometry and the mode-matching efficiency cannot be arbitrarily tuned. The resulting imperfect mode overlap introduces a constant background reflection that severely degrades the observable spin contrast in reflection, rendering this scheme impractical. We therefore employ transmission-based readout, which is intrinsically more robust against mode-matching imperfections. In transmission, the extinction contrast is solely determined by the cooperativity, yielding a fixed ratio $T_c^{g\neq 0}/T_{c,\max}^{g=0} = 1/(C+1)^2$, independent of mode matching. Imperfect mode matching thus only reduces the absolute transmission probability and hence the detected count rate, but not the achievable contrast. As a result, our approach prioritizes contrast robustness over photon collection efficiency.

A potential route to combine high contrast with efficient reflection-based readout is probing the cavity in free-space reflection, where the spatial mode matching can be independently optimized and is not constrained by the fixed fiber geometry. More generally, combining transmission- and reflection-based spin–photon entanglement at different stages of an entanglement distribution scheme can provide additional flexibility in circumventing limitations imposed by low transmission, with the optimal choice depending on the specific entanglement protocol and the relevant efficiencies.

7. Cavity-mediated collective emission from few emitters in a diamond membrane

This chapter is based on results published in *Physical Review X* (2024) as *"Cavity-Mediated Collective Emission from Few Emitters in a Diamond Membrane"* by M. Pallmann, K. Köster *et al.* [143]. Several figures in this chapter are adapted from this publication, which is licensed under CC BY 4.0. The experimental setup was realized by Maximilian Pallmann, the diamond membrane was fabricated by Julia Heupel, and the measurements and analysis were carried out jointly with Maximilian Pallmann. Numerical simulations were provided by Yuan Zhang, with a more extensive theoretical treatment reported in [144].

Introduction: Individual vs. collective emission in a cavity In the previous chapter, we discussed how a single quantum emitter interacts with an optical cavity. Individual effects such as the Purcell enhancement of the spontaneous emission rate and the modification of the cavity transmission spectrum at high cooperativity were demonstrated, providing clear signatures of cavity quantum electrodynamics at the single-emitter level.

A natural next step is to ask what happens when not one, but many emitters couple to the same cavity mode. In this case, the cavity provides a common radiation field (Fig. 7.1a) that can establish correlations between different emitters. If several emitters radiate into the same mode, their dipoles can become partially synchronized and collective emission processes can emerge (see also Sec. 3.3).

For solid-state systems, such behavior is not obvious. Color centers in diamond, and especially nitrogen-vacancy (NV) centers, exhibit broad inhomogeneous distributions of transition frequencies, spectral diffusion, and dephasing. One might expect these imperfections to entirely suppress cooperative effects. However, when the broad ensemble is coupled to the narrow resonance of a high-finesse cavity (Fig. 7.1b), only a subset of emitters falls within the cavity linewidth and effectively participates. The cavity thus enforces a common mode for the selected emitters, promoting collective correlations and enabling collective phenomena. Excitation occurs via the phonon sideband (PSB), and emission can proceed either through the cavity-enhanced zero-phonon line (ZPL) or through the PSB (Fig. 7.1c).

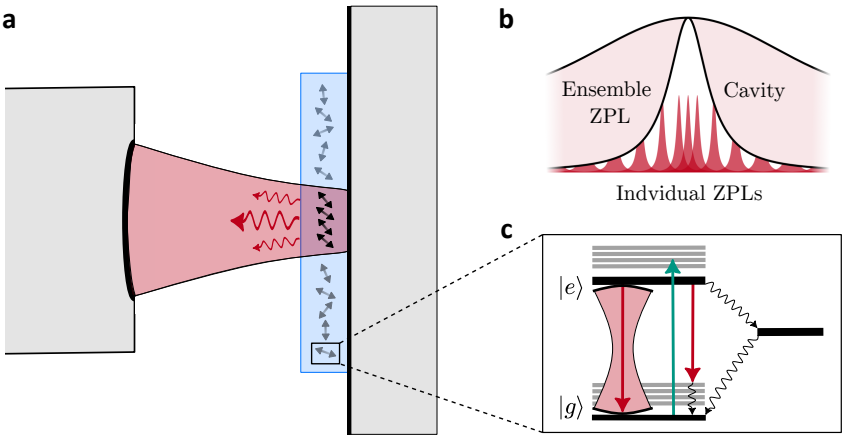

Figure 7.1: Overview of cavity-mediated emission from color centers in diamond. (a) A fiber-based Fabry–Pérot cavity couples to a thin diamond membrane containing a dense ensemble of emitters. The common cavity mode mediates interactions between the emitters, leading to partial synchronization of their dipoles. **(b)** Spectral picture: the ensemble zero-phonon line consists of many individual emitter transitions. The cavity resonance provides a narrow spectral filter that selects the resonant and correlated subset of emitters, which then contribute to the collective emission. **(c)** Emitters are incoherently excited via a phonon sideband transition and decay either through the cavity-enhanced zero-phonon line, through phonon-assisted channels, or via shelving states.

In this chapter, we investigate the transition from individual to collective emission in a cavity–membrane system. We begin by introducing the experimental platform, comprising a diamond membrane with dense shallowly implanted NV centers, a cryogenic cavity platform distinct from the previous chapter, and the optical setup. Subsequently, we revisit the signatures of individual emitters, including their spectral response, lifetime shortening, and photon correlation measurements. Building on this foundation, we then present evidence of collective emission, highlighted by a superlinear scaling of the cavity-enhanced fluorescence with excitation power and the appearance of short-timescale photon bunching. Finally, we compare the experimental observations with theoretical models formulated in the Dicke basis, which capture the role of collective states in a mesoscopic ensemble of only a few emitters.

7.1. Experimental platform

This section provides a brief overview of the experimental setup, which differs in several key aspects from the configurations described in the previous chapters. These differences concern the cavity platform, cryostat, diamond sample and color centers, and the optical setup.

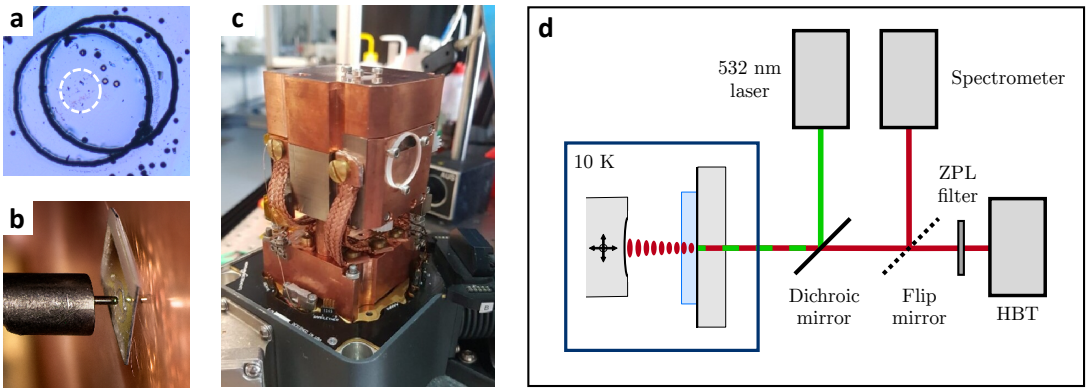

Figure 7.2: Experimental platform for cavity-mediated collective emission. **(a)** Optical microscope image of an etched diamond membrane on the planar mirror, with the measurement region marked in white. **(b)** Fiber mirror facing the planar mirror and diamond membrane, forming the plano–concave resonator. **(c)** Photograph of the home-built cryogenic cavity platform mounted in the closed-cycle cryostat; optical access is provided through the front glass window, while the remaining sides are thermally shielded with copper shielding. **(d)** Simplified optical setup: a 532 nm continuous-wave laser excites the sample inside the cavity via a dichroic mirror, and the resulting photoluminescence is directed either to a spectrometer or, after zero-phonon-line (ZPL) filtering, into a Hanbury Brown and Twiss (HBT) interferometer.

Diamond membrane with shallowly implanted NV centers. The NV ensemble is hosted in an electronic-grade, single-crystal diamond grown by chemical vapor deposition (CVD) with [100] surface orientation. The diamond plate, 40 µm thick, was implanted with nitrogen ions to a depth of about 10 nm by the manufacturer.[39] With a specified density of 300 NV/µm^2, this corresponds to a dense ensemble of a few hundred emitters within the cavity mode volume, as we verify below. The sample was cut to a footprint of 1.5×1.5 mm^2. A thin polymethyl methacrylate (PMMA) spacer layer was first applied to shift the cavity electric-field antinode to the depth of the NV centers, after which the diamond was van der Waals bonded to the planar mirror. Subsequently, the diamond was thinned by inductively coupled–plasma reactive–ion etching, yielding a membrane with a minimum thickness of 3.5 µm at the center of the etching windows (Fig. 7.2a). The final surface roughness after etching was 0.3 nm rms over an area of 4.0×4.0 µm^2. Further details on the fabrication process are given in Ref. [188].

A home-built cryogenic, scanning cavity setup. The experiments in this chapter were performed with a home-built fiber-based microcavity platform integrated into a closed-cycle cryostat.[40] The system provides a base temperature of 11 K measured in close proximity to the sample. The setup, developed in the group by Maximilian Pallmann

[39] Qnami
[40] Montana Cryostation CS1

in parallel to the commercial Qlibri system introduced in Chapter 4, follows the same Fabry–Pérot principle but with key differences. In the home-built platform the fiber is positioned with full *xyz* control, so the optical axis shifts during scanning. While this can complicate fluorescence collection in single-emitter experiments using narrow-aperture detectors, it poses no limitation for the ensemble measurements, since one can directly work at positions of high finesse.

In terms of mechanical stability, the platform achieves picometer-scale passive stability in contact operation, sufficient to keep the cavity resonant with the NV zero-phonon line over hours. Open-mode stability is reduced by vibrations of the closed-cycle cryostat, but contact mode operation is adequate for the ensemble experiments shown below. The cryostation's base temperature of 11 K is sufficient for NV centers, whose homogeneous linewidths saturate below about 15 K. For SnV centers, however, lower temperatures are required to achieve Fourier-limited optical transitions and to maintain sufficiently long spin T_1 times (see Sec. 2.2.3). Compared to the Qlibri platform operated in a dilution refrigerator at 1–4 K with a fixed fiber (optical) axis, the home-built system offered a robust and versatile solution for the NV ensemble experiments reported in this chapter.

The cavity platform itself is shown in Fig. 7.2c. The resonator is a plano–concave cavity formed between a macroscopic planar mirror and a CO_2-laser machined fiber mirror with a radius of curvature of 27.5 µm (Fig. 7.2b). The coatings are optimized for high finesse at the NV zero-phonon line (637 nm), with transmissions of 732 ppm (planar) and 52 ppm (fiber).

Further technical details on the cavity design, stability characterization, and mirror coatings can be found in the PhD thesis of Maximilian Pallmann [63] and in our related publication [143].

Optical setup. A simplified schematic of the optical setup is shown in Fig. 7.2d. The NV centers inside the cavity are off-resonantly excited with a continuous-wave 532 nm laser.[41] The laser is coupled in through the free-space port of the cryostat via a dichroic mirror. The same optical path is used to collect the emitted fluorescence, which is directed to either a spectrometer[42] or a Hanbury Brown and Twiss (HBT) interferometer consisting of two single-photon counting modules (SPCMs).[43] For the HBT measurements, the fluorescence is spectrally filtered to isolate zero-phonon line (ZPL) photons in a single fundamental cavity mode. This is achieved by combining two spectrally shifted bandpass filters.[44] The digital output pulses of the detectors are processed and time-tagged by a time-to-digital converter[45] for analysis.

[41] Hübner Photonics, Cobolt Samba 532
[42] Andor, iVac 316 LDC-DD
[43] Excelitas, SPCM-AQRH-12-TR; Laser Components, COUNT-T100
[44] Semrock, FF01-637/7-25; Semrock, TBP01-704/13
[45] Swabian Instruments, TimeTagger 20

A full description of the optical setup can be found in Ref. [63].

7.2. Cavity-enhanced ensemble fluorescence

Spectral and spatial cavity properties. To characterize both individual and collective cavity–ensemble coupling, we measured the spectral and spatial properties of the cavity. Laterally, the fiber was positioned at a location of maximum finesse, corresponding to an air-like optical mode. In contrast to the observations in Chapter 5 and the results of Chapter 6, where the highest Purcell factor occurred for diamond-like modes, the present configuration instead yields the strongest cavity–emitter coupling at an air-like mode. This behavior arises because losses outweigh the enhanced field of diamond-like modes, likely due to increased surface roughness (see Refs. [174, 63]). At this lateral position, we measure a finesse of $\mathcal{F}_a = 12\,000$. In contact mode—the configuration used throughout all experiments—the cavity linewidth extracted from a resonant laser scan is $\delta\nu_{\mathrm{cav}} = 1.0\,\mathrm{GHz}$.

The spatial cavity mode is determined by the air gap, diamond thickness, mode character, and beam waist, from which the mode volume can be simulated.[46] In contact mode, the air gap approximately equals the depth of the fiber depression profile, $t_a = 1.7\,\mu\mathrm{m}$. The diamond thickness and mode character were extracted by fitting a white-light mode dispersion measurement with a transfer-matrix model, following the procedure outlined in Sec. 5.2.5. The result agrees with independent interferometric measurements performed by our collaborators in Kassel, giving a diamond thickness of $t_d = 3.5\,\mu\mathrm{m}$. Simulations gave a beam waist of $w_0 = 1.35\,\mu\mathrm{m}$ (see Ref. [195]). These parameters form the basis for validating the Purcell factors measured in the following.

Fluorescence spectra. For all experiments presented below, the sample is cooled to 11 K to suppress thermal broadening of the ZPLs. This also enables us to exploit the full Purcell effect in the bad-cavity regime. The NV ensemble within the cavity mode is continuously excited off-resonantly by a laser, and the resulting photoluminescence (PL) is directed to a spectrometer to study cavity-enhanced emission. The cavity-filtered spectra in Fig. 7.3a display four dominant families of resonances, corresponding to the fundamental and several higher-order transverse cavity modes. When a fundamental mode is tuned into resonance with the ensemble ZPL at 637 nm (red spectrum), we observe a pronounced enhancement of the emission in that mode compared to the detuned case (teal spectrum). For comparison, a room-temperature confocal spectrum of the same sample is also shown, illustrating the improved ZPL-to-PSB ratio achieved under cryogenic, cavity-coupled

[46] In principle, the mode character is fixed by the exact diamond thickness. In practice, however, the uncertainty in the thickness is usually too large, so the mode character must be obtained from dispersion measurements.

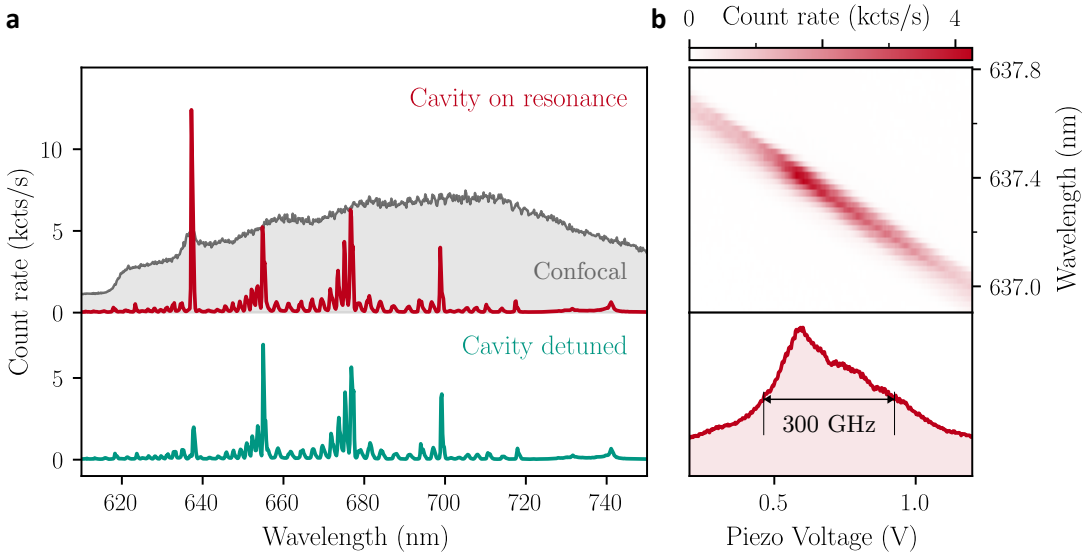

Figure 7.3: Cavity-enhanced fluorescence spectra of NV centers. (a) PL spectrum of NV centers in the cavity, with the cavity on resonance with the ensemble ZPL (red) or slightly detuned (teal). A room-temperature confocal spectrum of the same sample is shown in gray for comparison. **(b)** The inhomogeneously broadened ensemble ZPL is probed by recording spectra while stepwise changing the cavity length by adjusting the piezo voltage. The integrated counts trace out the inhomogeneous ZPL, with a FWHM linewidth of $\delta\nu_{\text{inh}} \approx 300\,\text{GHz}$.

conditions. To quantify the Purcell effect, this qualitative comparison is complemented by lifetime measurements, presented in Sec. 7.3.

Ensemble ZPL. The two spectra shown above (on- and off-resonant) represent the two extremes of a continuous trend observed when sweeping the cavity resonance across the ensemble ZPL. This inhomogeneously broadened line can be mapped by stepwise tuning the cavity length with the z-piezo in the vicinity of the resonance at 637.4 nm. The result is displayed in Fig. 7.3b: the fundamental cavity mode (red line, upper panel) is scanned across the ensemble ZPL, while the integrated counts (lower panel) map out the spectral distribution with a FWHM linewidth of $\delta\nu_{\text{inh}} \approx 300\,\text{GHz}$. Since the cavity linewidth is much narrower than the inhomogeneous ensemble width ($\delta\nu_{\text{cav}} \approx 1.0\,\text{GHz} \ll \delta\nu_{\text{inh}} \approx 300\,\text{GHz}$), the cavity thereby acts as a high-resolution spectral filter.

From the photon statistics discussed below, we estimate that only about 15 emitters contribute to the on-resonance count rate at the peak of the ZPL, whereas roughly 500 emitters within the cavity mode volume contribute to the spectrally much broader PSB. Consequently, the ZPL enhancement exceeds by more than an order of magnitude the apparent enhancement in Fig. 7.3a.

Superlinear power dependence. To investigate the saturation behavior of the PL intensity, we recorded spectra while varying the excitation power (Fig. 7.4a), with the cavity tuned

into resonance with the ZPL. The cavity mode coupled to the ZPL is highlighted in red; the PSB contribution is shown in teal. For quantitative analysis, we extract the count rates from the peak intensity of the ZPL mode and of the neighboring PSB mode, and plot them against the applied laser power P. An independent measurement performed at higher powers is used to normalize the data to the saturation power P_{sat}.

Since the data in Fig. 7.4b are taken well below the saturation threshold, the PSB emission scales linearly with excitation power, consistent with expectation. Fitting the power dependence with a power law $I \propto P^k$ gives an exponent of $k_{\mathrm{PSB}} = 1.00(1)$. In contrast, the ZPL shows a pronounced superlinear dependence with an exponent of $k_{\mathrm{ZPL}} = 1.42(1)$. This behavior is reproducible for different cavity lengths and lateral positions (inset of Fig. 7.4b), and highlights the clear distinction between the partially coherent ZPL emission and the incoherent PSB emission inside the cavity.

The observed superlinearity is consistent with expectations for ensembles of interacting emitters and has been reported in atomic gases and semiconductor systems [202, 203, 204, 205]. Its manifestation in a solid-state defect ensemble is remarkable: strong homogeneous and inhomogeneous broadening would ordinarily suppress the pair correlations responsible for such behavior, and indeed at room temperature the scaling reverts to linear because phonon-induced dephasing destroys the correlations. In the following, we show through numerical modeling that the cavity can nevertheless mediate collective states in this disordered environment, thereby enabling the emergence of the observed superlinear power dependence at cryogenic temperatures.

7.3. Photon statistics

We measure photon statistics of the cavity output using second-order intensity autocorrelations, $g^{(2)}(\tau)$, in a HBT setup. From these data, we extract single-emitter properties such as cavity-induced excited-state lifetime shortening and shelving-state bunching. In addition, short-timescale bunching provides evidence of collective effects. An exemplary $g^{(2)}$ function of the cavity-enhanced ZPL fluorescence at cryogenic temperatures is shown in Fig. 7.5 (red). The three contributions—few-emitter antibunching (a, τ_1), few-emitter shelving-state bunching (b, τ_2), and collective bunching (c, τ_3)—are described by the fit function

$$g^{(2)}(\tau) \;=\; 1 - (a+b)e^{-|\tau|/\tau_1} \;+\; b\, e^{-|\tau|/\tau_2} \;+\; \phi_{c,\tau_3}(\tau) + \Delta y, \tag{7.3.1}$$

where a variable offset Δy accounts for slow intensity drifts that shift the $g^{(2)}$ baseline. In contrast to the ZPL photon statistics (red), the PSB-only $g^{(2)}$ function at 11 K (gray) appears flat because of the large number of contributing emitters. The confocal measurement at room temperature (teal) reveals only a single antibunching dip, from which we infer the total number of emitters within the spatial mode. A detailed analysis will follow below.

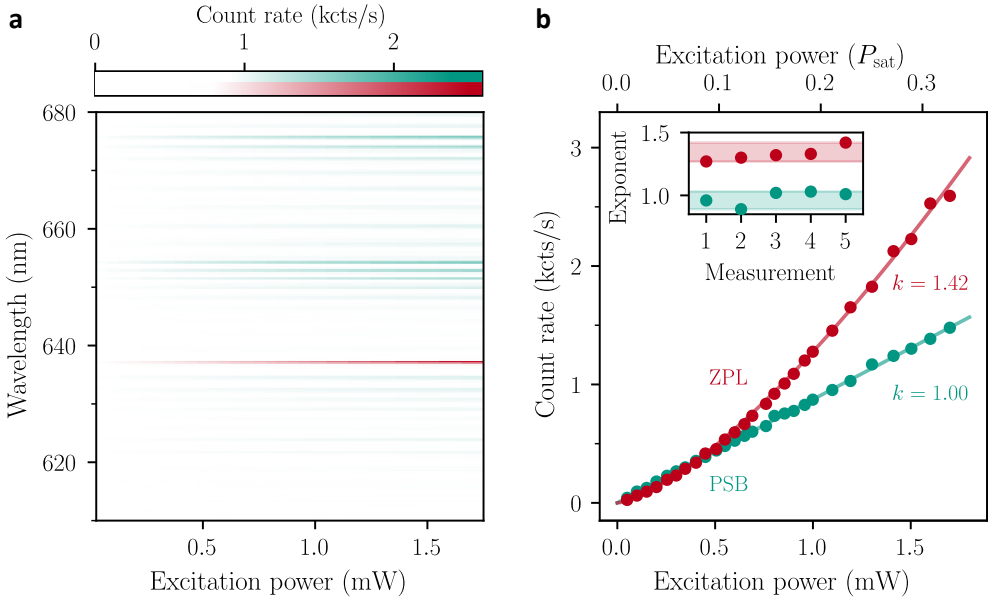

Figure 7.4: Superlinear power dependence of the ZPL emission. (a) Cavity-enhanced PL spectra as a function of excitation power. The ZPL contribution is highlighted in red, and the PSB contribution in teal. **(b)** Count rate of the ZPL-coupled cavity mode compared to the neighboring PSB mode as a function of excitation laser power. The upper axis is normalized to the saturation power P_{sat} obtained from an independent measurement at higher excitation. The inset shows the fitted power-law exponents k for several experimental realizations (different cavity lengths and lateral positions).

7.3.1. Few-emitter (anti-)bunching

In the following, we use the excitation-power-dependent time constant τ_1 to determine the cooperativity and Purcell factor, and the antibunching contrast a to estimate the number of contributing emitters within the spatially and spectrally filtered cavity mode.

Lifetime shortening. We measured $g^{(2)}$ functions in the cryogenic cavity and in the room-temperature confocal setup at varying excitation powers P. From these measurements, the antibunching time constants $\tau_1(P)$ were extracted and extrapolated to zero power, $\tau_1(0)$, corresponding to the excited-state lifetimes τ_0 (confocal) and τ_c (cavity), which serve as input for evaluating the cooperativity. The power-dependent antibunching time constants are shown in Fig. 7.6a. To describe the saturation behavior, we fit the relation (see Appendix B of Ref. [143])

$$\tau_1(P) = \frac{\tau_1(0)}{1 + \frac{P}{P_{sat}}}, \tag{7.3.2}$$

from which we extract lifetimes of $\tau_0 = 15.8(8)$ ns (confocal) and $\tau_c = 7.6(9)$ ns (cavity). The longer free-space lifetime compared to the reported bulk value of 13 ns is attributed to the modified dielectric environment of shallowly implanted NV centers, which reduces

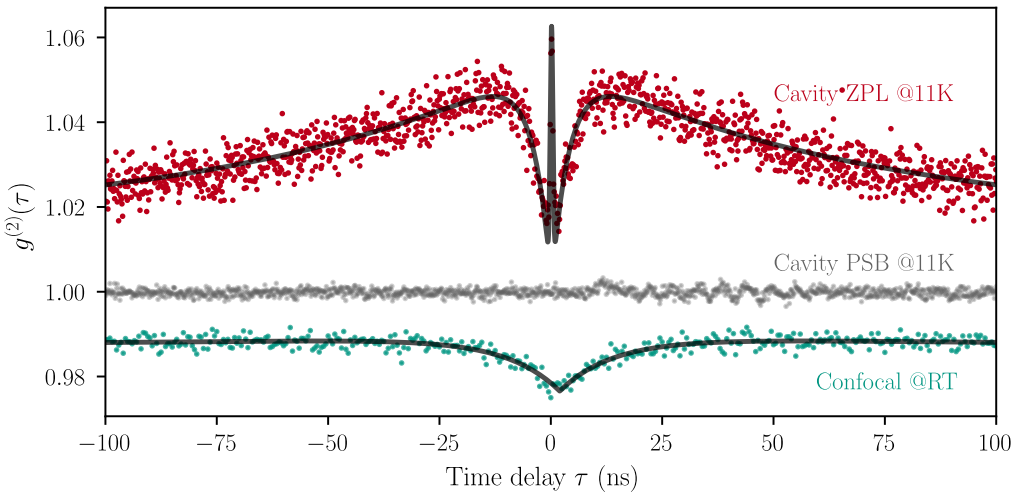

Figure 7.5: Second-order intensity autocorrelation functions $g^{(2)}(\tau)$ of cavity-enhanced fluorescence. The ZPL emission at 11 K (red) shows clear antibunching together with fast and slow bunching contributions, captured by the fit (black). In contrast, the PSB-only signal at 11 K (gray) appears flat because of the large number of contributing emitters. A confocal measurement at room temperature (teal), with a well-defined focal spot size, allows the emitter density to be inferred.

the decay rate [206, 207]. The horizontal axis in Fig. 7.6a is normalized by the respective fit parameters P_{sat}, which differ significantly due to the different excitation spot sizes in the confocal and cavity configurations.

From the ratio of lifetimes we infer the cooperativity C_0 according to Eq. (3.2.13), yielding $C_0 = 1.1(3)$. Taking into account the Debye–Waller factor of NV centers, $\beta_{\text{DW}} = 0.03$ [77], this corresponds to a Purcell factor of

$$F_P = \frac{C_0}{\beta_{\text{DW}}} = 36(11).$$

To compare this result with the expected Purcell enhancement, we evaluate Eq. (5.2.12) for an air-like mode using $\mathcal{I}_{A/D}^{-1} = n_d^{-1}$, and perform Monte Carlo sampling over the relevant experimental uncertainties ($\mathcal{F}_a, w_0, \xi^2$). The resulting distribution of Purcell factors F_P is shown in Fig. 7.6b. For the cavity finesse we take $\mathcal{F}_a = 12\,000$ with a 10% uncertainty, determined from repeated linewidth and free spectral range measurements. The mode waist $w_0 = 1.35\,\mu\text{m}$ is likewise taken with a 10% uncertainty, dominated by the imprecisely known air- and diamond-layer thickness. For randomly oriented NV dipoles on a (100) surface, the polarization overlap factor ξ^2 ranges from 1/3 to 1 depending on the in-plane angle between the cavity polarization and the NV axis projection [208]. Averaging over the four possible NV orientations yields an angle-independent mean value of $\langle \xi^2 \rangle = 2/3$. In simulations, we therefore either fix $\xi^2 = 2/3$ to represent the ensemble-averaged case (lower panel) or draw ξ^2 from a uniform distribution in ϕ to capture the full range of possible overlaps (upper panel).

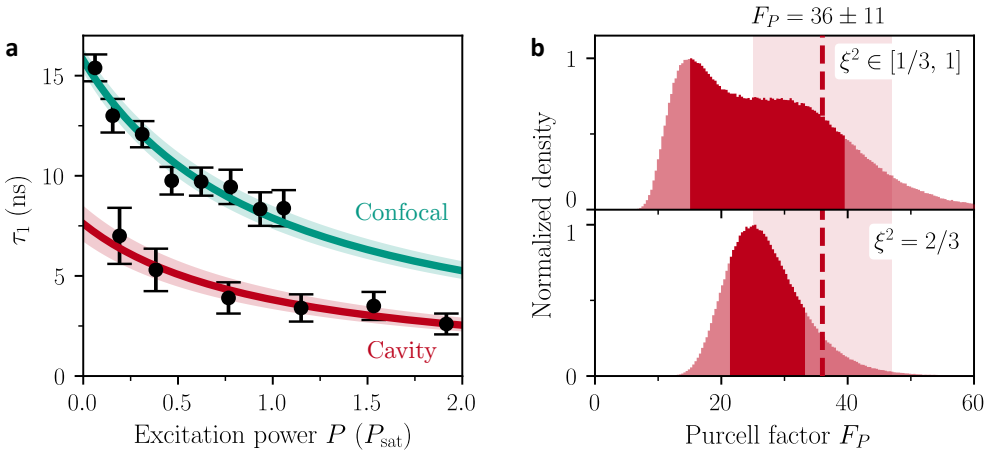

Figure 7.6: Measured and expected Purcell factor. (a) Excited-state lifetimes extracted from the power-dependent antibunching time constant, measured in the confocal case (teal) and inside the cavity (red). **(b)** Resulting Purcell factor $F_P = 36$ compared with Monte Carlo–sampled values of the analytical expression, accounting for uncertainties in finesse and mode waist. The in-plane dipole overlap ξ^2 is either fixed to the ensemble average (lower panel) or sampled from the full angular distribution (upper panel).

The experimentally determined value lies on the upper tail of the Monte Carlo distribution. This is reasonable, since the lifetime extracted from $g^{(2)}$ measurements is biased towards emitters that contribute the largest count rates, i.e., those most strongly coupled to the cavity and thus exhibiting the largest Purcell factors. The bias arises because the contribution of a single emitter to the intensity autocorrelation scales quadratically with its count rate, as two consecutive detection events are required to register a correlation. It is therefore more appropriate not to consider only the mean overlap factor, but rather to account for the full range of overlaps. Incorporating this intensity-squared detection bias, we evaluate a squared–Purcell-factor weighted mean[47] over the upper distribution, yielding an average Purcell factor of $F_P = 37.4$. This value is in remarkably good agreement with the experimentally determined result. In this evaluation we excluded the random spectral and spatial cavity overlap, which would reduce the expected Purcell factor further. However, the same argument applies here: because of the strong bias towards emitters with large coupling, no significant deviation from the scenario of perfect overlap is observed.

The slower bunching time constant τ_2 can also be evaluated at zero excitation power, giving a shelving-state lifetime of $\tau_{\mathrm{shelve}} = \tau_2(0) \approx 200\,\mathrm{ns}$. This is consistent with the reported value of 219 ns in Ref. [71]. A detailed discussion of the evaluation procedure and the full rate equations of the three-level system under incoherent pumping can be found in the PhD thesis of Maximilian Pallmann [63].

[47] Since $g^{(2)}$ scales with $I^2 \propto F_P^2$, the effective average Purcell factor is weighted accordingly.

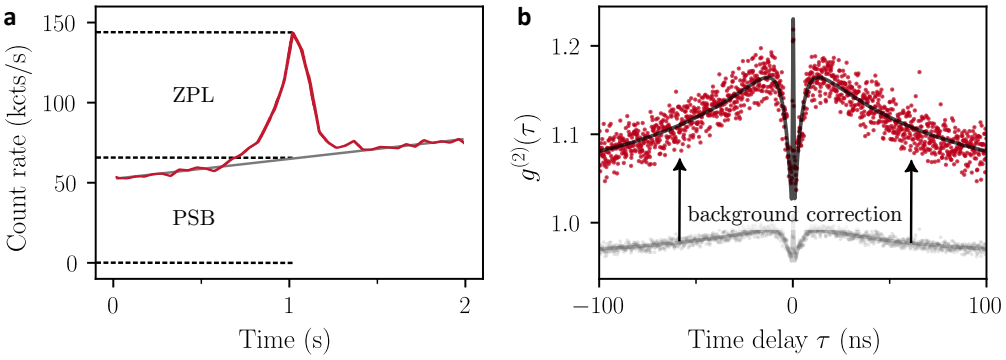

Figure 7.7: Background correction using the purity p. (a) Exemplary count-rate trace recorded while scanning over the inhomogeneously broadened ZPL, from which the purity is determined as $p = \mathrm{ZPL}/(\mathrm{ZPL} + \mathrm{PSB})$. **(b)** Background-corrected ZPL $g^{(2)}(\tau)$, obtained by applying the purity factor to the measured data (gray), resulting in the corrected curve (red).

Number of contributing emitters. The antibunching contrast provides an estimate of the number of emitters contributing to the cavity-enhanced ZPL fluorescence at the ensemble peak. The detected $g^{(2)}(\tau)$ consists of the coherent ZPL signal of interest plus a flat PSB background. This background contribution reduces the intrinsic contrast of the background-free $g^{(2)}_{\mathrm{ZPL}}(\tau)$, leading to the measured $g^{(2)}(\tau)$ according to

$$g^{(2)}(\tau) = 1 + \Delta y + p^2 \left[g^{(2)}_{\mathrm{ZPL}}(\tau) - 1 \right], \tag{7.3.3}$$

where the purity parameter, p, is defined as $p = \mathrm{ZPL}/(\mathrm{ZPL} + \mathrm{PSB})$, and Δy denotes the vertical offset.

The purity can be obtained by scanning the cavity across the inhomogeneous ZPL and evaluating the signal-to-background ratio, as shown in Fig. 7.7a. We estimate $p \approx 0.5$, which reduces the measured antibunching contrast by approximately a factor of four (Fig. 7.7b). From the corrected contrasts, the number of emitters contributing to the measured ZPL $g^{(2)}$ function can be estimated via Eq. (3.3.19), yielding $N = p^2/a = 15(3)$.

A similar analysis can be performed for the confocal $g^{(2)}$ function (Fig. 7.5), where we measure a contrast of $a = 0.014$, corresponding to about 70 emitters within a point-spread function of waist $w_0 = 0.474\,\mu\mathrm{m}$. This corresponds to an areal density of $n \approx 100\,\mathrm{NV}/\mu\mathrm{m}^2$, implying a total of about $N_{\mathrm{inh}} \approx 500$ emitters within the spatial cavity mode. Because of the large number of contributing emitters, the measured $g^{(2)}$ function in the PSB appears flat, as all emitters contribute through the spectrally broad emission. In contrast, the cavity spectrally selects only a small fraction of the ensemble that contributes to the measured ZPL signals, which justifies the schematic illustration in Fig. 7.1b.

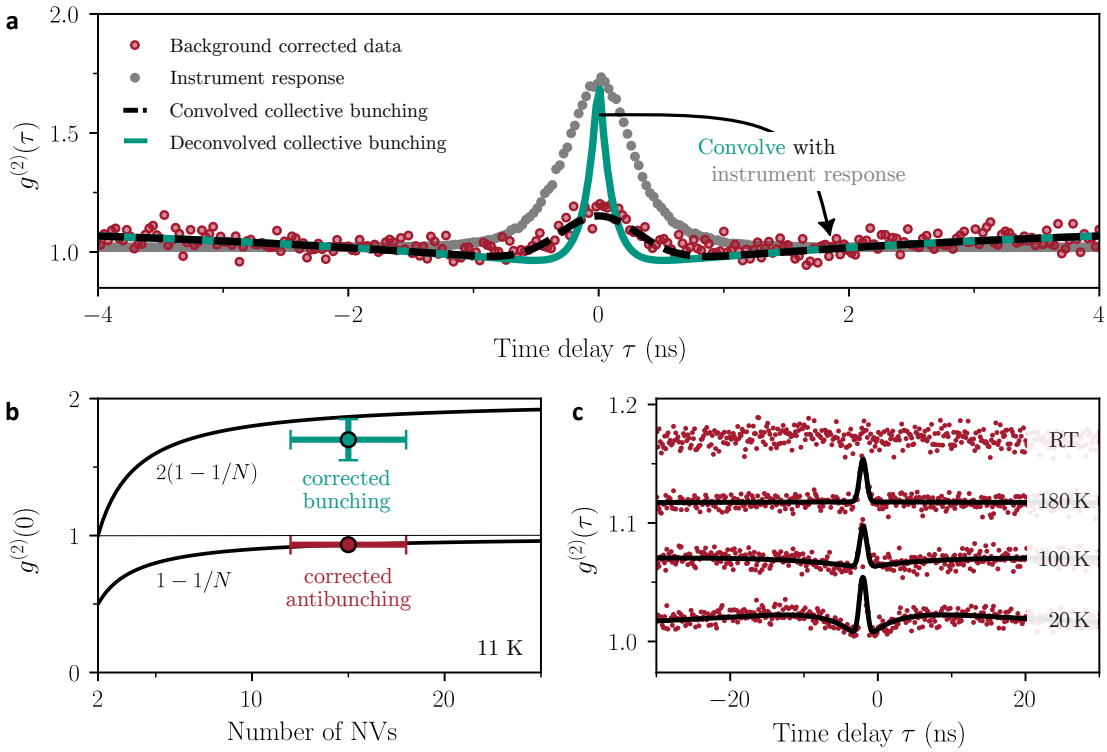

Figure 7.8: Collective bunching. **(a)** Modeled $g^{(2)}(\tau)$ (teal) is convolved with the measured instrument response (gray), yielding the convolved curve (black), which reproduces the background-corrected data (red). From this comparison we extract an intrinsic bunching amplitude of $g^{(2)}(0) \approx 1.7$. **(b)** The antibunching contrast yields an effective number of contributing emitters $N = 15$ (red). The measured bunching amplitude (teal) is compared to the expected value for a thermal ensemble, $2(1-1/N)$, in good agreement. **(c)** The bunching amplitude persists upon increasing temperature, confirming its robustness against additional dephasing.

7.3.2. Collective bunching

Finally, we address the central short-timescale bunching peak, $\phi_{c,\tau_3}(\tau)$, which was left unspecified in Eq. (7.3.1). As shown in Fig. 7.8a, the data reveal a Gaussian profile with a full width at half maximum (FWHM) of about 400 ps. To interpret the extracted time constant τ_3 and amplitude c of this peak, we first determine the temporal resolution of our HBT setup. For this purpose, we measured the instrument response using a short-pulsed laser with a pulse duration ($\sim$ 50 ps) well below the timing jitter of the SPCMs (gray points in Fig. 7.8a). The resulting $g^{(2)}$ signal exhibits the same time constant and functional form as the central bunching peak, indicating that the observed feature is fully limited by the timing jitter of the two detectors (242 ps and 325 ps, respectively). The fastest timescale that can be resolved in $g^{(2)}$ is set by the cavity intensity decay time, $\tau_{\mathrm{cav}} = \delta\nu_{\mathrm{cav}}^{-1} \approx 100$ ps. This behavior is consistent with the numerical model developed below for an ensemble of spectrally diluted emitters coupled to the cavity. Knowing the time constant and functional form of the bunching peak allows us to deconvolve the background-corrected $g^{(2)}$ data

and recover an intrinsic bunching amplitude of $g^{(2)}(0) \approx 1.7$, as shown in Fig. 7.8a. We compare this value with the thermal limit of $2(1-1/N)$ (see Eq. (3.3.18)) in Fig. 7.8b, where we find reasonable agreement.

The simultaneous presence of few-emitter antibunching and collective bunching marks an experimental regime that is typically difficult to access. As discussed by Auffèves *et al.* in Ref. [142], the collective bunching contribution $2(1-1/N)$ is, in principle, robust against pure dephasing. In practice, however, dephasing shortens the characteristic temporal width of the bunching feature by reducing the first-order coherence time, such that it can become narrower than the time resolution of the experimental setup. In this regime, the bunching peak is effectively averaged out by the finite temporal binning of the measured $g^{(2)}(\tau)$ function and therefore remains unobservable in most experiments.

In our case, the cavity acts as a spectral filter that increases the coherence time, i.e., prolongs the decay of $g^{(1)}(\tau)$. As a result, the bunching peak becomes just resolvable within the timing resolution of our setup, even though its intrinsic width is already roughly four times shorter than the detector jitter. These results show that, under suitable conditions, both $g^{(2)}$ contributions—the quantum statistics of individual emitters and the collective interference of multiple emitters approaching the thermal limit—can be resolved in a solid-state ensemble, thereby revealing the full functional form of Eq. (3.3.17).

The interpretation of the central peak as a collective bunching feature is further supported by its robustness against dephasing, consistent with the fact that pure dephasing does not suppress bunching in principle but only reduces its temporal extent by shortening the first-order coherence time. We demonstrate this by raising the temperature, thereby broadening the homogeneous linewidth well beyond the cavity linewidth. The peak height remains essentially unchanged, reflecting that the bunching amplitude is preserved as long as sufficient first-order coherence is maintained by the cavity filtering. At the same time, the increased linewidth enhances the number of emitters contributing to the collective response. This, in turn, reduces the antibunching contrast and gradually suppresses single-emitter statistics, pushing the ensemble toward fully thermal behavior, as shown in Fig. 7.8c. Surprisingly, no clear bunching was observed at room temperature, even though the cavity should still provide sufficient spectral filtering. The origin of this discrepancy remains unclear.

7.4. Numerical analysis

The purpose of this section is to provide qualitative and quantitative support for the experimental observations presented above. We focus on the main results and refer to Refs. [143, 144] for a detailed description of the underlying model and its subsequent refinements. The numerical model and simulation results presented here were developed and carried out by Y. Zhang and K. Mølmer and are summarized below to substantiate the experimental findings.

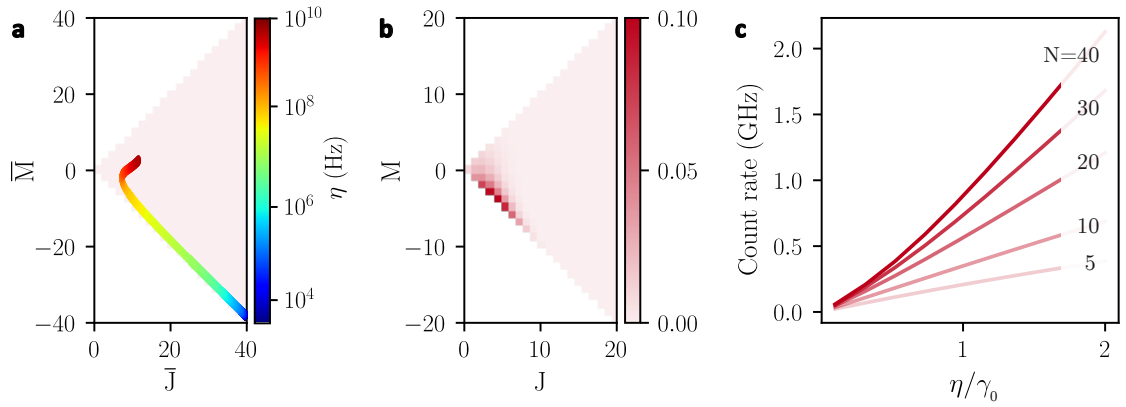

Figure 7.9: Emergence of the superlinear power dependence. **(a)** Mean Dicke-state occupation $|\overline{J}, \overline{M}\rangle$ versus excitation rate for 80 NV centers (adapted and reused with permission from Ref. [144]). **(b)** Exemplary occupation for 40 NV centers, showing the departure from the minimum-J boundary characteristic of incoherent emission. **(c)** Power-dependent emission rate, with the onset of superlinearity between 10 and 20 emitters.

7.4.1. Superlinear power dependence

Building on the framework introduced in Section 3.3, the Dicke-basis master-equation formalism is applied to simulate the observed superlinear power dependence. Each NV center is modeled as a two-level system with decay rate γ_0, pure dephasing $\gamma^\star$, and incoherent pumping η (see Fig. 3.7); the ensemble couples to a single cavity mode in the bad-cavity regime. A cavity loss rate of $\kappa/2\pi = 1.0\,\mathrm{GHz}$ and a coupling strength of $g/2\pi = 180\,\mathrm{MHz}$ are used, consistent with the cooperativity extracted in Sec. 7.3.

As recalled in Sec. 3.3, the emission rate of a Dicke state $|J, M\rangle$ follows Eq. (3.3.12). For a statistical mixture with populations ρ^J_{MM}, the total intensity is

$$I = \Gamma \sum_{J,M} |A^-_{J,M}|^2 \, \rho^J_{MM}. \tag{7.4.1}$$

For ensembles up to a few tens of emitters, the master equation can be solved numerically in the Dicke basis to obtain the steady-state populations as a function of the pump rate η.

At low pump rates, the ensemble remains near the minimum-J boundary of the Dicke manifold, which yields (approximately) linear scaling of the emission with excitation power. With increasing η, population flows into more symmetric manifolds (larger J), building up pair coherences and producing superlinear growth. This trend appears in Fig. 7.9a (mean $\overline{J}, \overline{M}$ versus η) and in Fig. 7.9b (exemplary population map for $N = 40$), where the occupation of higher-J manifolds becomes evident.

The corresponding power dependence in Fig. 7.9c shows an onset of superlinearity for ensembles of about 10–20 emitters; for $N \approx 40$ the scaling approaches the experimentally

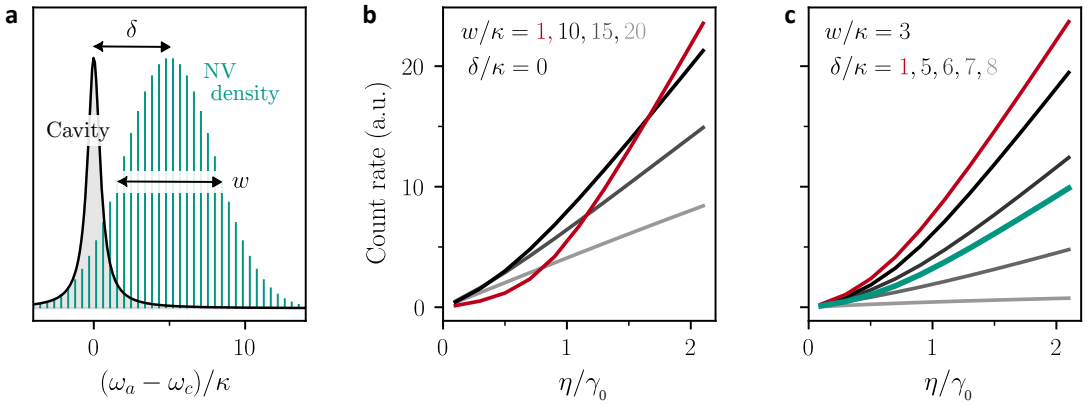

Figure 7.10: Superlinearity with inhomogeneous broadening and detuning. (a) Illustration of the subensemble approach: emitters are grouped into frequency classes of width w and mean detuning δ from the cavity resonance. **(b)** Calculated emission intensity versus pump power for different ensemble widths w, showing the gradual suppression of superlinear scaling as w increases. **(c)** Dependence of the superlinear response on the mean detuning δ for fixed width $w/\kappa = 3$. The teal curve shows the average over the experimentally determined inhomogeneous distribution ($\delta\nu_{\mathrm{inh}} \approx 300\,\mathrm{GHz}$).

observed exponent $k \approx 1.42$ (compare Fig. 7.4). While this calculation assumes identical emitters and neglects inhomogeneous broadening, it captures the essential mechanism: as the pump increases, the steady state shifts toward higher-J Dicke manifolds, and pair correlations drive the superlinear scaling. The impact of inhomogeneous broadening and disorder is introduced in the following subsection.

Inhomogeneously broadened subensembles. To account for frequency inhomogeneities, the model is extended by introducing subensembles of size N_k, each characterized by a detuning $\Delta_k = \omega_c - \omega_{a,k}$ (see Appendix C of Ref. [143]). The total number of NV centers is fixed to $N_{\mathrm{inh}} = \sum_k N_k = 500$, consistent with the experiment. Since the Hilbert space grows exponentially with N, a full density-matrix treatment is not feasible; instead, the steady state is determined using a second-order mean-field approach [209, 143, 144]. The distribution of subensembles is parameterized by a width w and a mean detuning δ, as sketched in Fig. 7.10a.

Resonant ensembles ($\delta = 0$) are considered first. When the inhomogeneous broadening is comparable to the cavity linewidth, a pronounced superlinear response is still obtained. With increasing width w, however, the effective number of emitters participating collectively is reduced, and the superlinearity diminishes (Fig. 7.10b). In a complementary analysis, the width is fixed ($w/\kappa = 3$) while the mean detuning δ is varied (Fig. 7.10c). Once the detuning exceeds the inhomogeneous linewidth, the superlinear response drops sharply, as only few emitters remain resonant with the cavity. Finally, weighting the results with the experimentally determined distribution ($\delta\nu_{\mathrm{inh}} \approx 300\,\mathrm{GHz}$) reproduces the persistence of superlinear scaling (teal line), in agreement with the experiment.

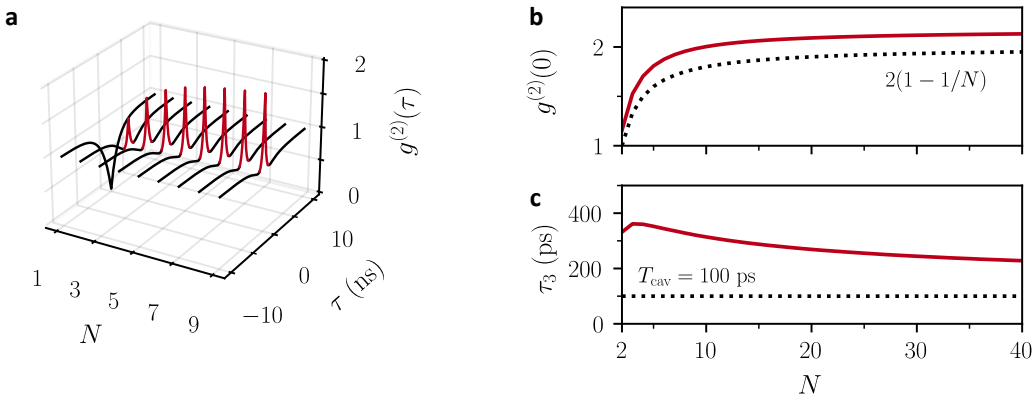

Figure 7.11: Numerical $g^{(2)}(\tau)$ for identical emitters. **(a)** Intensity autocorrelation $g^{(2)}(\tau)$ for increasing numbers of NV centers at $\eta/\gamma_0 = 2$. The short-timescale bunching contribution is highlighted in red. **(b)** Bunching amplitude $g^{(2)}(0)$ (red) versus emitter number compared with the thermal limit $2(1 - 1/N)$ (black, dotted), exceeding it slightly and indicating collective (superradiant) contributions. **(c)** Extracted rise time τ_3 versus emitter number, remaining well above the uncorrelated cavity limit $T_{\mathrm{cav}} = 100$ ps (black line).

We emphasize that this model is intended to demonstrate qualitative agreement only: quantitative predictions are hindered by uncertainties in parameters such as pure dephasing and spectral diffusion. Nonetheless, the analysis highlights that the cavity provides a sufficiently narrow decay channel to stabilize collective correlations even in strongly disordered ensembles.

7.4.2. Photon statistics

The second-order correlation function $g^{(2)}(\tau)$ was computed using the quantum regression theorem [210], which enables the evaluation of multi-time correlations from the master equation (see Appendix C of Ref. [143] for details).

The $g^{(2)}(\tau)$ functions for increasing numbers of identical NV centers are shown in Fig. 7.11a for a fixed excitation rate $\eta = 2\gamma_0$. The long-timescale bunching due to a shelving state is absent because that level is omitted in this simplified model. A clear evolution is observed from single-emitter antibunching with full contrast to a collective response exhibiting an increasingly pronounced short-timescale bunching peak. The peak amplitude in Fig. 7.11b lies slightly above the thermal limit, consistent with a superradiant contribution. The corresponding rise time τ_3 decreases with emitter number to about 230 ps.

This timescale can be connected to specific Dicke manifolds. For $\eta = 2\gamma_0$ and $N = 40$, states around $J = 4$ are populated (cf. Fig. 7.9b). Using Eq. (3.3.12), the decay times of $|J{=}4, M{=}-3\rangle$ and $|J{=}4, M{=}-2\rangle$ are estimated as $\tau \approx 330$ ps and $\tau \approx 150$ ps, respectively. These values bracket the simulated rise time of 230 ps, providing a consistency check for assigning τ_3 to transitions within this manifold.

To incorporate ensemble frequency inhomogeneity, it is approximated as an additional pure-dephasing channel—an effective description of fast spectral fluctuations justified in the Supplemental Material of Ref. [143]. The short-timescale bunching peak is preserved even for strong dephasing and broad inhomogeneities, consistent with the temperature series in Fig. 7.8c. In the strong-dephasing limit, the rise time approaches $\tau_3 \approx 110\,\mathrm{ps}$, close to the cavity ring-down time $\tau_{\mathrm{cav}} = 100\,\mathrm{ps}$. This motivates deconvolving the experimental $g^{(2)}(\tau)$ with the instrument response function, as discussed in Sec. 7.3.

7.5. Conclusion and outlook

We have shown that strongly inhomogeneous and dephasing solid-state ensembles can nonetheless exhibit signatures of collective emission when coupled to a common high-finesse cavity mode. Single-emitter Purcell enhancement was confirmed by lifetime measurements, yielding a cooperativity of $C_0 = 1.1$. This enhancement enabled a superlinear scaling of the cavity-emitted fluorescence with excitation power, which our numerical model links to population of higher-J Dicke manifolds, providing experimental evidence of collective emission. Photon-correlation measurements further revealed the coexistence of single-emitter antibunching on the Purcell timescale with a short-timescale thermal bunching peak, consistent with the cavity prolonging the first-order coherence function $g^{(1)}$. The numerical model developed in collaboration enabled a qualitative comparison and interpretation of these results. A more quantitative simulation would, however, require much tighter constraints on the experimental parameters, which was not feasible for this disordered emitter system.

While the observation of collective effects in strongly disordered ensembles is noteworthy, advancing both the experiments and their applications will benefit from emitters with much greater spectral stability and stronger light–matter coupling—such as the negatively charged tin-vacancy center (see Chapter 6). Suppressing spectral diffusion and inhomogeneous broadening would enable cleaner signatures of superradiance than observed here. Building on recent two-emitter demonstrations across multiple material systems, which already exhibit precise control over collective dynamics [211, 212, 213, 214], a natural next step is to realize cavity-mediated few-emitter ensembles of these more coherent defects. This would facilitate systematic studies of cooperative behavior and enable applications such as collectively enhanced light sources [203, 215], entanglement generation [216, 217], and improved sensing [218, 219].

8. Conclusion and outlook

Summary of the main achievements. In this work, we demonstrated a major step toward an efficient spin–photon interface based on tin-vacancy (SnV) centers embedded in diamond membranes and integrated into a cryogenic, tunable, open fiber-based microcavity platform.

We realized a versatile and unique experimental platform by combining an open microcavity with a table-top dilution refrigerator, achieving exceptional passive mechanical stability below 10 pm rms at temperatures down to 1 K. The setup was complemented by a superconducting magnetic field coil, enabling spin access to the integrated SnV centers. The combination of high mechanical stability, sub-4 K operation, and applied magnetic fields allowed the cavity–emitter system to be operated at high cooperativity and under conditions where temperature-induced spin relaxation rates are strongly suppressed.

Moreover, we established a robust and reproducible routine for integrating millimeter-sized diamond membranes hosting tin-vacancy centers into the open microcavity platform with high efficiency. The work also provided a detailed discussion of the theoretical description of hybrid air–diamond cavities, which predicts superior light–matter coupling in configurations where the electromagnetic energy density is concentrated inside the diamond membrane. While this so-called diamond-like regime is typically considered experimentally challenging due to excessive scattering losses at the diamond–air interface, we demonstrated experimentally that, through a careful and well-controlled sample fabrication procedure, these losses could be sufficiently reduced. This enabled operation of the cavity–emitter system in this favorable regime, resulting in enhanced light–matter interaction strengths.

This combination of a versatile cryogenic microcavity platform and cavity-integrated, SnV-hosting diamond membranes enabling diamond-like operation yielded single SnV centers coupled to a fiber-based microcavity with a five-fold Purcell-induced lifetime shortening, placing the system in the high-cooperativity regime. In this regime, we demonstrated coherent coupling of a single SnV center to the optical cavity, resulting in pronounced SnV-induced extinction in the cavity transmission when probed with a weak coherent field, with a contrast of 81 %, corresponding to a coherent cooperativity of $C = 1.4$. While the achieved cooperativity was primarily limited by homogeneous broadening of the respective color center, we estimated an ideal cooperativity of $C_0 = 6.3$ for a lifetime-limited SnV linewidth under otherwise identical conditions. Furthermore, applying a magnetic field using a superconducting coil enabled Zeeman splitting of the optical transition, constituting, to the best of our knowledge, the first observation of

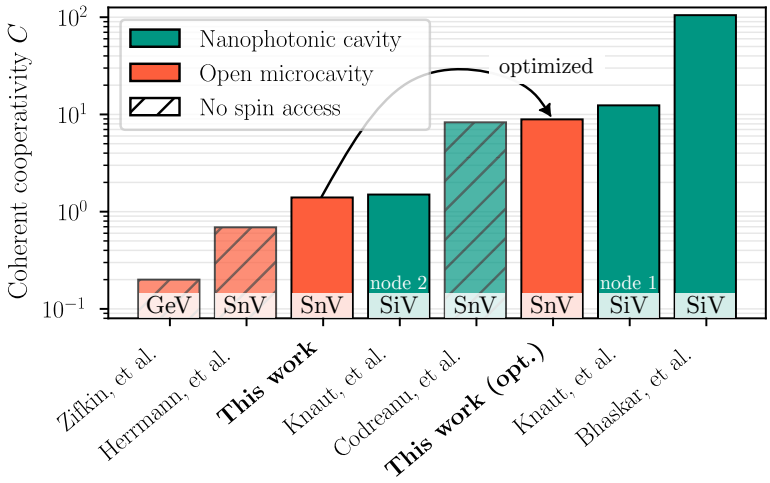

Figure 8.1: Cavity-coupled group-IV color centers in diamond. The figure situates our work within the active research field of cavity-integrated group-IV color centers in diamond. The experiments are ordered by their achieved coherent cooperativity C, with color indicating the cavity type and hatched bars marking works without demonstrated spin access. For the two-node network experiment by Knaut *et al.* [43], both nodes are shown to illustrate that even moderate cooperativities can enable quantum network demonstrations. This work achieves competitive cooperativities in open microcavities and, with experimentally realistic improvements, reaches among the highest values reported for SnV centers in diamond.

electron spin splitting for cavity-coupled SnV centers. We concluded with a discussion of the dominant limitations of the present system, highlighting realistic opportunities for short-term improvement within the current experimental configuration.

After focusing primarily on single color centers in diamond coupled to high-finesse cavities in the high-cooperativity regime, the thesis concluded with an exploration of the physical effects arising from coupling an ensemble of color centers (nitrogen-vacancy centers) to a cavity. We observed signatures of collective behavior, including a non-linear scaling of the emission rate with excitation power and pronounced photon bunching at short timescales in the intensity autocorrelation of the cavity-enhanced fluorescence. These observations were attributed to the combined effects of superfluorescence and cavity-enabled collective photon bunching with thermal-like statistics. The experimental findings were supported by a theoretical model that reproduced the observed behavior.

Placement within the research landscape. Before outlining the near- and mid-term steps required to transform the present experiment into a realistic building block for quantum network applications, we place the achieved results within the broader research landscape of cavity-integrated group-IV color centers in diamond. To this end, we compare the main figure of merit, the coherent cooperativity C, as summarized in Fig. 8.1, considering published experiments on group-IV defects that explicitly report a coherent cooperativity.

With a coherent cooperativity of $C = 1.4$, our work represents the highest value reported to date among microcavity-based platforms and constitutes, to the best of our knowledge, the only demonstration for cavity-integrated group-IV color centers heavier than the silicon-vacancy center in which optical Zeeman splitting is observed. These heavier group-IV centers are of particular interest due to their reduced sensitivity to phonon-induced decoherence and the resulting relaxation of cryogenic temperature requirements, in contrast to the well-established SiV platform.

We highlight that quantum networking experiments have already been realized in a two-node network demonstrated by Knaut *et al.* [43], in which one node exhibited a coherent cooperativity of $C = 1.5$, only slightly larger than the value demonstrated here. This comparison emphasizes that even moderate cooperativities are sufficient for implementing such network demonstrations. While nanophotonic cavity architectures currently achieve larger cooperativities due to their ultrasmall mode volumes, this comparison serves to motivate the next logical steps for optimizing the present microcavity platform and for incorporating additional functionality required for quantum network applications.

Near-term improvements. Several near-term improvements have been identified that could substantially enhance the performance of the present system and move it closer to a practical spin–photon interface for quantum network applications. As discussed in Sec. 6.4, a first step concerns the reduction of excess cavity losses observed at the current lateral position. Recovering the typical diamond-like finesse of $\mathcal{F}_a = 1\,700$, compared to the presently achieved $\mathcal{F}_a = 1\,200$, would already result in a noticeable increase of the coherent cooperativity.

A second, equally important aspect is the availability of emitters with lifetime-limited optical coherence. In the current sample, the shallow implantation depth of approximately 10 nm likely leads to charge-induced spectral diffusion, making such linewidths difficult to achieve. By contrast, lifetime-limited SnV centers were observed in samples with increased implantation depths, and the likelihood of identifying suitable emitters improves further for even deeper implantation. Motivated by these observations, the next diamond membrane currently under fabrication will feature an implantation depth of approximately 100 nm. In combination with restored diamond-like cavity performance, this is expected to enable significantly larger cooperativities. The combined effect of lifetime-limited emitters and recovery of the typical diamond-like finesse would increase the cooperativity to $C \approx 9$, as indicated in Fig. 8.1. Such realistic improvements would place the system among the largest coherent cooperativities reported for SnV centers and at values comparable to those employed in the two-node quantum network demonstration of Ref. [43].

At the same time, the realization of a functional quantum network node requires more than strong light–matter coupling alone. Efficient photon extraction and transmission, particularly into a fiber-based network, are equally crucial. Consequently, future efforts must also focus on improving mode matching, reducing overall optical losses, and optimizing the coupling of the cavity mode into single-mode fibers. As discussed in Sec. 6.4,

these system-level optimizations offer substantial room for improvement and represent essential next steps toward scalable quantum network demonstrations.

Towards a quantum network at Karlsruhe Institute of Technology (KIT). With the current platform, one central ingredient required for spin–photon entanglement is still missing, namely experimental access to efficient and coherent spin control. In principle, this can be achieved either via optical Raman driving schemes [100] or via direct microwave control [95, 96, 97]. In practice, microwave control is usually favorable, as it enables direct manipulation of the ground-state spin independently of the optical interface. By contrast, optical Raman control relies on two-tone, high-power laser driving via virtual excited states and can therefore be susceptible to optically induced charge instability, local heating, and residual excited-state population, all of which can degrade spin coherence and optical stability.

Microwave spin control can be integrated into fiber-based Fabry–Pérot cavities by incorporating microwave striplines on the mirror substrate, followed by bonding of the diamond membrane on top [221], with promising results demonstrated for cavity-integrated NV centers [180, 222]. This geometry enables efficient microwave delivery without obstructing the optical mode or compromising cavity performance. Extending this approach by employing superconducting microwave waveguides, as demonstrated in Refs. [97, 126], represents a promising route toward efficient microwave spin control with minimal heat load.

An alternative approach currently under investigation within our group employs an Ω-shaped wire loop surrounding the cavity fiber. This geometry allows the microwave conductor to be positioned in close proximity to the diamond membrane, enabling large magnetic field amplitudes and fast spin driving without direct contact to the sample, thereby

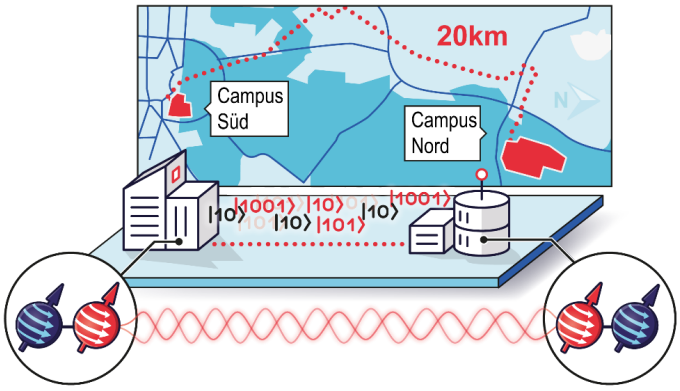

Figure 8.2: Glass-fiber testbed for quantum network demonstrations in Karlsruhe. Deployed fiber link connecting Campus South and Campus North of the Karlsruhe Institute of Technology over a distance of approximately 20 km. Figure adapted from Ref. [220].

minimizing local heating. Its compatibility with the microcavity platform employed here, as well as its feasibility under cryogenic operating conditions, remain to be demonstrated.

The second key ingredient for efficiently distributing entanglement over long distances is quantum frequency conversion of visible photons to telecom wavelengths, where fiber attenuation is minimal. Beyond loss reduction, frequency conversion enables spectral matching of solid-state quantum emitters, which are typically subject to significant spectral inhomogeneities, and is therefore essential for achieving photon indistinguishability. The feasibility of quantum frequency conversion for SnV centers in diamond has recently been demonstrated in Ref. [223], and frequency conversion has been successfully employed in long-distance quantum network experiments across several material platforms whose native emission wavelengths lie outside the telecom band [28, 224, 43].

Incorporating these two essential steps into the current experimental platform would enable a transition from a single spin–photon interface toward the entanglement of distant, cavity-integrated SnV centers in diamond. As a concrete midterm objective, a second quantum network node is envisioned in a laboratory at Campus North. A glass-fiber testbed spanning more than 20 km between Campus South and Campus North of the Karlsruhe Institute of Technology (KIT) is already in operation and serves as a research platform for quantum communication, as illustrated in Fig. 8.2 [220]. This testbed currently hosts commercial continuous-variable quantum key distribution (CV-QKD) links and provides a unique opportunity to extend established quantum cryptographic infrastructure toward memory-enhanced quantum network demonstrations. By leveraging efficient spin–photon interfaces based on cavity-integrated SnV centers in diamond, this existing infrastructure can support the next step of transmitting and entangling quantum states over real deployed fiber, thereby laying a foundation for scalable quantum networks.

A. Appendix

A.1. Useful dissipator relations

For reference, we collect a few dissipator identities used in the main text. These expressions assume unit-strength jump operators L (i.e. omitting prefactors such as $\sqrt{\kappa}$, $\sqrt{\gamma_0}$, $\sqrt{\gamma^\star/2}$), so that only the operator structure is shown. Prefactors can be reinserted as needed.

Cavity decay ($L = \hat{a}$).

$$\mathcal{D}^\dagger[\hat{a}]\,\hat{a} = -\tfrac{1}{2}\,\hat{a}.$$

Spontaneous emission ($L = \hat{\sigma}_-$).

$$\mathcal{D}^\dagger[\hat{\sigma}_-]\,\hat{\sigma}_- = -\tfrac{1}{2}\,\hat{\sigma}_-,$$
$$\mathcal{D}^\dagger[\hat{\sigma}_-]\,\hat{\sigma}_z = -(\hat{\sigma}_z + \mathbb{I}).$$

Pure dephasing ($L = \hat{\sigma}_z$).

$$\mathcal{D}^\dagger[\hat{\sigma}_z]\,\hat{\sigma}_- = -2\,\hat{\sigma}_-,$$
$$\mathcal{D}^\dagger[\hat{\sigma}_z]\,\hat{\sigma}_z = 0.$$

A.2. Purcell rate starting from the hybridized decay rates

On resonance ($\Delta = 0$), the hybridized cavity–emitter modes have coherence (polarization) decay rates

$$\Gamma_\pm \;=\; \frac{\gamma_0 + \kappa}{4} \;\pm\; \mathrm{Re}\left\{\sqrt{\left(\tfrac{\kappa-\gamma_0}{4}\right)^2 - g^2}\right\}. \tag{A.2.1}$$

Introduce the scale

$$a \;\equiv\; \tfrac{|\kappa-\gamma_0|}{4}, \tag{A.2.2}$$

so that in the weak-coupling/bad-cavity limit ($g \ll a$),

$$\sqrt{a^2 - g^2} \;=\; a\sqrt{1 - \tfrac{g^2}{a^2}} \;\approx\; a - \tfrac{g^2}{2a}. \tag{A.2.3}$$

For the typical case $\kappa > \gamma_0$ (hence $a = (\kappa - \gamma_0)/4$), the atom-like branch corresponds to the minus sign in (A.2.1). Using (A.2.3) gives

$$\begin{aligned}\Gamma_{\text{atom}} &= \frac{\gamma_0 + \kappa}{4} \;-\; \left(a - \tfrac{g^2}{2a}\right) \\ &= \tfrac{\gamma_0}{2} \;+\; \tfrac{g^2}{2a} = \tfrac{\gamma_0}{2} \;+\; \tfrac{2g^2}{\kappa - \gamma_0}.\end{aligned} \tag{A.2.4}$$

Equation (A.2.4) is the coherence decay rate of the atom-like mode. Since in the absence of pure dephasing the population decay rate is twice the coherence decay rate, the effective population decay becomes

$$\gamma_c \;=\; \gamma_0 \;+\; 2\big(\Gamma_{\text{atom}} - \tfrac{\gamma_0}{2}\big) \;=\; \gamma_0 \;+\; \tfrac{4g^2}{\kappa - \gamma_0}. \tag{A.2.5}$$

In the Purcell (bad-cavity) limit $\kappa \gg \gamma_0$, this simplifies to the familiar form

$$\gamma_c \;\approx\; \gamma_0 \;+\; \frac{4g^2}{\kappa}, \qquad C_0 \;=\; \frac{\gamma_c}{\gamma_0} - 1 \;\approx\; \frac{4g^2}{\kappa\,\gamma_0}. \tag{A.2.6}$$

This is the Purcell-enhanced spontaneous emission rate at zero detuning, as used in the main text.

A.3. Transmission and reflection

Empty cavity (no emitter). In steady state, the expectation value of the intracavity field operator obeys

$$0 = -\Big(\tfrac{\kappa}{2} - i\Delta_c\Big)\langle a\rangle + \eta \quad\Rightarrow\quad \langle a\rangle = \frac{\eta}{\frac{\kappa}{2} - i\Delta_c}, \qquad \Delta_c \equiv \omega_l - \omega_c. \tag{A.3.1}$$

With the symmetric input–output relations and driving through mirror 1 only,

$$\hat{a}_{1,\text{in}} + \hat{a}_{1,\text{out}} = \sqrt{\kappa_1}\,\hat{a}, \qquad \hat{a}_{2,\text{out}} = \sqrt{\kappa_2}\,\hat{a}, \qquad \langle \hat{a}_{1,\text{in}}\rangle = \eta/\sqrt{\kappa_1}, \quad \langle \hat{a}_{2,\text{in}}\rangle = 0, \tag{A.3.2}$$

the complex transmission and reflection amplitudes are

$$t_c(\omega_l) \equiv \frac{\langle \hat{a}_{2,\text{out}}\rangle}{\langle \hat{a}_{1,\text{in}}\rangle} = \frac{\sqrt{\kappa_1\kappa_2}}{\eta}\,\langle a\rangle = \frac{\sqrt{\kappa_1\kappa_2}}{\frac{\kappa}{2} - i\Delta_c}, \tag{A.3.3a}$$

$$r_c(\omega_l) \equiv \frac{\langle \hat{a}_{1,\text{out}}\rangle}{\langle \hat{a}_{1,\text{in}}\rangle} = \frac{\kappa_1}{\eta}\,\langle a\rangle - 1 = \frac{\kappa_1}{\frac{\kappa}{2} - i\Delta_c} - 1 = \frac{\kappa_1 - \frac{\kappa}{2} + i\Delta_c}{\frac{\kappa}{2} - i\Delta_c}. \tag{A.3.3b}$$

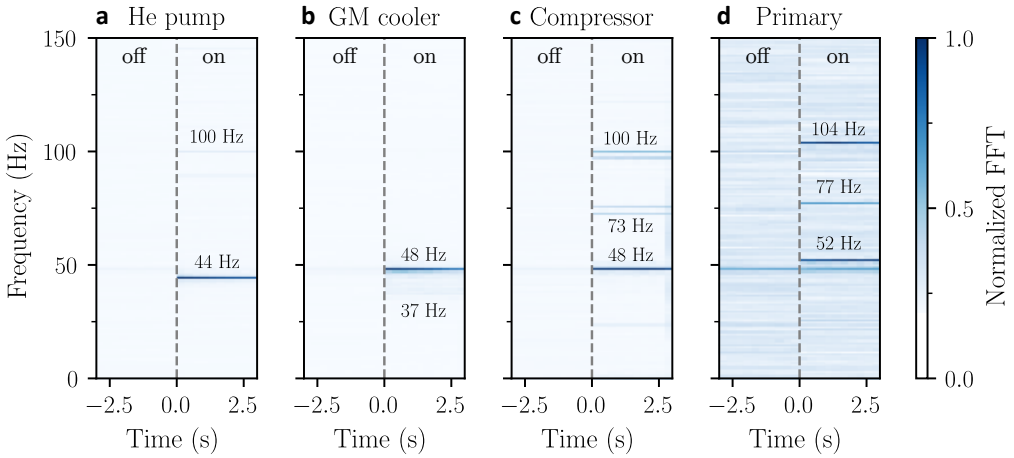

Figure A.1: Noise spectra of the Qinu gas handling system. Normalized vibration spectra measured near the helium pump **(a)**, GM cooler **(b)**, compressor **(c)**, and primary pump **(d)**. For each device, spectra recorded with the device switched off and on are shown for comparison; dominant frequency components are labeled. Each spectrum is normalized to its maximum peak height.

On resonance. For $\Delta_c = 0$,

$$t_c(0) = \frac{2\sqrt{\kappa_1\kappa_2}}{\kappa}, \qquad r_c(0) = \frac{2\kappa_1}{\kappa} - 1. \tag{A.3.4}$$

In particular, a symmetric cavity with $\kappa_1 = \kappa_2$ has unit transmission and zero reflection on resonance.

Power coefficients and loss. If the cavity is lossless ($\kappa = \kappa_1 + \kappa_2$), then

$$T(\omega_l) = |t_c|^2 = \frac{\kappa_1\kappa_2}{(\frac{\kappa}{2})^2 + \Delta_c^2}, \qquad R(\omega_l) = |r_c|^2 = \frac{(\kappa_1 - \frac{\kappa}{2})^2 + \Delta_c^2}{(\frac{\kappa}{2})^2 + \Delta_c^2}, \qquad T + R = 1. \tag{A.3.5}$$

With additional internal loss κ_{loss} (so $\kappa = \kappa_1 + \kappa_2 + \kappa_{\text{loss}}$), the corresponding scattered channel has amplitude $\ell_{\text{out}} = \sqrt{\kappa_{\text{loss}}}\, a$, which contributes the extra loss coefficient

$$L(\omega_l) = \frac{\kappa_1\kappa_{\text{loss}}}{(\frac{\kappa}{2})^2 + \Delta_c^2}, \qquad T + R + L = 1. \tag{A.3.6}$$

A.4. Noise spectra of the Qinu gas handling system

Although the cryostat gas handling system is located in a separate room, mechanical vibrations can still be transmitted to the cryostat via the tubing connecting the pumps and liquefier to the cryostat chamber mounted on the optical table. To quantify these effects, we analyzed the vibrational noise spectra of the four dominant mechanical noise sources:

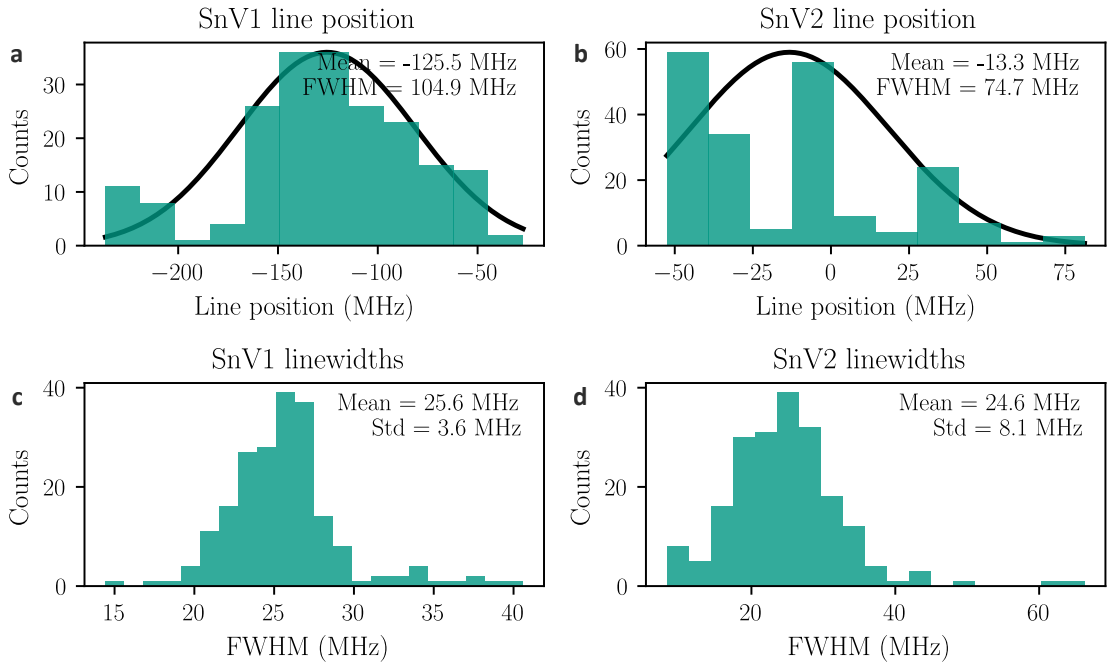

Figure A.2: Spectral diffusion and single-scan linewidths of sample CA1. (a,b) Histograms of the extracted central line positions of SnV1 and SnV2 under repeated resonant excitation, fitted with Gaussian distributions to quantify spectral diffusion. **(c,d)** Histograms of the corresponding single-scan FWHM linewidths, demonstrating lifetime-limited emission for both SnV centers.

the helium pump of the ^{4}He circuit, the GM cooler, and the compressor and primary pump circulating the ^{3}He/^{4}He mixture.

The spectra were measured using the built-in acceleration sensor of a standard smartphone placed in close proximity to the respective devices. Data acquisition and spectral analysis were performed using the *phyphox* application developed at RWTH Aachen University [225]. While this approach does not provide calibrated absolute acceleration values, it enables a robust comparison of relative spectral features and dominant frequency components across devices.

The resulting spectra are shown in Fig. A.1, comparing measurements with each device turned off and on. All spectra are normalized to their respective maximum peak height, and the dominant frequency components are indicated.

A.5. Detailed data on Stuttgart samples

Spectral diffusion and single-scan linewidths of sample CA1. The two SnV centers investigated in Sec. 5.1.3 are further analyzed with respect to their spectral diffusion and single-scan linewidths under resonant excitation. Each individual resonance scan is fitted

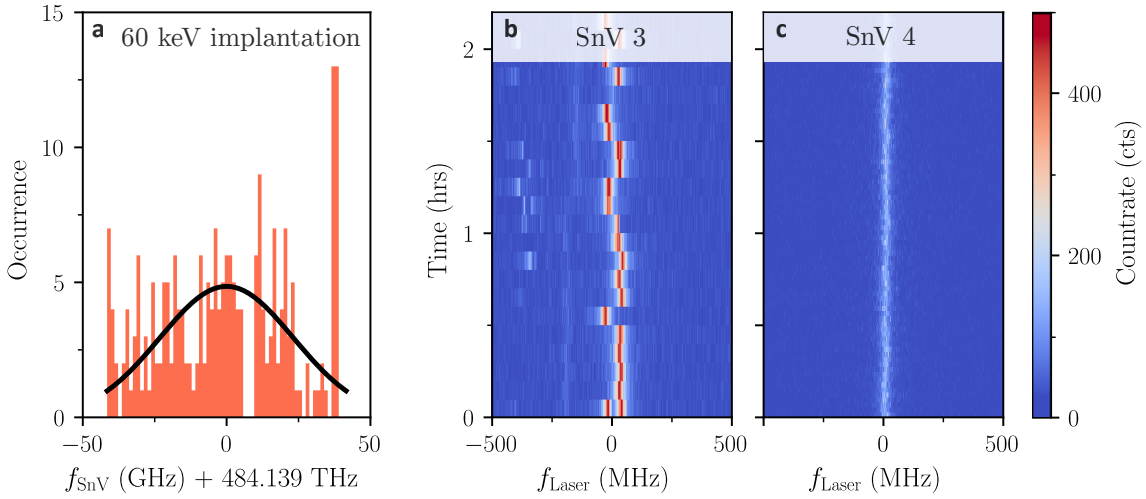

Figure A.3: Cryogenic resonant characterization of SnV centers implanted at 60 keV. (a) Histogram of the zero-phonon line (ZPL) frequencies of several hundred SnV centers measured within the confocal field of view. **(b,c)** Photoluminescence excitation (PLE) spectra of two representative emitters identified in the same region.

with a Lorentzian profile, from which the central line position and linewidth are extracted. The resulting distributions for SnV1 and SnV2 are shown in Fig. A.2.

Spectral diffusion is quantified by fitting a Gaussian to the distribution of central line positions shown in Fig. A.2(a,b), yielding full widths at half maximum of 105 MHz for SnV1 and 75 MHz for SnV2. In contrast, the distributions of single-scan linewidths, shown in Fig. A.2(c,d), reveal Fourier-limited emission for both emitters, with mean FWHM linewidths of 26(4) MHz and 25(8) MHz, respectively.

PLE measurements for 60 keV and 100 keV implantation energies. As discussed in Sec. 5.1.3, in addition to sample CA1 implanted with tin ions at an energy of 30 keV, a second diamond plate was prepared with two separate implantation regions at 60 keV and 100 keV. The results of cryogenic PLE measurements for these regions are presented in Fig. A.3 and Fig. A.4, respectively.

For all implantation energies investigated, the observed resonances are lifetime-limited and exhibit inhomogeneous ZPL frequency distributions centered at similar optical frequencies, as well as stable charge configurations over several hours of measurement. A systematic comparison of spectral diffusion across implantation energies would require the investigation of a larger number of individual emitters and was therefore not pursued here. Nevertheless, individual centers such as SnV4 (60 keV, see Fig. A.3c) and SnV6 (100 keV, see Fig. A.4c) display near-ideal spectral stability, indicating favorable conditions for the generation of highly indistinguishable photons.

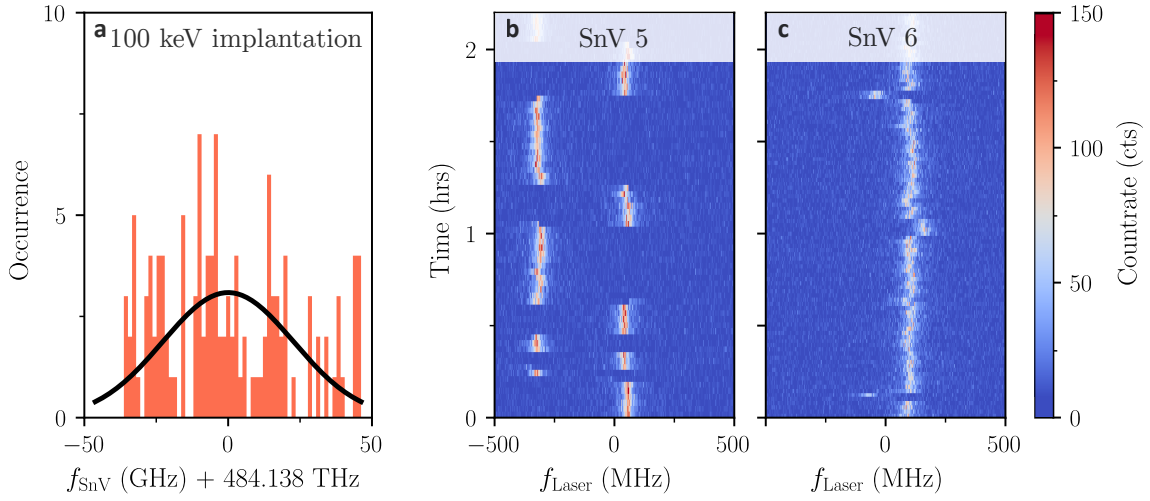

Figure A.4: Cryogenic resonant characterization of SnV centers implanted at 100 keV. (a) Histogram of the zero-phonon line (ZPL) frequencies of several hundred SnV centers measured within the confocal field of view. **(b,c)** Photoluminescence excitation (PLE) spectra of two representative emitters identified in the same region.

Taken together, these observations suggest that the bonding procedure and the resulting close proximity of the diamond–glass interface in the 30 keV implanted sample contribute to the non–lifetime-limited emission and reduced charge stability observed for cavity-integrated sample CA1. This indicates that deeper implantation depths may be advantageous for future cavity-integrated diamond membranes hosting SnV centers.

A.6. End-to-end detection efficiency

We estimate the probability for a photon incident on the cavity input fiber to be detected on the SPCM in transmission. Thus, we measure the on-resonance cavity transmission power P_{trans} and compare it to the optical power before fiber coupling P_{laser}, obtaining

$$P_{\text{trans}}/P_{\text{laser}} \approx 0.17\,\%.$$

This ratio can be written as the product of three dominant contributions,

$$\frac{P_{\text{trans}}}{P_{\text{laser}}} \approx \eta_{\text{fiber}}\,\eta_{\text{mm}}\,T_{c,\text{max}}, \qquad T_{c,\text{max}} = \frac{4\kappa_1\kappa_2}{\kappa^2},$$

where η_{fiber} is the fiber coupling efficiency, η_{mm} the spatial mode-matching efficiency, and the total cavity linewidth is $\kappa = \kappa_1 + \kappa_2 + \kappa_{\text{loss}}$.

The cavity linewidth was measured to be $\kappa/2\pi = 16.2$ GHz. The coupling rates κ_1 and κ_2 correspond to the fiber-side (incoupling) and sample-side (outcoupling) mirrors, respectively, while κ_{loss} accounts for all additional parasitic loss channels.

Assuming a fully diamond-like cavity mode, the mirror transmission losses are taken from a transfer-matrix model as $\mathcal{L}_{\mathrm{M,a}} = 623\,\mathrm{ppm}$ (fiber mirror) and $\mathcal{L}_{\mathrm{M,d}} \cdot n_d = 1\,364\,\mathrm{ppm}$ (sample mirror), corresponding to a design finesse of $\mathcal{F}_{\mathrm{design}} \approx 3160$. The measured finesse $\mathcal{F}_{\mathrm{meas}} \approx 1200$ implies additional round-trip parasitic losses of approximately 3 200 ppm, which we attribute to scattering and absorption. Partitioning the total linewidth according to these loss channels yields approximate values

$$\kappa_1/2\pi \approx 1.9\,\mathrm{GHz}, \qquad \kappa_2/2\pi \approx 4.2\,\mathrm{GHz}, \qquad \kappa_{\mathrm{loss}}/2\pi \approx 10.1\,\mathrm{GHz}.$$

Including these residual losses reduces the expected on-resonance cavity transmission to $T_{c,\mathrm{max}} \approx 12\,\%$.

Using this value together with the measured transmission ratio, we infer a combined mode-matching and fiber incoupling efficiency of

$$\eta_{\mathrm{mm}}\eta_{\mathrm{fiber}} \approx \frac{P_{\mathrm{trans}}}{P_{\mathrm{laser}} T_{c,\mathrm{max}}} \approx 3.5\%,$$

which should be regarded as a rough, order-of-magnitude estimate of the optical coupling into the cavity mode. The fiber coupling efficiency was measured by cutting the the fiber behind the connector after performing the measurements, where we determine $\eta_{\mathrm{fiber}} = 0.6$, which leaves us with a mode matching efficiency of $\eta_{\mathrm{mm}} = 0.023$.

To determine the losses and detection efficiency of the collection path, we apply several ($10^{-8} - 10^{-9}$) neutral density filters to bring the ~mW laser power into a regime detectable with a SPCM, which allows us to calculate the photon flux in cavity transmission which we compare to the detected photons on the SPCM which yields a detection efficiency of the free space cavity mode of $\eta_{\mathrm{fs}} = 26\,\%$[48].

This allows us to infer the photon flux impinging on the cavity from the detected on-resonance photon rate A as

$$|\langle a_{1,\mathrm{in}}\rangle|^2 = \frac{A}{\eta_{\mathrm{fs}}\, T_{c,\mathrm{max}}} \;\approx\; 32\,A, \tag{A.6.1}$$

Using the coherent cooperativity extracted in Chapter 6.3.1, the corresponding input photon number per Purcell-enhanced lifetime according to Eq. (3.2.28) is

$$n_{\mathrm{in}} = \frac{2\kappa_1}{\kappa}\frac{|\langle a_{1,\mathrm{in}}\rangle|^2}{(C+1)\gamma_0} \;\approx\; 0.24 \times (2.6\,\mathrm{ns}) \times 32\,A, \tag{A.6.2}$$

where $(C+1)\gamma_0$ is the Purcell-enhanced population decay rate of the emitter.

[48] Taking the SPCM quantum efficiency of $\eta_{\mathrm{SPCM}} \approx 75\,\%$, we can estimate the optical transmission in the detection path combined with the focusing efficiency on the detector aperture of $\eta_{\mathrm{opt}} \approx 35\,\%$.

A.7. Three more SnVs showing extinction

In the course of this work, we observed multiple (~10) extinction features in the cavity transmission originating from SnV centers. The emitter discussed in Sec. 6.3 was selected because it exhibited the most favorable charge stability and the largest light–matter coupling strength. In this appendix, we present extinction data for three additional SnV centers: two measured in sample AB2 and one in sample CA1 (see Fig. A.5). The corresponding cavity QED parameters extracted from fits to the transmission spectra are summarized in Table A.1.

Table A.1: Extracted cavity QED parameters for the SnV centers shown in Fig. A.5. The emitter CA1–1 (bold) is analyzed in detail in the main text. All parameters are given as angular frequencies divided by 2π.

Emitter	$g/2\pi$ (GHz)	$\kappa/2\pi$ (GHz)	$\gamma_{\mathrm{tot}}/2\pi$ (GHz)	C
CA1–1	**0.81(4)**	**16.2(5)**	**0.12(2)**	**1.4(4)**
AB2–1	0.15(2)	8.1(3)	0.027(9)	0.46(7)
AB2–2	0.16(5)	7.9(1)	0.07(2)	0.21(4)
CA1–2	0.72(5)	13.1(8)	0.16(4)	1.0(2)

The SnV center AB2–1 (Fig. A.5a,d) was the only emitter across both samples that exhibited a near transform-limited linewidth, with $\gamma_{\mathrm{tot}}/2\pi = 0.027(9)$ GHz. Sample AB2 was implanted at approximately twice the depth of sample CA1. Together with the linewidth observed for AB2–2, $\gamma_{\mathrm{tot}}/2\pi = 0.07(2)$ GHz—both of which are smaller than those measured in sample CA1—these observations suggest that deeper implantation can improve the homogeneous linewidth and may be an important ingredient for achieving large coherent cooperativities.

Overall, the SnV centers in sample AB2 exhibit lower cooperativities than those measured in sample CA1. We attribute this primarily to operation with an air-like hybrid cavity mode, as well as to non-optimal lateral mode overlap and imperfect polarization matching.

A.8. Charge stability in terms of photon budget

To further quantify the power-induced degradation of charge stability, beyond the number of consecutive scans for which the SnV center remains in the bright charge state shown in Fig. A.6a, we introduce the quantity N_{ext}. It is defined as the total number of photons extincted from the bare cavity transmission by the SnV center before a transition into a dark charge state occurs.

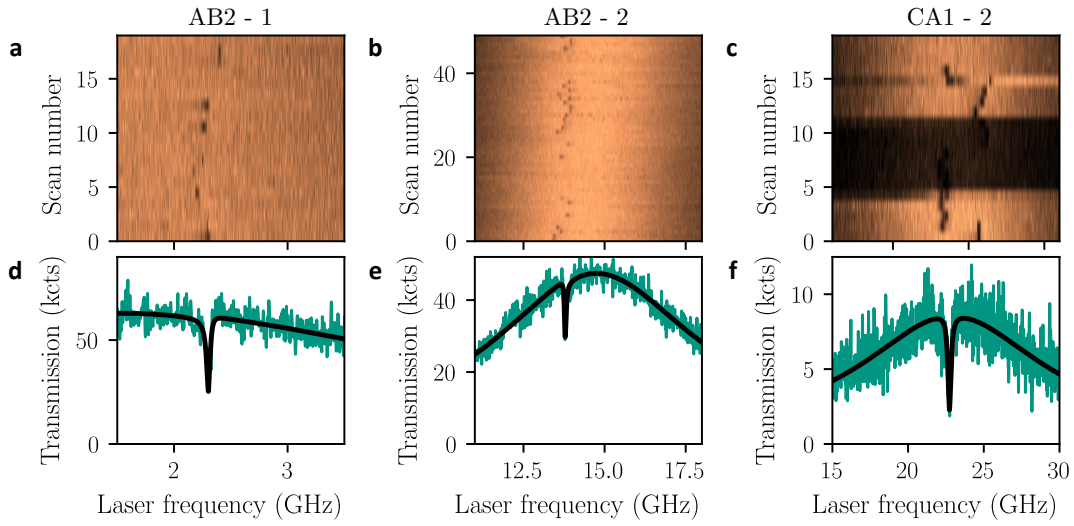

Figure A.5: Extinction signatures of three additional SnV centers. (a–c) Cavity transmission maps as a function of laser frequency and scan number for three different SnV centers (AB2–1, AB2–2, and CA1–2). Dark features indicate extinction of the cavity transmission when the emitter is resonant. **(d–f)** Corresponding single-scan transmission spectra (colored traces) together with fits to the cavity QED model (black lines). All spectra are plotted in transmission counts and referenced to the laser frequency. The extracted coupling parameters and cooperativities are summarized in Table A.1. For SnV CA1-2, the laser power was varie during the scan, which leads to the darker region in the scan.

Here, a *scan* refers to a complete linear frequency sweep of the probe laser across the emitter resonance. For such a linear sweep, the number of photons extincted during a single scan can be approximated as

$$N_{\mathrm{ph}}^{\mathrm{scan}} = A\,C\,\frac{\pi}{2}\,\frac{\gamma_{\mathrm{tot}}}{\dot{\nu}}, \tag{A.8.1}$$

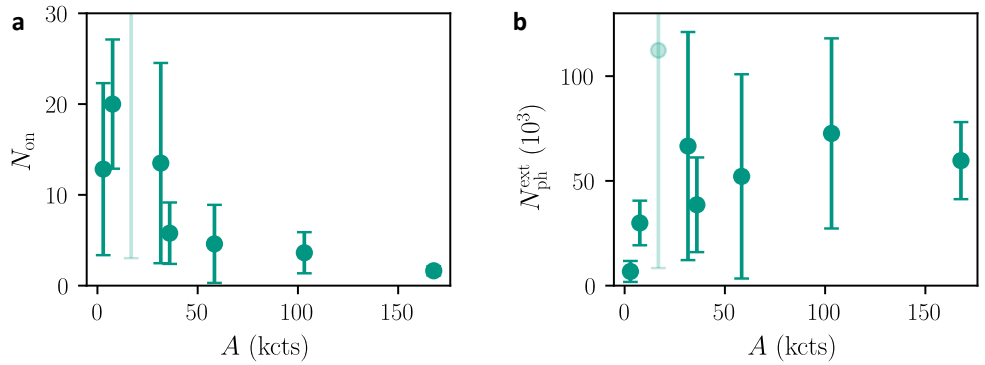

Figure A.6: Photon budget before charge-state switching. (a) Average number of consecutive frequency scans for which the SnV center remains in the bright charge state before switching. **(b)** Total number of photons extincted from the bare cavity transmission prior to a charge-state transition.

where A denotes the peak cavity transmission count rate (in counts per second), $C = 1-1/(C+1)^2$ is the on-resonant cavity extinction contrast, γ_{tot} is the total emitter linewidth, and $\dot{\nu}$ is the laser scan speed. The prefactor $\pi/2$ results from integrating an approximately Lorentzian extinction profile over a linear frequency sweep.

The total number of extincted photons prior to charge-state switching is then given by

$$N_{\mathrm{ext}} = N_{\mathrm{ph}}^{\mathrm{scan}}\, N_{\mathrm{on}}, \tag{A.8.2}$$

where N_{on} denotes the average number of consecutive scans for which the SnV center remains in the bright charge state. The resulting values of N_{ext} are shown in Fig. A.6b.

For peak transmission rates above $A \gtrsim 20\,\mathrm{kcts/s}$, we observe, within experimental uncertainty, an approximately constant photon budget of $N_{\mathrm{ext}} \approx 6 \times 10^4$ extincted photons prior to a charge-state transition.

A.9. List of symbols

This section summarizes the most important symbols used throughout the thesis. The list is not complete but emphasizes quantities that recur across multiple chapters or are prone to confusion.

Sq	Surface roughness (RMS)
Δ_g	Ground-state orbital splitting
Δ_u	Excited-state orbital splitting
$\Delta\nu_{\mathrm{spin}}$	Optical spin splitting of the C-transition (A1–B2)
f_{SnV}	Frequency of the SnV C-transition
f^0_{SnV}	Nominal (unstrained) SnV C-transition frequency
ϕ	Cavity round-trip phase
$\Delta\nu_{\mathrm{FSR}}$	Free spectral range (frequency units)
FSR	Free spectral range (length units)
$\delta\nu_{\mathrm{cav}}$	Cavity linewidth (FWHM)
Q	Cavity quality factor
$T_{1,2}$	Mirror transmission losses
τ_{cav}	Cavity ringdown time
$\mathcal{F}$	Cavity finesse (no membrane)
$\mathcal{L}$	Cavity loss per round trip (no membrane)
$\mathcal{F}_{\mathrm{a/d}}$	Finesse with membrane (air-/diamond-referenced)
$\mathcal{L}_{\mathrm{M,a/d}}$	Mirror losses (air-/diamond-terminated)
$\mathcal{L}_{\mathrm{M,eff,a/d}}$	Effective mirror losses per air/diamond round trip
$\mathcal{L}_{\mathrm{tot,a/d}}$	Total effective cavity losses per air/diamond round trip
t_d	Diamond membrane thickness
t_a	Cavity air gap
t_{pen}	Air-/diamond-like field penetration depth
$\mathcal{I}_{A/D}$	Air/diamond intensity ratio

L	Cavity length (no membrane)
$L_{\mathrm{eff,a/d}}$	Effective cavity length (air-/diamond-referenced)
ω_l	Probe laser angular frequency
ω_c	Cavity resonance angular frequency
ω_a	Emitter transition angular frequency
Δ_c	Cavity–laser detuning
Δ_a	Emitter–laser detuning
Δ_{ca}	Cavity–emitter detuning
χ	Cavity driving strength
g	Coherent emitter–cavity coupling strength (rad/s)
κ	Total cavity intensity decay rate (rad/s)
γ_0	Free-space spontaneous decay rate (rad/s)
$\gamma^\star$	Pure dephasing rate (rad/s)
$\gamma_\perp$	Transverse decoherence rate (rad/s)
γ_{tot}	Total emitter linewidth (rad/s, $\gamma_{\mathrm{tot}} = 2\gamma_\perp$)
γ_c	Cavity-enhanced decay rate (rad/s)
γ_{12}	Free-space decay rate of the Purcell-enhanced transition only (rad/s)
τ_0	Free-space excited-state lifetime
τ_c	Cavity-modified excited-state lifetime
V_m	Cavity mode volume
V_{eff}	Effective mode volume normalized at emitter position
w_0	Cavity mode waist
ξ	Dipole projection factor
F_P	Purcell factor
C_0	Cooperativity
C	Coherent cooperativity
β_{DW}	Debye–Waller factor

β_{QE}	Quantum efficiency
$\beta_{\mathrm{C/D}}$	Branching ratio of the SnV C-transition
β_{tot}	Overall branching ratio
β_{C}	Coherent β-factor
$\beta_{\mathrm{C_0}}$	Incoherent β-factor (Fraction of photons emitted into cavity mode)
t_c, r_c	Complex cavity transmission and reflection amplitudes
T_c, R_c, S_c	Transmitted, reflected, and scattered intensities
$T_{c,\mathrm{max}}$	On-resonance cavity transmission
$\mathcal{P}_t$	Transmission probability
C	Transmission contrast
C_{spin}	Spin-dependent transmission contrast
n_{in}	Input photon number per lifetime
n_{crit}	Critical photon number
s	Saturation parameter
η_{mm}	Mode-matching efficiency
η_{det}	Total detection efficiency
η_{SPCM}	SPCM quantum efficiency
η_{fs}	Free-space collection efficiency
η_{fiber}	Fiber coupling efficiency
η	Incoherent pump rate (superfluorescence context)

A.10. List of abbreviations

QR	Quantum repeater
QKD	Quantum key distribution
NV	Nitrogen-vacancy
SnV	Tin-vacancy
SiV	Silicon-vacancy
GeV	Germanium-vacancy
PbV	Lead-vacancy
cQED	Cavity quantum electrodynamics
ZPL	Zero-phonon line
PSB	Phonon sideband
HOM	Hong–Ou–Mandel
ODMR	Optically detected magnetic resonance
DFT	Density-functional theory
DD	Dynamical decoupling
FWHM	Full width at half maximum
WGM	Whispering-gallery mode
FIB	Focused ion beam
ROC	Radius of curvature
DBR	Distributed Bragg reflector
FSR	Free spectral range
APD	Avalanche photodiode
ASD	Amplitude spectral density
PSD	Power spectral density
FFT	Fast Fourier transform
RMS	Root-mean-square

GM	Gifford–McMahon
PID	Proportional–integral–derivative
AFM	Atomic force microscopy
CVD	Chemical vapor deposition
SRIM	Stopping and Range of Ions in Matter
TRIM	Transport of Ions in Matter
PL	Photoluminescence
PLE	Photoluminescence excitation
ICP–RIE	Inductively coupled plasma reactive ion etching
CW	Continuous wave
DM	Dichroic mirror
PBS	Polarizing beamsplitter
NF	Notch filter
SPCM	Single-photon counting module
SNSPD	Superconducting nanowire single-photon detector
TEM	Transverse electromagnetic mode
TCSPC	Time-correlated single-photon counting
PMMA	Polymethyl methacrylate
CV-QKD	Continuous-variable quantum key distribution

List of Figures

1.1. Quantum repeater scheme . . . 2

2.1. Nitrogen–vacancy center level structure . . . 10
2.2. Vibronic broadening of the NV center ZPL . . . 11
2.3. Inversion symmetry of the SnV center . . . 14
2.4. Tin–vacancy center level structure . . . 16
2.5. Phonon-induced optical and spin decoherence . . . 18

3.1. Fabry–Pérot cavity . . . 24
3.2. Gaussian mode in a plano–concave cavity . . . 26
3.3. Cavity–emitter coupling model . . . 27
3.4. Hybridized cavity–emitter modes . . . 30
3.5. Cavity transmission T_c, reflection R_c, and scattering S_c spectra . . . 34
3.6. Saturation of the extinction contrast in transmission . . . 36
3.7. Collective cavity–emitter coupling model . . . 41
3.8. Emission dynamics for the coherent (Dicke) and incoherent ensemble . . . 44

4.1. Quality factor and mode volume across different cavity platforms . . . 50
4.2. A fiber-based Fabry–Pérot microcavity . . . 52
4.3. Fiber mirror . . . 53
4.4. Qlibri microcavity platform . . . 55
4.5. Qlibri cavity operation . . . 58
4.6. Integration of a Qlibri microcavity platform into a Qinu dilution refrigerator 61
4.7. Cooldown and thermalization of the Qlibri microcavity platform inside the Qinu dilution refrigerator . . . 62
4.8. Cavity stability requirements . . . 64
4.9. Cavity stability at 5 K . . . 67
4.10. Cavity stability at different temperatures . . . 69
4.11. Integration of a superconducting magnetic coil . . . 72
4.12. Finite-element simulation of the magnetic field generated by the coil . . . 74

5.1. AFM topographies of different surface polishes . . . 78
5.2. SRIM simulation of tin implantation in diamond . . . 79
5.3. Crystal–TRIM simulation of tin implantation in diamond . . . 81
5.4. Room-temperature confocal microscopy of samples DDK1 and AB2 . . . 82
5.5. Cryogenic resonant characterization of sample CA1 . . . 83
5.6. Van der Waals bonding procedure . . . 85

5.7. Surface roughness, bonding, and etching of sample AB2 86
5.8. Electric-field distributions for air-like and diamond-like modes 88
5.9. Hybrid cavity mode dispersion 95
5.10. SnV mirror coating 96
5.11. Air-like and diamond-like cavity finesse $\mathcal{F}_{\mathrm{a}}$ 98

6.1. Cryogenic microcavity platform and optical setup 102
6.2. Cavity mode dispersion under off-resonant excitation 104
6.3. Hyperspectral fluorescence maps 105
6.4. Spectral properties of detected SnV centers 106
6.5. Saturation count rate of SnV 1 108
6.6. Lifetime shortening and Purcell factor 110
6.7. Lifetime shortening for air-like and diamond-like cavity modes 112
6.8. Monte–Carlo evaluation of expected Purcell factors 114
6.9. SnV-induced extinction in the cavity transmission profile 118
6.10. Distribution of the fitted cQED parameters 120
6.11. Power-dependent extinction properties 123
6.12. Cavity extinction with and without magnetic field 125
6.13. Evaluation of the Zeeman splitting 127
6.14. Spin contrast for variable cavity detuning and spin splitting 130

7.1. Overview of cavity-mediated emission from color centers in diamond 134
7.2. Experimental platform for cavity-mediated collective emission 135
7.3. Cavity-enhanced fluorescence spectra of NV centers 138
7.4. Superlinear power dependence of the ZPL emission 140
7.5. Second-order intensity autocorrelation functions $g^{(2)}(\tau)$ of cavity-enhanced fluorescence 141
7.6. Measured and expected Purcell factor 142
7.7. Background correction using the purity p 143
7.8. Collective bunching 144
7.9. Emergence of the superlinear power dependence 146
7.10. Superlinearity with inhomogeneous broadening and detuning 147
7.11. Numerical $g^{(2)}(\tau)$ for identical emitters 148

8.1. Cavity-coupled group-IV color centers in diamond 152
8.2. Glass-fiber testbed for quantum network demonstrations in Karlsruhe 154

A.1. Noise spectra of the Qinu gas handling system 159
A.2. Spectral diffusion and single-scan linewidths of sample CA1 160
A.3. Cryogenic resonant characterization of SnV centers implanted at 60 keV . . . 161
A.4. Cryogenic resonant characterization of SnV centers implanted at 100 keV . . 162
A.5. Extinction signatures of three additional SnV centers 165
A.6. Photon budget before charge-state switching 165

List of Tables

4.1. Overview of cavity stability measurements at various temperatures and operating conditions 68
4.2. Reported passive stabilities of cryogenic open-access microcavities 71

5.1. Summary of cavity-integrated diamond samples and processing conditions . 85
5.2. Design and experimental finesse and expected Purcell factor 99

6.1. Summary of the spectral distribution of the detected SnV zero-phonon lines 107
6.2. Monte–Carlo input parameters for the Purcell-factor simulations 115

A.1. Extracted cavity QED parameters for the SnV centers shown in Fig. A.5 . . . 164

Bibliography

[1] M. O. Scully and W. G. Unruh. "One hundred years of quantum mechanics". In: *Science* 390.6777 (2025), pp. 998–1000. DOI: 10.1126/science.ady6092.

[2] M. Planck. "Ueber das Gesetz der Energieverteilung im Normalspectrum". en. In: *Annalen der Physik* 309.3 (1901), pp. 553–563. DOI: 10.1002/andp.19013090310.

[3] A. Einstein. "Über einen die Erzeugung und Verwandlung des Lichtes betreffenden heuristischen Gesichtspunkt". en. In: *Annalen der Physik* 322.6 (1905), pp. 132–148. DOI: 10.1002/andp.19053220607.

[4] N. Bohr. "I. On the constitution of atoms and molecules". In: *The London, Edinburgh, and Dublin Philosophical Magazine and Journal of Science* 26.151 (1913), pp. 1–25. DOI: 10.1080/14786441308634955.

[5] J. P. Dowling and G. J. Milburn. "Quantum technology: the second quantum revolution". In: *Philosophical Transactions of the Royal Society A: Mathematical, Physical and Engineering Sciences* 361.1809 (2003). Ed. by A. G. J. MacFarlane, pp. 1655–1674. DOI: 10.1098/rsta.2003.1227.

[6] E. Altman, K. R. Brown, G. Carleo, et al. "Quantum Simulators: Architectures and Opportunities". In: *PRX Quantum* 2.1 (2021), p. 017003. DOI: 10.1103/PRXQuantum.2.017003.

[7] C. L. Degen, F. Reinhard, and P. Cappellaro. "Quantum sensing". In: *Reviews of Modern Physics* 89.3 (2017), p. 035002. DOI: 10.1103/RevModPhys.89.035002.

[8] H. J. Kimble. "The quantum internet". en. In: *Nature* 453.7198 (2008), pp. 1023–1030. DOI: 10.1038/nature07127.

[9] S. Wehner, D. Elkouss, and R. Hanson. "Quantum internet: A vision for the road ahead". In: *Science* 362.6412 (2018), eaam9288. DOI: 10.1126/science.aam9288.

[10] J. Preskill. "Quantum Computing in the NISQ era and beyond". en-GB. In: *Quantum* 2 (2018), p. 79. DOI: 10.22331/q-2018-08-06-79.

[11] F. Arute, K. Arya, R. Babbush, et al. "Quantum supremacy using a programmable superconducting processor". en. In: *Nature* 574.7779 (2019), pp. 505–510. DOI: 10.1038/s41586-019-1666-5.

[12] C. J. Ballance, T. P. Harty, N. M. Linke, et al. "High-Fidelity Quantum Logic Gates Using Trapped-Ion Hyperfine Qubits". In: *Physical Review Letters* 117.6 (2016), p. 060504. DOI: 10.1103/PhysRevLett.117.060504.

[13] H. Bernien, S. Schwartz, A. Keesling, et al. "Probing many-body dynamics on a 51-atom quantum simulator". en. In: *Nature* 551.7682 (2017), pp. 579–584. DOI: 10.1038/nature24622.

[14] A. Montanaro. "Quantum algorithms: an overview". en. In: *npj Quantum Information* 2.1 (2016), p. 15023. DOI: 10.1038/npjqi.2015.23.

[15] P. Shor. "Algorithms for quantum computation: discrete logarithms and factoring". In: *Proceedings 35th Annual Symposium on Foundations of Computer Science*. 1994, pp. 124–134. DOI: 10.1109/SFCS.1994.365700.

[16] D. J. Bernstein. "Introduction to post-quantum cryptography". en. In: *Post-Quantum Cryptography*. Ed. by D. J. Bernstein, J. Buchmann, and E. Dahmen. Berlin, Heidelberg, 2009, pp. 1–14. DOI: 10.1007/978-3-540-88702-7_1.

[17] N. Gisin, G. Ribordy, W. Tittel, et al. "Quantum cryptography". In: *Reviews of Modern Physics* 74.1 (2002), pp. 145–195. DOI: 10.1103/RevModPhys.74.145.

[18] C. H. Bennett and G. Brassard. "Quantum cryptography: Public key distribution and coin tossing". In: *Theoretical Computer Science*. Theoretical Aspects of Quantum Cryptography – celebrating 30 years of BB84 560 (2014), pp. 7–11. DOI: 10.1016/j.tcs.2014.05.025.

[19] J.-G. Ren, P. Xu, H.-L. Yong, et al. "Ground-to-satellite quantum teleportation". en. In: *Nature* 549.7670 (2017), pp. 70–73. DOI: 10.1038/nature23675.

[20] S.-K. Liao, W.-Q. Cai, W.-Y. Liu, et al. "Satellite-to-ground quantum key distribution". en. In: *Nature* 549.7670 (2017), pp. 43–47. DOI: 10.1038/nature23655.

[21] S.-K. Liao, W.-Q. Cai, J. Handsteiner, et al. "Satellite-Relayed Intercontinental Quantum Network". In: *Physical Review Letters* 120.3 (2018), p. 030501. DOI: 10.1103/PhysRevLett.120.030501.

[22] Y.-A. Chen, Q. Zhang, T.-Y. Chen, et al. "An integrated space-to-ground quantum communication network over 4,600 kilometres". en. In: *Nature* 589.7841 (2021), pp. 214–219. DOI: 10.1038/s41586-020-03093-8.

[23] J. I. Cirac, A. K. Ekert, S. F. Huelga, et al. "Distributed quantum computation over noisy channels". In: *Physical Review A* 59.6 (1999), pp. 4249–4254. DOI: 10.1103/PhysRevA.59.4249.

[24] A. Broadbent, J. Fitzsimons, and E. Kashefi. "Universal Blind Quantum Computation". In: *2009 50th Annual IEEE Symposium on Foundations of Computer Science*. 2009, pp. 517–526. DOI: 10.1109/FOCS.2009.36.

[25] P. Kómár, E. M. Kessler, M. Bishof, et al. "A quantum network of clocks". en. In: *Nature Physics* 10.8 (2014), pp. 582–587. DOI: 10.1038/nphys3000.

[26] Z. Eldredge, M. Foss-Feig, J. A. Gross, et al. "Optimal and secure measurement protocols for quantum sensor networks". In: *Physical Review A* 97.4 (2018), p. 042337. DOI: 10.1103/PhysRevA.97.042337.

[27] K. Azuma, S. E. Economou, D. Elkouss, et al. "Quantum repeaters: From quantum networks to the quantum internet". In: *Reviews of Modern Physics* 95.4 (2023), p. 045006. DOI: 10.1103/RevModPhys.95.045006.

[28] T. van Leent, M. Bock, F. Fertig, et al. "Entangling single atoms over 33 km telecom fibre". en. In: *Nature* 607.7917 (2022), pp. 69–73. DOI: 10.1038/s41586-022-04764-4.

[29] L. Hartung, M. Seubert, S. Welte, et al. "A quantum-network register assembled with optical tweezers in an optical cavity". In: *Science* 385.6705 (2024), pp. 179–183. DOI: 10.1126/science.ado6471.

[30] S. Daiss, S. Langenfeld, S. Welte, et al. "A quantum-logic gate between distant quantum-network modules". In: *Science* 371.6529 (2021), pp. 614–617. DOI: 10.1126/science.abe3150.

[31] V. Krutyanskiy, M. Galli, V. Krcmarsky, et al. "Entanglement of Trapped-Ion Qubits Separated by 230 Meters". In: *Physical Review Letters* 130.5 (2023), p. 050803. DOI: 10.1103/PhysRevLett.130.050803.

[32] L. J. Stephenson, D. P. Nadlinger, B. C. Nichol, et al. "High-Rate, High-Fidelity Entanglement of Qubits Across an Elementary Quantum Network". In: *Physical Review Letters* 124.11 (2020), p. 110501. DOI: 10.1103/PhysRevLett.124.110501.

[33] D. Hucul, I. V. Inlek, G. Vittorini, et al. "Modular entanglement of atomic qubits using photons and phonons". en. In: *Nature Physics* 11.1 (2015), pp. 37–42. DOI: 10.1038/nphys3150.

[34] A. Delteil, Z. Sun, W.-b. Gao, et al. "Generation of heralded entanglement between distant hole spins". en. In: *Nature Physics* 12.3 (2016), pp. 218–223. DOI: 10.1038/nphys3605.

[35] R. Stockill, M. J. Stanley, L. Huthmacher, et al. "Phase-Tuned Entangled State Generation between Distant Spin Qubits". In: *Physical Review Letters* 119.1 (2017), p. 010503. DOI: 10.1103/PhysRevLett.119.010503.

[36] A. Laneve, G. Ronco, M. Beccaceci, et al. "Quantum teleportation with dissimilar quantum dots over a hybrid quantum network". en. In: *Nature Communications* 16.1 (2025), p. 10028. DOI: 10.1038/s41467-025-65911-9.

[37] A. Ruskuc, C.-J. Wu, E. Green, et al. "Multiplexed entanglement of multi-emitter quantum network nodes". en. In: *Nature* 639.8053 (2025), pp. 54–59. DOI: 10.1038/s41586-024-08537-z.

[38] M. T. Uysal, L. Dusanowski, H. Xu, et al. "Spin-Photon Entanglement of a Single ${\mathrm{Er}}^{3+}$ Ion in the Telecom Band". In: *Physical Review X* 15.1 (2025), p. 011071. DOI: 10.1103/PhysRevX.15.011071.

[39] W. Tittel, M. Afzelius, A. Kinos, et al. "Quantum networks using rare-earth ions". en. In: *Quantum Science and Technology* 10.3 (2025), p. 033002. DOI: 10.1088/2058-9565/addd93.

[40] H. Bernien, B. Hensen, W. Pfaff, et al. "Heralded entanglement between solid-state qubits separated by three metres". en. In: *Nature* 497.7447 (2013), pp. 86–90. DOI: 10.1038/nature12016.

[41] B. Hensen, H. Bernien, A. E. Dréau, et al. "Loophole-free Bell inequality violation using electron spins separated by 1.3 kilometres". en. In: *Nature* 526.7575 (2015), pp. 682–686. DOI: 10.1038/nature15759.

[42] M. K. Bhaskar, R. Riedinger, B. Machielse, et al. “Experimental demonstration of memory-enhanced quantum communication”. en. In: *Nature* 580.7801 (2020), pp. 60–64. DOI: 10.1038/s41586-020-2103-5.

[43] C. M. Knaut, A. Suleymanzade, Y.-C. Wei, et al. “Entanglement of nanophotonic quantum memory nodes in a telecom network”. en. In: *Nature* 629.8012 (2024), pp. 573–578. DOI: 10.1038/s41586-024-07252-z.

[44] M. Pompili, S. L. N. Hermans, S. Baier, et al. “Realization of a multinode quantum network of remote solid-state qubits”. en. In: *Science* 372.6539 (2021), pp. 259–264. DOI: 10.1126/science.abg1919.

[45] F. Jelezko and J. Wrachtrup. “Single defect centres in diamond: A review”. en. In: *physica status solidi (a)* 203.13 (2006), pp. 3207–3225. DOI: 10.1002/pssa.200671403.

[46] L. Robledo, L. Childress, H. Bernien, et al. “High-fidelity projective read-out of a solid-state spin quantum register”. en. In: *Nature* 477.7366 (2011), pp. 574–578. DOI: 10.1038/nature10401.

[47] P. C. Maurer, G. Kucsko, C. Latta, et al. “Room-Temperature Quantum Bit Memory Exceeding One Second”. In: *Science* 336.6086 (2012), pp. 1283–1286. DOI: 10.1126/science.1220513.

[48] T. H. Taminiau, J. Cramer, T. van der Sar, et al. “Universal control and error correction in multi-qubit spin registers in diamond”. en. In: *Nature Nanotechnology* 9.3 (2014), pp. 171–176. DOI: 10.1038/nnano.2014.2.

[49] M. Ruf, N. H. Wan, H. Choi, et al. “Quantum networks based on color centers in diamond”. In: *Journal of Applied Physics* 130.7 (2021), p. 070901. DOI: 10.1063/5.0056534.

[50] F. Rozpędek, R. Yehia, K. Goodenough, et al. “Near-term quantum-repeater experiments with nitrogen-vacancy centers: Overcoming the limitations of direct transmission”. In: *Physical Review A* 99.5 (2019), p. 052330. DOI: 10.1103/PhysRevA.99.052330.

[51] Purcell, E. M. “Spontaneous Emission Probabilities at Radio Frequencies”. In: *Physical Review* 69.11-12 (1946), p. 681. DOI: 10.1103/PhysRev.69.674.2.

[52] A. Reiserer and G. Rempe. “Cavity-based quantum networks with single atoms and optical photons”. In: *Reviews of Modern Physics* 87.4 (2015), pp. 1379–1418. DOI: 10.1103/RevModPhys.87.1379.

[53] R. J. Thompson, G. Rempe, and H. J. Kimble. “Observation of normal-mode splitting for an atom in an optical cavity”. In: *Physical Review Letters* 68.8 (1992), pp. 1132–1135. DOI: 10.1103/PhysRevLett.68.1132.

[54] S. Haroche. “Nobel Lecture: Controlling photons in a box and exploring the quantum to classical boundary”. In: *Reviews of Modern Physics* 85.3 (2013), pp. 1083–1102. DOI: 10.1103/RevModPhys.85.1083.

[55] J. Vučković, M. Lončar, H. Mabuchi, et al. “Design of photonic crystal microcavities for cavity QED”. In: *Physical Review E* 65.1 (2001), p. 016608. DOI: 10.1103/PhysRevE.65.016608.

[56] D. Hunger, T. Steinmetz, Y. Colombe, et al. “A fiber Fabry–Perot cavity with high finesse”. en. In: *New Journal of Physics* 12.6 (2010), p. 065038. DOI: 10.1088/1367-2630/12/6/065038.

[57] E. N. Knall, C. M. Knaut, R. Bekenstein, et al. “Efficient Source of Shaped Single Photons Based on an Integrated Diamond Nanophotonic System”. In: *Physical Review Letters* 129.5 (2022), p. 053603. DOI: 10.1103/PhysRevLett.129.053603.

[58] Y. Herrmann, J. Fischer, J. M. Brevoord, et al. “Coherent Coupling of a Diamond Tin-Vacancy Center to a Tunable Open Microcavity”. In: *Physical Review X* 14.4 (2024), p. 041013. DOI: 10.1103/PhysRevX.14.041013.

[59] N. Codreanu, T. Turan, D. B. Rodriguez, et al. *Above-Unity Coherent Cooperativity of Tin-Vacancy Centers in Diamond Photonic Crystal Cavities*. 2025. DOI: 10.48550/arXiv.2511.13375.

[60] A. E. Rugar, S. Aghaeimeibodi, D. Riedel, et al. “Quantum Photonic Interface for Tin-Vacancy Centers in Diamond”. In: *Physical Review X* 11.3 (2021), p. 031021. DOI: 10.1103/PhysRevX.11.031021.

[61] R. Zifkin, C. D. Rodríguez Rosenblueth, E. Janitz, et al. “Lifetime Reduction of Single Germanium-Vacancy Centers in Diamond via a Tunable Open Microcavity”. In: *PRX Quantum* 5.3 (2024), p. 030308. DOI: 10.1103/PRXQuantum.5.030308.

[62] H. S. Kaupp. “Coupling nitrogen-vacancy centers in diamond to fiber-based Fabry-Pérot microcavities”. de. Text.PhDThesis. Ludwig-Maximilians-Universität München, 2017.

[63] M. B. Pallmann. “Purcell-enhanced emission and collective effects of nitrogen-vacancy centers in diamond coupled to a microcavity”. German. PhD Thesis. Karlsruher Institut für Technologie (KIT), 2023. DOI: 10.5445/IR/1000161130.

[64] D. Riedel. “Engineering of the photonic environment of single nitrogen-vacancy centers in diamond”. PhD Thesis. Philosophisch-Naturwissenschaftliche Fakultät der Universität Basel, 2018.

[65] M. Ruf. “Cavity-enhanced quantum network nodes in diamond”. en. PhD thesis. Delft University of Technology, 2021. DOI: 10.4233/UUID:933B37D4-7F00-4070-BECC-9C462BF9D8DF.

[66] A. Gruber, A. Dräbenstedt, C. Tietz, et al. “Scanning Confocal Optical Microscopy and Magnetic Resonance on Single Defect Centers”. In: *Science* 276.5321 (1997), pp. 2012–2014. DOI: 10.1126/science.276.5321.2012.

[67] G. Balasubramanian, I. Y. Chan, R. Kolesov, et al. “Nanoscale imaging magnetometry with diamond spins under ambient conditions”. en. In: *Nature* 455.7213 (2008), pp. 648–651. DOI: 10.1038/nature07278.

[68] J. R. Maze, P. L. Stanwix, J. S. Hodges, et al. “Nanoscale magnetic sensing with an individual electronic spin in diamond”. en. In: *Nature* 455.7213 (2008), pp. 644–647. DOI: 10.1038/nature07279.

[69] C. E. Bradley, J. Randall, M. H. Abobeih, et al. "A Ten-Qubit Solid-State Spin Register with Quantum Memory up to One Minute". In: *Physical Review X* 9.3 (2019), p. 031045. DOI: 10.1103/PhysRevX.9.031045.

[70] M. W. Doherty, N. B. Manson, P. Delaney, et al. "The nitrogen-vacancy colour centre in diamond". In: *Physics Reports*. The nitrogen-vacancy colour centre in diamond 528.1 (2013), pp. 1–45. DOI: 10.1016/j.physrep.2013.02.001.

[71] V. M. Acosta, A. Jarmola, E. Bauch, et al. "Optical properties of the nitrogen-vacancy singlet levels in diamond". In: *Physical Review B* 82.20 (2010), p. 201202. DOI: 10.1103/PhysRevB.82.201202.

[72] R. Albrecht, A. Bommer, C. Deutsch, et al. "Coupling of a Single Nitrogen-Vacancy Center in Diamond to a Fiber-Based Microcavity". In: *Physical Review Letters* 110.24 (2013), p. 243602. DOI: 10.1103/PhysRevLett.110.243602.

[73] M. Born and R. Oppenheimer. "Zur Quantentheorie der Molekeln". en. In: *Annalen der Physik* 389.20 (1927), pp. 457–484. DOI: 10.1002/andp.19273892002.

[74] J. Franck and E. G. Dymond. "Elementary processes of photochemical reactions". en. In: *Transactions of the Faraday Society* 21.February (1926), pp. 536–542. DOI: 10.1039/TF9262100536.

[75] E. Condon. "A Theory of Intensity Distribution in Band Systems". In: *Physical Review* 28.6 (1926), pp. 1182–1201. DOI: 10.1103/PhysRev.28.1182.

[76] R. Ulbricht, S. Dong, A. Gali, et al. "Vibrational relaxation dynamics of the nitrogen-vacancy center in diamond". In: *Physical Review B* 97.22 (2018), p. 220302. DOI: 10.1103/PhysRevB.97.220302.

[77] A. Faraon, P. E. Barclay, C. Santori, et al. "Resonant enhancement of the zero-phonon emission from a colour centre in a diamond cavity". en. In: *Nature Photonics* 5.5 (2011), pp. 301–305. DOI: 10.1038/nphoton.2011.52.

[78] K.-M. C. Fu, C. Santori, P. E. Barclay, et al. "Observation of the Dynamic Jahn-Teller Effect in the Excited States of Nitrogen-Vacancy Centers in Diamond". In: *Physical Review Letters* 103.25 (2009), p. 256404. DOI: 10.1103/PhysRevLett.103.256404.

[79] J. Wolters, N. Sadzak, A. W. Schell, et al. "Measurement of the Ultrafast Spectral Diffusion of the Optical Transition of Nitrogen Vacancy Centers in Nano-Size Diamond Using Correlation Interferometry". In: *Physical Review Letters* 110.2 (2013), p. 027401. DOI: 10.1103/PhysRevLett.110.027401.

[80] L. Orphal-Kobin, K. Unterguggenberger, T. Pregnolato, et al. "Optically Coherent Nitrogen-Vacancy Defect Centers in Diamond Nanostructures". In: *Physical Review X* 13.1 (2023), p. 011042. DOI: 10.1103/PhysRevX.13.011042.

[81] L. Robledo, H. Bernien, T. v. d. Sar, et al. "Spin dynamics in the optical cycle of single nitrogen-vacancy centres in diamond". en. In: *New Journal of Physics* 13.2 (2011), p. 025013. DOI: 10.1088/1367-2630/13/2/025013.

[82] J. Benedikter, H. Kaupp, T. Hümmer, et al. "Cavity-Enhanced Single-Photon Source Based on the Silicon-Vacancy Center in Diamond". In: *Physical Review Applied* 7.2 (2017), p. 024031. DOI: 10.1103/PhysRevApplied.7.024031.

[83] J. Görlitz, D. Herrmann, G. Thiering, et al. “Spectroscopic investigations of negatively charged tin-vacancy centres in diamond”. en. In: *New Journal of Physics* 22.1 (2020), p. 013048. DOI: 10.1088/1367-2630/ab6631.

[84] L. De Santis, M. E. Trusheim, K. C. Chen, et al. “Investigation of the Stark Effect on a Centrosymmetric Quantum Emitter in Diamond”. In: *Physical Review Letters* 127.14 (2021), p. 147402. DOI: 10.1103/PhysRevLett.127.147402.

[85] P. Tamarat, T. Gaebel, J. R. Rabeau, et al. “Stark Shift Control of Single Optical Centers in Diamond”. In: *Physical Review Letters* 97.8 (2006), p. 083002. DOI: 10.1103/PhysRevLett.97.083002.

[86] P. Tamarat, N. B. Manson, J. P. Harrison, et al. “Spin-flip and spin-conserving optical transitions of the nitrogen-vacancy centre in diamond”. en. In: *New Journal of Physics* 10.4 (2008), p. 045004. DOI: 10.1088/1367-2630/10/4/045004.

[87] M. Pasini, N. Codreanu, T. Turan, et al. “Nonlinear Quantum Photonics with a Tin-Vacancy Center Coupled to a One-Dimensional Diamond Waveguide”. In: *Physical Review Letters* 133.2 (2024), p. 023603. DOI: 10.1103/PhysRevLett.133.023603.

[88] E. Janitz, M. K. Bhaskar, and L. Childress. “Cavity quantum electrodynamics with color centers in diamond”. EN. In: *Optica* 7.10 (2020), pp. 1232–1252. DOI: 10.1364/OPTICA.398628.

[89] L. V. H. Rodgers, L. B. Hughes, M. Xie, et al. “Materials challenges for quantum technologies based on color centers in diamond”. en. In: *MRS Bulletin* 46.7 (2021), pp. 623–633. DOI: 10.1557/s43577-021-00137-w.

[90] G. Pieplow, C. G. Torun, C. Gurr, et al. “Quantum electrometer for time-resolved material science at the atomic lattice scale”. en. In: *Nature Communications* 16.1 (2025), p. 6435. DOI: 10.1038/s41467-025-61839-2.

[91] T. Iwasaki, Y. Miyamoto, T. Taniguchi, et al. “Tin-Vacancy Quantum Emitters in Diamond”. In: *Physical Review Letters* 119.25 (2017), p. 253601. DOI: 10.1103/PhysRevLett.119.253601.

[92] C. Hepp. “Electronic structure of the silicon vacancy color center in diamond”. en. doctoralThesis. 2014. DOI: 10.22028/D291-23020.

[93] G. Thiering and A. Gali. “Ab Initio Magneto-Optical Spectrum of Group-IV Vacancy Color Centers in Diamond”. In: *Physical Review X* 8.2 (2018), p. 021063. DOI: 10.1103/PhysRevX.8.021063.

[94] C. Hepp, T. Müller, V. Waselowski, et al. “Electronic Structure of the Silicon Vacancy Color Center in Diamond”. In: *Physical Review Letters* 112.3 (2014), p. 036405. DOI: 10.1103/PhysRevLett.112.036405.

[95] X. Guo, A. M. Stramma, Z. Li, et al. “Microwave-Based Quantum Control and Coherence Protection of Tin-Vacancy Spin Qubits in a Strain-Tuned Diamond-Membrane Heterostructure”. In: *Physical Review X* 13.4 (2023), p. 041037. DOI: 10.1103/PhysRevX.13.041037.

[96] E. I. Rosenthal, C. P. Anderson, H. C. Kleidermacher, et al. "Microwave Spin Control of a Tin-Vacancy Qubit in Diamond". In: *Physical Review X* 13.3 (2023), p. 031022. DOI: 10.1103/PhysRevX.13.031022.

[97] I. Karapatzakis, J. Resch, M. Schrodin, et al. "Microwave Control of the Tin-Vacancy Spin Qubit in Diamond with a Superconducting Waveguide". In: *Physical Review X* 14.3 (2024), p. 031036. DOI: 10.1103/PhysRevX.14.031036.

[98] H. Lee, H. C. Kleidermacher, A. J. M. Stein, et al. *Quantum Nanophotonic Interface for Tin-Vacancy Centers in Thin-Film Diamond*. 2025. DOI: 10.48550/arXiv.2511.05740.

[99] A. E. Rugar, C. Dory, S. Sun, et al. "Characterization of optical and spin properties of single tin-vacancy centers in diamond nanopillars". In: *Physical Review B* 99.20 (2019), p. 205417. DOI: 10.1103/PhysRevB.99.205417.

[100] R. Debroux, C. P. Michaels, C. M. Purser, et al. "Quantum Control of the Tin-Vacancy Spin Qubit in Diamond". In: *Physical Review X* 11.4 (2021), p. 041041. DOI: 10.1103/PhysRevX.11.041041.

[101] J. Görlitz, D. Herrmann, P. Fuchs, et al. "Coherence of a charge stabilised tin-vacancy spin in diamond". en. In: *npj Quantum Information* 8.1 (2022), p. 45. DOI: 10.1038/s41534-022-00552-0.

[102] M. V. Hauf, B. Grotz, B. Naydenov, et al. "Chemical control of the charge state of nitrogen-vacancy centers in diamond". In: *Physical Review B* 83.8 (2011), p. 081304. DOI: 10.1103/PhysRevB.83.081304.

[103] A. Sadzak and A. Krueger. "The influence of surface properties on colour centres in diamond". en. In: *Materials for Quantum Technology* 5.1 (2025), p. 013001. DOI: 10.1088/2633-4356/adab5e.

[104] T. Lühmann, J. Küpper, S. Dietel, et al. "Charge-State Tuning of Single SnV Centers in Diamond". In: *ACS Photonics* 7.12 (2020), pp. 3376–3385. DOI: 10.1021/acsphotonics.0c01123.

[105] A. A. Maradudin. "Theoretical and Experimental Aspects of the Effects of Point Defects and Disorder on the Vibrations of Crystals*—1". In: *Solid State Physics*. Ed. by F. Seitz and D. Turnbull. Vol. 18. 1966, pp. 273–420. DOI: 10.1016/S0081-1947(08)60350-1.

[106] C. Arend, J. N. Becker, H. Sternschulte, et al. "Photoluminescence excitation and spectral hole burning spectroscopy of silicon vacancy centers in diamond". In: *Physical Review B* 94.4 (2016), p. 045203. DOI: 10.1103/PhysRevB.94.045203.

[107] V. Sedov, K. Boldyrev, V. Krivobok, et al. "SiV Color Centers in Si-Doped Isotopically Enriched 12C and 13C CVD Diamonds". en. In: *physica status solidi (a)* 214.11 (2017), p. 1700198. DOI: 10.1002/pssa.201700198.

[108] V. Hizhnyakov, H. Kaasik, and I. Sildos. "Zero-Phonon Lines: The Effect of a Strong Softening of Elastic Springs in the Excited State". en. In: *physica status solidi (b)* 234.2 (2002), pp. 644–653. DOI: 10.1002/1521-3951(200211)234:2<644::AID-PSSB644>3.0.CO;2-E.

[109] V. Hizhnyakov, V. Boltrushko, H. Kaasik, et al. “Strong Jahn–Teller effect in the excited state: Anomalous temperature dependence of the zero-phonon line”. In: *The Journal of Chemical Physics* 119.12 (2003), pp. 6290–6295. DOI: 10.1063/1.1603216.

[110] V. Hizhnyakov, V. Boltrushko, H. Kaasik, et al. “Phase relaxation in the vicinity of the dynamic instability: anomalous temperature dependence of zero-phonon line”. In: *Journal of Luminescence*. Proceedings of the 8th International Meeting on Hole Burning, Single Molecule, and Related Spectroscopies: Science and Applications 107.1 (2004), pp. 351–358. DOI: 10.1016/j.jlumin.2003.12.025.

[111] Y. Narita, P. Wang, K. Ikeda, et al. “Multiple Tin-Vacancy Centers in Diamond with Nearly Identical Photon Frequency and Linewidth”. In: *Physical Review Applied* 19.2 (2023), p. 024061. DOI: 10.1103/PhysRevApplied.19.024061.

[112] T. Schröder, M. E. Trusheim, M. Walsh, et al. “Scalable focused ion beam creation of nearly lifetime-limited single quantum emitters in diamond nanostructures”. en. In: *Nature Communications* 8.1 (2017), p. 15376. DOI: 10.1038/ncomms15376.

[113] K. D. Jahnke, A. Sipahigil, J. M. Binder, et al. “Electron–phonon processes of the silicon-vacancy centre in diamond”. en. In: *New Journal of Physics* 17.4 (2015), p. 043011. DOI: 10.1088/1367-2630/17/4/043011.

[114] D. Chen, J. E. Fröch, S. Ru, et al. “Quantum Interference of Resonance Fluorescence from Germanium-Vacancy Color Centers in Diamond”. In: *Nano Letters* 22.15 (2022), pp. 6306–6312. DOI: 10.1021/acs.nanolett.2c01959.

[115] P. Wang, L. Kazak, K. Senkalla, et al. “Transform-Limited Photon Emission from a Lead-Vacancy Center in Diamond above 10 K”. In: *Physical Review Letters* 132.7 (2024), p. 073601. DOI: 10.1103/PhysRevLett.132.073601.

[116] S. Meesala, Y.-I. Sohn, B. Pingault, et al. “Strain engineering of the silicon-vacancy center in diamond”. In: *Physical Review B* 97.20 (2018), p. 205444. DOI: 10.1103/PhysRevB.97.205444.

[117] R. : Orbach. “Spin-lattice relaxation in rare-earth salts”. In: *Proceedings of the Royal Society of London. Series A. Mathematical and Physical Sciences* 264.1319 (1997), pp. 458–484. DOI: 10.1098/rspa.1961.0211.

[118] P.-J. Stas, Y. Q. Huan, B. Machielse, et al. “Robust multi-qubit quantum network node with integrated error detection”. In: *Science* 378.6619 (2022), pp. 557–560. DOI: 10.1126/science.add9771.

[119] Y.-I. Sohn, S. Meesala, B. Pingault, et al. “Controlling the coherence of a diamond spin qubit through its strain environment”. en. In: *Nature Communications* 9.1 (2018), p. 2012. DOI: 10.1038/s41467-018-04340-3.

[120] D. R. Assumpcao, C. Jin, M. Sutula, et al. “Deterministic creation of strained color centers in nanostructures via high-stress thin films”. In: *Applied Physics Letters* 123.24 (2023), p. 244001. DOI: 10.1063/5.0171558.

[121] M. Klotz, A. Tangemann, and A. Kubanek. “Ultra-high strained diamond spin register with coherent optical control”. en. In: *npj Quantum Information* 11.1 (2025), p. 91. DOI: 10.1038/s41534-025-01049-2.

[122] D. D. Sukachev, A. Sipahigil, C. T. Nguyen, et al. "Silicon-Vacancy Spin Qubit in Diamond: A Quantum Memory Exceeding 10 ms with Single-Shot State Readout". In: *Physical Review Letters* 119.22 (2017), p. 223602. DOI: 10.1103/PhysRevLett.119.223602.

[123] K. Senkalla, G. Genov, M. H. Metsch, et al. "Germanium Vacancy in Diamond Quantum Memory Exceeding 20 ms". In: *Physical Review Letters* 132.2 (2024), p. 026901. DOI: 10.1103/PhysRevLett.132.026901.

[124] R. A. Parker, J. Arjona Martínez, K. C. Chen, et al. "A diamond nanophotonic interface with an optically accessible deterministic electronuclear spin register". en. In: *Nature Photonics* 18.2 (2024), pp. 156–161. DOI: 10.1038/s41566-023-01332-8.

[125] I. B. W. Harris, I. Christen, S. M. Patomäki, et al. *High-Fidelity Control of a Strongly Coupled Electro-Nuclear Spin-Photon Interface*. 2025. DOI: 10.48550/arXiv.2505.09267.

[126] J. Resch, I. Karapatzakis, M. Elshorbagy, et al. *High-fidelity control of a ^{13}C nuclear spin coupled to a tin-vacancy center in diamond*. 2025. DOI: 10.48550/arXiv.2509.03354.

[127] M. Mader. "A scanning cavity microscope". de. Text.PhDThesis. Ludwig-Maximilians-Universität München, 2018.

[128] M. Fox. *Quantum optics: an introduction*. eng. Oxford master series in physics ARRAY(0x5597b93d5790). Oxford ; New York, 2006.

[129] B. E. A. Saleh and M. C. Teich. *Fundamentals of photonics*. eng. Second edition. Wiley Series in Pure and Applied Optics Ser. ; v.81. Hoboken, New Jersey, 2007.

[130] A. E. Siegman. *Lasers*. en. 1986.

[131] D. Plankensteiner, C. Sommer, M. Reitz, et al. "Enhanced collective Purcell effect of coupled quantum emitter systems". In: *Physical Review A* 99.4 (2019), p. 043843. DOI: 10.1103/PhysRevA.99.043843.

[132] D. Manzano. "A short introduction to the Lindblad master equation". In: *AIP Advances* 10.2 (2020), p. 025106. DOI: 10.1063/1.5115323.

[133] S. Deléglise, I. Dotsenko, C. Sayrin, et al. "Reconstruction of non-classical cavity field states with snapshots of their decoherence". en. In: *Nature* 455.7212 (2008), pp. 510–514. DOI: 10.1038/nature07288.

[134] J. P. Reithmaier, G. Sęk, A. Löffler, et al. "Strong coupling in a single quantum dot–semiconductor microcavity system". en. In: *Nature* 432.7014 (2004), pp. 197–200. DOI: 10.1038/nature02969.

[135] T. Yoshie, A. Scherer, J. Hendrickson, et al. "Vacuum Rabi splitting with a single quantum dot in a photonic crystal nanocavity". en. In: *Nature* 432.7014 (2004), pp. 200–203. DOI: 10.1038/nature03119.

[136] Y.-S. Park, A. K. Cook, and H. Wang. "Cavity QED with Diamond Nanocrystals and Silica Microspheres". In: *Nano Letters* 6.9 (2006), pp. 2075–2079. DOI: 10.1021/nl061342r.

[137] A. Aiello. "Input-output relations in optical cavities: A simple point of view". In: *Physical Review A* 62.6 (2000), p. 063813. DOI: 10.1103/PhysRevA.62.063813.

[138] H. Carmichael. *An Open Systems Approach to Quantum Optics: Lectures Presented at the Université Libre de Bruxelles, October 28 to November 4, 1991*. en. 1993.

[139] A. Auffèves-Garnier, C. Simon, J.-M. Gérard, et al. "Giant optical nonlinearity induced by a single two-level system interacting with a cavity in the Purcell regime". In: *Physical Review A* 75.5 (2007), p. 053823. DOI: 10.1103/PhysRevA.75.053823.

[140] D. Wang. "Cavity quantum electrodynamics with a single molecule: Purcell enhancement, strong coupling and single-photon nonlinearity". en. In: *Journal of Physics B: Atomic, Molecular and Optical Physics* 54.13 (2021), p. 133001. DOI: 10.1088/1361-6455/abf6e1.

[141] M. Gross and S. Haroche. "Superradiance: An essay on the theory of collective spontaneous emission". en. In: *Physics Reports* 93.5 (1982), pp. 301–396. DOI: 10.1016/0370-1573(82)90102-8.

[142] A. Auffèves, D. Gerace, S. Portolan, et al. "Few emitters in a cavity: from cooperative emission to individualization". en. In: *New Journal of Physics* 13.9 (2011), p. 093020. DOI: 10.1088/1367-2630/13/9/093020.

[143] M. Pallmann, K. Köster, Y. Zhang, et al. "Cavity-Mediated Collective Emission from Few Emitters in a Diamond Membrane". In: *Physical Review X* 14.4 (2024), p. 041055. DOI: 10.1103/PhysRevX.14.041055.

[144] Y.-D. Qu, Y. Zhang, P. Ni, et al. "Superradiance from nitrogen-vacancy centers coupled to an ultranarrow optical cavity". In: *Physical Review A* 111.3 (2025), p. 033711. DOI: 10.1103/PhysRevA.111.033711.

[145] D. Meiser and M. J. Holland. "Steady-state superradiance with alkaline-earth-metal atoms". In: *Physical Review A* 81.3 (2010), p. 033847. DOI: 10.1103/PhysRevA.81.033847.

[146] D. Meiser and M. J. Holland. "Intensity fluctuations in steady-state superradiance". In: *Physical Review A* 81.6 (2010), p. 063827. DOI: 10.1103/PhysRevA.81.063827.

[147] K. M. Birnbaum, A. Boca, R. Miller, et al. "Photon blockade in an optical cavity with one trapped atom". en. In: *Nature* 436.7047 (2005), pp. 87–90. DOI: 10.1038/nature03804.

[148] A. Stute, B. Casabone, P. Schindler, et al. "Tunable ion–photon entanglement in an optical cavity". en. In: *Nature* 485.7399 (2012), pp. 482–485. DOI: 10.1038/nature11120.

[149] P. Thomas, L. Ruscio, O. Morin, et al. "Efficient generation of entangled multiphoton graph states from a single atom". en. In: *Nature* 608.7924 (2022), pp. 677–681. DOI: 10.1038/s41586-022-04987-5.

[150] K. Srinivasan and O. Painter. "Linear and nonlinear optical spectroscopy of a strongly coupled microdisk–quantum dot system". en. In: *Nature* 450.7171 (2007), pp. 862–865. DOI: 10.1038/nature06274.

[151] N. Somaschi, V. Giesz, L. De Santis, et al. "Near-optimal single-photon sources in the solid state". en. In: *Nature Photonics* 10.5 (2016), pp. 340–345. DOI: 10.1038/nphoton.2016.23.

[152] D. Englund, D. Fattal, E. Waks, et al. "Controlling the Spontaneous Emission Rate of Single Quantum Dots in a Two-Dimensional Photonic Crystal". In: *Physical Review Letters* 95.1 (2005), p. 013904. DOI: 10.1103/PhysRevLett.95.013904.

[153] T. Pregnolato, M. E. Stucki, J. M. Bopp, et al. "Fabrication of Sawfish photonic crystal cavities in bulk diamond". In: *APL Photonics* 9.3 (2024), p. 036105. DOI: 10.1063/5.0186509.

[154] D. Riedel, I. Söllner, B. J. Shields, et al. "Deterministic Enhancement of Coherent Photon Generation from a Nitrogen-Vacancy Center in Ultrapure Diamond". In: *Physical Review X* 7.3 (2017), p. 031040. DOI: 10.1103/PhysRevX.7.031040.

[155] D. Najer, I. Söllner, P. Sekatski, et al. "A gated quantum dot strongly coupled to an optical microcavity". en. In: *Nature* 575.7784 (2019), pp. 622–627. DOI: 10.1038/s41586-019-1709-y.

[156] M. Ruf, M. Weaver, S. van Dam, et al. "Resonant Excitation and Purcell Enhancement of Coherent Nitrogen-Vacancy Centers Coupled to a Fabry-Perot Microcavity". In: *Physical Review Applied* 15.2 (2021), p. 024049. DOI: 10.1103/PhysRevApplied.15.024049.

[157] N. Tomm, A. Javadi, N. O. Antoniadis, et al. "A bright and fast source of coherent single photons". en. In: *Nature Nanotechnology* 16.4 (2021), pp. 399–403. DOI: 10.1038/s41565-020-00831-x.

[158] V. Yurgens, Y. Fontana, A. Corazza, et al. "Cavity-assisted resonance fluorescence from a nitrogen-vacancy center in diamond". en. In: *npj Quantum Information* 10.1 (2024), p. 112. DOI: 10.1038/s41534-024-00915-9.

[159] R. Berghaus, S. Sachero, G. Bayer, et al. "Cavity-enhanced emission and absorption of color centers in a diamond membrane with selectable strain". In: *Physical Review Applied* 23.3 (2025), p. 034050. DOI: 10.1103/PhysRevApplied.23.034050.

[160] M. Fujimaki, Y. Ohki, J. L. Brebner, et al. "Fabrication of long-period optical fiber gratings by use of ion implantation". EN. In: *Optics Letters* 25.2 (2000), pp. 88–89. DOI: 10.1364/OL.25.000088.

[161] F. Schiappelli, R. Kumar, M. Prasciolu, et al. "Efficient fiber-to-waveguide coupling by a lens on the end of the optical fiber fabricated by focused ion beam milling". In: *Microelectronic Engineering*. Micro and Nano Engineering 2003 73-74 (2004), pp. 397–404. DOI: 10.1016/j.mee.2004.02.077.

[162] A. Micco, A. Ricciardi, M. Pisco, et al. "Optical fiber tip templating using direct focused ion beam milling". en. In: *Scientific Reports* 5.1 (2015), p. 15935. DOI: 10.1038/srep15935.

[163] P. Maier, S. Rupp, N. Lettner, et al. "Fabrication of customized low-loss optical resonators by combination of FIB-milling and CO_2 laser smoothing". EN. In: *Optics Express* 33.9 (2025), pp. 19205–19219. DOI: 10.1364/OE.557212.

[164] D. Hunger, C. Deutsch, R. J. Barbour, et al. "Laser micro-fabrication of concave, low-roughness features in silica". In: *AIP Advances* 2.1 (2012), p. 012119. DOI: 10.1063/1.3679721.

[165] C. J. R. Sheppard. “Approximate calculation of the reflection coefficient from a stratified medium”. en. In: *Pure and Applied Optics: Journal of the European Optical Society Part A* 4.5 (1995), p. 665. DOI: 10.1088/0963-9659/4/5/018.

[166] C. Koks and M. P. v. Exter. “Microcavity resonance condition, quality factor, and mode volume are determined by different penetration depths”. EN. In: *Optics Express* 29.5 (2021), pp. 6879–6889. DOI: 10.1364/OE.412346.

[167] H. Kaupp, T. Hümmer, M. Mader, et al. “Purcell-Enhanced Single-Photon Emission from Nitrogen-Vacancy Centers Coupled to a Tunable Microcavity”. In: *Physical Review Applied* 6.5 (2016), p. 054010. DOI: 10.1103/PhysRevApplied.6.054010.

[168] S. P. Wadikhaye, Y. K. Yong, and S. O. Reza Moheimani. “A serial-kinematic nanopositioner for high-speed atomic force microscopy”. In: *Review of Scientific Instruments* 85.10 (2014), p. 105104. DOI: 10.1063/1.4897483.

[169] Attocube Systems AG. *Cryogenic Nanopositioners and Scanning Stages*.

[170] JPE B.V. (Janssen Precision Engineering). *Cryogenic Nanopositioning Stages*.

[171] Physik Instrumente (PI) GmbH & Co. KG. *Piezo Flexure Stages and Nanopositioning Systems*.

[172] M. Pallmann, T. Eichhorn, J. Benedikter, et al. “A highly stable and fully tunable open microcavity platform at cryogenic temperatures”. In: *APL Photonics* 8.4 (2023), p. 046107. DOI: 10.1063/5.0139003.

[173] F. Sigger, I. Amersdorffer, A. Hötger, et al. “Ultra-Sensitive Extinction Measurements of Optically Active Defects in Monolayer MoS2”. In: *The Journal of Physical Chemistry Letters* 13.44 (2022), pp. 10291–10296. DOI: 10.1021/acs.jpclett.2c02386.

[174] J. Körber, M. Pallmann, J. Heupel, et al. “Scanning Cavity Microscopy of a Single-Crystal Diamond Membrane”. In: *Physical Review Applied* 19.6 (2023), p. 064057. DOI: 10.1103/PhysRevApplied.19.064057.

[175] T. Eichhorn. “Cavity-enhanced Spectroscopy of Individual Europium-doped Nanoparticles”. PhD Thesis. Karlsruher Institut für Technologie (KIT), 2024. DOI: 10.5445/IR/1000177590.

[176] Qinu GmbH. *Table-top dilution refrigerator*. 2024.

[177] A. Zilz. “Investigation of the rarefied gas flow in the pumping tube of a \(^3\)He/\(^4\)He dilution refrigerator”. MA thesis. Karlsruhe Institute of Technology, 2022.

[178] Y. Fontana, R. Zifkin, E. Janitz, et al. “A mechanically stable and tunable cryogenic Fabry–Pérot microcavity”. In: *Review of Scientific Instruments* 92.5 (2021), p. 053906. DOI: 10.1063/5.0049520.

[179] L. Greuter, S. Starosielec, D. Najer, et al. “A small mode volume tunable microcavity: Development and characterization”. In: *Applied Physics Letters* 105.12 (2014), p. 121105. DOI: 10.1063/1.4896415.

[180] Y. Herrmann, J. Fischer, S. Scheijen, et al. “A low-temperature tunable microcavity featuring high passive stability and microwave integration”. In: *AVS Quantum Science* 6.4 (2024), p. 041401. DOI: 10.1116/5.0233296.

[181] B. Casabone, C. Deshmukh, S. Liu, et al. "Dynamic control of Purcell enhanced emission of erbium ions in nanoparticles". en. In: *Nature Communications* 12.1 (2021), p. 3570. DOI: 10.1038/s41467-021-23632-9.

[182] S. Vadia, J. Scherzer, H. Thierschmann, et al. "Open-Cavity in Closed-Cycle Cryostat as a Quantum Optics Platform". In: *PRX Quantum* 2.4 (2021), p. 040318. DOI: 10.1103/PRXQuantum.2.040318.

[183] T. Ruelle, D. Jaeger, F. Fogliano, et al. "A tunable fiber Fabry–Perot cavity for hybrid optomechanics stabilized at 4 K". In: *Review of Scientific Instruments* 93.9 (2022), p. 095003. DOI: 10.1063/5.0098140.

[184] A. Caciagli, R. J. Baars, A. P. Philipse, et al. "Exact expression for the magnetic field of a finite cylinder with arbitrary uniform magnetization". In: *Journal of Magnetism and Magnetic Materials* 456 (2018), pp. 423–432. DOI: 10.1016/j.jmmm.2018.02.003.

[185] I. Friel, S. L. Clewes, H. K. Dhillon, et al. "Control of surface and bulk crystalline quality in single crystal diamond grown by chemical vapour deposition". In: *Diamond and Related Materials*. Proceedings of Diamond 2008, the 19th European Conference on Diamond, Diamond-Like Materials, Carbon Nanotubes, Nitrides and Silicon Carbide 18.5 (2009), pp. 808–815. DOI: 10.1016/j.diamond.2009.01.013.

[186] P.-N. Volpe, P. Muret, F. Omnes, et al. "Defect analysis and excitons diffusion in undoped homoepitaxial diamond films after polishing and oxygen plasma etching". In: *Diamond and Related Materials* 18.10 (2009), pp. 1205–1210. DOI: 10.1016/j.diamond.2009.04.008.

[187] E. Saho, S. Hindmarsh, A. M. Sanchez, et al. "Microcracks in CVD diamond produced by scaife polishing". In: *Diamond and Related Materials* 144 (2024), p. 111008. DOI: 10.1016/j.diamond.2024.111008.

[188] J. Heupel, M. Pallmann, J. Körber, et al. "Fabrication and Characterization of Single-Crystal Diamond Membranes for Quantum Photonics with Tunable Microcavities". en. In: *Micromachines* 11.12 (2020), p. 1080. DOI: 10.3390/mi11121080.

[189] J. F. Ziegler and J. P. Biersack. "The Stopping and Range of Ions in Matter". en. In: *Treatise on Heavy-Ion Science: Volume 6: Astrophysics, Chemistry, and Condensed Matter*. Ed. by D. A. Bromley. Boston, MA, 1985, pp. 93–129. DOI: 10.1007/978-1-4615-8103-1_3.

[190] J. F. Ziegler, J. P. Biersack, and M. D. Ziegler. *SRIM : the stopping and range of ions in matter*. de. 2008.

[191] M. Posselt. "Crystal-trim and its application to investigations on channeling effects during ion implantation". In: *Radiation Effects and Defects in Solids* null.1 (1994), pp. 87–119. DOI: 10.1080/10420159408219774.

[192] G. Davies, S. C. Lawson, A. T. Collins, et al. "Vacancy-related centers in diamond". In: *Physical Review B* 46.20 (1992), pp. 13157–13170. DOI: 10.1103/PhysRevB.46.13157.

[193] V. Bushmakin, O. v. Berg, C. Sauerzapf, et al. *Two-Photon Interference of Photons from Remote Tin-Vacancy Centers in Diamond*. 2025. DOI: 10.48550/arXiv.2412.17539.

[194] S. A. Furman and A. V. Tikhonravov. *Basics of Optics of Multilayer Systems*. en. 1992.

[195] S. B. v. Dam, M. Ruf, and R. Hanson. "Optimal design of diamond-air microcavities for quantum networks using an analytical approach". en. In: *New Journal of Physics* 20.11 (2018), p. 115004. DOI: 10.1088/1367-2630/aaec29.

[196] S. Webster, Y. Chen, G. Turri, et al. "Intrinsic and extrinsic absorption of chemical vapor deposition single-crystal diamond from the middle ultraviolet to the far infrared". EN. In: *JOSA B* 32.3 (2015), pp. 479–484. DOI: 10.1364/JOSAB.32.000479.

[197] Y. Herrmann, J. M. Brevoord, J. Fischer, et al. "Laser-cut Patterned, Micrometer-thin Diamond Membranes with Coherent Color Centers for Open Microcavities". In: *Materials for Quantum Technology* 5.3 (2025), p. 035001. DOI: 10.1088/2633-4356/adfa5a.

[198] C. T. Nguyen. "Quantum Network Nodes Based on Diamond Qubits with an Efficient Nanophotonic Interface". In: *Physical Review Letters* 123.18 (2019). DOI: 10.1103/PhysRevLett.123.183602.

[199] T. G. Tiecke, K. P. Nayak, J. D. Thompson, et al. "Efficient fiber-optical interface for nanophotonic devices". EN. In: *Optica* 2.2 (2015), pp. 70–75. DOI: 10.1364/OPTICA.2.000070.

[200] M. J. Burek, C. Meuwly, R. E. Evans, et al. "Fiber-Coupled Diamond Quantum Nanophotonic Interface". In: *Physical Review Applied* 8.2 (2017), p. 024026. DOI: 10.1103/PhysRevApplied.8.024026.

[201] B. Zeng, C. De-Eknamkul, D. Assumpcao, et al. "Cryogenic packaging of nanophotonic devices with a low coupling loss <1 dB". In: *Applied Physics Letters* 123.16 (2023), p. 161106. DOI: 10.1063/5.0170324.

[202] K. Miyajima, Y. Kagotani, S. Saito, et al. "Superfluorescent pulsed emission from biexcitons in an ensemble of semiconductor quantum dots". en. In: *Journal of Physics: Condensed Matter* 21.19 (2009), p. 195802. DOI: 10.1088/0953-8984/21/19/195802.

[203] J. G. Bohnet, Z. Chen, J. M. Weiner, et al. "A steady-state superradiant laser with less than one intracavity photon". en. In: *Nature* 484.7392 (2012), pp. 78–81. DOI: 10.1038/nature10920.

[204] G. Haider, K. Sampathkumar, T. Verhagen, et al. "Superradiant Emission from Coherent Excitons in van Der Waals Heterostructures". en. In: *Advanced Functional Materials* 31.29 (2021), p. 2102196. DOI: 10.1002/adfm.202102196.

[205] G. Rainò, M. A. Becker, M. I. Bodnarchuk, et al. "Superfluorescence from lead halide perovskite quantum dot superlattices". en. In: *Nature* 563.7733 (2018), pp. 671–675. DOI: 10.1038/s41586-018-0683-0.

[206] M. Radtke, E. Bernardi, A. Slablab, et al. "Nanoscale sensing based on nitrogen vacancy centers in single crystal diamond and nanodiamonds: achievements and challenges". en. In: *Nano Futures* 3.4 (2019), p. 042004. DOI: 10.1088/2399-1984/ab5f9b.

[207] M. Zahedian, J. Liu, R. Vidrio, et al. “Modeling of Radiative Emission from Shallow Color Centers in Single Crystalline Diamond”. en. In: *Laser & Photonics Reviews* 17.4 (2023), p. 2200529. DOI: 10.1002/lpor.202200529.

[208] R. J. Epstein, F. M. Mendoza, Y. K. Kato, et al. “Anisotropic interactions of a single spin and dark-spin spectroscopy in diamond”. en. In: *Nature Physics* 1.2 (2005), pp. 94–98. DOI: 10.1038/nphys141.

[209] Q. Wu, Y. Zhang, X. Yang, et al. “A superradiant maser with nitrogen-vacancy center spins”. en. In: *Science China Physics, Mechanics & Astronomy* 65.1 (2021), p. 217311. DOI: 10.1007/s11433-021-1780-6.

[210] M. O. Scully and M. S. Zubairy. *Quantum Optics*. en. 1997.

[211] D. M. Lukin, M. A. Guidry, J. Yang, et al. “Two-Emitter Multimode Cavity Quantum Electrodynamics in Thin-Film Silicon Carbide Photonics”. In: *Physical Review X* 13.1 (2023), p. 011005. DOI: 10.1103/PhysRevX.13.011005.

[212] R. Reimann, W. Alt, T. Kampschulte, et al. “Cavity-Modified Collective Rayleigh Scattering of Two Atoms”. In: *Physical Review Letters* 114.2 (2015), p. 023601. DOI: 10.1103/PhysRevLett.114.023601.

[213] R. E. Evans, M. K. Bhaskar, D. D. Sukachev, et al. “Photon-mediated interactions between quantum emitters in a diamond nanocavity”. In: *Science* 362.6415 (2018), pp. 662–665. DOI: 10.1126/science.aau4691.

[214] J.-H. Kim, S. Aghaeimeibodi, C. J. K. Richardson, et al. “Super-Radiant Emission from Quantum Dots in a Nanophotonic Waveguide”. In: *Nano Letters* 18.8 (2018), pp. 4734–4740. DOI: 10.1021/acs.nanolett.8b01133.

[215] D. Meiser, J. Ye, D. R. Carlson, et al. “Prospects for a Millihertz-Linewidth Laser”. In: *Physical Review Letters* 102.16 (2009), p. 163601. DOI: 10.1103/PhysRevLett.102.163601.

[216] A. C. Santos, A. Cidrim, C. J. Villas-Boas, et al. “Generating long-lived entangled states with free-space collective spontaneous emission”. In: *Physical Review A* 105.5 (2022), p. 053715. DOI: 10.1103/PhysRevA.105.053715.

[217] A. Roulet and C. Bruder. “Quantum Synchronization and Entanglement Generation”. In: *Physical Review Letters* 121.6 (2018), p. 063601. DOI: 10.1103/PhysRevLett.121.063601.

[218] D. Braun, G. Adesso, F. Benatti, et al. “Quantum-enhanced measurements without entanglement”. In: *Reviews of Modern Physics* 90.3 (2018), p. 035006. DOI: 10.1103/RevModPhys.90.035006.

[219] M. Koppenhöfer, P. Groszkowski, H.-K. Lau, et al. “Dissipative Superradiant Spin Amplifier for Enhanced Quantum Sensing”. In: *PRX Quantum* 3.3 (2022), p. 030330. DOI: 10.1103/PRXQuantum.3.030330.

[220] Physikalisches Institut, Karlsruhe Institute of Technology. *Quantenfaser – Glasfaser-Teststrecke für Quantennetzwerke. Available at: https://www.phi.kit.edu/quantenfaser.php.* 2024.

[221] S. Bogdanović, M. S. Z. Liddy, S. B. van Dam, et al. “Robust nano-fabrication of an integrated platform for spin control in a tunable microcavity”. In: *APL Photonics* 2.12 (2017), p. 126101. DOI: 10.1063/1.5001144.

[222] J. Fischer, Y. Herrmann, C. F. J. Wolfs, et al. “Spin-photon correlations from a Purcell-enhanced diamond nitrogen-vacancy center coupled to an open microcavity”. en. In: *Nature Communications* 16.1 (2025), p. 11680. DOI: 10.1038/s41467-025-66722-8.

[223] J. M. Brevoord, J. F. Geus, T. Turan, et al. *Quantum Frequency Conversion of Single Photons from a Tin-Vacancy Center in Diamond*. 2025. DOI: 10.48550/arXiv.2509.01661.

[224] V. Krutyanskiy, M. Canteri, M. Meraner, et al. “Telecom-Wavelength Quantum Repeater Node Based on a Trapped-Ion Processor”. In: *Physical Review Letters* 130.21 (2023), p. 213601. DOI: 10.1103/PhysRevLett.130.213601.

[225] S. Staacks, S. Hütz, H. Heinke, et al. “Advanced tools for smartphone-based experiments: phyphox”. en. In: *Physics Education* 53.4 (2018), p. 045009. DOI: 10.1088/1361-6552/aac05e.

Erklärung zum Einsatz generativer KI

Der Einsatz generativer künstlicher Intelligenz (KI), insbesondere in Form großer Sprachmodelle, gewinnt in Forschung und wissenschaftlicher Praxis zunehmend an Bedeutung. Unterstützende Anwendungen zur sprachlichen Überarbeitung und zum Copyediting sind mittlerweile so weit verbreitet, dass führende wissenschaftliche Fachverlage hierfür keine gesonderte Offenlegung mehr vorsehen. Vor diesem Hintergrund wurde die vorliegende Arbeit unter Beachtung der Leitlinien zum Einsatz generativer KI des Karlsruher Instituts für Technologie (Stand: 30.06.2025) sowie unter Berücksichtigung der Grundsätze guter wissenschaftlicher Praxis der Deutschen Forschungsgemeinschaft (DFG) und der Handlungsempfehlungen der Helmholtz-Gemeinschaft erstellt.

In dieser Arbeit wurde generative KI ausschließlich als unterstützendes Werkzeug für klar abgegrenzte, nicht-inhaltliche Aufgaben eingesetzt. Dies umfasste insbesondere die sprachliche Überarbeitung von Textpassagen (z. B. hinsichtlich Grammatik, Stil und Verständlichkeit), die technische Unterstützung bei der Erstellung und Formatierung von LaTeX-Dokumenten (z. B. Gleichungen, Tabellen und Abbildungen) sowie punktuelle Hilfestellungen bei der technischen Umsetzung von Programmcode, etwa in Bezug auf Syntax, Visualisierung oder numerische Auswertung.

Nicht eingesetzt wurde generative KI zur Entwicklung wissenschaftlicher Fragestellungen, zur theoretischen Modellbildung, zur Generierung, Analyse oder Interpretation experimenteller oder numerischer Daten, zur Ableitung wissenschaftlicher Schlussfolgerungen oder zur Bewertung der wissenschaftlichen Qualität, Originalität oder Relevanz der in dieser Arbeit dargestellten Ergebnisse.

Die Verantwortung für sämtliche Inhalte dieser Dissertation liegt vollständig beim Autor. Alle durch generative KI unterstützten Inhalte wurden kritisch geprüft, eigenständig überarbeitet und inhaltlich verifiziert. Die Verwendung generativer KI erfolgte in dem Bewusstsein ihrer Grenzen sowie unter Wahrung der geltenden rechtlichen, ethischen und wissenschaftlichen Standards.

Danksagung

Manchmal ist es schon ein bisschen random. Vor knapp fünf Jahren noch kurz davor, in Göttingen zu bleiben und nach dem Master eine Promotion dranzuhängen, und jetzt in Karlsruhe meine Doktorarbeit abzuschließen – nach knapp fünf Jahren in der besten Arbeitsgruppe und in der Nähe meiner besten Freunde und meiner Familie. Hätte eigentlich kaum besser kommen können, und daran haben so unglaublich viele Menschen Anteil.

Allen voran möchte ich **David** danken für die Möglichkeit, in deiner Gruppe und unter deiner Betreuung an meiner Promotion zu arbeiten. Ohne dich hätte es wohl kein Karlsruhe-Comeback gegeben und somit auch nicht die wundervolle akademische und persönliche Reise der letzten Jahre. Aber selbstverständlich geht dein Beitrag weit über ein „Danke für den Job“ hinaus. Deine Ideenvielfalt, deine Begeisterungsfähigkeit und die pure und ehrliche Freude, mit der du einem entgegnest, wenn man von Ergebnissen (auch wenn es noch so kleine Schritte sind) berichtet, sind so ansteckend, dass sie mich durch manche ernüchternde Phasen getragen haben. Vielen Dank für alle weinlastigen Abende inklusive Marktlückenbesuch, für viele offene Gespräche in den nicht allzu rosigen Wochen und für deine persönliche Nähe zu uns allen, womit du einen riesigen Anteil an der außergewöhnlichen Gruppenatmosphäre hast, die einen jeden Morgen mit einem Lächeln aufs Rad hüpfen lässt.

Ein großer Dank gilt zudem **Wolfgang**, selbstredend für das Übernehmen der Zweitbetreuung, aber eigentlich noch viel mehr fürs Übernehmen des persönlichen Kryo-Kummerkastens. Du kannst dir gar nicht vorstellen, wie glücklich mich das gemacht hat, als du innerhalb von einer halben Stunde am Wochenende geschwind meinen Kryo umgebaut hast, um meine finalen und wichtigsten Messungen noch einzutüten. Vielen, vielen Dank!

Wir hatten es schon vom Lächeln, mit dem ich morgens aus dem Bett hüpfe. Vielleicht ist das etwas übertrieben, aber wenn mich meine Freunde oder meine Familie gefragt haben, wie es an der Uni läuft, war meine Antwort häufig dieselbe: Auch wenn es manchmal etwas schleppend im Labor vorangeht (lässt sich wohl kaum vermeiden), gehe ich super gerne ins Labor, ins Büro, und vor allem in die Kaffeeküche. Es ist wie damals in der Schule: Man trifft sich mit seinen Freunden. Und da kommen die Hungerharken ins Spiel. Ein riesiger Teil der Motivation und meiner guten Laune in der Uni kommt durch euch, jeden einzelnen, und dafür bin ich mega dankbar.

- **Andras.** Vom Mikrowellen-Masteranden zum Erfinder des Karlsruher Quanteninternets (good luck). Du als Chefingenieur hast einen riesigen Anteil an einem Großteil

dieser Arbeit. Aber nicht nur dafür danke, sondern auch für alle musikerfüllten, MacGyver-style Laborstunden, für das Übernehmen der immensen Kaffeeverantwortung und für alle Schmunzler (bis lauten Gelächters) deines staubtrockenen Humors. Es war mir ein Fest!

- **Evgenij.** Danke für alle gewonnenen Wetten und Bierpongduelle! Spaß beiseite: Ich habe es unglaublich genossen, mit dir jahrelang im Büro zu sitzen, sich gegenseitig bis kurz vors Limit zu piesacken (google das ruhig), um sich danach gemeinsam bei Spaß und Bier zu amüsieren. Ich drücke dir alle Daumen der Welt für deine Jobsuche, du rockst das!

- **Ioannis.** El Greco, du bist quasi auch ein Hunger-Familienmitglied, und darüber bin ich sehr glücklich. Danke für deinen Olivenöl-Rabattcode Ioannis10 (streng geheim) und deinen Support im Labor und beim Muscle-Up-Lernen. Ich bleib da dran! Und du gönnst dir mal 'ne Massage, um deinen Nacken zu lockern.

- **Jannis.** Cavity-Kummerkasten deluxe. Vielen, vielen Dank für jeden Input (beim Korrekturlesen, aber auch sonst über die gesamte Promotion) und für jedes Mal Zuhören, wenn die beiden sich gegenüberstehenden Spiegel nicht das taten, was sie sollten (also oft). Bei dir wusste man eigentlich immer, dass es hilfreich wird. Und ganz viel Erfolg bei der Jobsuche, ich würde dich einstellen.

- **Jeremias.** Mitstreiter von Anfang bis Ende. Ich bin mega dankbar für dich als durchgehenden Büro- und Diamantbuddy, für das traditionelle freitägliche Nutellacroissantfrühstück, für deine unglaubliche Hilfsbereitschaft und freue mich sehr auf den Denver-Trip im März. Und ich musste aufpassen, hier nicht komplett in Superlativen zu verfallen – hättest du auf jeden Fall verdient! Ganz dickes Danke.

- **Jonas.** Jooooonis Wege sind unergründlich, aber eins steht fest: Deine fast unerschütterlich gute Laune (wenn morgens Keeeeri durch den Gang hallt) ist ansteckend, und ohne den konstanten, ebenso unerschütterlichen IT-B-Support wäre ich an vielen Stellen verzweifelt. Ich bin definitiv sehr dankbar, dass wir die komplette PhD-Zeit zusammen malochen, feiern und verzweifeln konnten. Und entschuldige meine begrenzte Aufmerksamkeitsspanne bei unseren grundlegendsten Physikdiskussionen.

- **Dr. Pallmann.** Es war mir ein riesiges Vergnügen, mit dir persööööönlich die ersten Jahre zusammen im Labor stehen zu dürfen, beim Großmeister höchstpersönlich in die Cavity-Grundausbildung gehen zu dürfen, mit 80er-Vibes im Labor und Orangenjonglage nach Feierabend – danke!

- **Nick.** Hellooooooow! Thank you for all the delicious cakes, all the wonderful teas, and even for all the exotic food that I stubbornly refused to eat. You were such a great, lively, funny, and truly lovely addition to the group. Tschüssi Süßes!

- **Shalom.** Ich bin jetzt auch nicht unbedingt bekannt dafür, Nervosität oder Stress auszustrahlen, aber falls das irgendwann mal passieren sollte, dann komme ich zu dir.

Danke fürs Ruhepolsein, danke für sämtliche Tea-Teas, und ich drücke alle Daumen, dass du eine wunderbare Zeit bei deinem USA-Aufenthalt hast.

- **Svenja.** Auch wenn erst gegen Ende (wobei das auch schon wieder ewig her ist) hinzugestoßen, ein wundervoller Zugewinn für die Gruppe. Danke für deine Leichtigkeit und konstant gute Laune (wahrscheinlich kommt's vom vielen Skifahren). Der einzige Moment, wo man dich mal verbissen sieht, ist beim monatlichen Erdnussmus-Glattrühren!

- **Timon.** Ich warte eigentlich nur drauf, dass du endlich in die Politik gehst und ich mein Kreuz bei dir setzen kann, jetzt, wo der Heiland das Feld verlassen hat. Ich habe alle Kaffeepausen, alle Physikdiskussionen, alle Polit-Talks (uni-intern und extern) mit konstant 10 % Stromberg-Slang sehr genossen.

- **Vishnu.** You were the only person who immediately noticed when I entered the room that I had had a rough night. Stay as considerate and thoughtful as you are, and keep being passionate about your home - I loved listening to all your hometown stories. One day I'll visit you and finally eat some proper mangos!

Auch außerhalb der AG Hunger möchte ich einigen weiteren Menschen danken, die mich bei der Arbeit unterstützt haben: Steffi und Claudia, fürs Rückenfreihalten und den immer unkomplizierten, angenehmen und sehr kurzen Draht. Herrn Meyer und seinem Feinmechanik-Team für alle noch so simplen und komplizierten Fertigungen. Herrn Rose für so ziemlich alles Handwerkliche im Labor, und ganz besonders für den ultraschnellen Kühlwasserumbau, der die letzten und wichtigsten Ergebnisse dieser Arbeit ermöglicht hat. Dem E-Werkstatt-Team für alle Lötarbeiten und das Reparieren meiner eigenen kläglichen Lötversuche. Dennis, Alex und Marcel für sämtlichen Kryo-Support. Manuel und Thomas fürs Qlibri-Troubleshooting. Máté für die riesige Hilfe beim Wickeln und Betreiben der supraleitenden Spule. Steffen Pfeifer (IPQ) für den kurzfristigen Splice-Service. Und wahrscheinlich noch 20 anderen Personen, die ich vergessen habe.

Außerdem hatte ich das Privileg, durch die Max-Planck-School of Photonics (MPSP) an vielen und außergewöhnlich schönen Spring/Autumn Schools, MPS Days und anderen Events teilzunehmen. Dafür ein riesiges Dankeschön an alle MPSPler. Ich bin froh, so viele liebenswerte Menschen kennengelernt haben zu dürfen. Shave the Future!

Wenn ich jetzt anfange, bei Family&Friends genauso ausführlich loszulegen, dann wird's ein Buch. Deswegen nur ganz kurz: Vielen Dank an meine wundervollen Freunde, die mir mit Tante-Edith-Mittagspausen, Abendkochdates, Fußball-Watchpartys, Gutenbergplatz-Samstagsfrühstücken und Infernoaufgüssen den Alltag versüßt haben – unbezahlbar.

Vor einem Jahr hätte ich den Part hier noch etwas leichtherziger geschrieben: Eine ganz, ganz dicke Umarmung an meine Familie, an Mama, meine beiden Brüder und alle, die dazugehören. Und eine noch viel dickere, aber leider etwas andere Umarmung an Papa, der bestimmt irgendwo stolz zugeschaut hat – du fehlst!